Title
Solar Impulsive Energetic Electron Events

Author
Wang, Linghua

Publication Date
2009

Peer reviewed|Thesis/dissertation

Solar Impulsive Energetic Electron Events

by

Linghua Wang

A dissertation submitted in partial satisfaction of the

requirements for the degree of

Doctor of Philosophy

in

Physics

in the

Graduate Division

of the

University of California, Berkeley

Committee in charge:

Professor Robert P. Lin, Chair
Professor Stuart D. Bale
Professor Imke de Pater

Fall 2009

Solar Impulsive Energetic Electron Events

by

Linghua Wang

Abstract

Solar Impulsive Energetic Electron Events

by

Linghua Wang

Doctor of Philosophy in Physics

University of California, Berkeley

Professor Robert P. Lin, Chair

The Sun is capable of accelerating ions from ~ tens of keV up to tens of GeV and electrons from ~ tens of eV up to hundreds of MeVs in transient events such as flares and fast coronal mass ejections (CMEs). The energized particles escaping into the interplanetary medium are referred to as Solar Energetic Particle (SEP) events. The great majority of SEP events are impulsive SEP events that are dominated by ~1-100 keV electrons and ~MeV/nucleon ion emissions, with enhanced ^{3}He/^{4}He ratios up to 10^4 times the coronal values (also called electron/^{3}He-rich SEP events). This thesis is focused on solar impulsive energetic electron events, the electron part of impulsive SEP events, using electron observations from the 3-D Plasma and Energetic Particle instrument (3DP) on the WIND spacecraft near the Earth.

First, I present the first comprehensive statistical study of solar energetic electron events over almost one solar cycle. I find that the occurrence rate of solar electron events shows a strong solar-cycle variation; after correction for the background effect, the estimated occurrence frequency exhibits a good power-law distribution, and the estimated occurrence rate near the Earth is ~1000/year at solar maximum and ~30/year at solar minimum for the instrumental sensitivity (~2.9×10^{-4} (cm^2 s str eV)$^{-1}$ for the 40 keV channel) of WIND/3DP, about one order of magnitude larger than the observed occurrence rate. Solar energetic electron events have a one-to-one association with type III radio bursts and a poor association with flares, but a close association with ^{3}He-rich ion emissions. These ^{3}He-rich electron events also have a poor association with flares but a close (~ 60%) association with west-limb CMEs.

Then I present two case studies: one investigating the temporal relationship between solar impulsive electrons and type III radio emissions, and the second studying the temporal relationship between solar impulsive electrons and ^{3}He-rich ions. For both studies, I chose nearly scatter-free electron events and developed a forward-fitting method that assumes an isosceles triangular injection profile (equal rise and fall times) at the Sun. I find that in electron/^{3}He-rich SEP events, the low-energy (~0.4 to 6-9 keV) electron injection starts ~9 min before the coronal release of the type III radio burst; the high-energy (~13 to ~300 keV) electron injection starts ~8 min after the type III burst; and the injection of ~MeV/nucleon, ^{3}He-rich ions begins ~1 hour

later. I also find that the selected electron/^{3}He-rich SEP events have a remarkable one-to-one association with fast west-limb CMEs, and most of the associated CMEs are narrow.

Finally, I present a case study to investigate the propagation of different energy electrons in solar impulsive electron events. I find that in the interplanetary medium, low-energy (<~ 10-30 keV) and high-energy (>~ 10-30 keV) electrons propagate differently, with more scattering at high energies. Such scattering appears to be caused by resonance with waves/turbulence at scale greater than ~ the thermal proton gyroradius in the solar wind. Although a transition to more scattering occurs at energies where the electron injection delays are detected, I show that the scattering is not enough to produce these delays.

Based on the results of this thesis, a coherent picture of electron/^{3}He-rich SEP events can be built up. At the Sun, the low-energy (~0.4 to 6-9 keV) electrons may be accelerated in jets that are ejected upward from magnetic reconnection sites between closed and open field lines; these low-energy electrons generate the type III radio bursts. The jets may appear as CMEs high in the corona, and the high-energy (~13 to ~300 keV) electrons may then be accelerated at >~ 1 R_S by CMEs, acting on the seed electrons provided by the low-energy injection. The ~MeV/nucleon, ^{3}He-rich ions may be accelerated by selective resonance with electron-beam generated waves and/or by fast, narrow CMEs. In the interplanetary medium, both low and high energy electrons often propagate nearly scatter-free, but the high-energy electrons experience more scattering than the low-energy electrons, likely by waves/turbulence generated by solar wind ions. In the future, the upcoming missions to visit the inner heliosphere within ~0.2 AU (Solar Orbiter) or ~10 R_S (Solar Probe Plus) will provide the near-Sun measurements to improve our understanding of SEP events.

献给我的父母

This thesis is dedicated to my parents.

Table of Contents

List of Figures

List of Tables

Acknowledgments

It is a pleasure to express my gratitude to all the people who have helped and inspired me during my Ph.D. study.

My utmost appreciation to my advisor, Professor Robert P. Lin, for his encouragement, support and guidance during all the time of my research and writing of this thesis. His perpetual enthusiasm in research, rigorous scientific attitude, and strict scientific thinking will always influence my career development in a positive way.

My sincere thanks to my committee, Professor Stuart Bale and Professor Imke de Pater, for reviewing an earlier version of this thesis and providing valuable comments and suggestions.

Special thanks to my colleagues at Space Sciences Lab, especially Säm Krucker, George Parks, Davin Larson, Hugh Hudson and Stuart Bale, and to my collaborators Jack Gosling, Glenn Mason and Gang Li, for their expertise, help and insightful conservations. Many thanks to my fellow graduate students at Space Sciences Lab for all their help over the past seven years.

Warm thanks to all of my friends for the wonderful conversations and camaraderie, especially Xiaomei and Lihua, who have always kept my spirits up with their positive and happy attitudes towards life.

Last but not least, my deepest gratitude to my parents Jianzhi Luo and Zhengliang Wang, my sister Chunhua, and my brother Haiqing, for everything they had done, especially their continued effort to try to understand the topic of this thesis.

1. Introduction

1.1 The Sun

The Sun, the center of our Solar System, was born about 4.6 billion (4,600,000,000) years ago from the gravitational collapse of a vast cloud of gas and dust. Material in the center of the cloud (i.e., the core of the Sun) was squeezed so tightly that it became hot enough (~1.5×10^7 °K) to ignite nuclear fusion in which four hydrogen nuclei come together to create one alpha particle or helium nucleus and the difference in mass is released as energy according to Albert Einstein's mass-energy equivalence formula $E = mc^2$. Every second, the fusion process converts 600 million tons of hydrogen into helium, releasing the energy to keep up the high temperature and gas pressure in the core and stop further gravitational collapses. Now the Sun is made up of about 2×10^{30} kilograms of gas (about 99.9% of the total mass of the solar system), consisting of ~75% hydrogen, ~24% helium and less than 2% of heavier elements including iron, nickel, oxygen, silicon, sulfur, magnesium, carbon, neon, calcium, and chromium. It is estimated that the Sun will run out of the fuel in about 5 billion years.

The Sun is the closest star to Earth, with an average distance of 1 AU (astronomical unit; about 1.5×10^8 kilometers). It has always been the most important celestial body in our sky, and has inspired mythological stories in cultures around the world, including those of the Aztecs of Mexico, the Chinese, the ancient Egyptians, and many others. For example, one Chinese myth tells that a solar eclipse was caused by the dog of heaven biting off a piece of the sun, and the referred event is believed to have occurred around 2160 BC.

1.1.1 Solar structure

The Sun is the largest object in the solar system. Its body has four layers from the inside to the outside (see Figure 1.1): the core, the radiation zone, the convection zone and the photosphere, with a total radius R_S of ~6.9×10^8 m (equal to ~ 109 times the Earth's radius R_E). The three layers below the photosphere are opaque to visible light. It is generally thought that the energy produced by nuclear fusion in the core (0 to ~0.3 R_S) is transported outward, in turn, by photons through the radiation zone (~0.3 to ~0.7 R_S) and by convective motions of gas through the convection zone (~0.7 to 1.0 R_S), before reaching the photosphere. It is also hypothesized that the turbulent motions of plasma below the photosphere generate solar magnetic fields (the solar dynamo). The photosphere, the visible surface of the Sun, is a ~ 500-kilometer-thick layer where gas becomes tenuous enough so that light from inside the Sun can finally freely escape into space. The photosphere has a black-body temperature T of ~5800 °K and appears as a bright disk, but often with dark spots – sunspots on it that are marked by intense magnetic field and cooler temperature (about 3700 °K at the sunspot's center). The observations of sunspots provide the first evidence that the Sun rotates on it axis. Since the Sun is gaseous, its surface rotates at different rates for different latitudes ("differential rotation"), e.g., the rotation period is approximately 25.4 days at the equator and 36 days at the poles.

Above the photosphere is the atmosphere of the Sun (see Figure 1.1), consisting of three regions: the chromosphere, the corona and the heliosphere. The inner region is the chromosphere (from the Greek root chromos, meaning color), so-called because it appears as a reddish "ring of fire" during a total solar eclipse when the Sun's disk and photosphere are covered by the Moon.

The chromosphere is roughly 2000 kilometers thick, with the temperature increasing outward to 20,000 °K at its top. Its visual spectrum is dominated by the deep red Hα spectral line of hydrogen (wavelength of 656.3 nanometers) that is emitted by hot, low density gases. The next region is the corona that extends millions of kilometers into space. The corona is visible as a pearly-white glow around the Sun's disk during an eclipse, caused by sunlight scattering off free electrons. Its temperature is about 1-3 million °K, much hotter than the Sun's surface, for reasons that have not been fully understood. The uppermost region of the Sun's atmosphere is the heliosphere. It is a vast bubble in space "blown" into the interstellar medium (the hydrogen and helium gas that permeates the galaxy) by the solar wind, extending out well beyond the orbit of Pluto. The solar wind, a stream of charged particles ejected from the corona, carries the Sun's magnetic field through the heliosphere (see § 1.2.5.1).

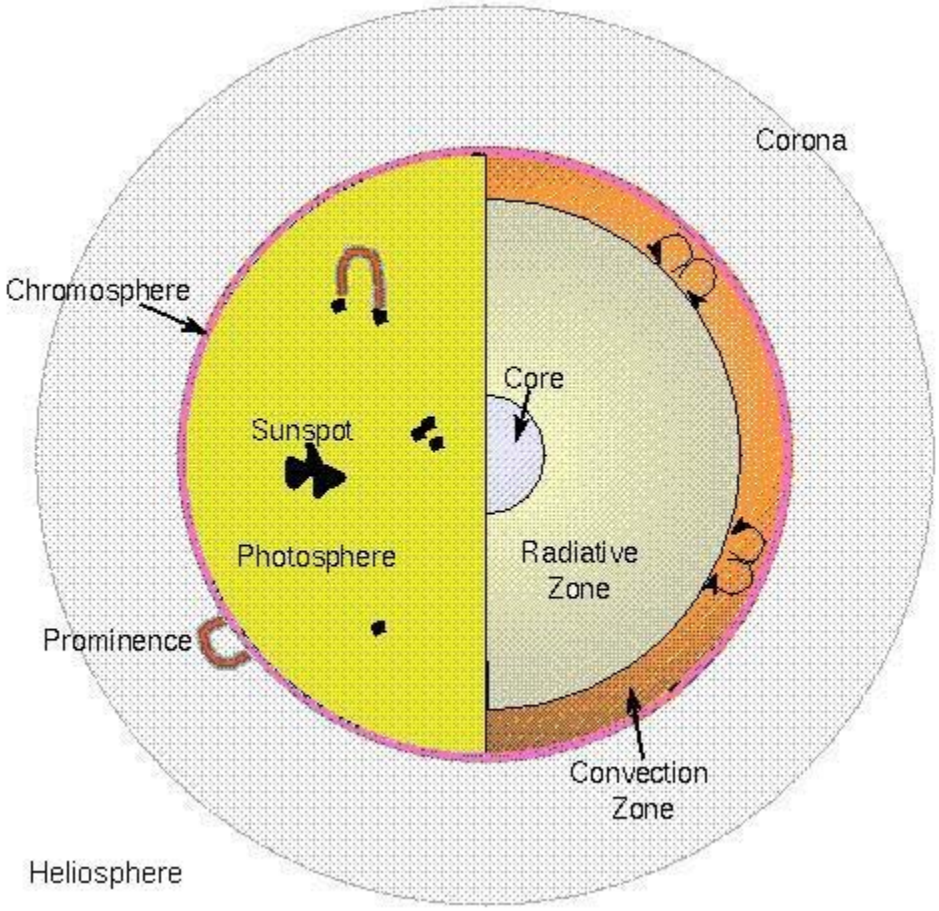

Figure 1.1: Sketch of the Sun's structure.

1.1.2 Solar activities

The Sun's activities range from producing dark sunspots on the photosphere to expelling matter in huge explosions called coronal mass ejections, and they all follow an approximate 11-year "solar cycle" from quiet minimum to active maximum and then to quiet minimum. The longest recorded aspect of solar cycles is changes in sunspots. The first record of sunspots was made by Chinese astronomers around 800 BC. In 1610, astronomer Thomas Harriot and others began using the telescope to make observations of sunspots and their motions. In 1843, Heinrich Schwabe first discovered the cyclic variation of the number of sunspots, after 17 years of observations. This led Rudolf Wolf to start systematic observations of sunspots in 1848 that have been maintained by his successors. Figure 1.2 summaries the ~ 400 years of sunspot number observations since 1610. The most evident feature is the average 11-year periodic cycle, showing the natural waxing and waning of solar activity, which is related to a 22-year cycle for the reversal of the Sun's magnetic field. The Sun has also shown considerable activity variability on longer time scales, including the Maunder Minimum (~ 1645 to 1715) when almost no sunspots were observed, the less severe Dalton Minimum (~ 1790 to 1830), and the Modern Maximum (~ 1950 to 2004) with increased sunspot activity; but the causes for these long-scale variations are not understood.

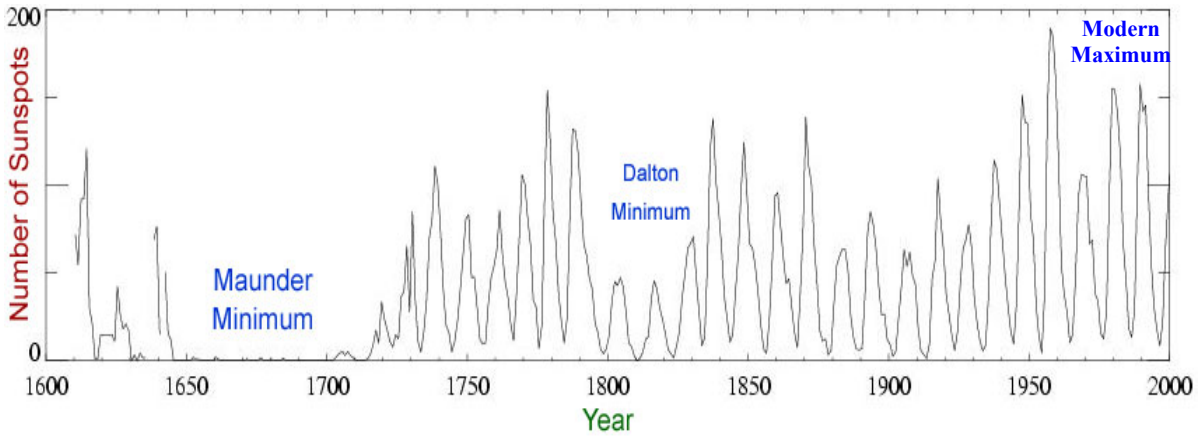

Figure 1.2: The yearly sunspot number from 1610 through 2000. The observed solar cycles range from 9 years to 14 years, with an average length of ~ 11 years.

1.1.3 Solar explosive phenomena

Although nearly everything that happens in and on the Sun affects the Earth and the interplanetary space, two kinds of explosive solar phenomena impact most severely: the solar flare and the coronal mass ejection (CME).

1.1.3.1 Solar flares

A solar flare is a sudden, rapid, intense and localized variation in brightness (Figure 1.3), resulting from a sudden release of magnetic energy stored in the solar atmosphere. It typically occurs low in the corona, heats plasma to tens of million °K, accelerates electrons, protons and heavier ions to near the speed of light *c*, and emits radiations across virtually the entire electromagnetic spectrum, from radio waves to X-rays and γ-rays. The energy released during a solar flare is typically on the order of 10^{27} ergs per second. Large flares can emit up to 10^{32} ergs of energy in about 10^{3} seconds. The first recorded observation of a solar flare was made in 1859 by Richard Carrington [Carrington, 1859], who saw a sudden brightening in white light while observing sunspots and referred to this phenomenon as "two patches of intensely bright and white light", an "outburst", and a "sudden conflagration". In the 1940s, solar flares came to be called "flares", and Harold Newton first used this term in the title of a paper [Newton, 1943].

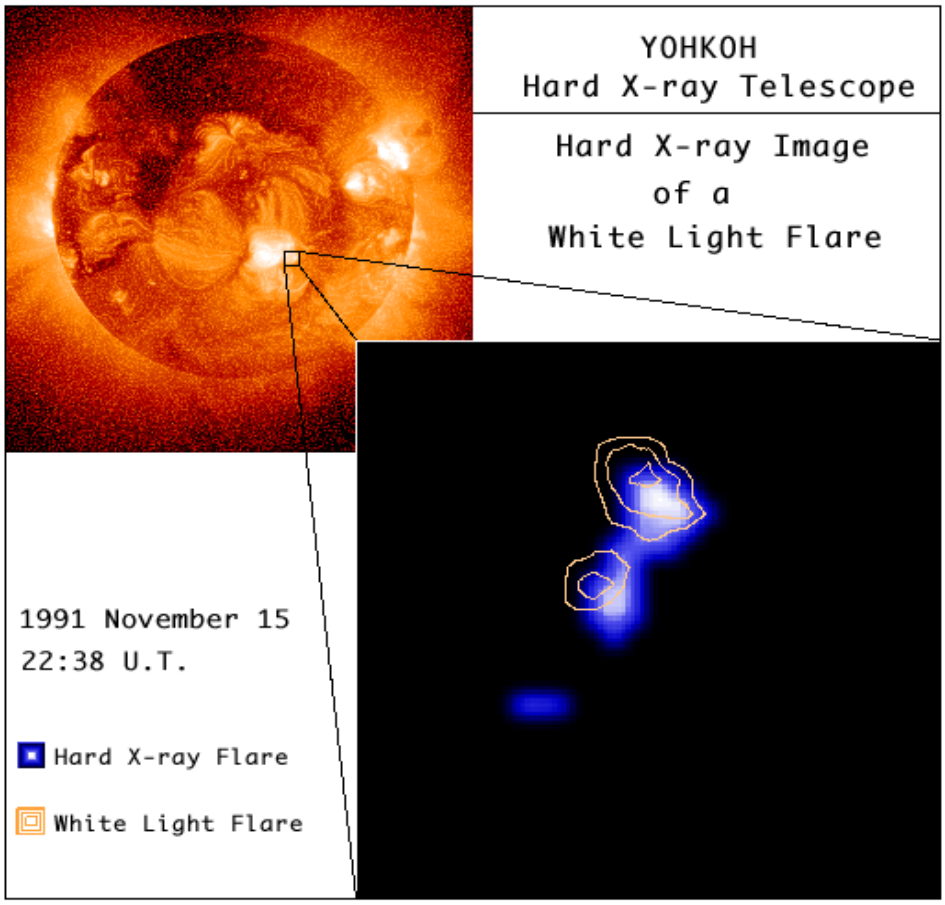

Figure 1.3: Example of the solar flare observed in while light and X-rays. The image in the top left corner shows the full Sun detected in soft X-rays by the YOHKOH satellite. The location of the flare is shown by the small rectangle that is expanded to show the white light (contours) and hard X-ray (blue-gray scale) images.

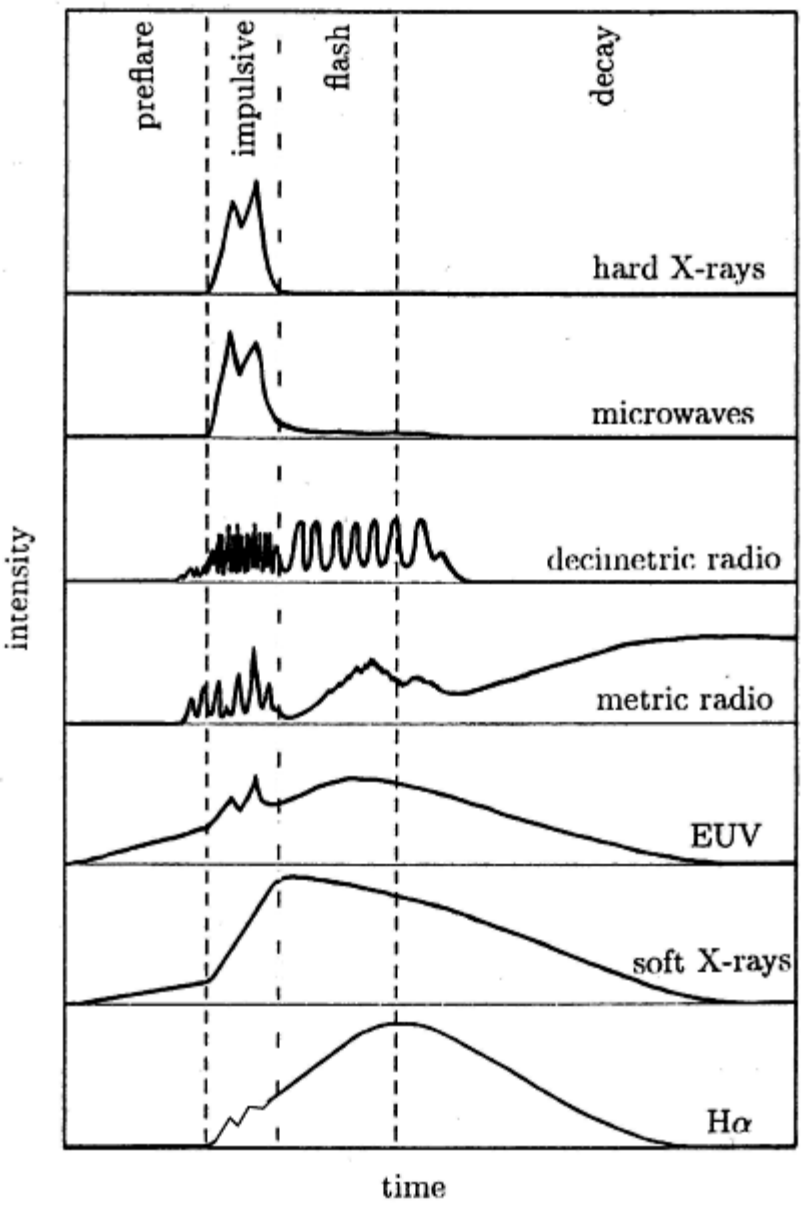

Figure 1.4: A schematic evolution of the flare intensity at several wavelengths. The various phases indicated at the top vary greatly in duration. In a large event, the preflare phase typically lasts a few minutes, the impulsive phase 3 to 10 minutes, the flash phase 5 to 20 minutes, and the decay one to several hours. Adopted from [Benz, 2002].

Solar flares often start with small-scale brightening in soft X-rays and EUV due to the plasma heating in the flare region during the preflare phase (see Figure 1.4). Most of the flare energy is released in the impulsive phase. This phase is characterized by hard X-ray, γ-ray, non-thermal (synchrotron) microwaves and white-light continuum emissions, indicating strong acceleration of both electrons and ions. Some high-energy particles are trapped and produce intensive radio emissions. The growing thermal soft X-ray and Hα emissions finally reach their

maximum after the impulsive phase. The rapid increase in Hα intensity and line width has been termed the flash phase that coincides largely with the impulsive phase. Finally, the flare develops gradually into the decay phase, during which the thermal flare emissions disappear.

Solar flares develop almost exclusively in magnetic active regions. The frequency of solar flares coincides with the Sun's 11-year cycle. At solar minimum, active regions are small and rare, and solar flares occur about once per day; at solar maximum, active regions increase in size and number, and solar flares occur at an average rate of ~10-20/day [Crosby et al., 1993]. Large flares are less frequent than smaller ones. The "importance" of solar flares are typically classified as A, B, C, M or X according to the peak flux (W/m²) of the 1-8 Å soft X-rays measured by GOES (the Geostationary Orbiting Environmental Satellites) near the Earth (See Figure 1.5). X-class flares correspond to a GOES flux in excess of 10^{-4} W/m², and successive classifications decrease in decades; within a class there is a linear scale from 1 to 9, e.g., C1 to C9, and X1 to X9.

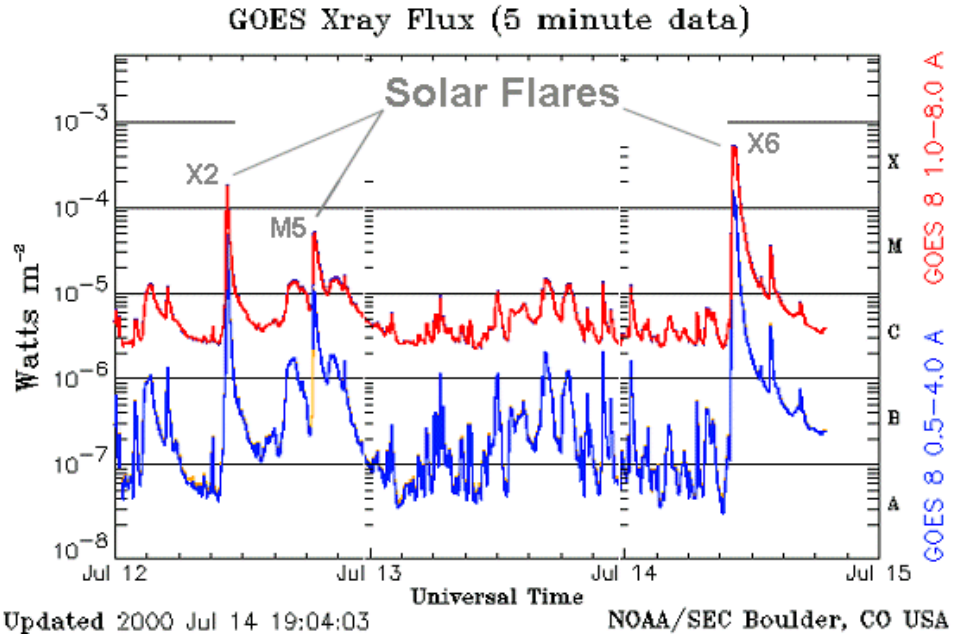

Figure 1.5: Example of Soft X-ray flare classification. The red curve represents the total flux in the band of 1 to 8 Å, and the blue curve is the flux in 0.5 to 4 Å.

1.1.3.2 CMEs

A CME is a bubble of plasma and embedded magnetic field that is ejected from the solar corona into the interplanetary space. The first record of a CME was probably made during the total solar eclipse on July 18, 1860 (Figure 1.6), and the first "modern" detection was made on December 14, 1971 by Richard Tousey [1973] using the white-light coronagraph on the 7th Orbiting Solar Observatory (OSO-7) satellite. Since the 1970s, CMEs have been detected usually with spacecraft-mounted white-light coronagraphs which employ an occulting disk to block out the Sun's disk creating an "artificial" solar eclipse and measure the visible light scattering off free electrons in the corona to determine the density distribution of those electrons (see Figure

1.7). Their occurrence frequency varies with the solar cycle, from about 0.5/day near the solar minimum to > 5/day near the solar maximum [Gopalswamy et al., 2004].

CMEs carry a mass of ~10^{13}-10^{16} g and an energy of ~ 10^{27}-10^{32} ergs [Vourlidas, 2002] into the interplanetary space. They range in speed from ~30km/s to ~2600 km/s with an average of ~400 km/s, and in angular width from a few degrees to > 300° with an average of ~50° [Yashiro et al., 2004]. During their propagation, CMEs disrupt the solar wind and the interplanetary magnetic field (IMF). When the speed of the CME in the frame moving with the solar wind is faster than the local fast magnetosonic speed, the leading edge of the CME will drive shock waves before it that can energize particles up to >~ GeVs [Kahler, 1994]. When CMEs reach the Earth, they can seriously disturb the Earth's environment, especially the terrestrial magnetic fields.

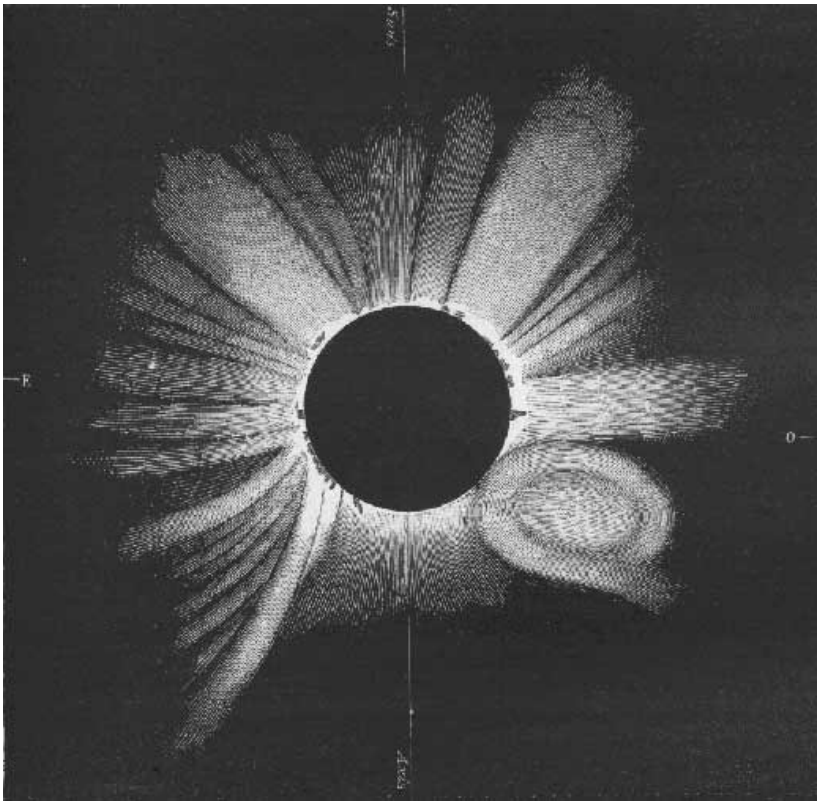

Figure 1.6: The first sketch of a CME during the 1860 total solar eclipse. The peculiar feature in the southwest (lower right) portion of the corona likely represents a CME.

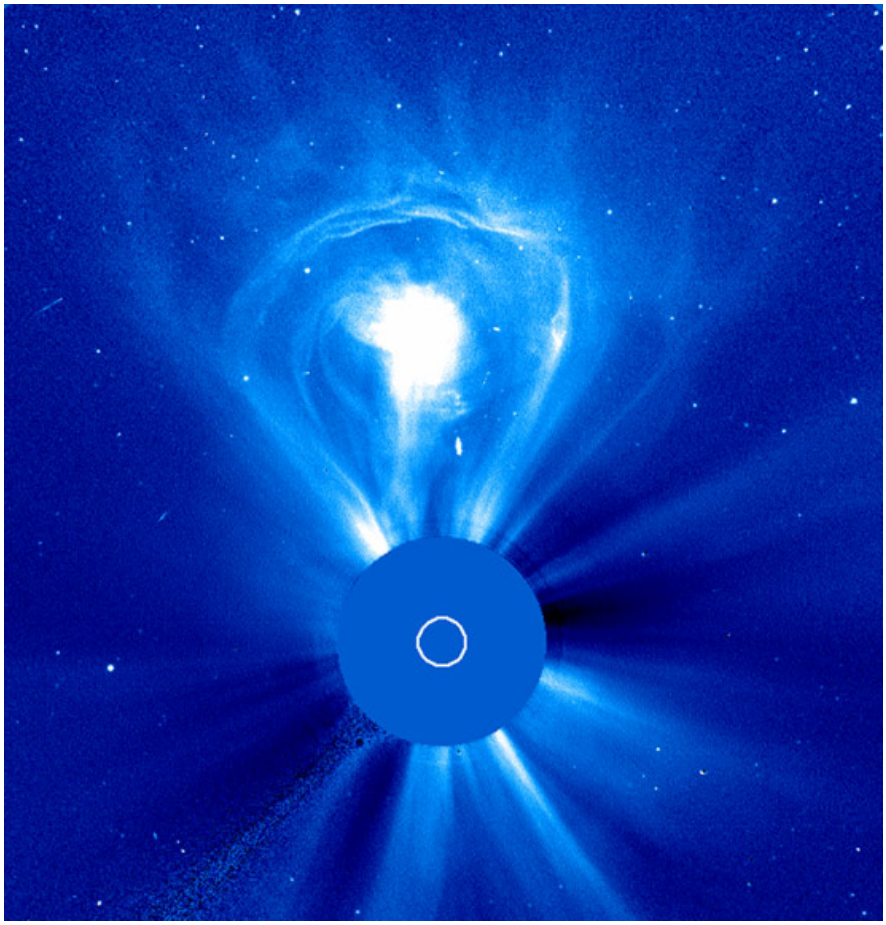

Figure 1.7: Example of a CME imaged by LASCO (The Large Angle Spectrometric Coronagraph) white-light coronagraphs on board the SOHO (Solar and Heliospheric Observatory) satellite. Dense plasma structures in the corona become visible via photospheric light Thomson-scattered off the free electrons in the plasma, in the color-scaled image. A typical CME consists of three parts: a cavity of low electron density, a dense core embedded in this cavity, and a bright leading edge.

1.1.3.3 Flare/CME models

Both solar flares and CMEs are believed to be driven by energy release from the magnetic field, involving the magnetic reconnection[†]. These two phenomena also appear to have some correlation: about 60% of M-class and stronger flares are associated with CMEs [Andrews, 2003], and about 50% of CMEs are associated with flares [Sheeley et al., 1983; St. Cyr & Webb, 1991; Harrison, 1995]. There are many attempts to model solar flares and CMEs, but here we only describe two popular field configurations which seem to account for most of the essential geometric features.

[†] Magnetic reconnection is a process whereby magnetic field lines from different magnetic domains break and reconnect in the magnetic diffusion region, rapidly converting magnetic energy into thermal and kinematic energies.

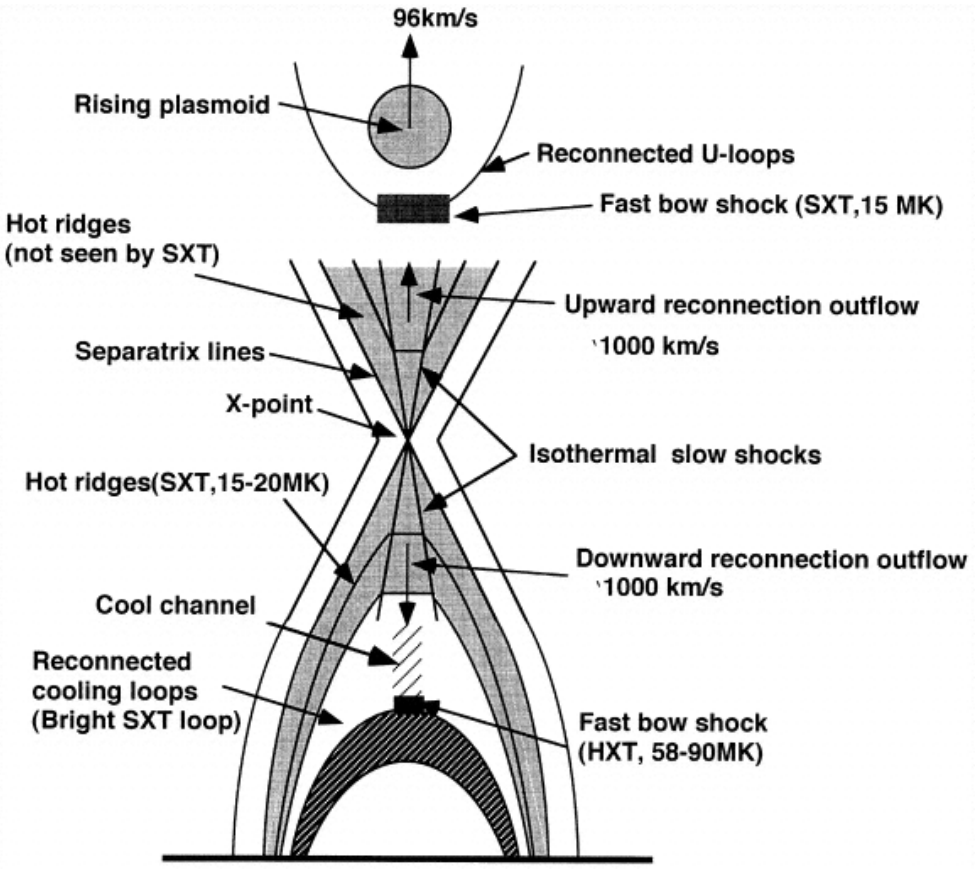

Figure 1.8: The 2-D schematic of the stand solar flare models (from Tsuneta [1997]).

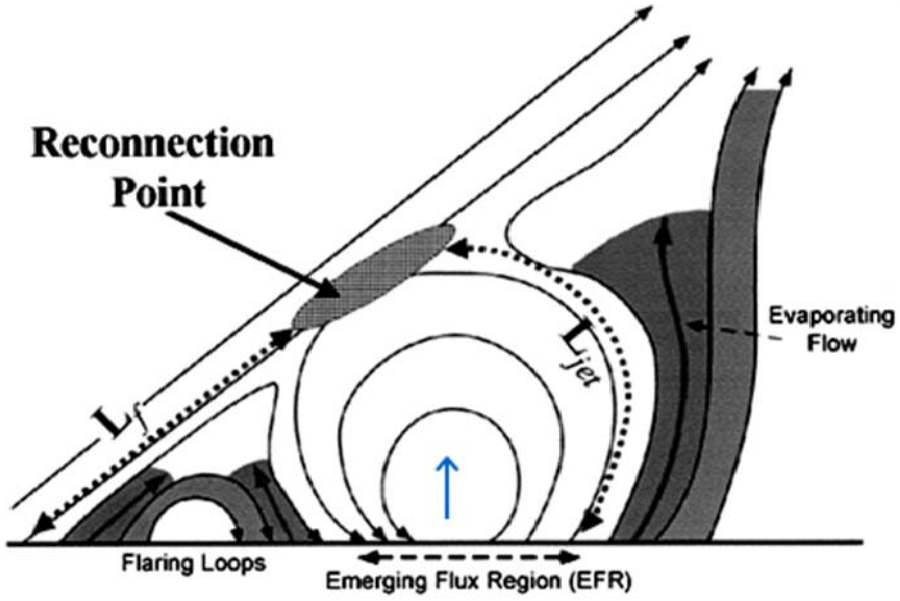

Figure 1.9: The 2-D schematic of the emerging flux flare model (from Shimojo & Shibata [2000]).

One has a "helmet and streamer" like geometry (see Figure 1.8) [e.g., Hirayama, 1974; Tsuneta, 1997], involving magnetic loops that are pinched at their legs. A vertical, X-type magnetic reconnection occurs where oppositely directed (anti-parallel) fields meet. As a result of reconnection, the magnetic energy is released to accelerate particles and heat the plasma and the bottom of the loop becomes a new closed loop, producing the solar flare; the top of the loop is ejected as a plasmoid, forming the CME. Another configuration has an "emerging flux" geometry (see Figure 1.9) [e.g., Heyvaerts et al., 1977; Shimojo & Shibata, 2000]. The closed magnetic loop emerging from the solar interior bumps into the overlying pre-existing field in the corona, forcing a horizontal or oblique, X-type magnetic reconnection. The new closed loops formed below the reconnection site become the flare loops, while jets or plasmoids ejected upward from the reconnection site appear as CMEs.

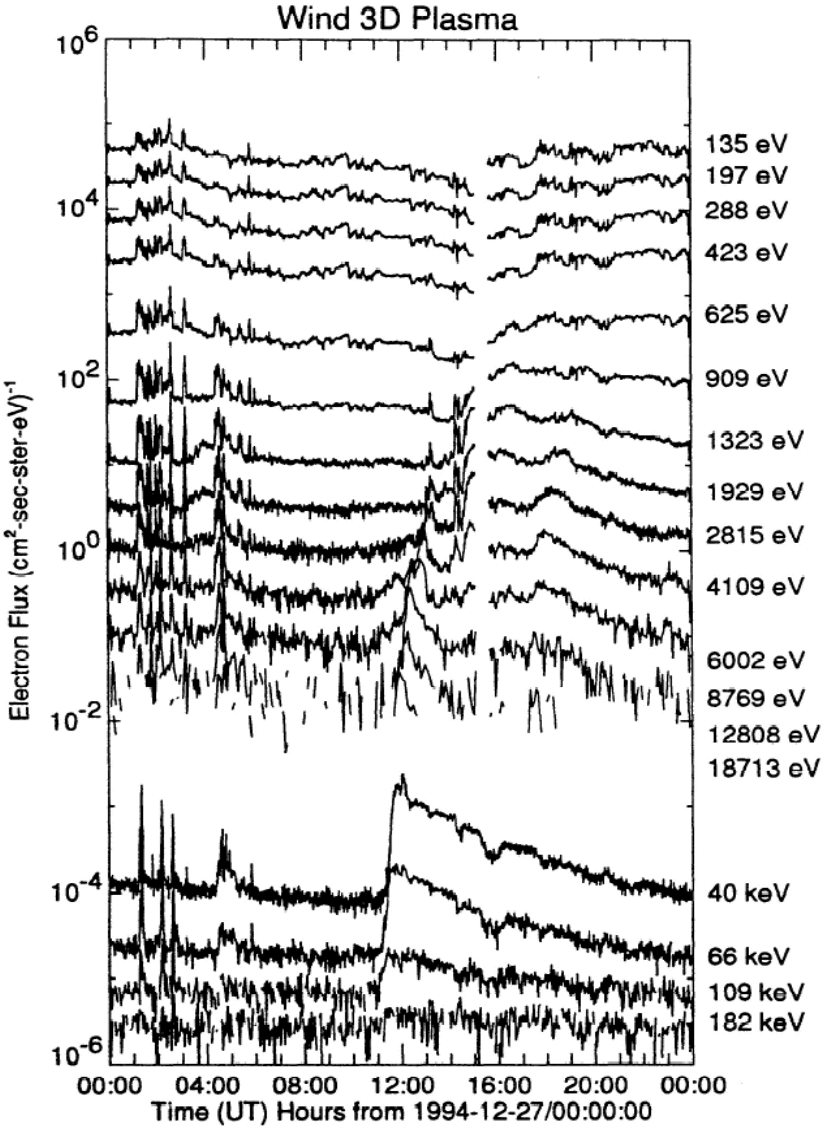

Figure 1.10: Example of a solar electron event observed on 27 December 1994 (from Lin et al. [1996]). Velocity dispersion is clearly evident from ~0.6 to ~100 keV.

1.2 Solar Energetic Particle Events

The Sun is the most energetic particle accelerator in the solar system, capable of accelerating ions up to tens of GeV and electrons up to hundreds of MeVs [Lin, 2005]. When the acceleration site is connected with open magnetic field lines, energized particles can escape into the interplanetary medium (IPM). These particles are observed *in situ* as the velocity-dispersed increase in particle fluxes well above plasma energies (see Figure 1.10), i.e., faster particles arriving earlier, as expected if the particles of all energies were simultaneously accelerated at the Sun and then traveled the same distance along the IMF to reach the spacecraft. This phenomenon is referred to as Solar Energetic Particle (SEP) events.

SEP events were first observed as sudden increases in intensity in ground-level ion chambers on February 28 and March 7, 1942 [Forbush, 1946], each following an exceptionally large solar flare. Such increases were caused by SEP protons with energies of ~ 1 GeV penetrating the Earth's neutral atmosphere. Later, meter wave radio observations suggested two distinct particle accelerators contributing to SEP events [Wild et al., 1963]: solar flares and coronal/interplanetary shock waves. Fast-drifting type III radio bursts are the signature of the particle acceleration process in solar flares, while slow-drifting type II bursts manifests the acceleration by coronal shock waves (see § 1.2.1). After the discovery of CMEs in the 1970s, Kahler et al. [1978, 1984, 1987] found a high correlation between large SEP proton events and fast CMEs, sometimes even for large SEP events that lacked flares. These observations suggest that shock waves driven by fast CMEs are a second accelerator of SEP events, besides solar flares. Figure 1.11 sketches the two SEP acceleration scenarios. However, many studies show that solar electron events often have neither associated flares [e.g. Lin, 1985] nor CMEs (Chapter 3 in this thesis).

Starting with Cane et al. [1986], SEP events are generally classified into two groups: "gradual" and "impulsive" (table 1.1), so-called because the associated soft X-ray burst (when present) is of short duration and of long duration, respectively [see Reames, 1999 for review]. However, the term "gradual" and "impulsive" poorly resolve the particle acceleration mechanisms.

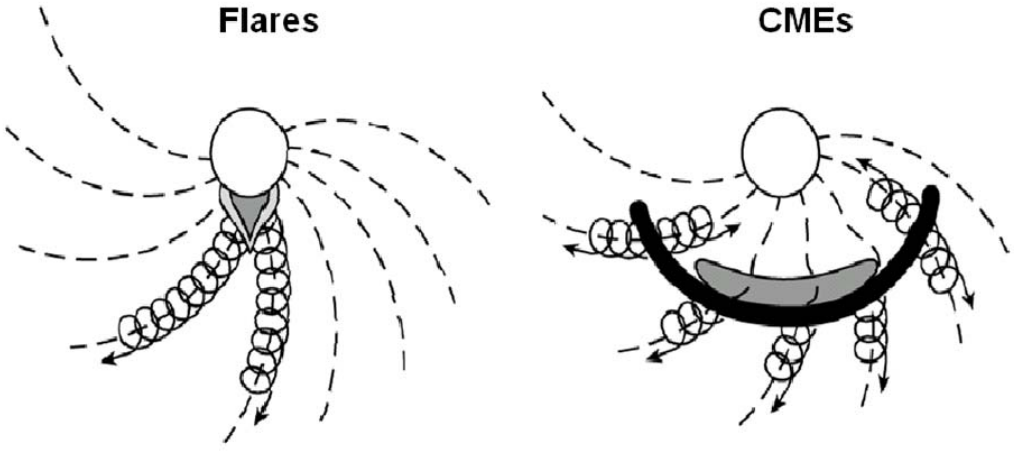

Figure 1.11: Sources of SEP events. After SEPs are accelerated in solar flares (left) or CME-driven shocks, they escape and spiral along "open" interplanetary magnetic field lines.

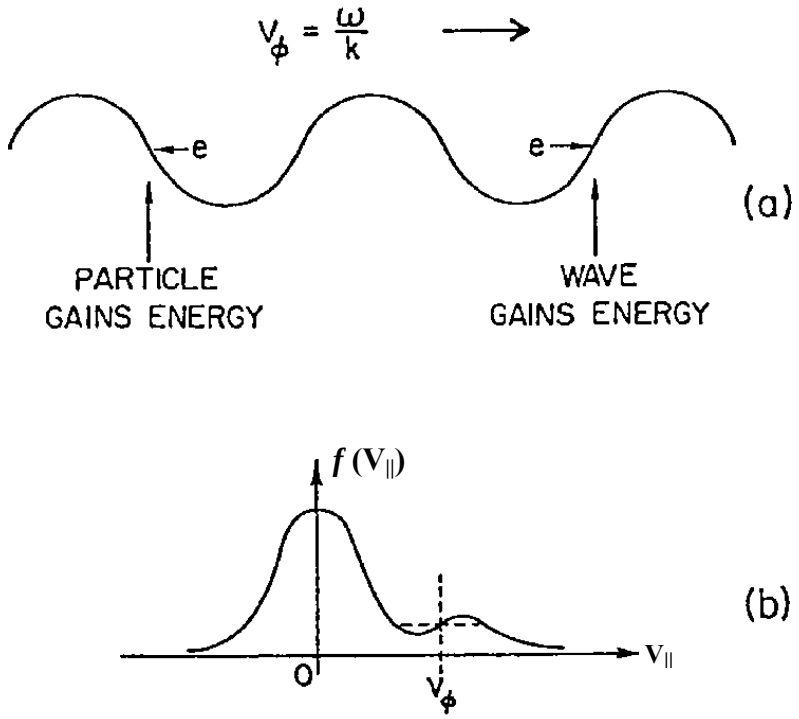

Figure 1.12: (a): Schematic illustration of the interaction between the plasma wave and particles. In the rest frame of the wave, particles moving slightly faster (slower) will give (lose) energy to (from) the wave. (b): If there is a positive slope in the particle distribution at the wave phase velocity, then the wave can grow. As the wave grows, it will eventually flatten or "plateau" the bump. Adapted from [Lin, 1990].

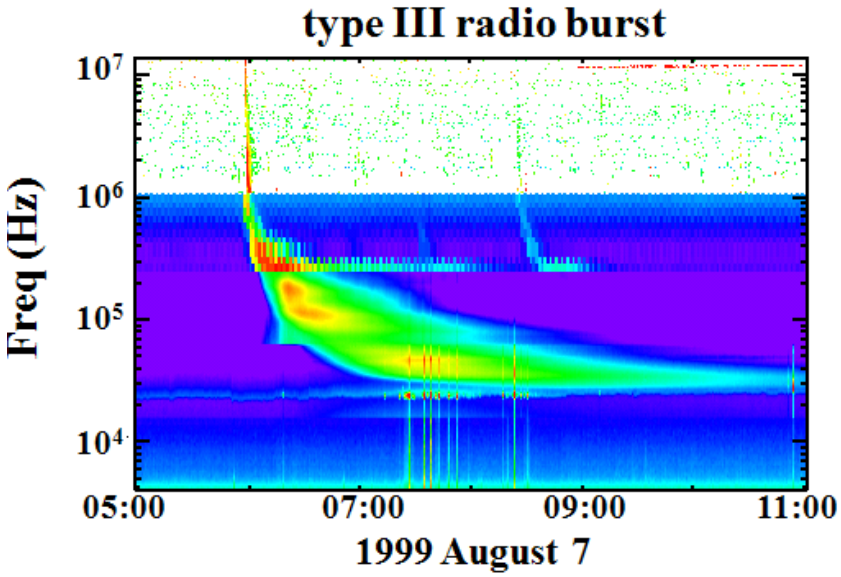

Figure 1.13: Spectrogram of a type III radio burst from WIND/WAVES.

1.2.1 Radio bursts associated with SEP events

Solar radio bursts were discovered more than six decades ago by Hey [1946] as results of their interference in early defensive radar systems during the Second World War. The first interference occurred on February 28, 1942, related to the intense solar activity that produced the first-ever measured SEP event [Forbush, 1946]. Since their discovery, solar radio bursts have been classified into five major types (I to V) based on their morphology in dynamic spectra [see Dulk, 1985 for review].

Type III bursts, characterized by fast drift from high to low frequency, are one kind of solar radio bursts closely associated with SEP events. They are believed to be generated by electron beams escaping from the Sun into the interplanetary space via the plasma emission process. As energetic electrons travel along the magnetic field lines, faster electrons will run ahead of slower ones to produce a bump-on-tail in the local electron reduced parallel velocity distribution function, with a positive slope at the plasma wave phase velocity V_ϕ (see Figure 1.12b). Electrons moving slightly faster (slower) than V_ϕ will give (lose) energy to (from) the plasma wave (see Figure 1.12a). Thus, such a bump-on-tail distribution has more electrons giving energy to the wave than taking energy away, unstable to the growth of the Langmuir (electrostatic longitudinal) waves. Then Langmuir waves will generate electromagnetic radio waves near the local plasma frequency $f_p \sim \sqrt{n_e}$ (n_e is the local plasma electron density) or its 2nd harmonic via nonlinear interactions [see Lin, 1990 for summary]. The fast frequency drift of type III bursts corresponds to the rapidly decreasing local n_e encountered by energetic electrons as they move outwards at ~0.1c through the corona and the IPM. Figure 1.13 shows an example of type III bursts that drifts from 14 MHz (f_p at ~ 2 R_S from the Sun's center) all the way down to ~20 kHz (f_p near the Earth).

Type II bursts are another type of radio bursts associated with SEP events. These bursts appear in dynamic spectra as slowly drifting bands, often in pairs differing in frequency by a factor of ~2 (Figure 1.14). They are generally interpreted in terms of a coronal/interplanetary shock wave accelerating electrons, driving Langmuir waves near f_p and producing radio emissions near f_p and 2 f_p [Wild et al., 1954, Nelson & Melrose, 1985]. The slow decrease in frequency corresponds to the outward motion of shock waves at ~ 1000 km/s, e.g., those driven by fast CMEs, through the corona and the IPM. Thus, type II bursts are known as indicators of traveling shock waves.

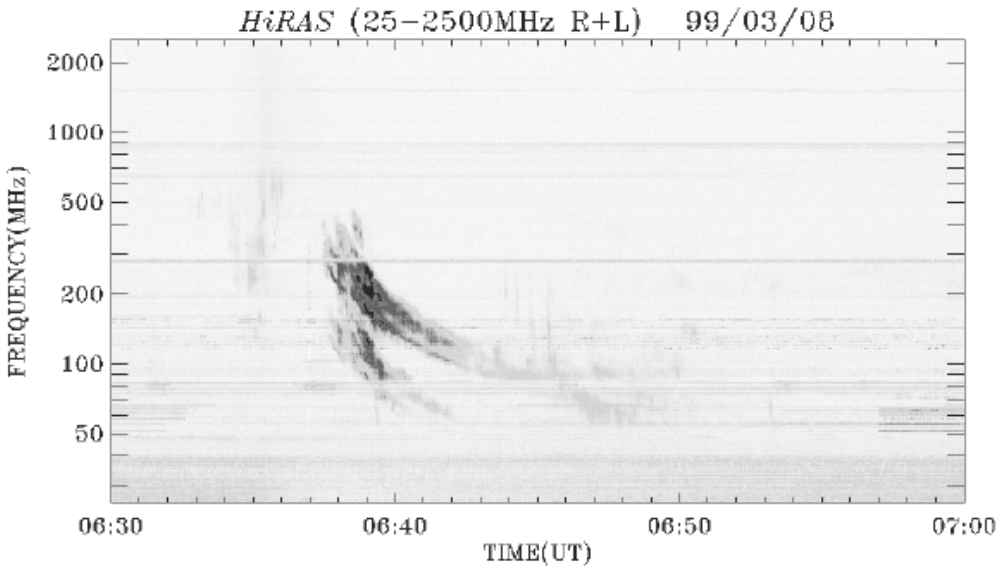

Figure 1.14: Spectrogram of a type II radio burst. Adapted from Mancuso et al. [2003].

Table 1.1 Two classes of SEP events

Characteristic	Large SEP events (Gradual SEP events)	Electron/^{3}He-rich SEP events (Impulsive SEP events)
Dominant particle species	>~ 10 MeV protons	~ 1-100 keV electrons
Electron to proton ratio	small	large
^{3}He/^{4}He	'normal' coronal, ~ 5×10^{-4}	~ 1
Heavy nuclei	'normal' coronal	enhanced abundances of Fe, Mg, Si, S
Fe/O	~0.1	~1
Q_{Fe}	~ 14	~20
Duration	Days	<~ hours
Longitude cone	>~ 100°	<~ 30°
Event rate (at solar maximum)	~ 10/year	>~ 10^3/year
Association		
Flares	large flares (but sometimes missing)	mostly small flares but often no flares
Soft X-ray bursts	gradual (~ hours)	impulsive (< 10s min)
CMEs	fast CMEs	—
Radio bursts	type III	type II

1.2.2 Gradual SEP events

As the first SEP event discovered by Scott Forbush [1946] shows, gradual SEP events [see Cliver, 2009 for review] are dominated by protons (small electron-to-proton ratios) up to GeV energies with large particle intensities (also called large SEP events). These events are characterized by normal coronal abundances (e.g., $^3He/^4He$ ~5×10^{-4}) and charge states (e.g. the iron ionization state Q_{Fe} ~ 14) corresponding to typical coronal quiet temperatures of 1-2×10^6 K. They occur about ~10/year at solar maximum, extend ~100-180° in solar longitude, last for days, and are strongly associated with solar flares (but sometimes missing), fast CMEs and type II radio bursts. These suggest that gradual SEPs are accelerated by the CME-driven shock. Figure 1.15a displays the intensity-time profiles of one typical gradual SEP event that is dominated by protons and lasts for days.

Figure 1.16a shows the source longitude of the associated flares for gradual SEP events detected near the Earth. It is nearly uniformly distributed across the face of the Sun, although only the west limb (~W60º) of the Sun magnetically well connects to the Earth through the Parker spiral IMF line (see § 1.2.5.1). This broad solar source distribution supports the wide longitude span of gradual SEP events, indicative of the existence of large-scale shock waves. On the other hand, Kahler [1994] estimated the proton injection profiles at the sun from *in situ* observations for five gradual SEP events, by assuming a 1.3 AU particle travel length. They suggested that the particle acceleration in gradual SEP events takes place when the associated CMEs reach heights of a few to tens of solar radii R_S, while it appears too late to result from the associated flares.

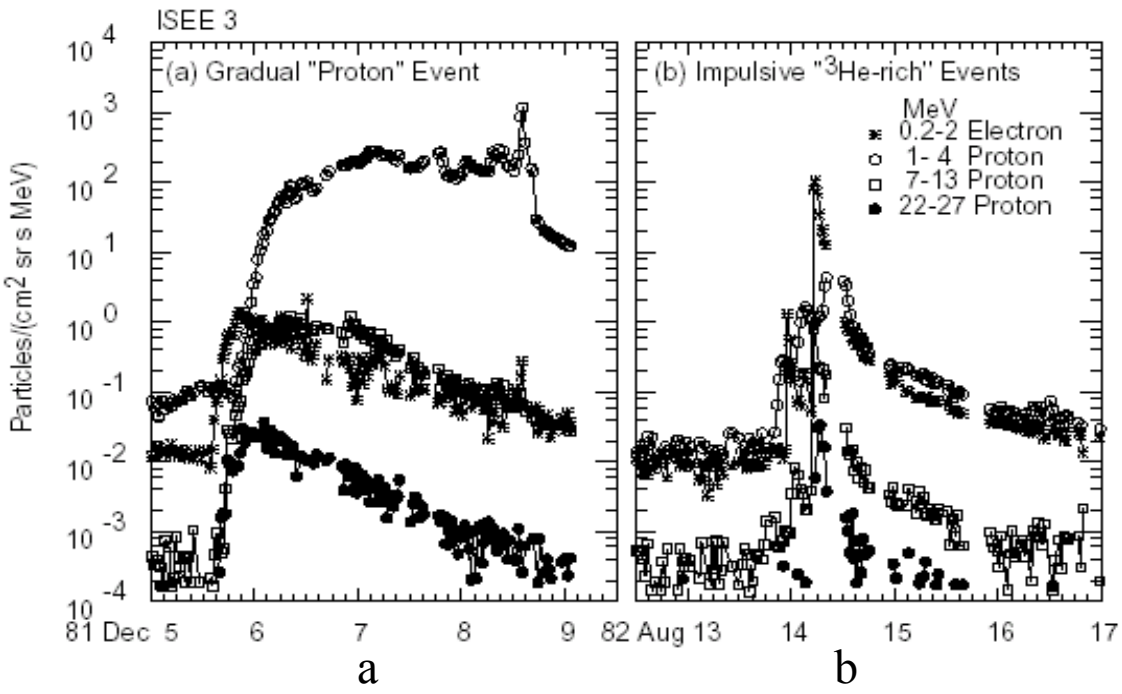

Figure 1.15. Intensity-time profiles of electrons and protons in gradual (a) and impulsive (b) SEP events on the same scale (from Reames [1999]). The gradual SEP event has a CME but no impulsive flare. It is dominated by protons, with a small peak occurring at ~ 1 MeV near the time of the *in situ* passage of CME-driven shock. The impulsive event is associated with a flare but no CMEs, and is dominated by electrons.

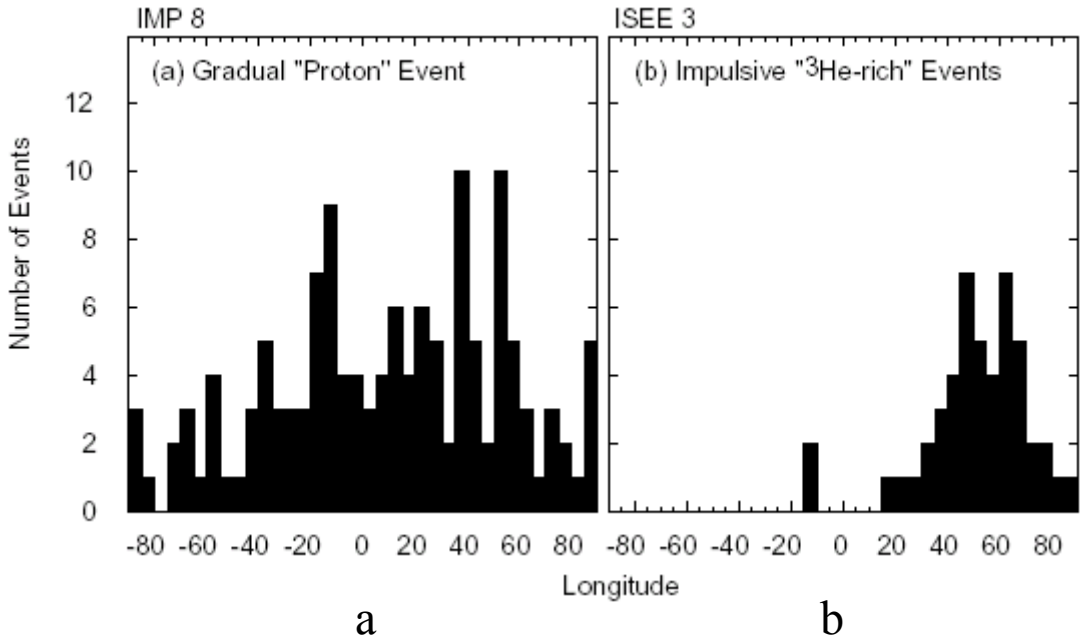

Figure 1.16. Histograms of the solar source longitude distributions of observed gradual (a) and impulsive (b) SEP events (from Reames [1999]). The positive (negative) longitude means west (east).

1.2.3 Impulsive SEP events

Impulsive SEP events are dominated by ~1-100 keV electrons (high electron-to-proton ratios) and low-energy, ~MeV/nucleon ion emissions with small particle intensities, enhanced ^{3}He/^{4}He ratios (first discovered by Hsieh & Simpson [1970]) up to 10^4 times the coronal values, significant enhancements (~10) of heavy nuclei such as Fe, extreme (factor of >200) enhancements of ultra-heavy nuclei up to > 200 amu, and high heavy-ion ionization states [see Mason, 2007 for review], and are associated with an impulsive SXR burst (when present). Thus, impulsive events are also called "electron/^{3}He-rich SEP events". They span <~30º in longitude, last for <~ hours, and are associated with type III radio bursts and small flares (but often missing). Figure 1.15b displays the intensity-time profiles of one typical impulsive SEP event that has high electron-to-proton ratios and a short (~ hours) duration at half maximum. Figure 1.16b shows the source longitude of the associated flares for impulsive SEP events detected near the Earth. It is mostly located around W60º where the Earth well connects to through the Parker spiral IMF line. This distribution is consistent with the <~30º longitude span of impulsive SEP events, indicating that these events are injected into and contained well within a narrow cone.

Near solar maximum, impulsive SEP events occur at a rate of >~10^3/year over the whole Sun, representing the most common impulsive solar particle acceleration phenomenon. The average ionization state is ~20 for Fe and ~14 for Si, which was interpreted as being due to either heating to ~ 10^7 K [Klecker et al., 1984; Luhn et al., 1987] or stripping[†] of the ions by the intense electron beams [Miller & Viñas, 1993] in impulsive flares. Thus, Reames [1995, 1999] and references therein suggested that impulsive SEP events are accelerated in impulsive solar flares, low in the corona. However, many impulsive SEP events lack associated flares. In addition, many impulsive electron events have a power-law spectrum extending down to ~1-2 keV [Lin, 1985; Lin et al., 1996], indicating that the acceleration of such low-energy electrons must occur high in the corona since at those energies, Coulomb collisions would prohibit electrons from escaping from low in the corona.

1.2.4 Particle acceleration

Particle acceleration in electron/^{3}He-rich (impulsive) SEP events has been studied for a few decades. For electrons, possible mechanisms are acceleration by the DC electric field in the magnetic reconnection region [e.g., Speiser, 1965], stochastic acceleration by resonance with waves, e.g., whistler waves [e.g, Melrose, 1974] or fast mode MHD waves [e.g., Miller et al., 1996], or Fermi reflection in contracting magnetic islands during the magnetic reconnection [Kliem, 1994; Drake et al., 2006]. The stochastic acceleration is a process in which particles can either gain or lose energy, depending on the relative phase between their motion and resonant waves, on short time scales, but they will gain energy on long time average. For ^{3}He-rich ions, one possible acceleration mechanism is resonance with wave modes that can preferentially heat/accelerate ^{3}He and heavy ions due to their unique mass-to-charge ratios [e.g., Fisk, 1978; Möbius et al., 1982; Temerin & Roth 1992; Miller et al., 1996; Roth & Temerin, 1997; Zhang, 1999; Liu et al., 2006]. Fisk [1978] proposed the first viable mechanism for selective heating of ^{3}He by absorption of electrostatic ion cyclotron waves produced above the ^{4}He gyrofrequency. Temerin & Roth [1992] and Roth & Temerin [1997] noted an analogy of the presence of electron

[†] A process in which the electrons of an ion are stripped due to collisions with other particles.

beams in impulsive SEP events with *in situ* terrestrial observations showing that precipitating electron beams generate oblique electromagnetic ion cyclotron (EMIC) waves that accelerate ions to produce the aurora. Then they suggested that a similar process might occur in solar flares: downward streaming electrons generate EMIC waves that resonate with the gyrofrequency of ^{3}He or the second harmonic of the gyrofrequencies of heavy ions. Several other people proposed resonant acceleration by shear Alfvén waves [Miller & Viñas, 1993], cascading MHD waves [e.g., Miller, 1998], plasma waves propagating parallel to the magnetic field [e.g., Liu et al., 2006], and firehose instability due to electron temperature anisotropy [Paesold et al., 2003]. For ^{3}He-rich ions, Drake et al. [2009] suggested another acceleration scenario related to magnetic reconnection: first, ions entering reconnection regions act like "pickup" particles and gain a thermal velocity equal to the Alfvén speed, with high mass-to-charge ratio threshold; second, super-Alfvénic ions, like electrons, can gain energy through Fermi reflection in contracting magnetic islands. However, none of the present models can self-consistently explain all the features of electron/^{3}He-rich (impulsive) SEP events: non-relativistic electrons, enhancements of ^{3}He and heavier ions, high ionization states, etc..

Gradual SEP events are believed to be accelerated at shock waves driven by fast CMEs. This acceleration process basically falls into two categories: shock drift acceleration [e.g., Armstrong at al., 1985] and diffusive shock acceleration [e.g., Lee, 1983; Zank, 2000]. In the shock drift acceleration, particles gain energy while drifting along the induced electric field ($\vec{\boldsymbol{E}} = -\vec{\boldsymbol{V}} \times \vec{\boldsymbol{B}}$) at the shock surface, with the maximum ratio of the final to initial energy related to the shock compression [Ball & Melrose, 2001]. Since the electric field appears under the condition that there is a finite angle between the magnetic field $\vec{\boldsymbol{B}}$ and fluid velocity $\vec{\boldsymbol{V}}$, this acceleration works mainly in quasi-perpendicular ($45^\circ < \theta_{Bn} < 90^\circ$, where θ_{Bn} is the angle between the shock normal and upstream magnetic field) shocks. The diffusive shock acceleration is a more efficient mechanism, in which particles are accelerated as they scatter many times back and forth across the shock front due to magnetic turbulence such as MHD waves (but those turbulent waves are not often seen during the shock passage at 1 AU). Although it is the mostly accepted acceleration mechanism for gradual SEP events [Reames, 1999], the diffusive acceleration requires the pre-accelerated seed particles, which still remains unresolved for electron acceleration [Treumann & Terasawa, 2001]. Recently, Tylka and Lee [2006] proposed that the acceleration in gradual SEP events is affected by two factors: the geometry of the CME-driven shock (quasi-perpendicular vs. quasi-parallel) and different seed populations (suprathermals from flares and suprathermals from the corona and/or the solar wind), and that quasi-perpendicular shock can preferentially accelerate suprathermals from flares and also produce the hard energy spectrum. However, the acceleration of high-energy (>~ tens of MeV) particles have never been detected *in situ* during the passage of the CME-driven shock (even very fast shocks) at 1 AU (see Figure 1.15 a, for example), providing a challenge to the efficiency of shock acceleration.

1.2.5 Particle propagation in the IPM

1.2.5.1 IPM

The solar wind results from expansion of the corona. In the mid 1950s, Eugene Parker [1958] developed the first hydrodynamic model of a continuously expanding solar corona driven by the large pressure difference between the solar corona and the interstellar plasma, and predicted the presence of the supersonic solar wind above a few solar radii R_S which was later confirmed by observations from the Mariner 2 spacecraft near the Earth [Snyder et al., 1963]. Parker [1958] also predicted the the spiral shape of the IMF. The electrical conductivity of the solar wind plasma is so high that the solar magnetic field is "frozen into" the solar wind flow as it expands outward from the Sun, forming the IMF. Because of the rotation of the Sun, the IMF lines in the solar equatorial plane are bent into an Archimedean spiral pattern (Figure 1.17), named the "Parker Spiral", that at 1 AU makes an angle of ~45º to the solar radial direction for a 400 km/s solar wind speed V_{SW}. In the equatorial plane, at the heliocentric distance r, the magnetic field strength is

$$B(r) = B(R_S)\left(\frac{R_S}{r}\right)^2\left[1+\left(\frac{\Omega}{V_{sw}}\right)^2\left(r-R_S\right)^2\right], \tag{1.1}$$

the field line length is

$$L(r) = \frac{V_{sw}}{2\Omega}\left[\frac{r\Omega}{V_{sw}}\sqrt{1+\left(\frac{r\Omega}{V_{sw}}\right)^2} + \ln\left(\frac{r\Omega}{V_{sw}}+\sqrt{1+\left(\frac{r\Omega}{V_{sw}}\right)^2}\right)\right], \tag{1.2}$$

and the angle between the magnetic field and the radial solar wind velocity, φ, is given by

$$\tan(\varphi) = \frac{\Omega\left(r-R_S\right)}{V_{sw}}, \tag{1.3}$$

where Ω represents the angular velocity of solar rotation.

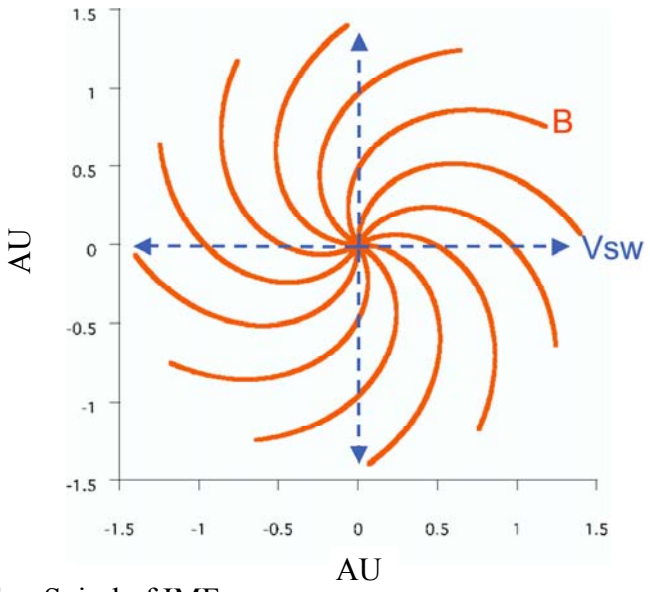

Figure 1.17. The Parker Spiral of IMF.

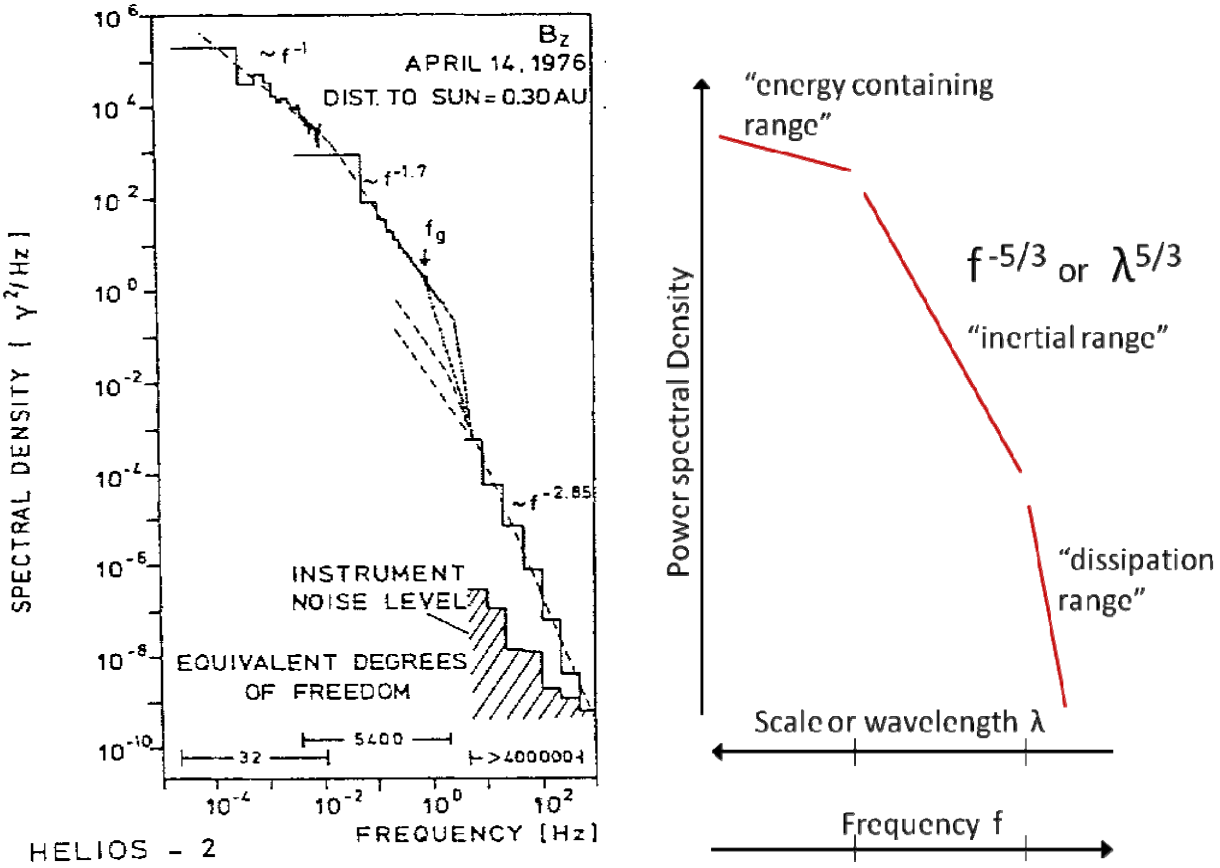

Figure 1.18. Left: Magnetic power spectrum measured at ~ 0.3 AU (adopted from [Denskat & Neubauer, 1983]). The spectral enhancement at 1 Hz is due to the spin of the spacecraft. Right: Schematic power spectrum of the solar wind turbulence in a logarithm plot.

1.2.5.2 Particle propagation

The transport of particles through the IPM is mainly governed by two processes [e.g., Earl, 1976]: the adiabatic magnetic focusing and the nonadiabatic pitch angle scattering. As energetic particles propagate outward from the Sun along diverging IMF lines, adiabatic motion (the invariance of $\sin^2\alpha/B$) would focus them to small pitch angle (the angle between the direction of the particle's velocity and the magnetic field), α, but nonadiabatic wave-particle interactions can scatter them to large pitch angle. Thus, the essentially scatter-free propagation will result in a narrow pitch angle distribution, while the diffusive (scattered) propagation will give rise to a broad pitch angle distribution. On the other hand, such changes in pitch angle distributions would sooner or later be reflected in the time-intensity profiles [e.g., Lin, 1974]. During propagation in the IPM, scatter-free particle populations will keep their intensity vs. time profiles similar to the profile injected at the Sun, while scattered populations tend to spread out in space and time due to the smaller $v_{\|}=v\cos(\alpha)$ along the IMF and thus they will have a "diffusive" profile with a slow rise followed by a strong, much slower decay (Figure 1.19).

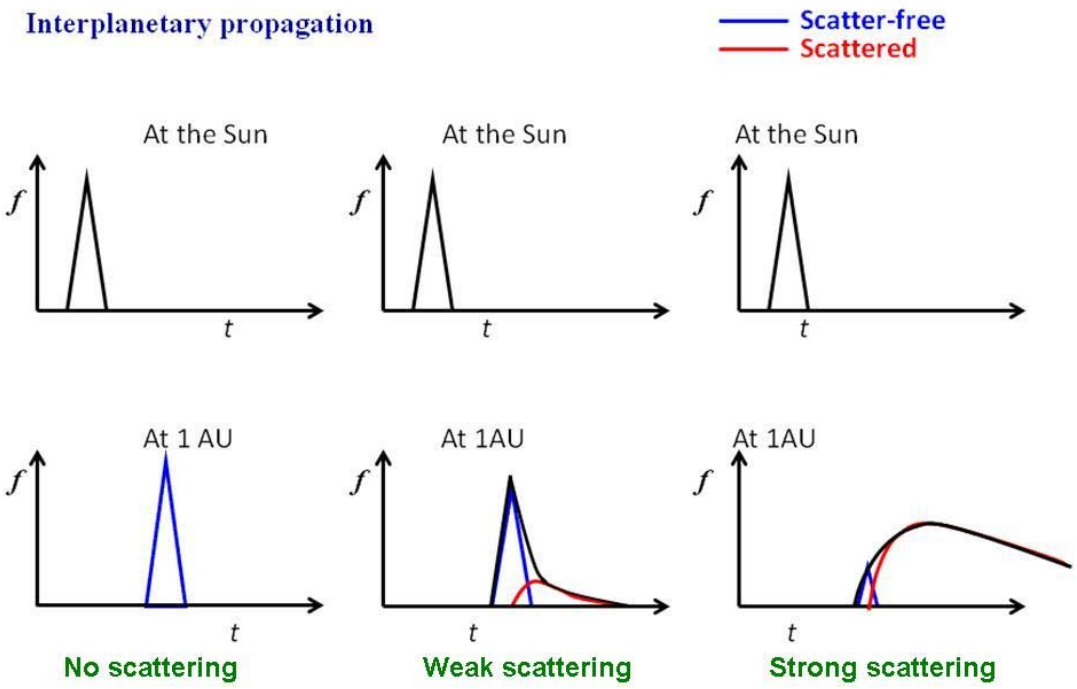

Figure 1.19. Schematic of the time-intensity profile of SEP events at the Sun (top) and 1 AU (bottom). The blue curve represents the time-intensity profile of scatter-free particle populations, the red curve the scattered populations, and the black curve the superposition of them.

1.3 Motivation and outline of this thesis

After about four decades of studies, many features of electron/^{3}He-rich SEP events are still not well understood. One is the relation between electrons and type III radio bursts. Krucker et al. [1999] found the injection of the >25 keV electrons at the Sun were often delayed by ~10 to ~30 minutes after the release of the associated type III radio burst, and Haggerty & Roelof [2002] also reported a median delay of ~10 min for 38-315 keV electrons. They suggested that the delay is related to acceleration by large-scale coronal EIT waves or CME-driven shock waves. But Cane & Erickson [2003] and Cane [2003] argued from radio observations that the delays of high-energy electrons are due to propagation effects in the IPM. Another complex feature is the relation between electrons and ^{3}He-rich ions. Reames et al. [1985] reported one electron/^{3}He-rich SEP event that has ^{3}He onsets with a time lag of <~ 10-15 min after electron measurements. Recently, however, Ho et al. [2003] examined nine electron/^{3}He-rich SEP events, and found that the <1 MeV/nucleon ions show significant delays (> 40 min) in the solar release for five events and no delays for the other four events, compared to 38-50 keV electrons.

This thesis is focused on solar impulsive energetic electron events, the electron part of electron/^{3}He-rich SEP events. It aims to provide a comprehensive understanding of electron/^{3}He-rich SEP events, by addressing the following questions:

1) What are the statistical properties of solar energetic electron events? How does the event occurrence vary over one solar cycle? How is the correlation between electrons and ^{3}He-

rich ions? How is the association of solar electrons with solar flares, CMEs and solar radio bursts?

2) What is the temporal relationship between different energy electrons and type III radio emissions? What energy electrons are responsible for the production of type III radio emissions?
3) What is the temporal relationship between electrons and ^{3}He-rich ions? When and where are these particles accelerated?
4) How do the different energy electrons propagate through the IPM: scatter-free or diffusively?

In this thesis, Chapter 2 describes the WIND mission and in particular the details of the 3-D Plasma and Energetic Particle instrument. Chapter 3 presents a statistical study of solar energetic electron events measured over one solar cycle, to address the question #1. Chapter 4 gives a case study of the timing of solar impulsive energetic electron events, to address the question #2. Chapter 5 is a case study of the timing of electron/^{3}He-rich SEP events, to address the question #3. Chapter 6 investigates the pitch angle distributions and temporal variations of solar impulsive electron events, to address the question #4. Finally, Chapter 7 summaries the conclusions of this thesis, and discusses the future work.

2. The Three-Dimensional Plasma and Energetic Particle Instrument on WIND spacecraft.

2.1 WIND mission

The WIND spacecraft is the first of NASA's Global Geospace Science (GGS) program, which is part of the International Solar-Terrestrial Physics (ISTP) Science Initiative. Its main scientific goal is to measure the mass, momentum and energy of the solar wind that somehow is transferred into the space environment around the Earth.

2.1.1 Orbit

The WIND spacecraft was launched November 1, 1994 by a Delta II rocket from Cape Canaveral Air Station, Florida. The dry weight of the spacecraft is 875 kilograms, with an additional 368 kilograms of hydrazine propellant for orbit and attitude control. The nominal mission life is three years. During the three years, WIND was placed initially into a highly elliptical orbit (apogee > ~60 Re, where the Earth radius Re = 6370 km), followed by a dayside double lunar swingby orbit in which the apogee from the Earth was up to ~250 Re and the perigee was at least 4.5 Re [Franz et al., 2001]. Figure 2.1 and 2.2 show the projection of such orbit trajectories onto the X-Y plane in Geocentric Solar Ecliptic (GSE) coordinate that has an origin at the center of Earth, the X axis pointing towards the center of the Sun, the Y axis lying in the ecliptic plane and pointing in the opposite direction of the Earth's orbital motion, and the Z axis pointing towards the Ecliptic North. The double lunar swingby utilizes pairs of lunar gravity assists (through close encounters with Moon) to shape the orbit. First, a trailing edge, "outbound" swingby raises the orbit apogee, sending the spacecraft into an outer loop with duration of 1-8 lunar months. The outer loop is terminated with a leading edge, "inbound" swingby, which lowers the orbit apogee, returning the spacecraft to an inner loop orbit to repeat the cycle (see Figure 2.1, for example). Each swingby pair rotates the orbital line of apsides such that the mean apsidal rotation rate equals that of the Earth-Sun line.

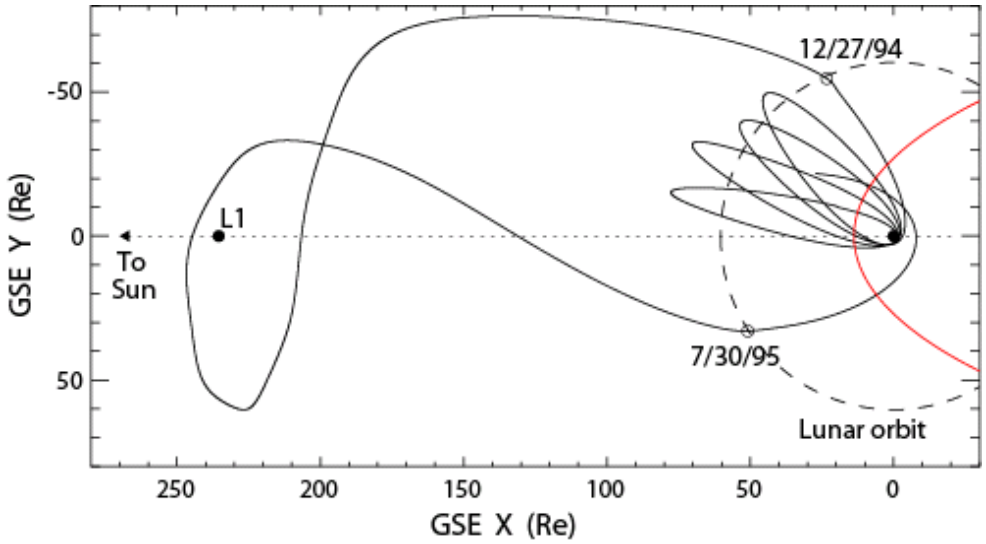

Figure 2.1. Orbit overview of the first dayside lunar swingby cycle. The solid line curve shows the projection of WIND's trajectory onto the X-Y plane in the GSE coordinate. The dashed circle displays the approximate lunar orbit trace at distances of ~ 60 Re from the Earth; the red curve sketches the Earth's bow shock. After launch, WIND completed 4.5 revolutions in a highly eccentric orbit. The first lunar gravity assist occurred on December 27, 1994, sending WIND into a 7-month outer loop that reached the first Lagrangian point L1. This initiated the double lunar swingby phase of the mission. This outer loop was ended by the second lunar swingby on July 30, 1995, returning to an inner loop.

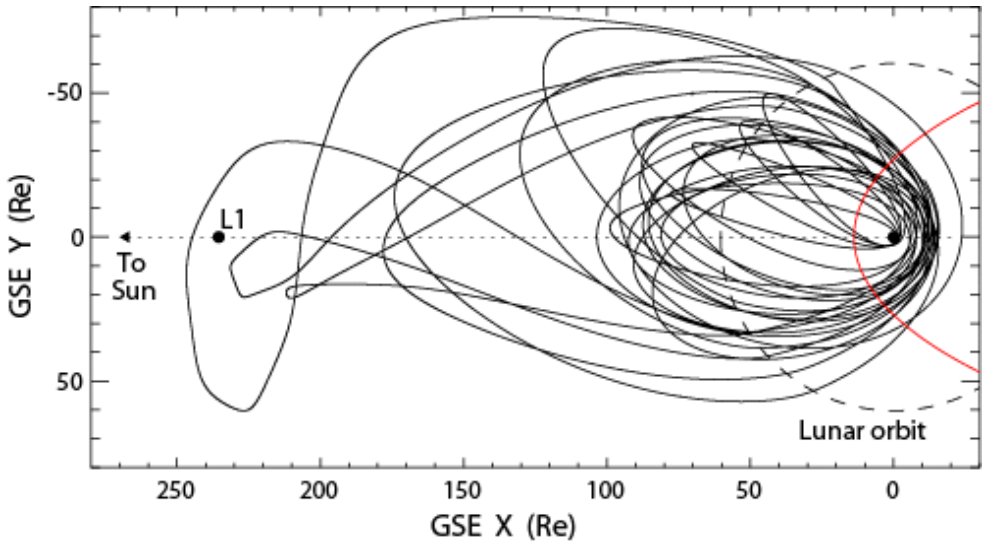

Figure 2.2. Overview of the WIND spacecraft's orbit from November 1994 through September 1997. The solid line represents the projection of orbit trajectories onto the X-Y plane in the GSE coordinate. The dashed circle displays the approximate lunar orbit trace, and the red curve sketches the Earth's bow shock.

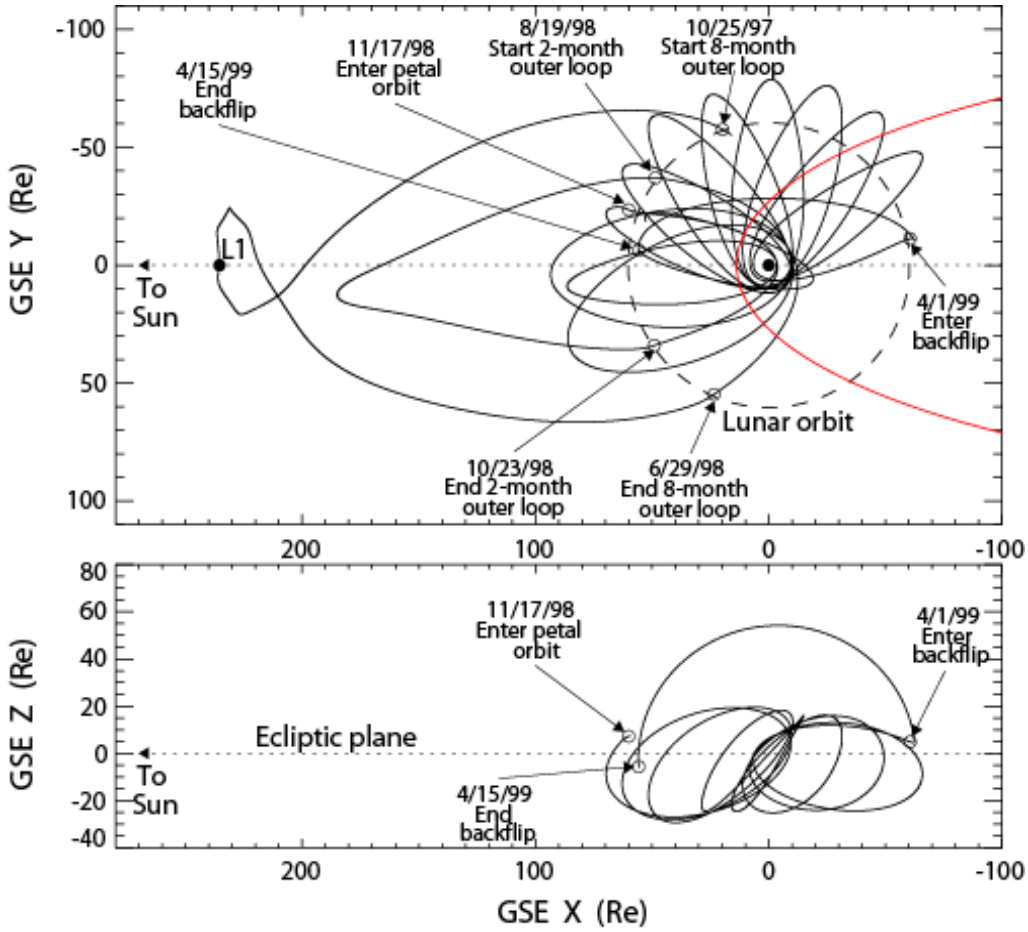

Figure 2.3. Top: Projection of the WIND spacecraft's orbit trajectory onto the GSE X-Y plane from October 1997 through April 1999. Bottom: Projection of WIND petal orbit onto the GSE X-Z plane from November 1998 through April 1999. After the dayside double lunar swingby orbit, the lunar flyby in November 1998 raised the orbital inclination to ~ 50° from the ecliptic plane to begin the petal orbit with an apogee of ~80 Re. After ~4.5 months in this orbit, a backflip propelled WIND over the ecliptic plane to return to the dayside on April 15, 1999.

The lunar flyby in October 1997 sent the spacecraft into an 8-month outer loop that approximated one revolution in a halo orbit around the Lagrange 1 point, which is a point of Earth-Sun gravitational equilibrium occurring about 1.5 million km (~ 235 Re) from Earth on the day side (between the Sun and Earth). This flyby marked the completion of the nominal mission phase and the inauguration of the extended mission. The extended mission has comprised various orbital phases and concepts (see Figure 2.3, for example), including the halo orbit at L1 and L2[†], high-inclination "petal" orbit, lunar backflip (that uses a pair of lunar flybys to achieve the transition from nightside to dayside orbit), nightside double lunar swingby, deep-magnetotail

[†] L2, the second Earth-Sun Lagrange point, is located about 1.5 million km from Earth on the night side of the Earth-Sun line.

excursion, distant prograde orbit (with excursions of up to 320 Re in the Y_{GSE} direction). Since mid-May in 2004, WIND has remained in a halo orbit around the L1 point.

2.1.2 Instruments

The WIND spacecraft is a spin-stabilized (20 rpm) cylinder-shaped satellite measuring 2.4 m in diameter and 1.8 meter in height (see Figure 2.4), with the spin axis pointing towards the Ecliptic South. It carries 8 instruments: the Solar Wind Experiment (SWE) to measure the solar wind electrons and ions, the Solar Wind and Suprathermal Ion Composition Studies (SMS) experiment to determine the abundance, velocity, spectra, temperature and thermal speeds of solar wind ions, the Three-Dimensional Plasma & Energetic Particles (3DP) experiment to measure electrons and ions from the solar wind plasma to low energy cosmic rays, the Energetic Particle Acceleration, Composition and Transport (EPACT) experiment to measure high-energy ions in the solar wind, the Magnetic Fields Instrument (MFI) to measure the intensity, direction and fluctuation of the interplanetary magnetic field (IMF), the Plasma and Radio Waves (WAVES) experiment to measure radio waves and other wave modes of the plasma over a very wide frequency range., the Transient Gamma-Ray Spectrometer (TGRS) to observe transient gamma-ray events, and the Gamma Ray Burst Detector (KONUS) to study gamma-ray bursts. The NASA Deep Space Network is used to command the spacecraft and collect the data via radio link.

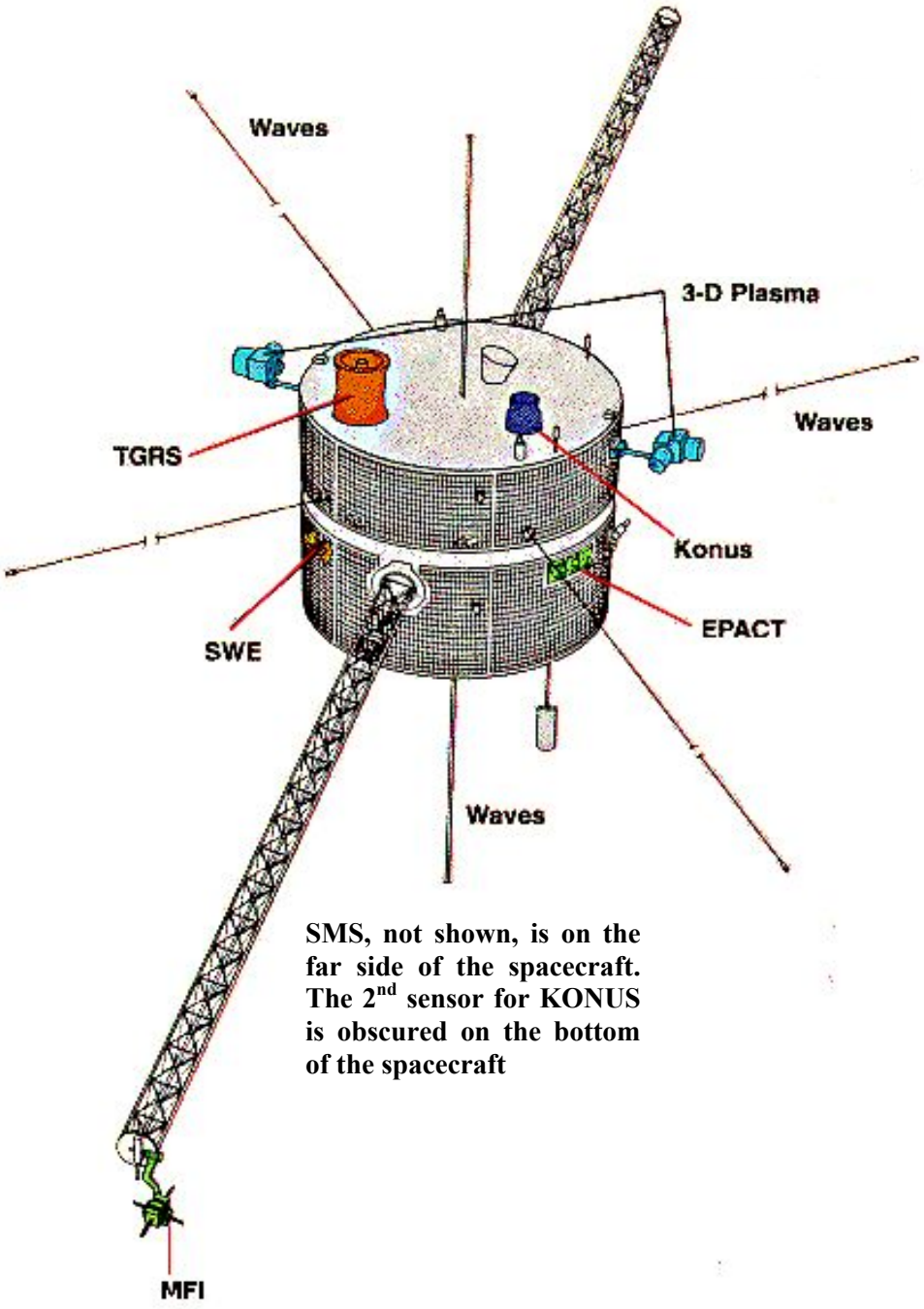

Figure 2.4. WIND satellite configuration.

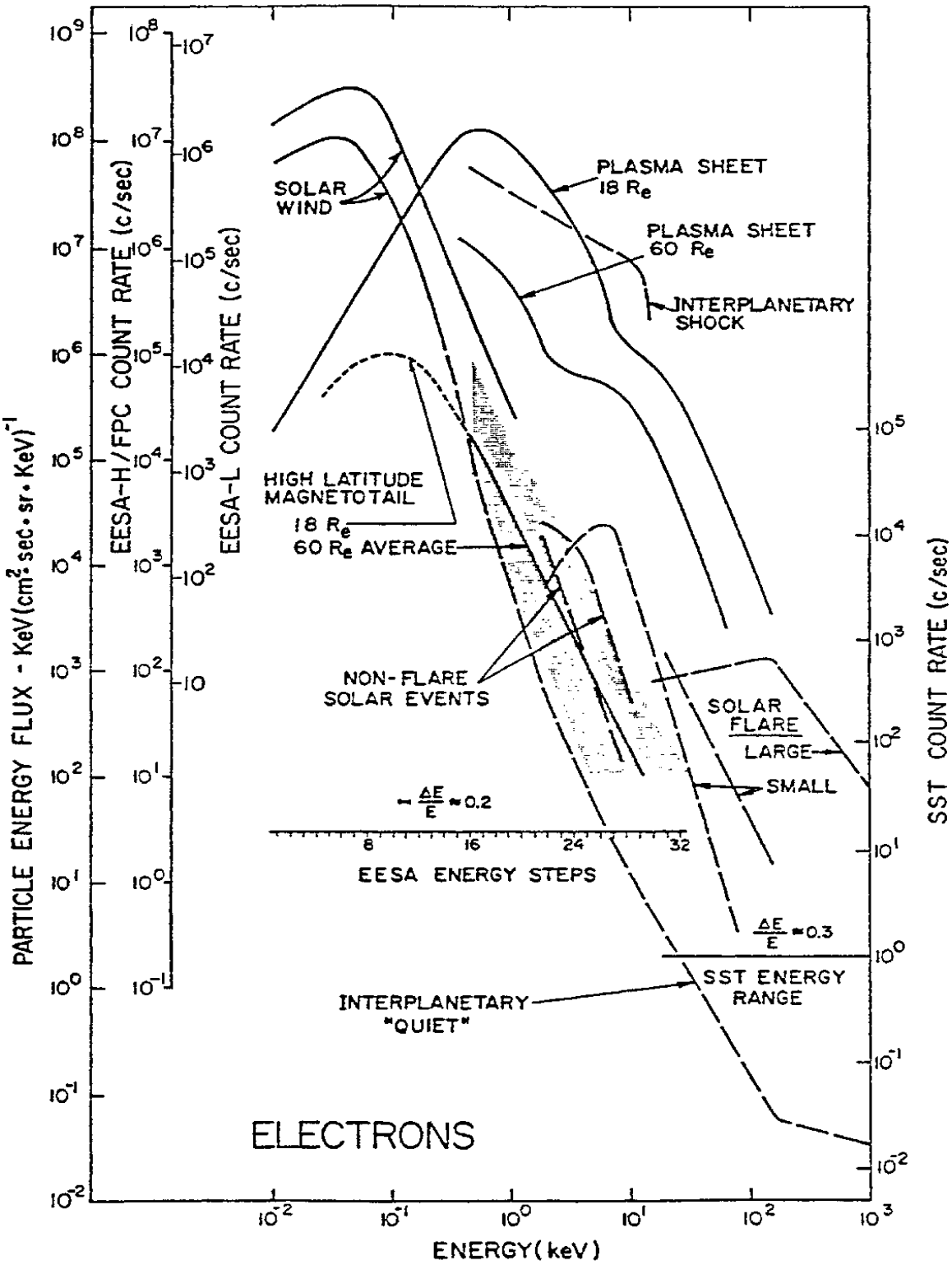

Figure 2.5. Typical electron energy flux (E(dJ/dE)) in the IPM and outer magnetosphere. Counting rates per channel for the EESA and SST are indicated on the left and right axes, respectively; the energy range is indicated by horizontal lines (adapted from Lin et al. [1995]).

2.2 The 3-D Plasma and Energetic Particle instrument

The 3-D Plasma and Energetic Particle (3DP) instrument on WIND, developed by Space Sciences Laboratory at University of California, Berkeley, provides full three-dimensional measurements of suprathermal electron and ion distributions from solar wind thermal plasma to low energy cosmic rays, with high sensitivity, wide dynamic range, good energy and angular resolution, and high time resolution [Lin et al., 1995]. It consists of three detector systems: the silicon semiconductor telescopes (SST), the electron electrostatic analyzers (EESA), and the ion electrostatic analyzers (PESA). SST measures electrons from ~25 keV to 1 MeV and ions from ~20 keV to 11 MeV. EESA-L (low sensitivity) and –H (high sensitivity) measure electrons from ~3 eV to 30 keV, while PESA-L and –H measure ions at the same energy range. In addition, a Fast Particle Correlator (FPC) combines electron data from EESA-H with plasma wave data from the WAVES experiment to study wave-particle interactions. To minimize the effects of the spacecraft potential on the low energy particle trajectories, EESA-L and EESA-H are mounted on the end of a 0.5 m boomlet, while PESA-L, PESA-H and SST are mounted on the end of an opposing 0.5 m boomlet (See Figure 2.4). Here, we focus on electron measuring sensors: EESA-L and –H, and SST. Figure 2.5 indicates the energy range for the EESA and SST, as well as counting rates based on typical electron energy fluxes measured in the interplanetary medium (IPM) and outer magnetosphere.

2.2.1 EESA

EESA-L and EESA-H are top-hat symmetric spherical section electrostatic analyzers followed by microchannel plate (MCP) detectors in a chevron pair configuration (see Figure 2.6, for example). These electrostatic analyzers consist of two closely spaced, concentric metal hemispheres, with an aperture at the apex of outer hemisphere, providing the energy resolution of $\Delta E/E \approx 0.2$ and the elevation angular acceptance of ±7° (in vertical direction). This geometry forces at least a 2 bounce light path and the smooth inner and scalloped outer hemispheres have a gold black coating applied to further reduce scattered light. The outer hemisphere is grounded, while the inner hemisphere is biased to an adjustable negative voltage that deflects electrons within a specific energy range onto the MCPs below. MCP detectors will give an electron multiplier gain of ~ 2×10^6 and a narrow pulse height distribution. In EESA-L (H), a 180º half ring (a 360º full ring) of MCPs is used, and the produced charge pulses are collected by 16 (24) anodes, providing a total 180° (360°) planar field-of-view (FOV) with angular resolution varying from 5.6° (within ±22.5° of the ecliptic plane) to 22.5° (see Figure 2.7).

EESA-H has an L-shaped plastic anticoincidence scintillator that surrounds the MCPs (see Figure 2.6). The scintillator rejects MCP pulses coincident with penetrating particles, achieving high-sensitivity measurements. EESA-H also has curved plates placed at the analyzer entrance aperture that can electrostatically deflect the elevation FOV from nominal ±7° up to ±45°, by applying a voltage to the plates. This mode is used primarily to increase the measurement time of field aligned electrons during strong wave activity, for the FPC experiment. The total geometric factor of EESA-H is about $0.1E$ cm^2·sr, where E is the electron energy in eV.

EESA-L has no anticoincidence scintillator (so-called low sensitivity analyzer) and no electrostatic deflectors. In EESA-L, a +500 V potential is applied to the front of the MCPs to post-accelerate electrons, and the total geometric factor is about $0.013E$ cm^2·sr.

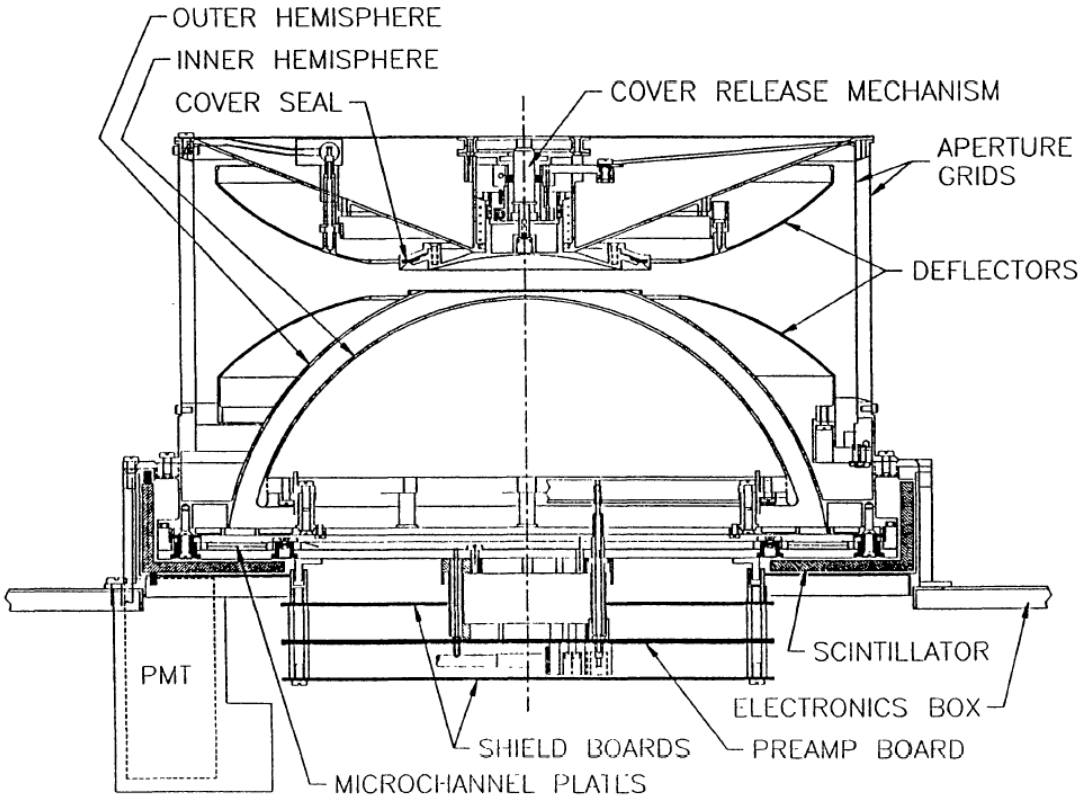

Figure 2.6. Cross section of the EESA-H analyzer (adapted from Lin et al. [1995]).

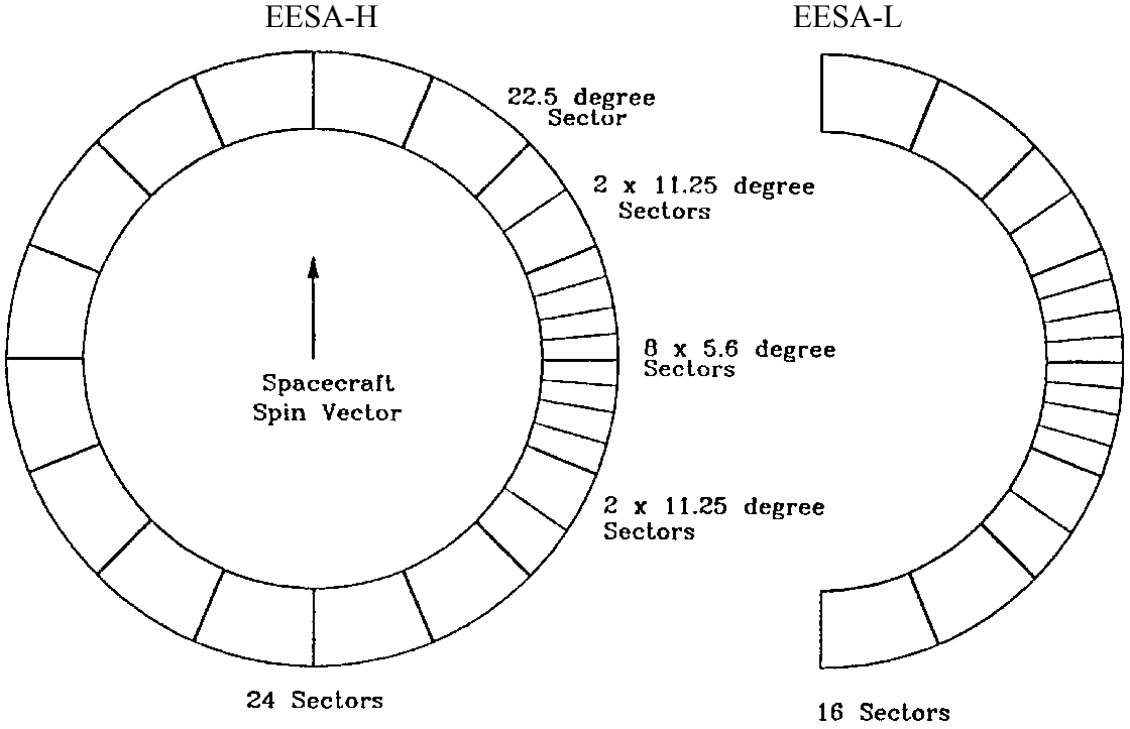

Figure 2.7. The pattern of discrete anodes for EESA-H and -L (from Lin et al. [1995]).

2.2.2 SST

SST is made up of three arrays of two double-ended telescopes (Figure 2.8 and 2.9), with four telescopes (#1, 3-5) each consisting of a pair of closely-sandwiched silicon semiconductor detectors and the other two telescopes (#2, 6) each consisting of a triplet of closely-sandwiched detectors. The center detector of the triplet is 1.5 cm^2 by 500 microns, while all other detectors are 1.5 cm^2 by 300 microns. These silicon detectors are fully depleted, passivated ion-implanted detectors, with low leakage current, ≤ 10 nA at room temperature, and SST is thermally isolated from the spacecraft to achieve temperatures of ~ 0º C to reduce detector thermal noise to negligible levels.

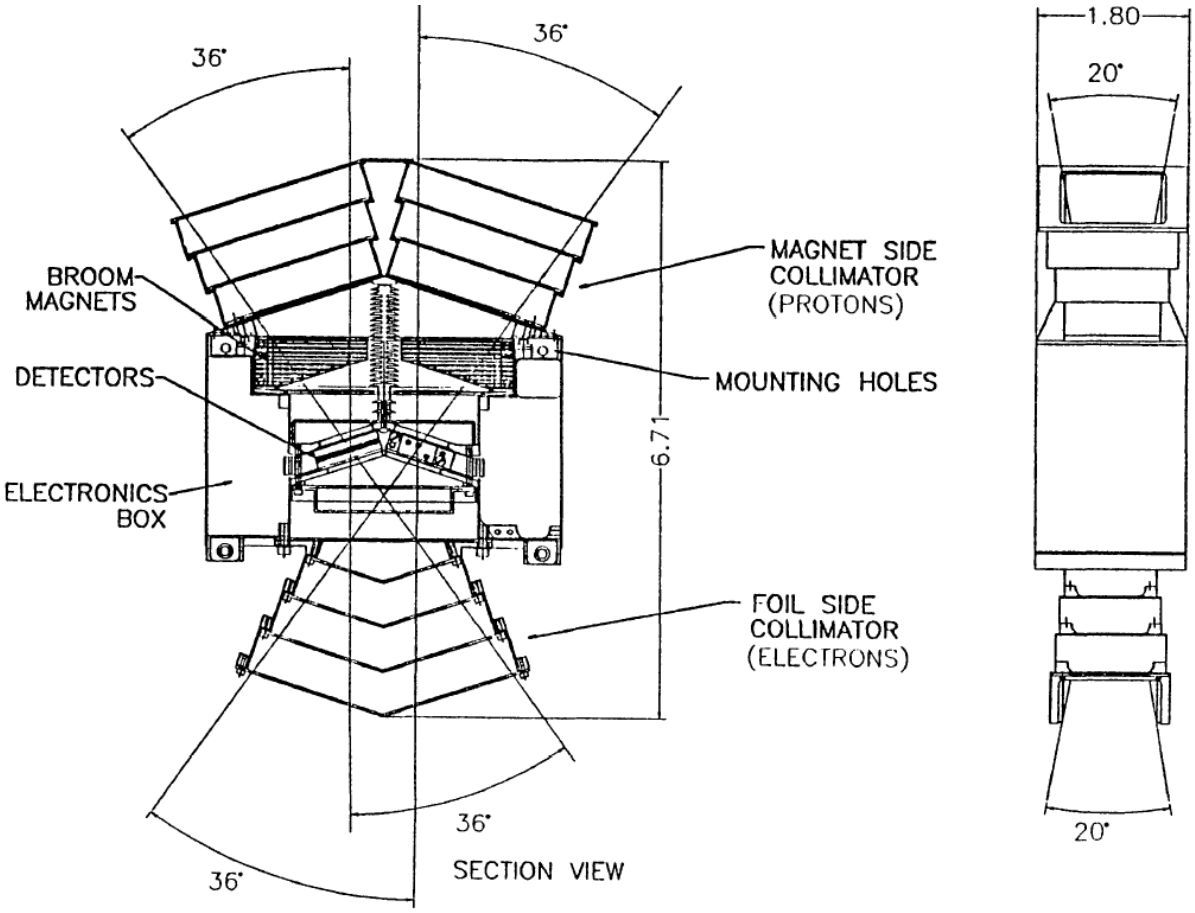

Figure 2.8. Section view of an array of two double-ended telescopes. Particles entering the two upper collimators pass through a sweep magnet while those entering the lower collimator pass through a thin lexan foil (adapted from Lin et al. [1995]).

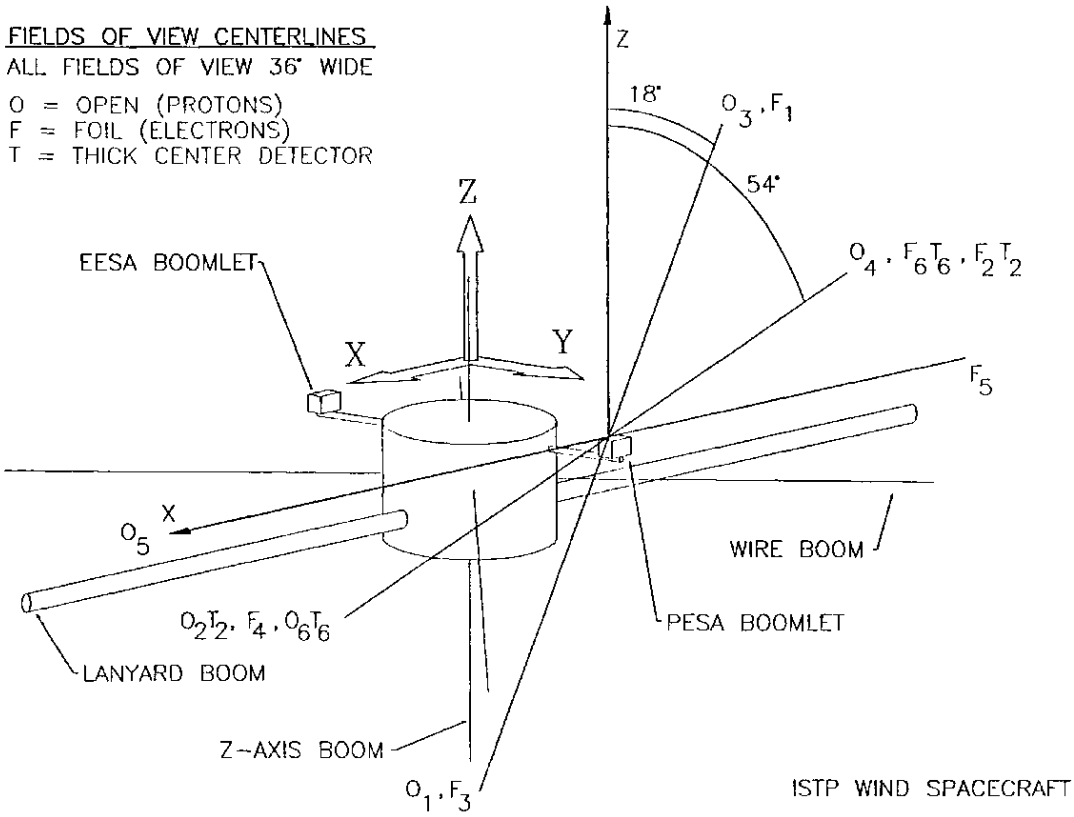

Figure 2.9. Schematic indicating the centers of the FWHM FOV of the SSTs relative to the spacecraft spin axis (adapted from Lin et al. [1995]).

In each double-ended telescope, one end of sandwiched detectors is covered with a thin Lexan foil (F) that rejects protons up to ~400 keV but leaves >~ 25 keV electrons essentially unaffected. The opposite end is open (O) but looks through a broom magnet, which sweeps away electrons below ~400 keV but leaves ions unaffected. Thus, at energies below ~ 400 keV and in the absence of contamination by higher energy particles, the foil (F) detectors count only electrons while the magnet or open (O) detectors count only ions. An anti-coincidence circuit, with an adjacent detector, is used to eliminate counts from penetrating particles and achieve low background. The foils in front of the F detectors are coated on each side with 1500 Å of aluminum to completely eliminate sunlight.

At energies above ~400 keV, most electrons will penetrate the front detector and be rejected by anti-coincidence with the adjacent detector, but some electrons will stop in the front detectors due to straggling. Electrons at ~400 keV to >1 MeV can be cleanly detected by summing the outputs of the front and center detector (FT or OT) of the triplet when they are in coincidence. Protons up to ~6 MeV will stop in the front detectors, and ~6-11 MeV protons can be detected by the combination of the front and center (OT) detectors in the triplet.

Each double-ended telescope has two 36º×20º FWHM FOVs, so five telescopes (#1, 3-6) cover a 180º×20º FOV for foil and for open (magnet) detectors (see Figure 2.9). Telescope 1 and 3 cover the FOV of 0º-36º and 144º-180º to the spin axis, telescope 4 and 6 cover 36º-72º and 108º-144º, and telescope 5 covers 72º-108º. Each end of a telescope (foil or open) has a

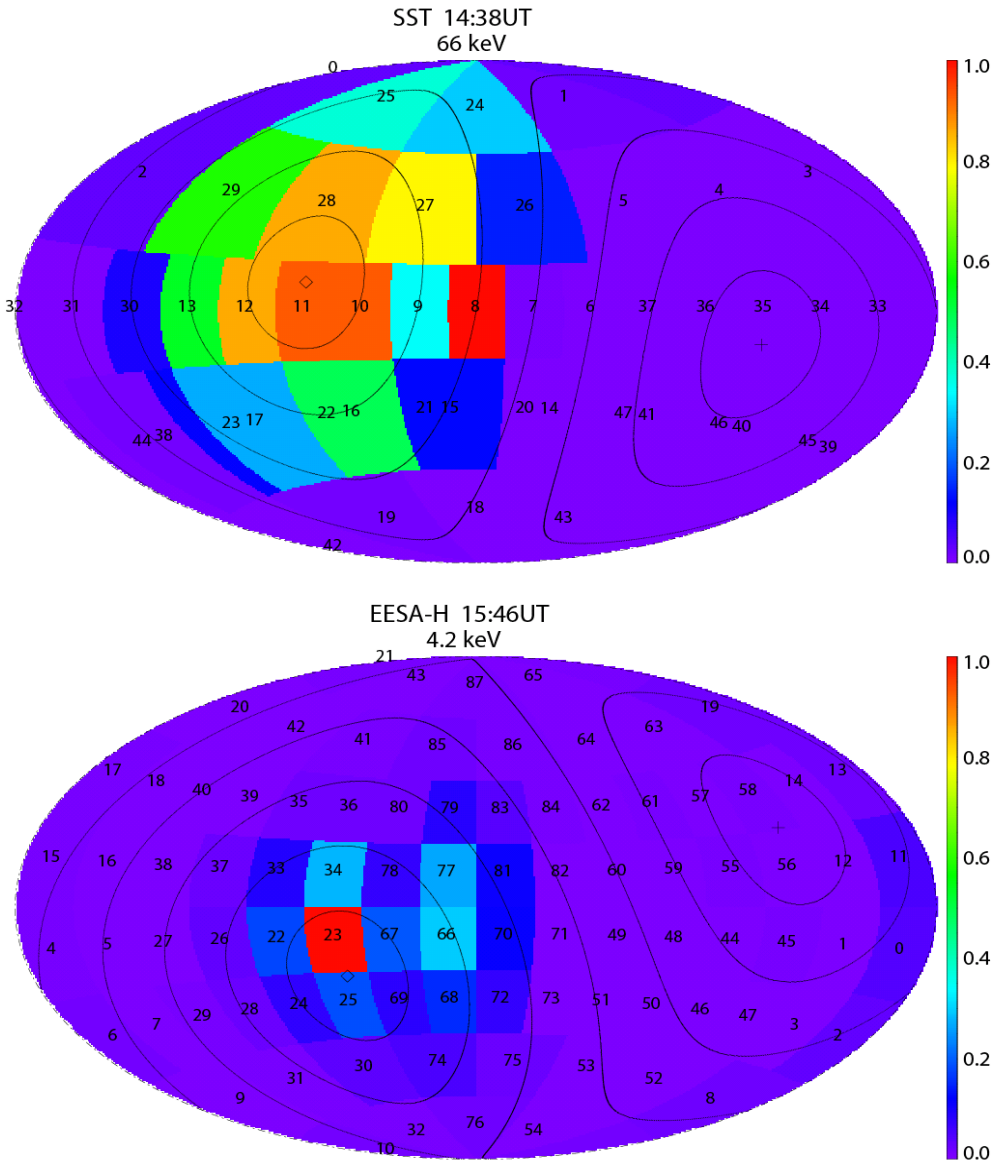

Figure 2.10. Examples of full 3-D angular distribution of electrons measured at 66 keV by SST and at 4.2 keV by EESA-H for the 20 October 2002 SEP event. The Hammer-Aitoff equal area projection is used to display the 4π steradians angular coverage, with the center being the sunward direction. The SST distribution (top) has 48 angular bins (labeled as 0-47) while the EESA distribution (bottom) has 88 angular bins (labeled as 0-87), each with electron fluxes normalized to the maximum value and color-coded. The cross (diamond) indicates the direction parallel (anti-parallel) to the IMF direction. The black curves represent the iso-pitch-angle contours at 22.5º, 45º, 67.5º, 90º, 112.5º, 135º, 157.5º PA. During this SEP event, the IMF was pointing toward the Sun, and then outward-traveling electrons were beaming along the anti-parallel direction of the IMF.

geometric factor of 0.33 $cm^2 \cdot sr$. Telescope 2 views the same angle (36º-72º and 108º-144º) to the spin axis as telescope 6, but both ends are equipped with a drilled tantalum cover that reduces the geometric factor by a factor of ten (0.03 $cm^2 \cdot sr$) to accommodate the most intense fluxes.

The output from each detector is fed to low-noise charge-sensitive pre-amplifiers that are mounted next to the detectors, and then to shaping amplifiers. The shaped pulses are multiplexed into linear analog to digital converters (ADCs). The outputs of the ADCs are pseudo-log compressed to 24 energy channels for all O, OT and FT detectors, and 16 energy channels for the F detectors, with $\Delta E/E \approx 30\%$ over the range of energies.

All the SSTs are calibrated in flight by various combinations of three linear ramp pulsers, one each for the F, O T detectors. The absolute energy calibration is performed by monitoring the highest energy of protons that stop in the detectors, and by placing the pairs or triplets of detectors in coincidence and monitoring the minimum ionizing energy for penetrating particles. Both of these energies depend only on the detector thickness.

2.2.3 Operation

EESA-L (-H) is swept over its energy range from ~ 3 eV to 1.3 keV (from ~100 eV to 30 keV) 32 or 64 times per 3-second spacecraft spin period to cover the full 4π steradians, with 15 logarithmically spaced energy steps ($\Delta E/E \approx 0.2$) per sweep. The three-dimensional distribution data are sorted on board the spacecraft into 88 angular bins, each with roughly equal solid angle (see bottom of Figure 2.10). In the zenith angle direction, although the EESA anodes have angular resolution varying from 5.6° to 22.5° (see Figure 2.7), the outputs are usually binned into eight sectors, each covering a 22.5º FOV. During one spin, the 0º-22.5º FOV and 157.5º-180º FOV to the spin axis are each accumulated in 4 equal azimuth bins; the 22.5º-45º FOV and 135º-157.5º FOV are each accumulated in 8 equal azimuth bins; the FOVs of 45º-67.5º, 67.5º-90º, 90º-112.5º and 112.5º-135º are each accumulated in 16 equal azimuth bins. Each angular bin can be assigned a pitch angle (PA) calculated for its central axis using the IMF direction measured by the WIND MFI instrument [Lepping et al., 1995]. Then the three-dimensional data are re-binned into eight PA bins with a 22.5° angular resolution, with a small degree of overlap between adjacent bins. The PA is measured relative to the IMF direction. Thus, if the IMF points sunward (anti-sunward), then the four PA bins – 90-112.5°, 112.5-135°, 135-157.5°, 157.5-180° – cover electrons traveling outward from (toward) the Sun and the other four bins – 0-22.5°, 22.5-45°, 45-67.5°, 67.5-90° – cover inward-traveling (outward-traveling) electrons. The 3-D angular bins # 66, 68, 70, 72, 77, and 81 look in or near the sunward direction and angular bins #0 and 11 look in the anti-sunward direction, and thus they usually have high background due to solar wind protons entering the electrostatic analyzer and producing significant secondary electrons in these directions. Figure 2.11 compares the count rates in these angular bins with representative measurements in other bins during quiet times. These contaminated bins have the excess background, especially at energies above ~ 1 keV, so they are excluded in the process of binning pitch-angle distributions (PADs). Moments (density, velocity, pressure tensor, heat flux) and omni-directional fluxes are also computed. The differential flux, J, is obtained from the count, C, through the relation:

$$J = C/(\Delta t \times \Delta E \times G) \qquad (2.1),$$

where Δt is the accumulation time, ΔE is the energy bandwith and G is the detector geometric factor in cm^2 str.

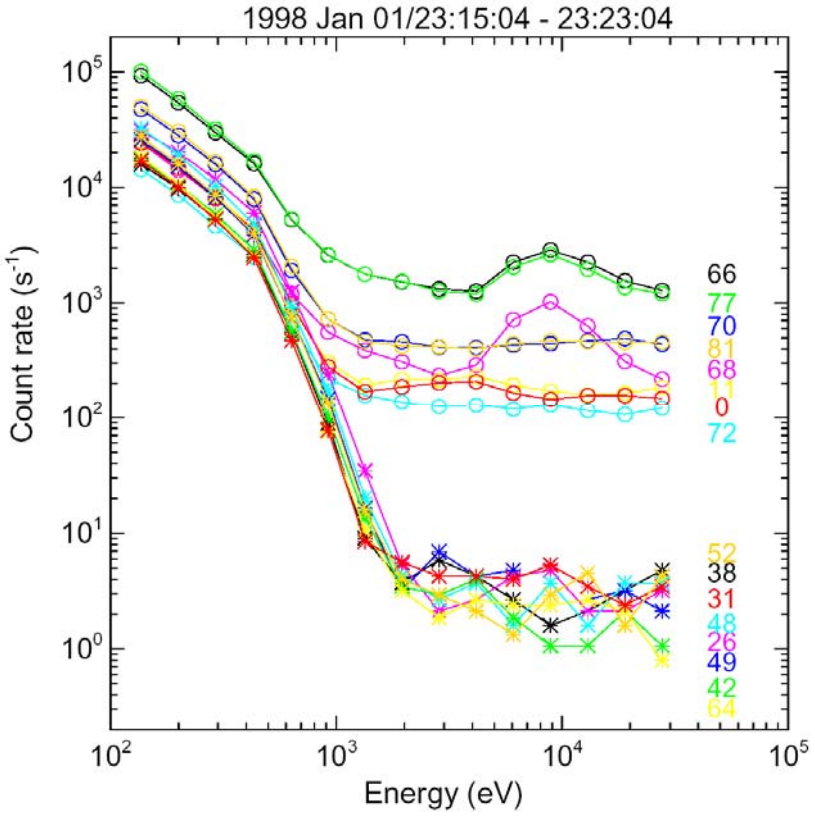

Figure 2.11. Examples of EESA-H count rates at quiet times. Open circles show the sunward angular bin #66, 68, 70, 72, 77, and 81 and anti-sunward bins #0 and 11 that have secondary electron contaminations produced by solar wind protons entering EESA-H. Asterisks show the angular bin #26, 31, 38, 42, 48, 49, 52 and 64, representing typical EESA-H measurements.

SST collects data 16 times per spin in 16 energy channels for F detectors and 24 energy channels for O, OT and FT detectors, with ΔE/E≈ 30%. Three-dimensional distributions are computed with reduced energy resolution - 7 logarithmically spaced energy channels for F and FT detectors, and 9 channels for O and OT detectors. The SST data used in this thesis are the electron data from F detectors, covering the energy range from ~ 23 to 650 keV. The 3-D distribution data from F detectors are sorted on board into 40 angular bins, each with roughly equal solid angle (see top of Figure 2.10). The 0º-36º FOV (telescope 1) and 144º-180º FOV (telescope 3) to the spin axis are each accumulated in 4 equal azimuth bins; the 36º-72º FOV (telescope 6) and 108º-144º FOV (telescope 4) are each accumulated in 8 equal azimuth bins; the 72º-108º FOV (telescope 5) is accumulated in 16 equal azimuth bins. The 8 angular bins (#20-23, 44-47) collected from telescope 2 have similar FOVs to those from telescope 6 but have a 10-times-smaller geometric factor. In addition, the sunward angular bins (#7-9, 15) and anti-sunward bins (# 31-33) usually have high background, respectively, due to solar X-rays entering

and being detected by the F detector and the O detector located behind, or due to direct sunlight saturating the O detector when it faces the Sun and the effect of the anti-coincidence with the F detector behind it. Figure 2.12 shows that these angular bins tend (except #9) to have the excess background at all energies or certain energies, compared to typical SST measurements. Thus, these bins are excluded from the calculation of PADs and omni-directional fluxes for the SST F detectors. The differential flux, J, is obtained from the count, C, through the relation:

$$J = C/ (\Delta t \times \Delta E \times G \times feff) \qquad (2.2),$$

where feff is the efficiency for F detectors because of scattering and straggling in the foil.

In normal modes, the data of 3-D distributions, PADs and omni-directional fluxes are telemetered with a time resolution of ~12 seconds for SST, with a time resolution of ~97 seconds for EESA-L and –H and PESA-H, and with a ~ 24-second time resolution for PESA-L, while the data of electron and proton moments are computed on-board and telemetered with a unique time resolution of 3 seconds for EESA-L and PESA-L. In burst modes, all the telemetered data have a 3-second (one spin) time resolution.

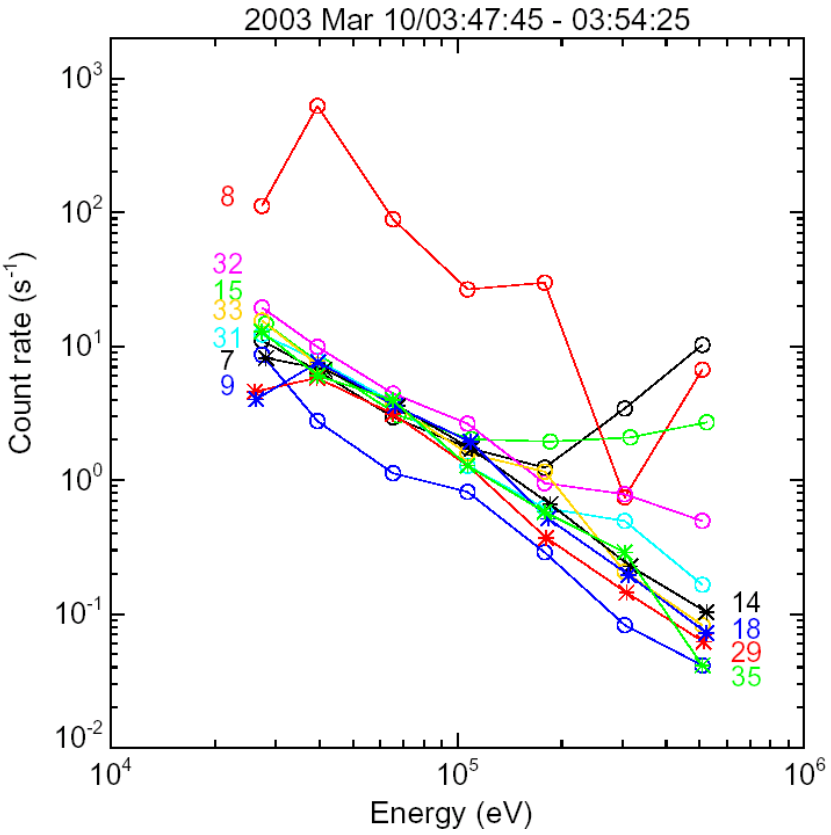

Figure 2.12. Examples of SST F count rates at quiet times. Open circles show the angular bin #7-9, 15 and 31-33 that have solar X-ray contaminations. Asterisks show the angular bin # 14, 18, 29 and 35, representing typical SST measurements.

2.2.4 Count correction for SST

For SSTs, laboratory calibration shows that an approximately 15% of incident electrons will scatter back out of each F detector before fully depositing their incident energy E_{in} (Figure 2.13); these events are roughly evenly distributed over the energy range from zero up to E_{in} [Berger et al., 1969], contaminating the energy channels below E_{in}. This can lead to erroneous results for studies of velocity dispersion (see Figure 2.14) if not taken into account. For the studies presented in this thesis, this effect has been corrected for by assuming that in the energy channel j (with the energy band [E_{j-}, E_{j+}]), a ~10%-25%, a_j, of incident electrons, N_{jin}, will scatter out and these electrons will be evenly distributed over the energy range of 0 to E_{j-}, i.e., they can produce counts, $\Delta N = a_j \times N_{jin} \times \Delta E / E_{j-}$, at an lower energy channel with the energy band of ΔE. Figure 2.14 shows that at 27-108 keV, solar energetic electrons appear to arrive a few minutes earlier in the uncorrected data (black) than in the corrected data (red).

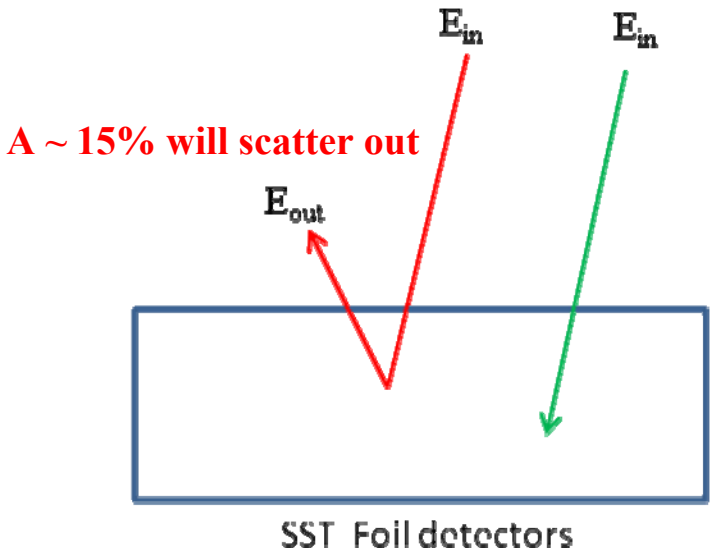

Figure 2.13. Sketch of scattering-out electrons (red) in SST foil detectors.

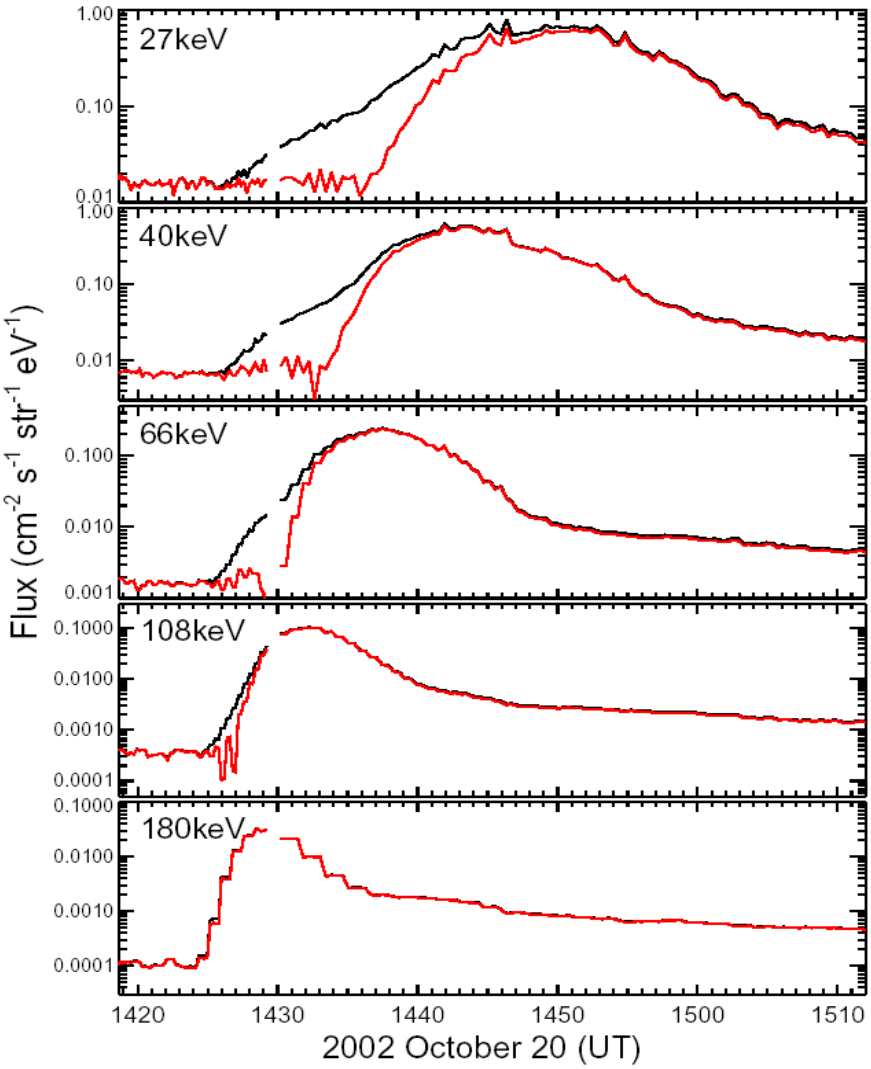

Figure 2.14. Examples of the electron flux-vs-time profiles before (black) and after (red) correction for scattered-out electrons in SST for the 20 October 2002 solar electron event. A correction of ~15%- 25%, varying with energy, is made for electrons that scatter out of the detector and leave less than their incident energy.

3. A Statistical Study of Solar Electron Events over one Solar Cycle

3. 1 Introduction

Solar electron events were first observed at energies above ~40 keV [Van Allen & Krimigis, 1965; Anderson & Lin, 1966], and later were detected down to keV energies [Potter et al., 1980] (and even to ~0.1 keV [Gosling et al., 2003]). ISEE-3 measurements in 1978-1979 suggested that near solar maximum, $>\sim 10^2$ events/month occur over the whole Sun [see Lin, 1985 for review], with ~ 40% only detected below ~10-15 keV. These events are often accompanied by low-energy, ~MeV/nucleon ion emissions that are highly enriched in ^{3}He [Reames et al., 1985]. ^{3}He-rich events were first discovered by Hsieh & Simpson [1970], and Fisk [1978] proposed the first viable mechanism for selective heating of ^{3}He by absorption of electrostatic ion cyclotron waves produced above the ^{4}He gyrofrequency. These electron/^{3}He-rich events form the class of "impulsive" SEP events, so-called because the associated flare soft X-ray (SXR) bursts, when present, have a duration of < 1 hour [Pallavicini et al., 1977]. They appear to fill a cone of about ~30º in solar longitude at 1AU [Lin & Anderson, 1967] and last for from tens of minutes (for nearly scatter-free events) to hours (for diffusive events). They are also characterized by significant enhancements (factor of ~10) of heavy nuclei such as Fe and high heavy-ion ionization states [see Mason, 2007 for review]. The average ionization state was found to be ~20 for Fe and ~14 for Si, which was interpreted as being due to either heating to ~ 10^7 K [Klecker et al., 1984; Luhn et al., 1987] or stripping of the ions by the intense electron beams [Miller & Viñas, 1993] in impulsive flares. Thus, Reames [1995, 1999] and references therein suggested that electron/^{3}He-rich SEP events are produced in impulsive flares at the Sun, due to selective resonant acceleration of ^{3}He and certain heavy ions. Based on the electron/^{3}He-rich association in analogy with auroral phenomena, Temerin & Roth [1992] suggested that the selective acceleration was due to electron-beam generated waves. More recently, Kleckler et al. [2006] reported that the typical ionization states measured in electron/^{3}He-rich SEP events by ACE/SEPICA and SOHO/STOF show a large increase with energy at <~ 1 MeV/nucleon, indicating that the previous interpretation of high heavy-ion charge states being due to high plasma temperature in flares is too simplistic.

Solar electron events also accompany large solar proton events that have small electron-to-proton ratios and accelerate ions up to GeV energies with large particle intensities and little or no ^{3}He enhancements. These electron/proton events form the class of "Gradual" SEP events, so-called because the associated flare SXR bursts have a duration of >~ 1 hour [Pallavicini et al., 1977]. They occur about ~10/year at solar maximum, extend over ~100-180° in solar longitude, last for days and are closely associated with fast CMEs and type II radio bursts (indicator of shock waves). These properties suggest that gradual SEP events are accelerated by shocks driven by fast CMEs through the IPM [e.g., Reames, 1999].

Previous studies suggested that solar impulsive electron events have the complex correlation with other solar phenomena. For solar impulsive electron events measured from ~1- > ~100 keV by ISEE-3 from 1978 August to 1979 November, Lin [1985] found that most of them were unaccompanied by Hα flares and hard X-ray bursts; some were even unaccompanied by SXR bursts, i.e., no flare-related activities at all; but about 90% had a type III solar radio burst detected within ~20 minutes. Haggerty & Roelof [2002] selected 79 solar impulsive electron

events measured at high energies, 38-315 keV, from 1997 August through 2000 September, and found that out of the 79 events, 62 have GOES SXR bursts, 47 have Hα flares, and all have a type III radio burst. Simnett et al. [2002] further found that among the 53 of these 79 impulsive electron events that have coronagraph data from SOHO/LASCO, 47 have a CME that is located primarily off the west limb of the Sun. Then they suggested that these near-relativistic electron events may be accelerated by CME-driven shocks at radial distances of ~ 2-3 R_S from the Sun's center. Recently, Wang et al. [2005] and Y.-M. Wang et al. [2006] reported that some impulsive SEP events appear to be associated with rather fast (>~ 500 km/s) and narrow (<30º) CMEs/jets that take off from the solar west limb.

For solar energetic electron events, no comprehensive statistical study has been done to examine their frequency of occurrence, their association with other solar phenomena and their event minimum and maximum energy, over an entire solar cycle. Thus, here we survey the WIND/3DP electron observations (~0.1-400 keV) from 1995 through 2005, and we select 1191 solar electron events with a velocity dispersion occurring at three and more energy channels (§3.2.2). We investigate their frequency of occurrence over this solar cycle and their correlation with energetic ions (§3.2.3), their possible association with GOES SXR flares, CMEs, and type III and II radio bursts, (§3.2.4), and the detected event minimum and maximum electron energies (§3.2.5). We find that most of solar energetic electron events lack flare SXR bursts reported in Solar Geophysical Data (SGD), so the general impulsive and gradual SEP event categorization (see Chapter 1) is not applicable. In this study, we therefore use the associated $^3He/^4He$ ratio (available since 1998) to classify solar electron events into "^{3}He-rich" ($^3He/^4He$ >= 0.01, as measured by the Ultra Low Energy Isotope Spectrometer on the ACE spacecraft) and "not-^{3}He-rich" ($^3He/^4He$ <0.01) events (see §3.2.3 for details). We expect that all the electron events in the ^{3}He-rich category are impulsive events, while the not-^{3}He-rich category includes all gradual events, plus events that may be mildly ^{3}He-rich (since the coronal/solar wind $^3He/^4He$ is ~$5x10^{-4}$) but not measurable by present instruments. Then we select the not-^{3}He-rich electron events that are associated with gradual (>~ 1 hour) SXR bursts for a third category of gradual electron events, as defined by Pallavicini et al. [1977].

3.2 Observations

3.2.1 Instrumentation

The WIND spacecraft was launched November 1, 1994, with a trajectory consisting mostly of highly elliptical earth orbits (apogees ~60-100 Re) or orbits around the Lagrange 1 point (see Chapter 2). The 3DP instrument on WIND, has been operating nominally since launch to the present time, and it has been described in Chapter 2 of this thesis.

The Advanced Composition Explorer (ACE) spacecraft was launched August 25, 1997 into a halo orbit around the Lagrange 1 point. The Ultra Low Energy Isotope Spectrometer (ULEIS) on ACE is a time-of–flight mass spectrometer with high mass resolution (σ_m ~ 0.2 amu) and low background, measuring both elemental and isotopic compositions of elements He-Ni from ~20 keV/nucleon to 10 MeV/nucleon [Mason et al., 1998]. It views the sunward hemisphere at an angle of 60° to the ACE spin axis that generally points along the Earth-Sun line.

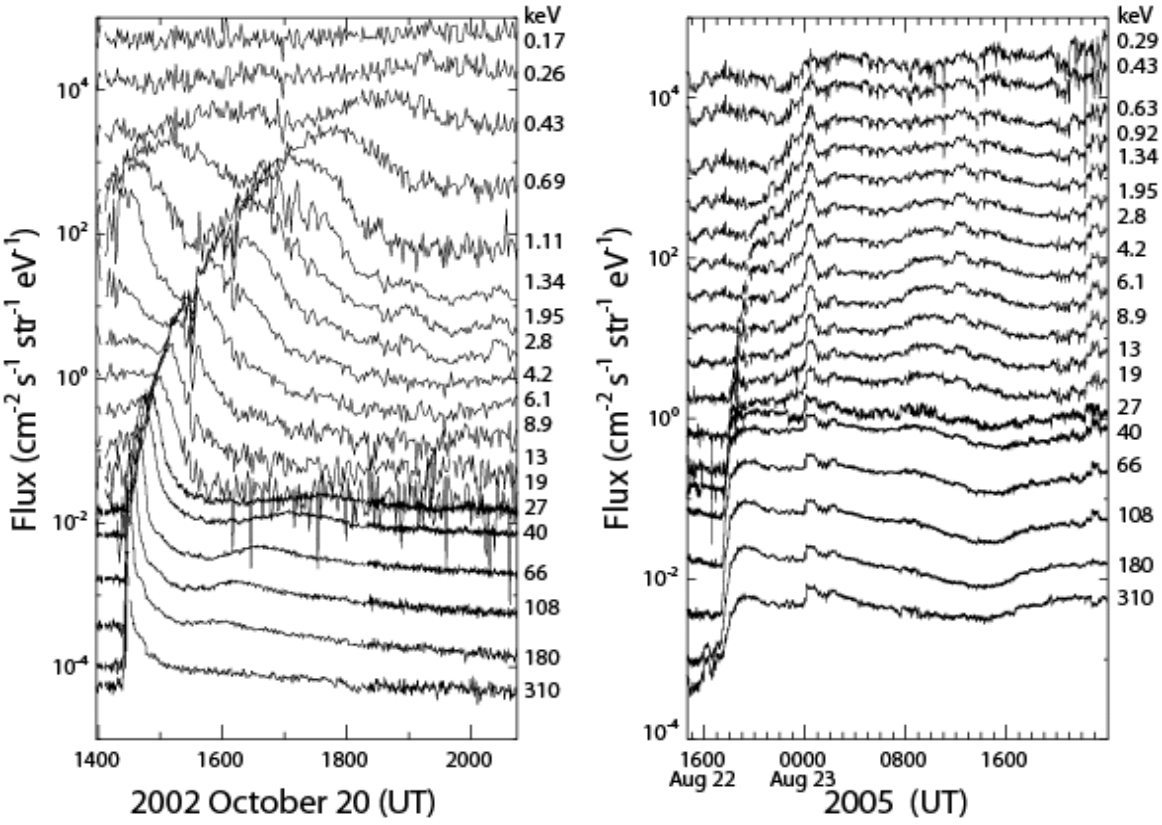

Figure 3.1. Overview plot for the 20 October 2002 event (left) and 22 August 2005 event (right). Left panel shows the flux of outward-traveling electrons observed by EESA-L (0.17-1.11 keV), EESA-H (1.34-19 keV) and SST (27-310 keV). The 20 October 2002 event was preceded by another electron event. Right panel shows the flux of outward-traveling electrons observed by EESA-H (0.29-19 keV) and SST (27-310 keV).

3.2.2 Event selection

We surveyed the WIND/3DP electron data from 1995 through 2005, and identified 1191 solar electron events[†] based on the presence of velocity dispersion – the faster electrons arriving earlier at 1 AU than the slower electrons - at three and more energy channels. Figure 3.1 shows the outward-traveling electron fluxes versus time in energy channels from ~0.2 to 310 keV (channel center energies) for the 20 October 2002 event (left) and from ~0.3 to 310 keV for the 22 August 2005 event (right). The 20 October 2002 event is a solar impulsive electron events, accompanied by an impulsive ion event with the ^{3}He/^{4}He ratio of ~1.47±0.05 observed at 0.5-2 MeV/nucleon by ACE/ULEIS and by no proton events observed at >~ 10 MeV by GOES. Velocity dispersion is evident from 310 keV down to 0.26 keV. This electron event is nearly scatter-free (see Chapter 5) with a duration at the 1/e-fold peak intensity of ~ 4 min at 310 keV and ~110 min at 0.7 keV. It has a reported impulsive SXR burst with duration of ~11 minutes and intensity of C6.6 class.

[†] http://sprg.ssl.berkeley.edu/~windsound/WIND_electron/electron_event.html

The 22 August 2005 event is a solar gradual electron events detected from ~0.4 to >~310 keV, accompanied by a gradual ion event with the ^{3}He/^{4}He ratio of ~0.0009±0.001 and intense proton fluxes with the peak intensity of ~300 (cm^2 s str)$^{-1}$ above ~10 MeV. It has a reported gradual SXR burst with duration of ~76 minutes and intensity of M5.6 class. This event lasts for more than four days.

For all the 1191 solar electron events, the release time at the Sun is roughly estimated from the *in situ* onset at the detected highest energies, after subtracting the electron travel time along a nominal 1.2 AU path length (the Parker spiral IMF length for V_{SW} ~350 km/s) from the Sun to Earth.

3.2.3 Frequency of occurrence

Figure 3.2a shows a histogram of the yearly number of solar electron events detected near 1 AU from 1995 through 2005. The event occurrence rate (black) has a minimum of 12/year in 1996 and a double peak at solar maximum, with a major peak (192/year) in 2002 and a secondary peak (162/year) in 2000, separated by a dip (140/year) in 2001. For electron events detected since 1998, ion measurements of elements He-Ni are available at ~0.02 to 10 MeV/nucleon from ACE/ULEIS, but many electron events have no ion events (identified by the presence of velocity dispersion), due to the low ion fluxes relative to the instrument detection sensitivity near 1 AU. For each electron event, thus, we define a time interval to calculate the associated ^{3}He/^{4}He ratio that starts 5 hour after the estimated electron release at the Sun, corresponding to the transit of ~0.5 MeV/nucleon ions to the Earth, and ends at the earlier of i) 9 hour later or ii) 5 hour after the release of the next electron event. Then we use the associated ^{3}He/^{4}He ratio in this interval (even if no solar energetic ion event can be identified through velocity dispersion) to classify solar electron events (since 1998, but very few electron events were observed in 1995-7; see Fig. 3.2 a) into "^{3}He-rich" and "not-^{3}He-rich" categories. We find that about 78% of these electron events are accompanied by low-energy ion emissions with the ^{3}He/^{4}He ratio of ≥ 0.01 at ~0.5-2 MeV/nucleon, referred to as "solar ^{3}He-rich electron events". Based on previous findings, we expect that all the electron events in this category are impulsive electron events. Their occurrence rate (red) also shows a double peak at solar maximum with a rate of 120/year in 2000, 87/year in 2001 and 157/year in 2002. If impulsive electron events come from a solar longitude cone of <~ 30°, then these *in situ* observations near the Earth suggest that >~1000-2000 events/year occur over the whole Sun at solar maximum. The other 22% of electron events are accompanied by ion emissions with the ^{3}He/^{4}He ratio < 0.01, referred to as "not-^{3}He-rich electron events". We expect that this category includes all gradual electron events, plus some impulsive electron events with small ^{3}He enhancements. Only ~11% (28 events) of the not-^{3}He-rich electron events are associated with gradual (>~ 1 hour) SXR bursts reported in SGD; we take these 28 events to comprise the solar "gradual" electron event category. Their occurrence rate (blue) is 5/year in 2001 and 7/year in 2005.

This temporal variation of solar electron events is similar to that of sunspot number and SXR flare number. In Figure 3.2b, the monthly sunspot number (black) has a double peak, similar to the electron event distribution, but the yearly number (pink) shows only a single peak, at solar maximum; both have a minimum in 1996. Figure 3.2c shows the histogram of the yearly number of GOES SXR flares reported in SGD. It also has a minimum in 1996 and a broad peak in 2000-2002.

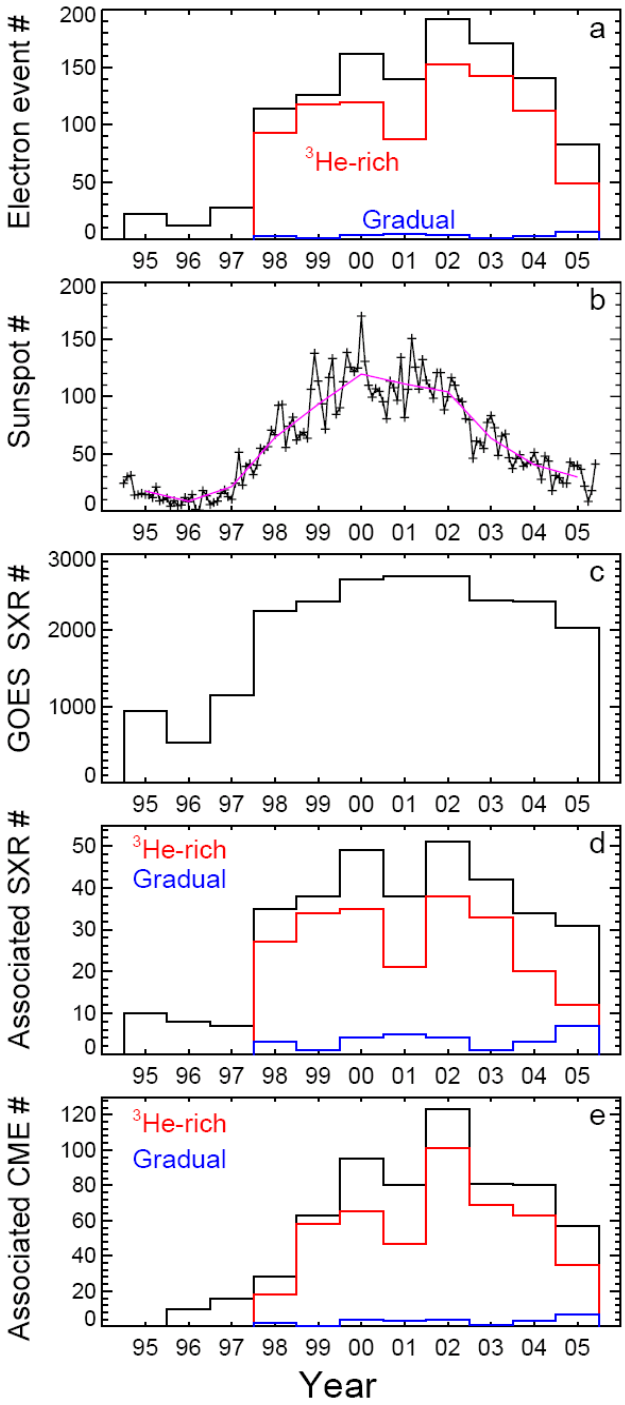

Figure 3.2. Time distribution from 1995 to 2005. a): The yearly number of all the solar electron events (black), ^{3}He-rich electron events (red) and gradual electron events (blue). b): The monthly (black) and yearly (pink) sunspot number. c): The yearly number of GOES SXR flares reported in the SGD. d): The yearly number of SXR flares associated with ^{3}He-rich electron events (red), gradual electron events (blue) and all the electron events (black). e): The yearly number of SOHO/LASCO CMEs associated with ^{3}He-rich electron events (red), gradual electron events (blue) and all the electron events (black).

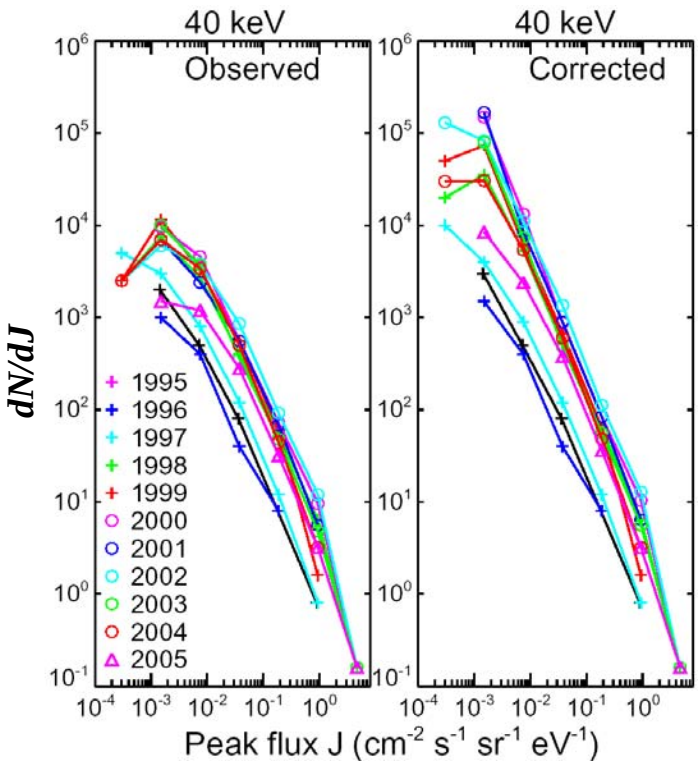

Figure 3.3. The event occurrence frequency distribution at 40 keV from 1995 to 2005. *N* represents the yearly event number and *J* represents the peak flux. Left panel shows observations and right panel shows the extrapolation after correction for the background effect. Colored symbols show the data at different years.

The yearly occurrence frequency distribution of solar electron events observed near the Earth are shown in the left panels of Figure 3.3 and 3.4, respectively, at 40 and 2.8 keV from 1995 to 2005. The observed occurrence frequency fits to a power-law at high fluxes but bends down at low fluxes. However, we are unable to detect small events if the background is relatively high, e.g., during the strong, long decay of electron events (see right panel of Figure 3.1, for example) or when the WIND spacecraft is inside the Earth's bow shock (see Chapter 2). We can correct for such high background and then estimate the expected event number. For the peak-flux interval [*J, J+dJ*] at energy *E*, first, we find the detected weakest event and arbitrarily define one half of its peak flux to be a flux threshold J_b to determine high (>J_b) and low (>J_b) background; then we calculate the expected yearly event number *dN* by assuming the same event occurrence rate during high (>J_b) and low (>J_b) background. The right panels of Figure 3.3 and 3.4 show the corrected occurrence frequency distribution near the Earth, respectively, at 40 and 2.8 keV.

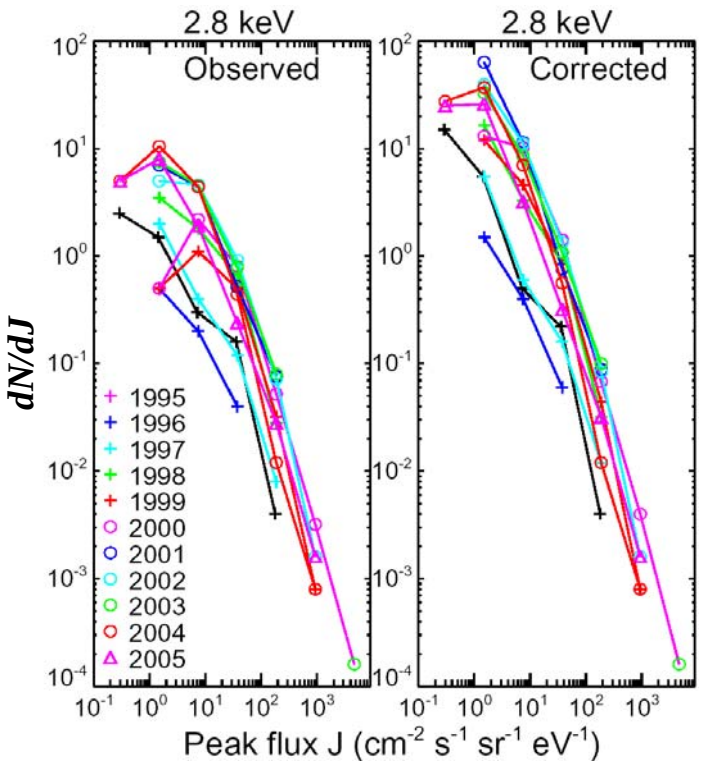

Figure 3.4. The event occurrence frequency distribution at 2.8 keV from 1995 to 2005. *N* represents the yearly event number and *J* represents the peak flux. Left panel shows observations and right panel shows the extrapolation after correction for the background effect. Colored symbols show the data at different years.

At 40 keV, the corrected event occurrence frequency fits well to a power-law relation above 10^{-3} (cm^2 s str eV)$^{-1}$ (about the instrument sensitivity in SST that leads to the bend-down of *dN/dJ* below it) for all years (see the right panel of Figure 3.3):

$$\frac{dN}{dJ} = A_i \times J^{-\gamma_i} \qquad (3.1),$$

where the index *i* indicates the year from 1995 to 2005. A corrected (expected) yearly event number can be estimated by integrating *dN* from the observed minimum *J* of ~2.9×10^{-4} (cm^2 s str eV)$^{-1}$ to infinity. Figure 3.5 shows the time variation of the derived power-law index γ (top) and coefficient *A* (bottom), and Figure 3.6 compares the observed event occurrence rate (circles) with the corrected occurrence rate (crosses) above ~2.9×10^{-4} (cm^2 s str eV)$^{-1}$. At 40 keV, on average, the occurrence frequency distribution is ~ $(0.48\pm0.83) \times J^{-1.17\pm0.17}$ around solar minimum (1995-1997) and ~ $(2.02\pm0.16) \times J^{-1.50\pm0.03}$ around solar maximum (2000-2002). Above ~2.9×10^{-4} (cm^2 s str eV)$^{-1}$, the corrected event occurrence rate is ~ 30/year at solar minimum and ~1000/year at solar maximum, while the observed occurrence rate is ~10/year at solar minimum and ~ 130/year at solar maximum.

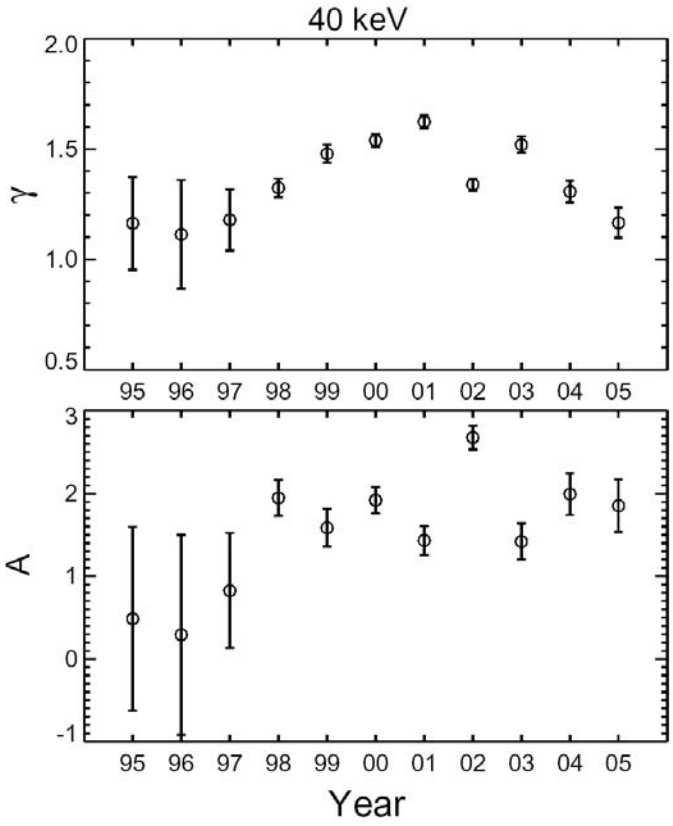

Figure 3.5. The derived power-law index and coefficient for the occurrence frequency distribution at 40 keV after correction for the background effect.

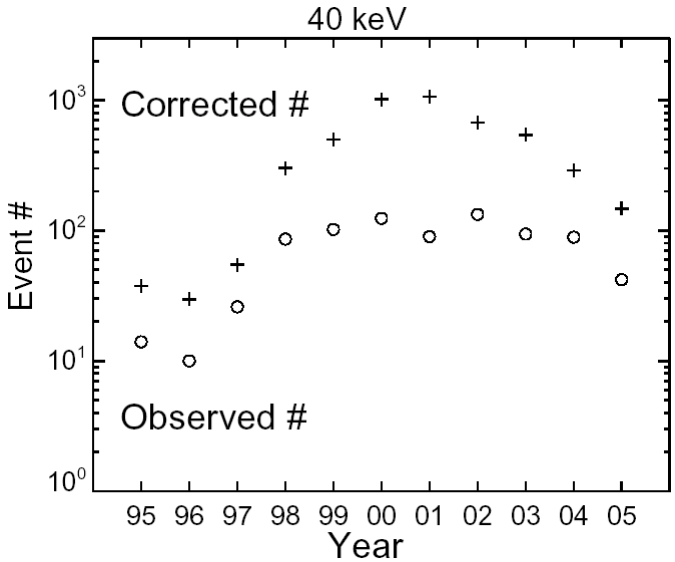

Figure 3.6. The yearly event number at 40 keV from 1995 to 2005. Circles indicate the observed occurrence rate, and crosses indicate the integrated occurrence rate after correction for the background effect.

At 2.8 keV, the corrected event occurrence frequency still appears to slightly bend down at low fluxes (see the right panel of Figure 3.4), likely due to the high instrumental background in EESA that limits the correction at low fluxes. We arbitrarily fit the corrected occurrence frequency above 1 $(cm^2\ s\ str\ eV)^{-1}$ to a power-law relation (Equation 3.1) for all years. Figure 3.7 displays the time variation of the derived power-law index γ and coefficient A, and Figure 3.8 shows the observed and corrected event occurrence rate above ~0.33 $(cm^2\ s\ str\ eV)^{-1}$. At this energy, on average, the occurrence frequency distribution is ~ $(1.86\pm0.40) \times J^{-1.12\pm0.15}$ around solar minimum (1995-1997) and ~ $(4.53\pm0.10) \times J^{-1.24\pm0.04}$ around solar maximum (2000-2002). Above ~0.33 $(cm^2\ s\ str\ eV)^{-1}$, the corrected occurrence rate is ~ 25/year at solar minimum and ~600/year at solar maximum, while the observed occurrence rate is ~5/year at solar minimum and ~120/year at solar maximum. This is similar to the results at 40 keV, implying that many small electron events might be "buried" by the background.

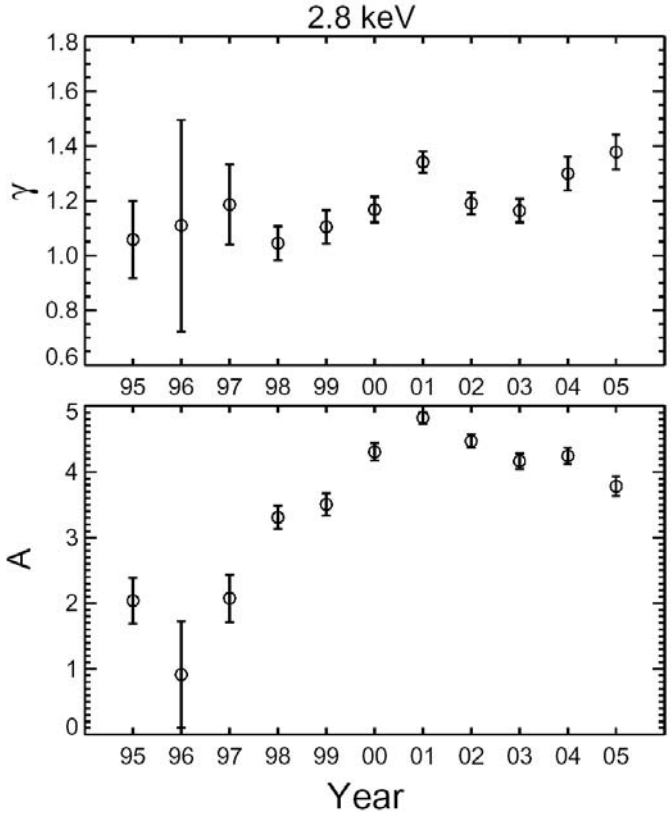

Figure 3.7. The derived power-law index and coefficient for the occurrence frequency distribution at 2.8 keV after correction for the background effect.

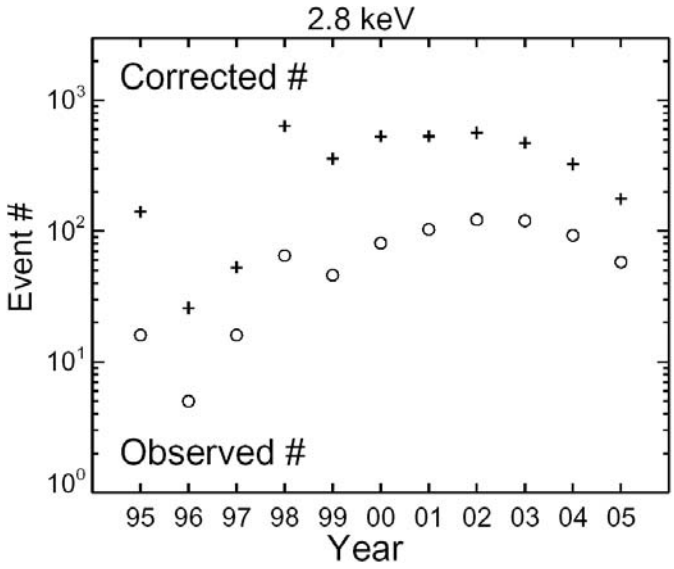

Figure 3.8. The yearly event number at 2.8 keV from 1995 to 2005. Circles indicate the observed occurrence rate, and crosses indicate the integrated occurrence rate after correction for the background effect.

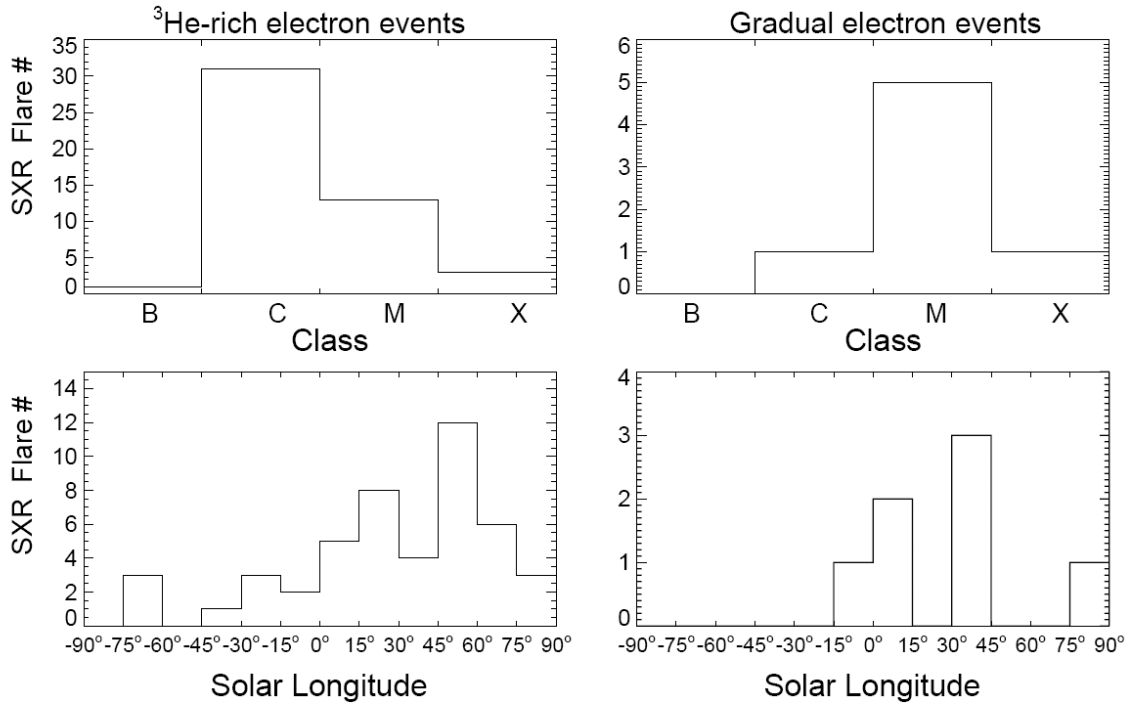

Figure 3.9. The histogram of the intensity (top) and solar longitude (bottom) of the associated SXR flares for ^{3}He-rich (left) and gradual (right) electron events. The positive (negative) longitude means west (east).

3.2.4 Association with other solar phenomena

For SXR flares, here we use GOES SXR bursts reported in SGD (down to B class). We identify an SXR burst to be associated with a solar electron event, if the SXR impulsive phase (approximately from start to peak) overlaps with the uncertainty interval of the estimated electron solar release (that is estimated from the uncertainty of *in situ* onsets, after subtracting the electron travel time along a nominal 1.2 AU path length). We find that only ~ 25% of ^{3}He-rich electron events have a possible association with a SXR flare, while due to our definition, all gradual electron events have a SXR flare. Figure 3.2d displays the histogram of SXR flares associated with ^{3}He-rich electron events (red), gradual electron events (blue) and all solar electron events (black), which strongly reflects the corresponding time variation in electron events. The location of SXR flares can be determined by Hα observations (when available in SGD). Figure 3.9 plots the intensity (top) and solar longitude (bottom) histograms for associated SXR flares. For ^{3}He-rich electron events (left panels), most of the associated flares occur at solar longitude ~W10°-80° that magnetically connects to the vicinity of Earth through the Parker spiral IMF field line, and most are low-intensity C-class flares; the several eastern flares, identified by time coincidence, are not actually associated with ^{3}He-rich electron events. For gradual electron events (right panels), most of the associated flares also occur at longitude ~W10°-80°, but ~ 86% of the associated flares are modest-intensity M-class or high-intensity X-class flares.

White-light CME observations are available from SOHO/LASCO since 1996. From the CME height-time plot, we define a CME to be associated with a solar electron event, if the CME takes off/covers the solar west limb that magnetically connects to the Earth and it reaches an altitude of <~10 R_S at the estimated electron solar release. The latter criterion is based on the study by Kahler [1994] that suggests the acceleration by fast-CME-driven shocks for gradual SEP events likely occur at altitudes of 5-15 R_S, and the evidence (see Chapter 5) that ^{3}He-rich ions may be accelerated by CMEs at ~ 2-10 R_S. Figure 3.2e shows the time variation histogram of CMEs associated with ^{3}He-rich electron events (red), gradual electron events (blue) and all solar electron events (black). Figure 3.10 displays the histogram of the CME speed (bottom) and angular width (top) associated with ^{3}He-rich and gradual electron events. About 60% of ^{3}He-rich electron events have a possible CME, with an average width of 58°±48º, excluding halo CMEs[‡], and average speed of 581±345 km/s; ~16% of ^{3}He-rich electron events have fast (>500km/s), narrow (<60º) CME. Out of the 28 gradual electron events, 24 (~86%) have a possible CME, with an average width of 155°±62º, excluding halo CMEs, and average speed of 1475±650 km/s. Note that ~25% of CMEs associated with ^{3}He-rich electron events are pretty narrow (<20°) with speed of 200-1400 km/s, while ~50 % of CMEs associated with gradual events are very wide, halo CMEs with speed of 1200-2900 km/s.

[‡] CMEs aimed at Earth are called "halo" CMEs, because in coronagraph images these CMEs appear as a halo enveloping the Sun with the apparent angular width of 360º.

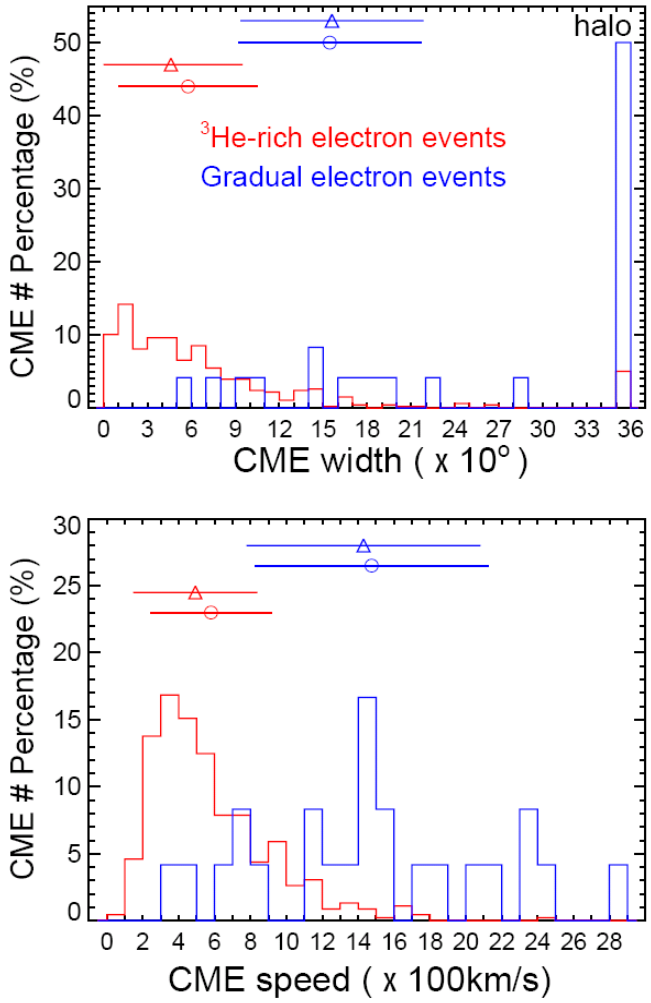

Figure 3.10. The histogram of the CME angular width and speed associated with ^{3}He-rich (red) and gradual (blue) electron events. The Y-axis shows the CME # percentage. In top panel, the mark "halo" indicates halo CMEs that have the apparent width of 360º at the Sun. The triangles (circles) with error bar indicate the median (average) CME width (excluding halo CMEs) and speed with the r.m.s. deviation.

Out of the 1191 solar electron events, 1176 (98.75%) have a type III solar radio burst detected by the WIND WAVES instrument (~10 kHz t o 14 MHz), and <~ 10% of these type III bursts are detected only below ~1-2 MHz. This indicates a one-to-one correlation between electron beams and interplanetary type III radio emissions. The 15 events with no type III bursts are all detected only below ~13 keV: 11 are "^{3}He-rich", 2 are "not-^{3}He-rich" but not "gradual", and 2 have no ACE/ULEIS coverage. Previous studies [Wang et al., 2006; see Chapter 4) suggest that type III radio bursts are produced by electrons below ~10-13 keV. However, since these 15 low-energy electron events are not strong, type III radio emissions generated by them may be too weak to be detected by WIND/WAVES. On the other hand, 95 out of the 1191 electron events (~8%) have a type II solar radio burst detected by WIND/WAVES. Among these 95 events, 17 are "gradual" (~61% of gradual electron events), 52 are "not-^{3}He-rich" but not "gradual", 22 are "^{3}He-rich" (~2% of ^{3}He-rich electron events) but with a moderately enhanced

^{3}He/^{4}He ratio of 0.01-0.15, and 4 have no ACE/ULEIS coverage. These type II radio bursts are closely associated with wide, fast CMEs.

3.2.5 The event minimum and maximum electron energies

Figure 3.11 displays the histogram of the minimum (top) and maximum electron energy (bottom) observed in solar ^{3}He-rich (red) and gradual (blue) electron events. For ^{3}He-rich events, ~ 62% are detected at energies down to < ~3 keV, ~51% are detected up to > ~ 100 keV, and ~ 6% are detected above 500 keV; ~ 25% are detected only below 10 keV and ~31% are detected only above. For gradual events, ~75% are detected down to < ~3 keV, ~79% are detected up to > ~ 100 keV, and ~ 36% are detected above 500 keV; ~11% are detected only below 10 keV and ~18% are detected only above. These suggest that electrons in gradual events tend to be accelerated to higher energies than in ^{3}He-rich events.

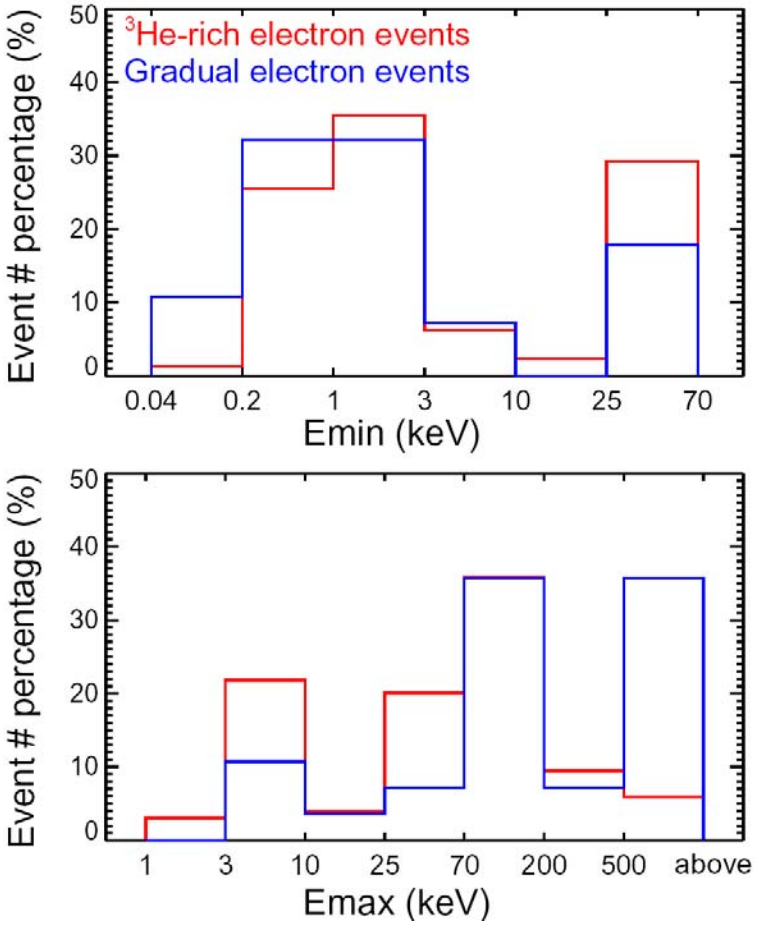

Figure 3.11. The distribution of the minimum and maximum electron energy observed in solar ^{3}He-rich (red) and gradual (blue) electron events. The Y-axis shows the electron event # percentage.

Figure 3.11 also indicates three types of event energy range: only below ~10 keV, only above ~25 keV, and from < 10 keV to > 25 keV. However, the presence of electron events detected only above ~25 keV could be due to the much better sensitivity of SST (above 25 keV) compared to EESA (below 30 keV), i.e., these events (or a fraction of them) could have the <~ 10-25 keV electrons with low intensity that are unable to be detected by EESA. Figure 3.12 shows the percentage of events detected only below 10 keV for ^{3}He-rich (red), gradual (blue) and all (black) electron events, every year of the solar cycle. For all solar electron events, this yearly percentage appears to increase with time from ~4% in 1997 (about solar minimum) to ~25% in 2001 (solar maximum) and then to 43 % in 2005 (approaching the next solar minimum). The yearly percentage for ^{3}He-rich electron events shows a similar temporal tendency, but the yearly percentage for gradual electron events fluctuates with time from 0 to ~33%.

Figure 3.13 shows the histogram of the electron peak flux J observed at 40 (top) and 2.8 (bottom) keV. At these two energies, ^{3}He-rich electron events (red) appear to be less intense (especially at 40 keV), compared to gradual electron events (blue). This indicates that fewer electrons are accelerated in ^{3}He-rich events, especially at high energies, than in gradual events

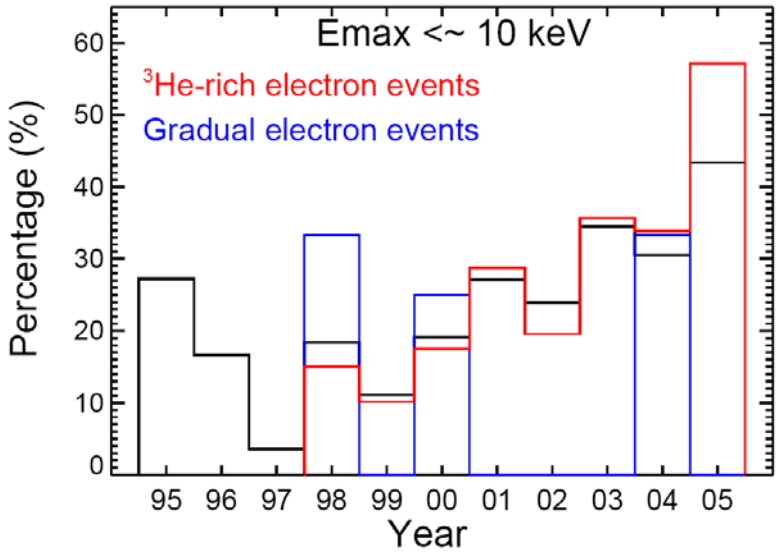

Figure 3.12. Time histogram of the yearly percentage of electron events detected only below 10 keV for ^{3}He-rich (red), gradual (blue) and all (black) electron events.

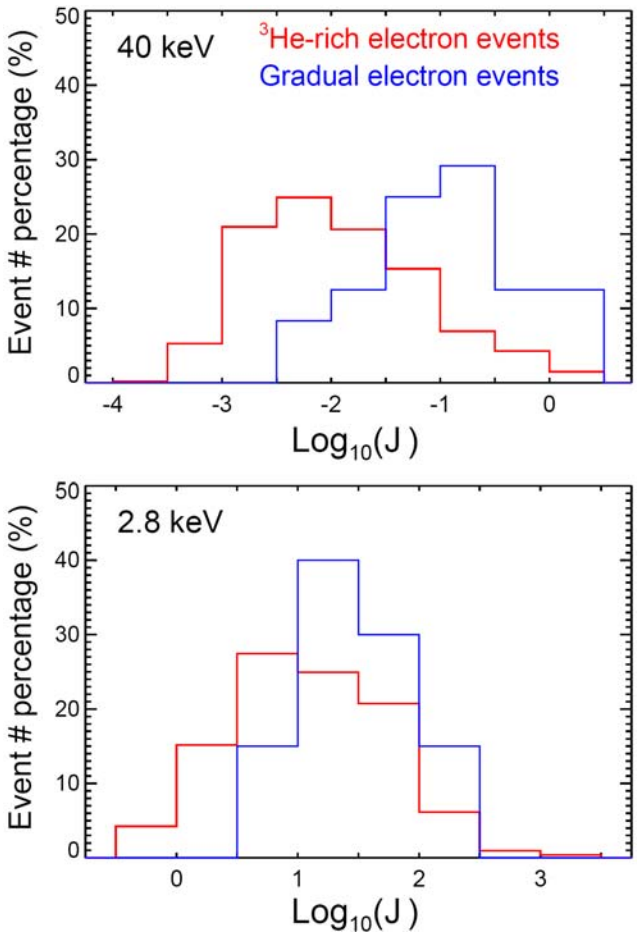

Figure 3.13. The distribution of the electron peak flux observed at 40 and 2.8 keV. Solar ^{3}He-rich electron events are shown in red, and gradual electron events are shown in blue. The X-axis shows the base-10 logarithm of the peak flux J. The Y-axis shows the electron event # percentage.

3.3 Summary and discussion

We have surveyed 1191 solar electron events observed by WIND/3DP from 1995 through 2005. The event occurrence rate shows a strong solar-cycle variation, similar to sunspots and GEOS SXR flares. It is ~10/year at solar minimum but ~190/year at solar maximum. After taking into account the high foreground effect, the corrected occurrence frequency of solar electron events exhibits a good power-law distribution: $dN/dJ=A\times J^{-\gamma}$. At 40 keV (2.8 keV), the integrated occurrence rate above ~2.9×10^{-4} (~0.33) (cm^2 s str eV)$^{-1}$ near the Earth is ~1000/year (~600/year) at solar maximum and ~30/year (~25/year) at solar minimum, up to one order of magnitude larger than the observed occurrence rate. This implies that the observed event number near 1 AU may be strongly underestimated since many small electron events are likely missed due to high background or limited instrument sensitivity. If impulsive electron events (the majority of solar electron events) come from a solar longitude span of ~30°, then ~10^4 events/year may occur over the whole Sun at solar maximum. In the future, the utilization of solid state detectors extending down to ~ keV (e.g., STE on STEREO that provides up to 2 orders of magnitude increase in sensitivity at energies of ~ 2 to ~ 20-30 keV, compared to EESA on WIND) or *in situ* particle observations close to the Sun (e.g., by the Solar Orbiter and Solar Probe Plus) would be very valuable for verifying such occurrence rate estimate of solar electron events. For the spacecraft vantage points at heliocentric distances of <~0.2 AU, one advantage is that the *in situ* particle flux of SEP events would be more than 25 times larger than the *in situ* flux at 1 AU. This will allow detection of weak SEP events that are undetectable at 1 AU due to the high background and the instrumental sensitivity. Another advantage is that at such distances, propagation effects in the IPM that strongly affect measurements at 1 AU, would be greatly diminished. This will allow more accurate investigation of particle acceleration and release at the Sun.

Out of the 1191 solar electron events, 1176 have a type III solar radio burst – a one-to-one correlation; only 95 have a type II solar radio burst. We classify these electron events into two categories according to the associated ^{3}He/^{4}He ratio observed at ~0.5-2 MeV/nucleon by ACE/ULEIS (available since 1998): ~78% of electron events are accompanied by low-energy ion emissions with ^{3}He/^{4}He $\geq$ 0.01 (solar ^{3}He-rich electron events), and the other 22% are accompanied by ion emissions with ^{3}He/^{4}He < 0.01 (solar not-^{3}He-rich electron events). This suggests a close correlation between solar electron beams and ^{3}He-rich ions. We expect that all the electron events in the ^{3}He-rich category are impulsive events, while the not-^{3}He-rich category includes all gradual events, plus events that may be mildly ^{3}He-rich (since the coronal/solar wind ^{3}He/^{4}He is ~$5\text{x}10^{-4}$) but not measurable by present instruments. Then we select the not-^{3}He-rich electron events that are associated with gradual (>~ 1 hour) SXR bursts for a third category of gradual electron events, and we find 28 gradual electron events. These gradual events are closely (~ 61%) associated with type II radio bursts.

For ^{3}He-rich electron events, ~25% have a possible SXR flare, with most being C-class flares and located at W10-80°; ~ 60% have a possible CME, with an average width of 58° (excluding halo CMEs) and speed of 581 km/s. For the 28 gradual electron events, all have a possible SXR flare (due to our definition), with most being M- and X-class flares and at W10-80°; ~86% have a possible CME, with an average width of 155° (excluding halo CMEs) and speed of 1475 km/s. These associations are consistent with previous studies (see [Reames, 1999] for review). Compared to ^{3}He-rich electron events, thus, gradual electron events tend to be associated with

stronger SXR flares and faster and wider CMEs. One the other hand, gradual electron events tend to be accelerated to higher energies and to be more intense than ^{3}He-rich electron events.

Solar ^{3}He-rich electron events have a one-to-one association with type III radio bursts and a close association with west-limb CMEs, with ~58% of the associated CMEs being narrow (<~ 60º). Previous studies have shown that type III radio bursts are closely associated with coronal jets (when present) observed in SXR and EUV [Aurass et al., 1994; Kundu et al., 1995; Raulin et al., 1996; Christe et al., 2008], and such jets might appear as faint and narrow CMEs high in the corona [Kahler et al., 2001]. These suggest that in electron/^{3}He-rich SEP events, the electron acceleration may be related to those jets/narrow CMEs, and the selective acceleration of ^{3}He-rich ions may be due to electron-beam generated waves [Temerin & Roth, 1992]. In addition, the detection of low-energy electrons down to 0.04-1 keV favors a source high in the corona, at altitudes of >~ 1 R_S [Lin et al 1996], since such low energy electrons are strongly susceptible to the energy loss due to Coulomb collisions and thus they cannot survive escaping from low in the corona.

For solar energetic electron events, the yearly percentage of events detected only below ~10 keV appears to increase with time from ~4% in 1997 (about solar minimum) to 43 % in 2005 (approaching the next solar minimum) (Figure 3.12). ^{3}He-rich electron events show a similar tendency, while gradual electron events have this yearly percentage of the < 10 keV events fluctuating with time from 0% to ~33%. These may indicate a temporal variation of low-energy ^{3}He-rich electron events on the scale of at least 10 years. As mentioned in the previous paragraph, low-energy electrons are likely produced high in the corona. Thus, this temporal variation suggests that the evolution of active regions with time, from compact regions in the beginning of solar cycle to larger regions close to the end of solar cycle, i.e., the magnetic loops getting bigger with time and reaching higher altitudes, may allow low-energy electrons to escape to the IPM.

4. Timing of impulsive solar electrons

4.1 Introduction

Solar impulsive electron events were first observed at energies above ~40 keV [Van Allen & Krimigis, 1965; Anderson & Lin, 1966], with fast rise-slow decay temporal profiles indicative of significant scattering in the IPM. Later, events were detected down to keV energies (and more recently to ~0.1 keV [Gosling et al., 2003]), occasionally with fast rise-fast decay profiles that imply essentially scatter-free propagation in the IPM [Lin, 1974]. Near solar maximum, $>\sim 10^2$ events/month occur over the whole Sun [see Lin, 1985, and Chapter 3], making these the most common impulsive solar particle acceleration phenomenon. They are often accompanied by low-energy, ~MeV/nucleon ion emissions that are highly enriched in ^{3}He [Reames et al., 1985]. These electron/^{3}He-rich events form the class of "impulsive" SEP events. For about 99% of impulsive electron events observed near 1 AU by WIND/3DP, a type III solar radio burst was detected within ~20 minutes (see Chapter 3).

Using WIND observations, Krucker et al. [1999] found the injection at the Sun of the high energy, >25 keV electrons were often delayed by of order ~10 minutes after the type III radio bursts, and suggested that the delays may be related to propagation of large-scale coronal transient waves (also called EIT waves or coronal Moreton waves) to the field line connected to the vicinity of the Earth. Haggerty & Roelof [2002] confirmed the delays, finding a median delay of ~10 minutes for 38-315 keV electrons; they and Simnett et al. [2002] suggested acceleration by shock waves associated with coronal mass ejections (CMEs). Maia & Pick [2004] and Klein et al. [2005] proposed that these events are related to the coronal magnetic restructuring in the aftermath of CMEs, while Cane & Erickson [2003] and Cane [2003] argue from radio observations that the electrons are injected simultaneously with the type III burst, and that the delays are due to propagation effects in the IPM.

With WIND electron observations from ~0.4 to 300 keV, we infer the solar injection profile for three electron events that have strongly scatter-free time profiles. We find a double injection: one for ~0.4 to ~6-9 keV electrons that begins early enough to account for the type III burst, and a second for electrons above ~10-13 keV that starts ~8 min after the type III burst.

Much of this chapter was published in Geophysical Research Letters [Wang et al., 2006]

4.2 Observations and data analysis

From Haggerty & Roelof's list of delayed >38 keV electron events, we selected three events – onset time 1720 UT August 7, 1999; 1908 UT June 28, 2000; and 0030 UT August 22, 2000 – with strongly scatter-free temporal profiles that were observed by WIND/3DP from ~0.4 to 300 keV. Figure 4.1 shows the outward-traveling electron fluxes versus time from ~0.4 to 310 keV (channel center energies) for the August 1999 event. The temporal profiles at all energies exhibit nearly symmetric rapid-rise, rapid-decay peaks, followed by slow decays at flux levels much lower than the peak values. Such profiles imply that most of the electrons (those in the peak) propagated through the IPM essentially scatter-free [Lin 1974], and that the injection at the Sun was impulsive and nearly symmetric. The electron pitch angle distributions (Figure 4.2) are

strongly peaked along the magnetic field through the rapid-rise, rapid-decay phase, with the half maximum of <~30º at <~1 keV up to ~50º at >~100 keV (also see Chapter 6).

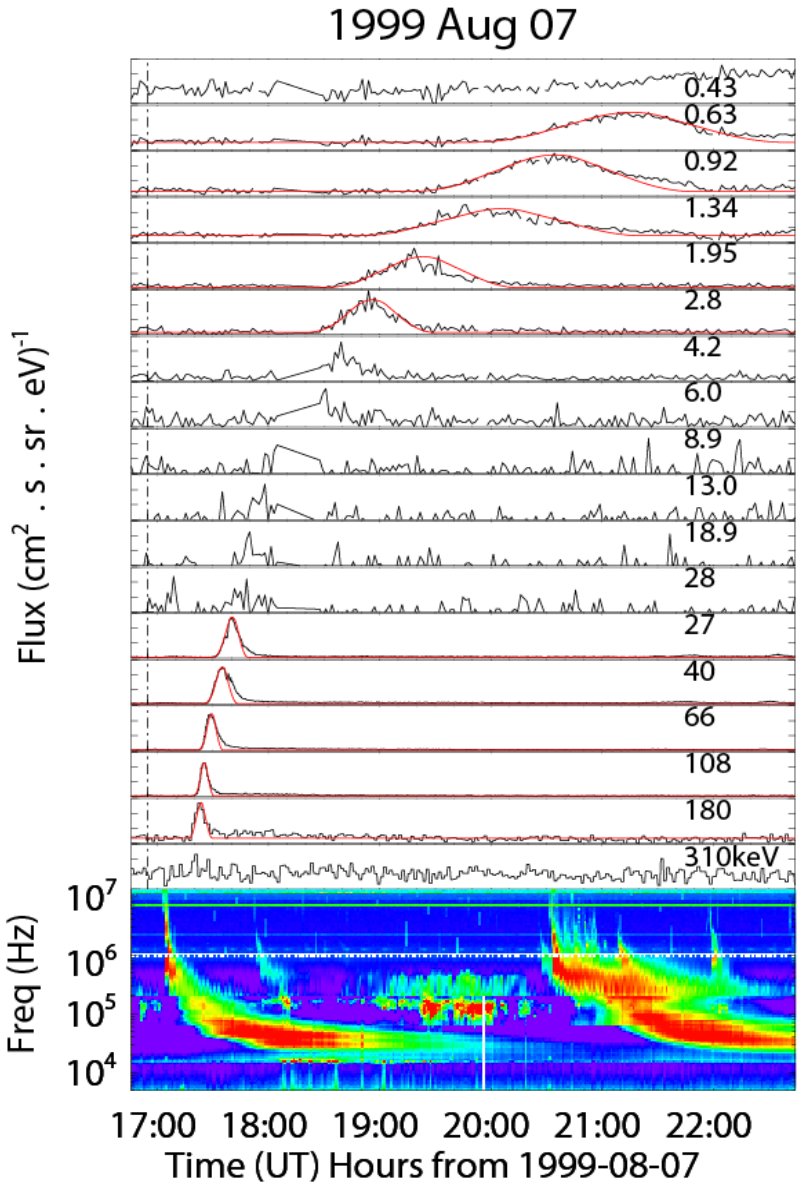

Figure 4.1. Overview plot for the 7 August 1999 event. The top panels show the flux of electrons traveling parallel to the magnetic field direction (outward) on a linear scale: observations (black curves) by EESA-H (0.43-28 keV) and by SST (27-310keV), and best fits (red curves) superimposed on the pre-event background. The vertical scales in units of $cm^{-2}s^{-1}sr^{-1}eV^{-1}$ from top to bottom are: 2200 to 4700; 360 to 1500; 100 to 480; 20 to 180; 2 to 130; 1 to 40; 0 to 18; 0 to 3; 0 to 1; 0 to 0.7; 0 to 0.4; 0 to 0.25; 0 to 0.1; 0 to 0.04; 0 to 0.013; 0 to 2×10^{-3}; 2×10^{-5} to 9×10^{-5}; 6.0×10^{-6} to 1.8×10^{-5}. A data gap occurred in the interval from 1804 to 1827 UT in the energy channels of EESA-H. The bottom panel shows a radio spectrogram observed by the WIND/WAVES experiment. A type III radio burst was observed with an Earth-observed onset at 1703 UT (the solar onset is indicated by vertical dash line in the top panels). Langmuir plasma waves (thin green spikes at ~17 kHz) were detected from ~1805 to 1920 UT.

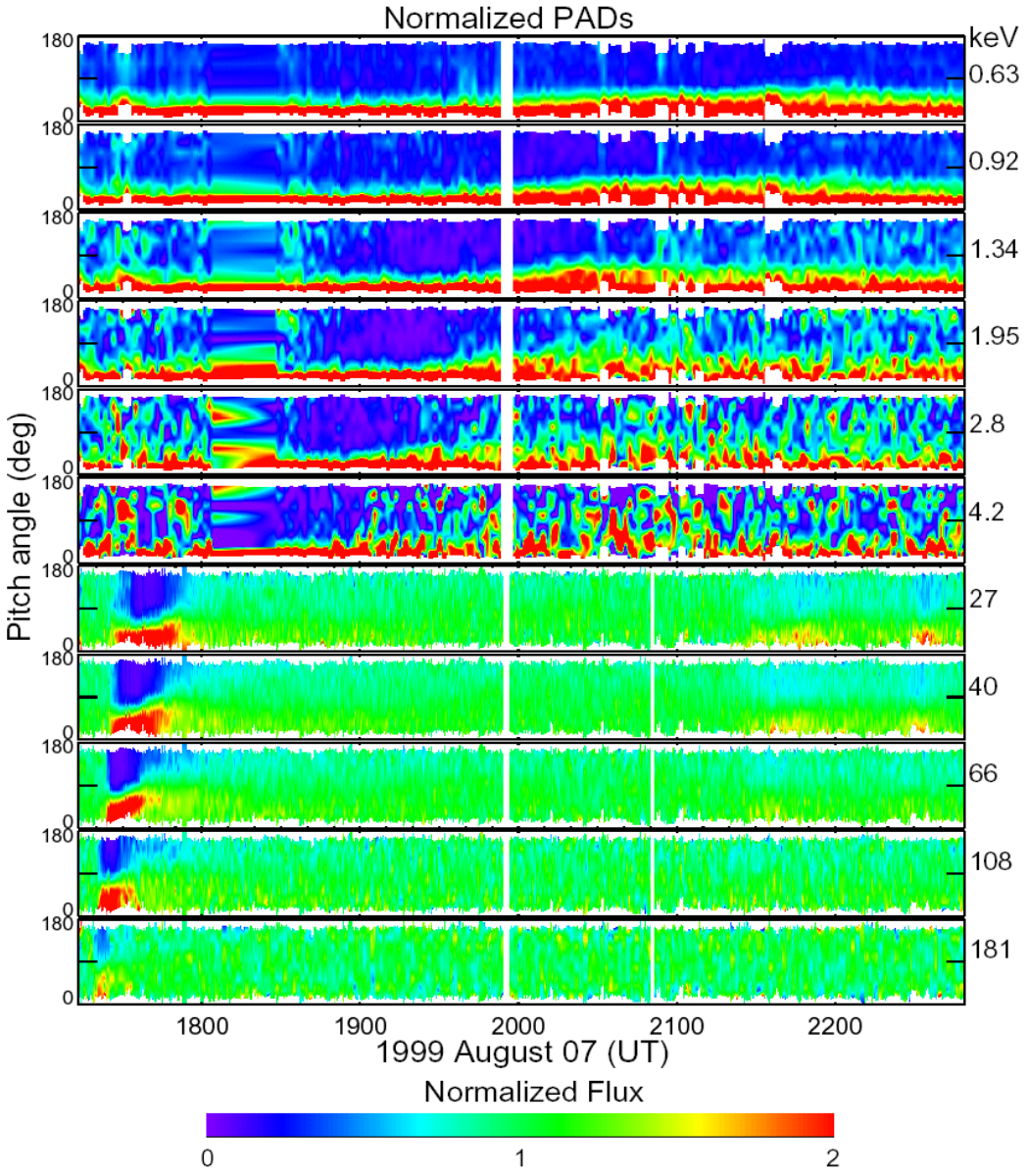

Figure 4.2. The normalized electron pitch angle distributions for the 7 August 1999 event. In each energy channel, the pitch angle distribution is normalized by the pitch-angle averaged flux for each time bin. Isotropic distributions show normalized values around 1 (green) in all PA directions, but beamed distributions have larger values (red) in the beaming direction and lower values (indigo) in the opposite direction.

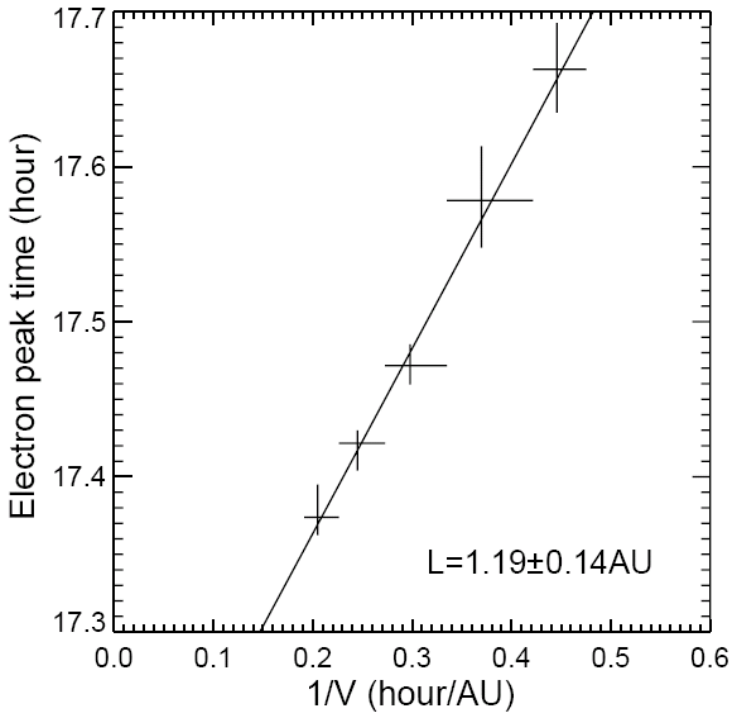

Figure 4.3. The velocity dispersion analysis of peak-flux time versus inverse speed above 25 keV for the 7 August 1999 event. These times align well on a straight line as a function of inverse speed, $t_i = t_o + L/v_i(E)$, giving estimates of the path length L (slope) and the release time t_0 (y-axis intercept). The shown error bars indicated the measurement uncertainty.

Velocity dispersion is clearly evident from ~0.4 to ~310 keV. For electrons above ~25 keV (see Figure 4.3), the times, t_i, of the peak fluxes at different velocities, v_i, fit well to a straight line, $L=v_i[t_i - t_o]$, implying a simultaneous solar injection at these energies followed by travel along the same path of length L=1.19±0.14 AU (comparable to the smooth spiral field length of 1.13 AU for the observed solar wind speed of 450 km/s). Using the observed onset at 180 keV (after correcting for contamination of lower-energy channels due to higher-energy electrons scattering out of the silicon detectors and depositing only part of their energy) and this path length, we find ~1703 UT as the earliest electron release time at the Sun. The solar type III radio burst (bottom of Figure 4.1) observed by the Wind/WAVES instrument (12 MHz to ~20 kHz), and by ground observatories up to >~80 MHz, left the Sun at ~1655 UT (vertical dashed line). Thus, the injection of electrons above 25 keV is delayed by ~8 minutes after the type III burst injection. No Hα flare or GOES soft X-ray (SXR) burst were reported at this time in Solar Geophysical Data (SGD). Langmuir waves at the local plasma frequency (~17 kHz) were observed from 1805 to ~1920 UT (Figure 4.1, bottom), during the rise of the ~1.34 to ~8.9 keV electron fluxes.

Based on electron observations of Figure 1, we assumed the injection flux at the Sun was an isosceles triangle-shaped pulse f:

$$f\left(t_0(E),\Delta t(E),A(E),t\right)=\begin{cases} A\cdot E^{-\beta}\cdot\left(1-\dfrac{\left|t-t_0-\Delta t/2\right|}{\Delta t/2}\right) & 0\le t-t_0\le\Delta t; \\ 0 & otherwise, \end{cases} \tag{4.1}$$

where $t_0(E)$ and $\Delta t(E)$ are the start time and the time duration of electron injection at energy E; $A(E)\cdot E^{-\beta}$ represents the electron injection flux intensity, and β is the power-law index of electron peak flux spectrum observed at 1 AU. Assuming that the propagation is scatter-free without energy losses (to be discussed later), and $t_0(E) = t_{0j}$, $\Delta t(E) = \Delta t_j$ and $A(E) = A_j$ within the energy band (from E_{j-} to E_{j+}) of the channel j, we find that the electron flux F_j at the propagation distance L from the Sun is:

$$F_j(L,t)=\frac{\int_{E_{j-}}^{E_{j+}} f\left(t_{0j}+\dfrac{L}{v(E)},\Delta t_j,A(E),t\right)dE}{E_{j+}-E_{j-}}, \tag{4.2}$$

where $v(E)$ is the electron speed. The solar injection pulse $F_j(0,t)$ is determined by fitting $F_j(1.2AU,t)$ to the observed electron flux profile for energy channel j, varying the start time t_{0j}, the duration Δt_j and the intensity A_j. This forward-fitting method is referred to as "triangular fitting".

For the 7 August 1999 event, this analysis was applied to energy channels from 0.63 to 180 keV, excluding 4.2 to 18.9 keV because of a data gap or poor statistics. The best fits (shown as red curves in Figures 4.1 and 4.4) are generally very good through the rapid-rise, rapid-fall phase. Afterwards, the observed electron fluxes show a much slower decay and the pitch angle distributions become broader, as expected from scattering in the IPM. The corresponding electron injection profiles are shown as triangles in the left panel of Figure 4.5.

The uncertainties in the start-time of the injection $F_j(0,t)$ were estimated from the fit of $F_j(1.2AU,t)$ to *in situ* observations, as shown in Figure 4.4 for the 630 and 920 eV channels. The green and blue curves were chosen as upper and lower limits of fitting to the rise of electron flux profiles; the limits on the start times of the corresponding $F_j(0,t)$ are shown as error bars on the injection time in Fig.4.5.

Figure 4.5 (left) shows that the electron injections above ~27 keV have short durations (~8-12 min) and clearly delayed starts (7.3±1.2 minutes) relative to the coronal release time of the type III radio burst (dash line), while electron injections at energies below ~3 keV start 9.9±5.8 minutes before the type III burst and have much longer durations (~50-130 min).

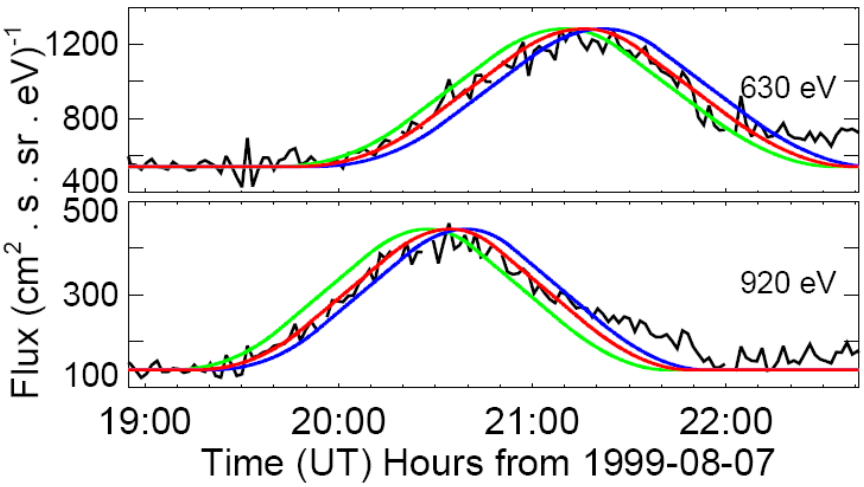

Figure 4.4. Examples of error analysis for two energy channels: 630 eV (top) and 920 eV (bottom). The red curves are the best fits to the rise of *in situ* electron flux profiles (black curves). The green and blue curves are the upper and lower limits of fitting, respectively.

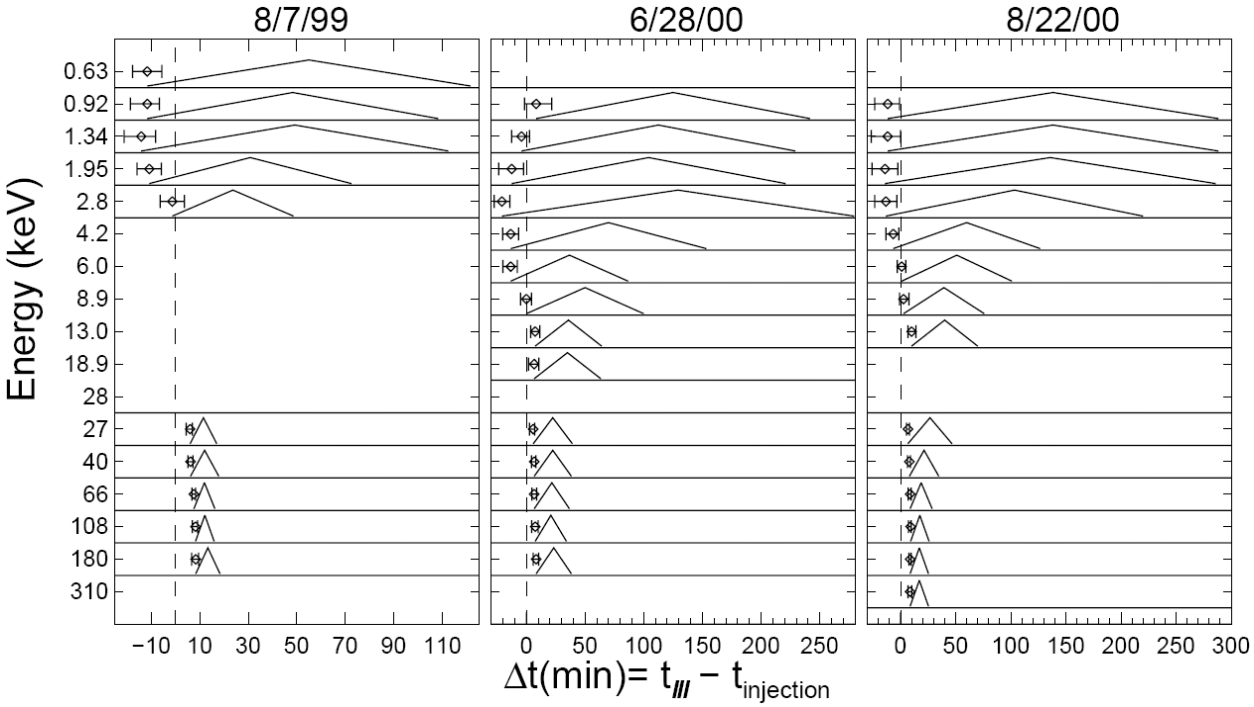

Figure 4.5**.** Comparison of the start times of inferred electron injections at different energies (diamonds) and the release time of type III burst (dash line) at the Sun for the three events. The electron delay (X-axis) is shown in minutes. The inferred injection profiles are shown by triangles. The injection analysis was not available at some channels due to a data gap or poor statistics.

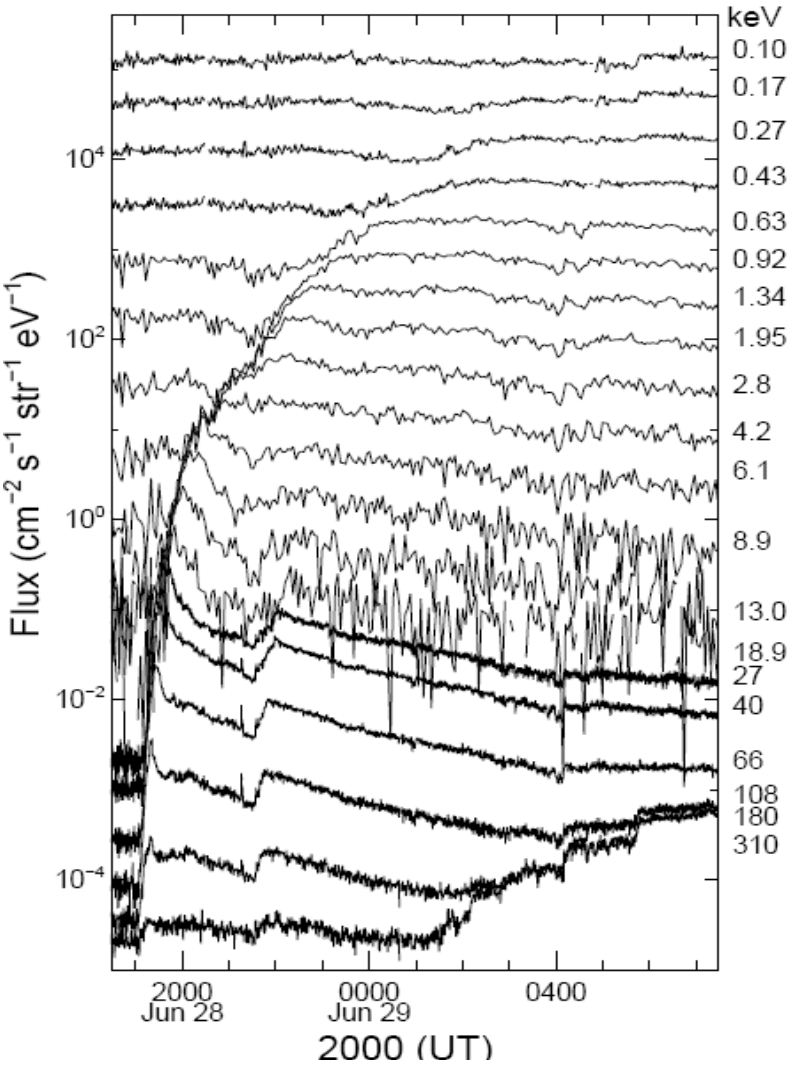

Figure 4.6**.** The temporal profiles of the flux of outward-traveling electrons for the 28 June 2000 event. A slow increase occurs at 108-310 keV on June 29, caused by contamination of > 400 keV solar energetic protons entering the SST foil detectors.

The 28 June and 22 August events in 2000 have similar scatter-free time profiles (Figure 4.6 and 4.7), and the same triangular injection analysis was applied. In the 28 June event (Figure 4.6), a 1.12±0.17 AU path length is obtained from the velocity dispersion analysis of the peak flux times for the high-energy (>25 keV) channels. About two hours after the onset, an increase in fluxes occurred simultaneous at all energies above ~ 4 keV, suggesting that the magnetic connection to the Sun had changed. In the 22 August event (Figure 4.7), a second injection occurred ~15-20 min after the first, and the *in situ* peaks were well separable only at energies above 100 keV. The dispersion analysis of those peak times gives 1.33±0.95 AU and 1.15±0.70 AU path lengths for the two injections. Both events show some back-streaming electrons due to magnetic connection to the Earth's bow shock. As these electrons travel towards the Sun along the converging IMF lines, they will sooner or later be mirrored back and propagate outward again, leading to the strong, long decay of *in situ* flux-time profiles. Thus, the triangular

injections for the two events were constrained almost entirely by the fits to the rise to maximum, especially at the lower energies.

Solar type III radio bursts were observed by WIND/WAVES up to 12 MHz and by ground measurements (~80-170 MHz) for both events. A coronal type II burst was reported for the 28 June event, and possibly for the 22 August event (listed as "uncertain emissions"). Also GOES C2.5 and C3.7 SXR bursts were associated with these events, respectively, but no Hα flares were reported. The SOHO/EIT (Extreme ultraviolet Imaging Telescope) difference images show flaring on, or partly behind, the western limb for the 28 June event (see Figure 4.8).

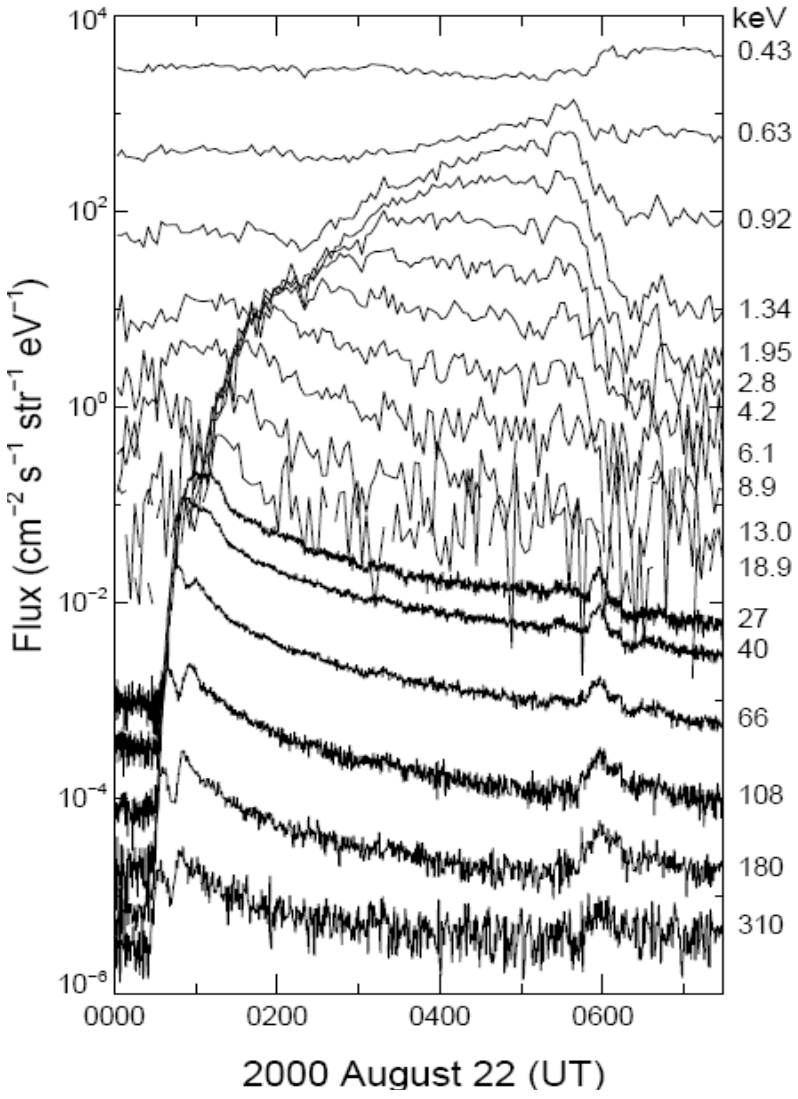

Figure 4.7**.** The temporal profiles of the flux of outward-traveling electrons for the 22 August 2000 event.

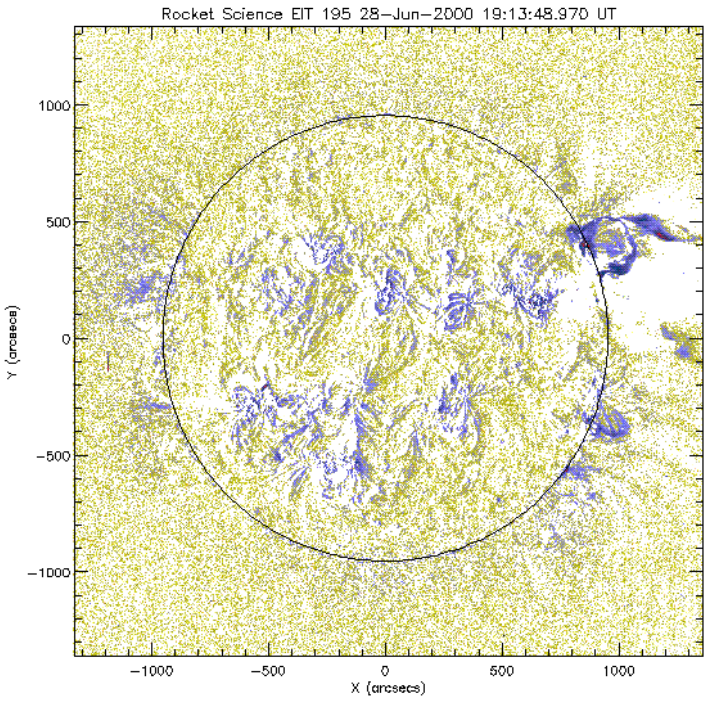

Figure 4.8**.** The SOHO EIT difference image at 1914 UT on 28 June 2000. The black circle represents the limb of the Sun. The image is obtained by subtracting an earlier image, revealing a flaring structure on the western limb.

Figure 4.5 (right side) compares the start times of electron solar injections to the coronal release time of type III radio bursts for these two events. It is evident that electrons above ~9-13 keV are injected with a median delay of 7.8±1.8 min after the coronal release of type III radio bursts, while electrons below ~6-9 keV are injected starting 8.7±6.4 min earlier than type III bursts. The durations range from ~30 and 15-30 min for energies above ~30 keV, to 230-300 min and 230-300 min below ~3 keV, for the 28 June and 22 August events, respectively. *In situ* Langmuir waves were observed during the onset of the ~1-13 keV electrons for both of these events as well.

Figure 4.9 shows *in situ* background-subtracted electron spectra (black color) for the three events, constructed by taking the outward flux at the time of maximum in each energy channel. Such spectra should be representative of the injection spectrum (see [Lin, 1974]). For the 7 August 1999 event, the *in situ* fluence spectrum (black color), obtained by integrating the net outward flux over the event duration in each energy channel, is also shown. All of the spectra fit to a double power-law with exponents of 2.1-2.6 (2.9 for the fluence spectrum) below the break and 4.5-4.6 above. There is no obvious change in the *in situ* spectra across the transition between the early injection (<~ 6-9 keV) and late injection (>~ 13 keV) electrons. For the 7 August 1999 event, the fluence spectrum is softer below the break but has the same exponent above the break, compared with the peak flux spectrum, likely due to the longer durations at lower energies.

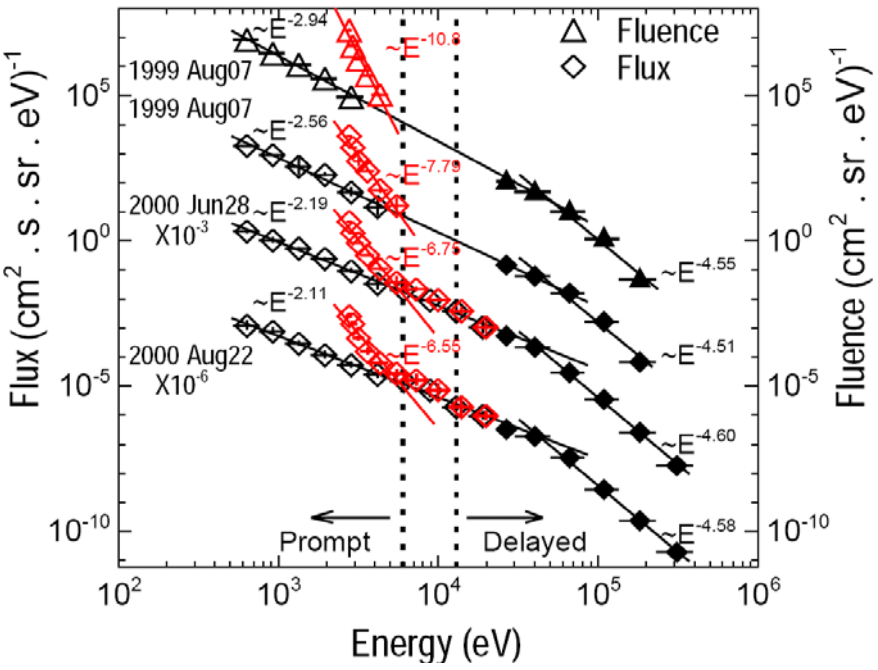

Figure 4.9. Background-subtracted peak flux spectra (open symbols for EESA-H; solid symbols for SST) for the three electron events and fluence spectrum for the 7 August 1999 event: *in situ* spectra (black color) and source spectra (red color; not shown above 20 keV). The spectra of the two events in 2000 have been multiplied by 10^{-3} and 10^{-6}, respectively. The dotted vertical lines indicate the transition (~6-13 keV) between electrons with prompt injections and delayed injections with respect to type III radio emissions.

4.3 Summary and discussion

By taking into account the effects of interplanetary propagation and instrument response (energy band) in these highly scatter-free events, we have shown that there are double impulsive electron injections at the Sun: a low-energy (~0.4 to 6-9 keV) injection that begins 9.1±4.7 minutes earlier than the type III radio bursts and lasts for ~50-300 min, and a high-energy (>~13 to 300 keV) injection that starts 7.6±1.3 minutes after the type III bursts but has durations ~5-10 times shorter. (e.g., triangles in Figure 4.5). The source of the type III radio burst can be identified with the low-energy electron injection; some delay is needed for the injected electrons to rise above the ambient background plasma to produce the significant positive slopes in the electron reduced parallel velocity distribution function required for the growth of the Langmuir waves that, in turn, scatter to produce the type III radio emission at the fundamental and harmonic of the plasma frequency [see Lin, 1990 for summary]. This is also consistent with the detection of Langmuir waves *in situ* when the ~1-10 keV electrons arrive near 1 AU in these events and previous events [Ergun et al., 2000], and with the drift rate of decametric type III bursts indicating exciter† speeds of ~0.1 c [Haggerty & Roelof, 2002].

For all three events the associated type III radio bursts start at frequencies >~ 80 MHz, implying that the injection occurs at coronal densities of >~10^8 cm^{-3}, corresponding to an

† Electrons that generate/excite waves.

overlying column depth of ~ 10^{18} cm^{-2} and ~0.1-0.2 R_S altitude for a quiet-Sun model [Saito et al., 1977]. Electrons escaping from there will lose energy to Coulomb collisions and to the ambipolar electrostatic potential that results from the fact that coronal ions are gravitationally bound while hot coronal electrons are not: $dE/dr=(dE/dr)_{Coll}+(dE/dr)_{AEP}$. The Coulomb collision term in ionized hydrogen [Trubnikov, 1965] can be estimated as: $(dE/dr)_{Coll}=-1.82\times10^{-7}n_i(r)/E$, where E is the electron energy in keV, r is the radial distance from the Sun's center in R_S, and n_i is the density of hydrogen in cm^{-3}. The electrostatic potential term in hydrostatic equilibrium [Lemaire & Scherer, 1973] can be written: $(dE/dr)_{AEP}=-0.994/r^2$. A ~0.4 keV electron detected at 1 AU thus begins as a ~2.6-3.2 keV electron in the metric type III source region. The resultant change on inferred solar injection times is small (e.g., ~160 s for 630 eV and ~1 s for 18.9 keV) compared to the difference in injection times of low-energy electrons, high-energy electrons and type III bursts. This result is, of course, model-dependent; to our knowledge, the interplanetary potential has never been measured directly.

We can obtain the electron source spectrum by assuming a constant flow: $S_0 \cdot J_{0n} \cdot \Delta E_{0n} = S_1 \cdot J_{1n} \cdot \Delta E_{1n,}$, where J_{0n} (J_{1n}) is the flux of channel n, ΔE_{0n} (ΔE_{1n}) is the energy bandwidth and S_0 (S_1) is the cross-sectional area at the Sun (at 1 AU). In order to compare with *in situ* spectra at 1 AU, we assume the energy-independent expanding factor of S_1/S_0 =1 (not the actual value). For all the three events, the resultant fluxes (fluences) and energies at the Sun are shown in red in Figure 4.9. Using an active coronal density model would change the altitude of the source region, but the power-law indices of the source spectra would only change by <~10% (mainly due to the change in ambipolar electrostatic potential). Above ~10 keV, the source spectra are essentially the same as the spectra measured *in situ* at 1 AU. Below ~ 6 keV, the source spectra break upward with a steep power-law (indices of ~6.5-11). The break to the flatter power law appears to be at ~6 keV for all three events. It is surprising that these energy loss processes, however, would be just what is required to produce a power-law below 6 keV that matches the power-law above 6 keV, as observed. Another possibility is that for the three impulsive electron events, the location of solar source of low-energy electrons moves with time: it is low in corona at the start of injection that produces type III radio bursts at frequencies >~ 80 MHz, and by the time of peak injection, the acceleration has to move to high altitudes from which the escaping electrons only suffer small or negligible energy losses. Thus, the observed *in situ* peak-flux spectrum would have a similar shape to the source peak-flux spectrum.

For the delayed high-energy electron injection, recent studies suggested acceleration by some propagating phenomena such as EIT waves and their coronal counterparts [Krucker et al., 1999], or upward moving shocks driven by CMEs [Haggerty and Roelof, 2002; Simnett et al., 2002]. All three events had associated west-limb CMEs (SOHO/LASCO CME Catalog); the CME speeds and angular widths were ~570 km/s and ~7º for the 1999 event, and >950 km/s and >100º for the two events in 2000. From the CME height-time plots, we find that for the 1999 event, the CME is at ~1-2 R_S altitude when the high-energy electrons are injected, and for the two events in 2000, the projected altitudes are ~2-6 R_S and ~2-5 R_S. By the time the prompt electrons reach those altitudes, they will have already suffered most of their energy losses so their spectra will be similar to the spectra observed at 1 AU. The relatively smooth transition across the transition energy range suggests that the prompt electrons may provide the seed particles for the delayed electron acceleration.

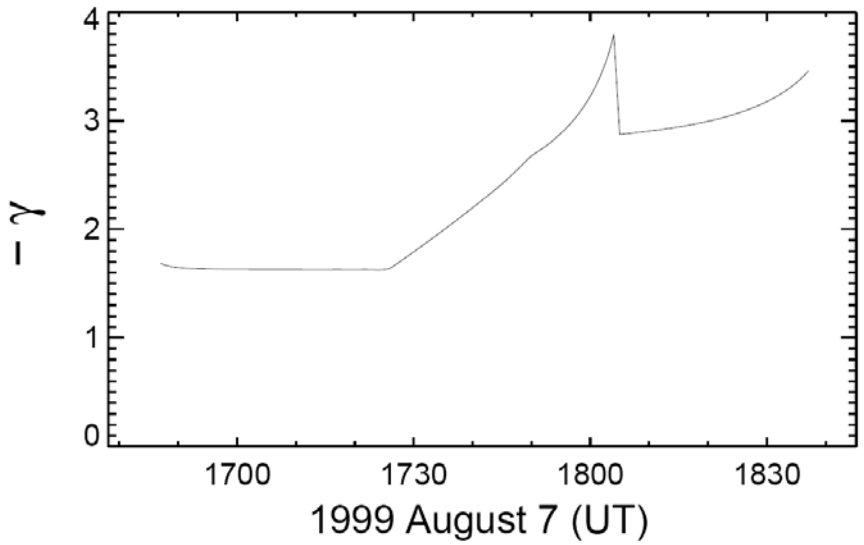

Figure 4.10**.** The temporal variation of the power-law exponent of the source spectrum below ~ 3 keV for the 7 August 1999 event. The spike around 1800 UT is an artifact produced by the extremely small fluxes at ~2 keV at those times (see left panel of Figure 4.5) that sharpen the fitting power-law.

The inferred low-energy injections at the Sun have durations of from ~50 min to several hours. This is consistent with the finding that many electron events at energies of ~0.1-1.4 keV have a beam duration >3 hours [Gosling et al., 2003]. We have made a rough calculation to estimate the propagation effects on the determination of injection duration. Assuming a constant IMF that points outward from the Sun with a nominal 1.2AU field line length to Earth, we estimated the injection profile from the *in situ* flux-time profile for two cases: all the electrons are at 0º pitch angle (case 1, the assumption used in this study); electrons have the flux that decreases linearly with pitch angle from the maximum at 0º to the half maximum at 30º and then to zero at 60º (case 2, similar to the observed pitch angle distributions at low energies shown in Figure 4.2). The comparison of the simulated injection durations between case 1 and 2 shows that pitch-angle scattering and dispersion in the IPM might only cause an error of <~10% in the determination of time duration for highly scatter-free events. Thus, these long durations are unlikely to be due to propagation in the IPM. If the acceleration is rapid but the electrons are temporarily stored in the corona and gradually released, the injection spectrum should harden with time since lower-energy electrons lose energy to Coulomb collisions more rapidly than higher-energy ones. For the 7 August 1999 event, however, the spectrum of the derived injections generally softens with time (see Figure 4.10). On the other hand, near-Sun radio/X-ray observations do not show evidence for long-lived (>~hour) electron acceleration, e.g., no long-duration radio or X-ray emission.

The start time of the prompt low-energy electron injection occurs close to the start of the CME eruption, as extrapolated from the height-time plots. Thus, one possibility is that the low-energy injection and type III burst may be related to the initial CME eruption, with the injection continuing as the corona restructures while the CME continues outward [Maia & Pick, 2004; Klein et al., 2005]. The delayed high-energy injection may be related to a propagating shock

(although it may be difficult to explain the short injection duration of high-energy electrons) or other phenomena whose formation/start is delayed relative to the CME initiation, with the acceleration acting on the seed low-energy electrons. The 7 August 1999 and 22 August 2000 events were both associated with strongly ^{3}He-rich solar energetic ion events (G. Mason, private communication, 2004). The 28 June 2000 event was not ^{3}He-rich, and it had an associated type II radio burst, indicating it is likely a "gradual" event while the other two events are "impulsive" events.

Based on the results of this chapter, we can conclude the following:

1) The observed delay of high-energy (above ~13 keV) electrons are generally due to the injection at the Sun, not the propagation in the IPM, contrary to the explanation suggested by Cane & Erickson [2003] and Cane [2003]. Also see Chapter 6 for more details of the propagation analysis of solar impulsive electron events.

2) Solar impulsive electron events have clearly two distinct injections. The prompt low-energy (below ~ 6-9 keV) injection produces type III radio bursts, leading to a one-to-one correlation between solar energetic electron events and type III bursts reported in Chapter 3.

3) The delayed high-energy electron injection may occur at higher altitudes, related to the passage of the associated CMEs, than the prompt low-energy injection that provides seed electrons for acceleration of high-energy injection.

4) Solar energetic electron events have a close association with ~MeV/nucleon, ^{3}He-rich ion emissions (also see Chapter 3). See Chapter 5 for the temporal relationship between electrons and ^{3}He-rich ions.

5. Timing of impulsive solar electrons and ^{3}He-rich ions

5.1 Introduction

SEP events are generally classified into two groups: "gradual" and "impulsive", respectively, so-called because the SXR burst (when present) is of short duration (<1 hour) and of long duration (> 1 hour) [see Reames, 1999 for review]. Gradual SEP events were first observed in 1942 as sudden increases in intensity in ground-level ion chambers following large solar flares [Forbush, 1946]. These events are dominated by > 10 MeV protons (with small electron-to-proton ratios) with high particle intensities (so-called large SEP events) and observed up to GeV energies, and they have normal coronal abundances (e.g., ^{3}He/^{4}He ~5×10^{-4}) and charge states (e.g. the iron ionization state Q_{Fe} ~ 14) corresponding to typical coronal temperatures of 1-2×10^6 K [see Cliver, 2009 for review]. They occur about ~10/year at solar maximum, extend over ~100-180° in solar longitude, last for days, and are closely associated with fast CMEs and type II radio bursts (indicator of shock waves). These suggested that gradual SEP events are accelerated by shocks driven by CMEs through the IPM [e.g., Reames, 1999].

^{3}He-rich SEP events were discovered by Hsieh & Simpson [1970]; these are small SEP events with greatly enhanced abundances of ^{3}He, usually only observed up to ~MeV/nucleon energies. These ^{3}He-rich events were found to be always accompanied by a non-relativistic electron event [Reames et al, 1985], and so they are also called "electron/^{3}He-rich SEP events". These are dominated by ~1-100 keV electrons (with high electron-to-proton ratios) and low-energy, ~MeV/nucleon ion emissions with low particle intensities, enhanced ^{3}He/^{4}He ratios (up to 10^4 times the coronal values), significant (factor of ~10) enhancements of heavy nuclei such as Fe, extreme (factor of >200) enhancements of ultra-heavy nuclei up to > 200 amu [Mason et al., 2004], and high ionization states for heavy ions. They extend over ~30º in longitude, last for <~ hours, and are associated with type III radio bursts and sometimes with small flares. The average ionization state is ~20 for Fe and ~14 for Si, which was interpreted as being due to either heating to ~ 10^7 K [Klecker et al., 1984; Luhn et al., 1987] or stripping of the ions by the intense electron beams [Miller & Viñas, 1993] in impulsive flares. Thus, Reames [1995, 1999] and references therein suggested that electron/^{3}He-rich SEP events are produced in impulsive flares at the Sun, e.g., due to selective resonant acceleration of ^{3}He and certain heavy ions, possibly by electron-beam generated waves [Temerin & Roth, 1992].

With improved instrumentation, recent studies revealed some new properties of the source of electron/^{3}He-rich SEP events. Using WIND/EPACT and SOHO/LASCO observations, Kahler et al. [2001] reported one electron/^{3}He-rich SEP event on 2000 May 1, associated with a fast (~1000km/s), narrow (~20º) CME above the Sun's northwest limb. They favored acceleration in the context of the impulsive flare model of Shimojo & Shibata [2000] (see Figure 1.9) in which jets or plasmoids are ejected upward from magnetic reconnection sites between closed and open field lines over active regions, and suggested that such jets might appear as faint and narrow CMEs. Y.-M. Wang et al. [2006] surveyed 25 electron/^{3}He-rich SEP events observed by ACE/ULEIS. Using potential field source surface (FFSS) extrapolations, they indentified the source regions of these events as typically small, flaring active regions next to coronal holes containing Earth-connected open field lines, located between longitudes ~ W25° and 72°, which were also identified in imaging radio observations of type III bursts [Pick et al., 2006]. Y.-M. Wang et al. [2006] also found that most of the 25 electron/^{3}He-rich SEP events were

accompanied by fast (~500-1000 km/s) and narrow (<30º) white light and/or EUV eruptions/jets observed by SOHO, and they interpreted the observed jets as signatures of magnetic reconnection between closed active-region loops and the open filed lines (also see the model of Shimojo & Shibata [2000]). More recently, Nitta et al. [2008] reported one electron/^{3}He-rich SEP event associated with an X-ray jet observed by Hinode, originating in an active region at longitude W50°. In addition, many studies have shown that type III radio bursts are closely associated with coronal jets (when present) observed in SXR and EUV [Aurass et al., 1994; Kundu et al., 1995; Raulin et al., 1996; Christe et al., 2008]. On the other hand, Kleckler et al. [2006] reported that the typical ionization states measured in electron/^{3}He-rich SEP events by ACE/SEPICA and SOHO/STOF show a large increase with energy at <~ 1 MeV/nucleon. The comparison of such observations with model calculations [see Klecker et al. 2007, for review] suggest that if the ion acceleration has a time scale of 1-10s, then it would occur low in the corona, typically at altitudes <~ 0.2 R_S, accompanied and followed by stripping via impact ionization through a dense column density.

In electron/^{3}He-rich SEP events, the timing relationship between electrons and ^{3}He-rich ions provides an important clue to understand the solar source of these particles. Using ISEE 3 observations, Reames et al. [1985] reported one electron/^{3}He-rich SEP event that had ^{3}He onsets with a time lag of <~ 10-15 min after electron measurements, and thus they suggested that electrons and ^{3}He ions were accelerated nearly simultaneously by the same process. Recently, Ho et al. [2003] examined the timing of nine electron/^{3}He-rich SEP events observed by ACE with ^{3}He/^{4}He ≥ 1 % at 0.4-2.0 MeV/nucleon, and found that the <1 MeV/nucleon ions showed significant delays (> 40 min) in the solar release for five events and no delays for the other four events, compared to 38-50 keV electrons. They proposed two possible explanations for the ion delay after electrons: one is that ions were accelerated by CME-driven shocks further from the Sun, and another is that ions underwent further scattering than electrons through the IPM.

Here we survey the WIND/3DP electron observations (~0.4-300 keV) and the ACE/ULEIS ion observations (~0.02-10 MeV/nucleon) from November 1997 through December 2003, and select ten electron/ ^{3}He-rich SEP events with a clear velocity dispersion, a ^{3}He/^{4}He ratio > 0.1, and an electron energy range from ~0.4 to 100-300 keV (§5.2). For these events, we estimate the particle path length in the IPM and investigate the solar injection of electrons and ^{3}He-rich ions (§5.3). Then we examine their association with Hα and GOES SXR flares, CMEs and solar radio bursts (§5.4).

5.2 Observations

5.2.1 Data sets

The electron data used here are obtained from the WIND/3DP instrument, and the low-energy ion data is obtained from ACE/ULEIS. In this study, we use the observations of carbon and heavier elements to achieve better ion timing, since they have lower background than helium. We bin the ion data linearly into 30 bins of the ion inverse velocity ($1/V$) from 0 to 20 hour/AU (bin center values from 0.33 to 19.67 hour/AU), corresponding to logarithmically binning the particle speed from infinity to 15.7 keV/nucleon (~0.0058c) (bin center values from 93.5 MeV/nucleon (~0.42c) to 23.3 keV/nucleon (~0.007c)).

Table 5.1 the Ten Electron/^{3}He-rich SEP Events

		Ions			Electron below ~6-9 keV		Electrons above ~9-13 keV		Type III/II	GOES X-ray Flare[b]	Hα Flare[b]	CME[c]			
N	Date	^{3}He/^{4}He [a]	Release (UT)	Duration (min)	Release (UT)	Duration (min)	Release (UT)	Duration (min)	Release (UT)	Beg/Max Time (UT)	Beg/Max Time (UT)	Launch[d] (UT)	V (km/s)	P. A. (deg)	Width (deg)
(1)	(2)	(3)	(4)	(5)	(6)	(7)	(8)	(9)	(10)	(11)	(12)	(13)	(14)	(15)	(16)
1	1998 Aug 18	1.32±0.26	02:41±00:31	190-320	01:58±00:07.6	90-170	02:12±00:04.2	12-60	III			….[e]	….[e]	….[e]	….[e]
2	1999 Aug 7	1.52±0.08	18:37±00:50	280-530	16:45±00:05.8	50-130	17:02±00:01.2	8-12	III/16:55	18:44/19:17 M1.2	18:39:18:41 S15W24	16:42	577	297	7
3	2000 Apr 1	0.11±0.02	19:53±00:37	200-530	19:04±00:07.4	60-230	19:20±00:03.9	20-25	III/19:05		19:35/19:44 N10W54	18:50	586	291	33
4	2000 Jun 4	0.30±0.02	07:36±00:13	170-300	06:41±00:08.7	80-150	07:01±00:01.5	15-23	III/06:54			06:51	597	295	17
5	2002 Jun 30	0.16±0.06	11:54±00:43	290-800	08:58±00:12.1	130-270	09:06±00:01.9	20-30	III	09:07/12:49 C2.1		08:28	623	299	30
6	2002 Sep 22	0.54±0.02	24:04±00:29	170-250	23:32±00:04.4	80-120	23:36±00:02.0	15-40	III/23:36			23:31	960	287	140
7	2002 Sep 24	0.75±0.05	11:50±00:25	170-280	10:52±00:05.5	100-180	11:07±00:01.5	8-18	III/10:50			10:56	1104	277	62
8	2002 Oct 20	1.47±0.05	14:46±00:33	240-570	13:33±00:06.9	70-130	14:06±00:01.8	5-40	III/14:03 II/14:24	14:02/14:05 C6.6	14:03/14:07 S13W63	13:52	1011	247	20
9	2002 Dec 12	1.11±0.07	01:24±00:43	190-400	00:11±00:05.2	80-130	00:35±00:01.4	17-18	III/00:32			00:33	624	297	13
10	2002 Dec 12	0.39±0.03	13:29±01:02	220-420	12:16±00:06.6	60-150	12:35±00:01.2	10-20	III/12:28			12:13	723	287	51

[a] The ^{3}He/^{4}He ratio is calculated at 0.5-2.0 MeV/nucleon.
[b] The flare information is from the SGD (ftp://ftp.ngdc.noaa.gov/STP/SOLAR_DATA/), after taking into account the photon travel time of 500 seconds from the Sun to Earth.
[c] The CME information is from the SOHO LASCO CME catalog (http://cdaw.gsfc.nasa.gov/CME_list/).
[d] The CME launch time is estimated from linear extrapolation to the photosphere (1 R_S from the Sun's center), after taking into account the photon travel time of 500 seconds.
[e] The SOHO/LASCO data are unavailable.

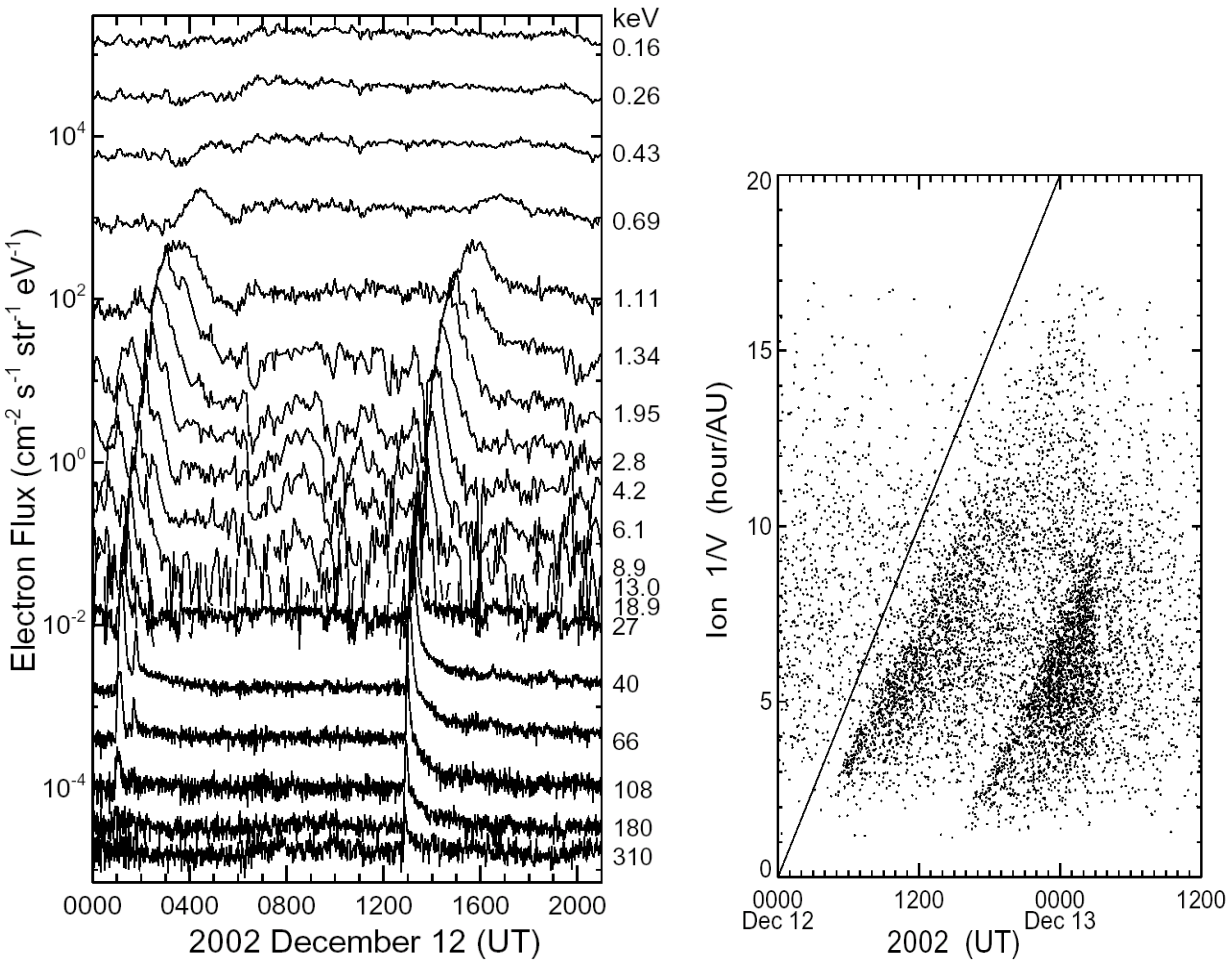

Figure 5.1. Overview plot for event #9 and 10 on 12 December 2002. The IMF was pointing towards the Sun. Left panel shows the flux of electrons travelling anti-parallel (outward) to the IMF observed by EESA-L (0.17-1.11 keV), EESA-H (1.34-18.9 keV) and SST (27-310 keV). Right panel shows the ion spectrogram of 1/speed versus arrival times of 10-70 amu ions on 12-13 December 2002. The slanted line shows the arrival times of ions at different velocities after a simultaneous injection at the Sun followed by the same propagation along a nominal 1.2 AU IMF spiral.

5.2.2 Event selection

We survey the WIND/3DP electron data and the ACE/ULEIS ion data from November 1997 through December 2003, and select ten electron/^{3}He-rich SEP events based on the following criteria: (1) a clear velocity dispersion, (2) an electron event energy range from ~0.4 up to above 100 keV and (3) a ^{3}He/^{4}He ratio >0.1 at ~0.5-2.0 MeV/nucleon. Here we define an ion event to be associated with the corresponding electron event, if the *in situ* onset of the ~2 MeV/nucleon ions ($V \sim 0.06c$) occurs within 4 hours of the *in situ* onset of the ~ 1 keV electrons ($V \sim 0.06c$). Table 5.1 lists the properties of the selected ten events. Column 2 gives the date for each event; Column 3 gives the event-average ^{3}He/^{4}He ratio at ~0.5-2 MeV/nucleon.

Figure 5.1 shows energetic particle data for two representative events (#9 and 10). The left panel shows the outward-traveling electron fluxes versus time from ~0.16 to 310 keV (channel center energies) observed by WIND/3DP on December 12, 2002. For event #9 (#10), the electron velocity dispersion is clearly evident from ~0.4 keV (0.3 keV) up to 180 keV (310 keV): faster electrons arrive at 1 AU before slower ones. The electron temporal profiles at all energies exhibit nearly symmetric rapid-rise, rapid-decay peaks, followed by slow decays at flux levels much lower than the peak values. Such profiles imply that most of the electrons (those in the peak) propagated through the IPM essentially scatter-free [Lin 1974], and that the injection at the Sun was impulsive and nearly symmetric. Note that the event #9 was preceded by one electron event at ~1.3-6 keV that began to arrive about 25 min earlier, and was followed by another event at ~1.3-66 keV that started about 40 min later with small intensities. The right panel shows an ion spectrogram where the arrival time of each ion is plotted versus the inverse speed ($1/V$) for carbon and heavier ions observed by ACE/ULEIS on December 12-13, 2002. The slanted line represents the ion velocity-dispersed arrival at 1 AU, if ions at all energies were injected simultaneously at the Sun and then traveled along a spiral field line of a nominal 1.2 AU length to Earth. For the two successive events (#9 and 10), the leading edge of observed ion arrivals at all energies (i.e. the ion velocity dispersion) is nearly parallel to the slanted line, indicating that at least the first-arriving ions propagated essentially scatter-free through the IPM. Also note that a sharp intensity drop occurred around 0300 UT on December 13 simultaneously at all energies, likely due to the passage of an emptier flux rope [Mazur et al., 2000].

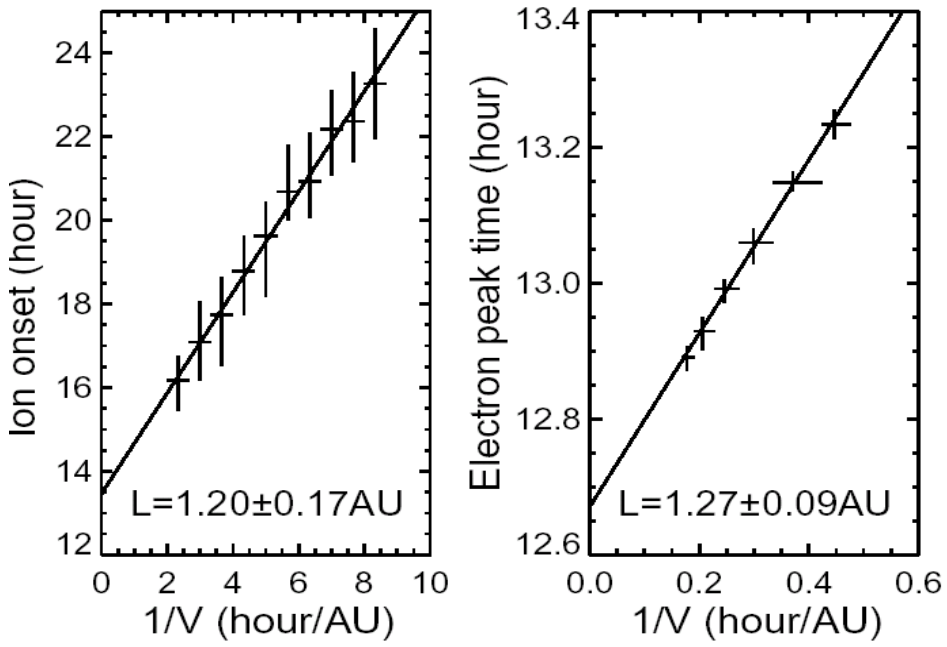

Figure 5.2. Velocity dispersion analysis for event #10 on 12 December 2002. Left panel shows the *in situ* onset time of ions versus 1/ion speed. Right panels shows the *in situ* peak-flux time of electrons above 25 keV versus 1/electron speed. The slope of linear fit, $t_i = t_o + L/V_i$, gives an estimate of path length from the Sun to Earth, respectively, for ions and electrons.

5.3 Data analysis

5.3.1 Determination of path length

If particles at different velocities, V_i, are injected at the same time, t_0, at the Sun and then travel along the same path length, L, to the spacecraft, then the *in situ* arrival times, t_i, can fit to a straight line: $L=V_i [t_i - t_0]$. Thus, we can estimate the particle path length from the Sun to the spacecraft using the velocity dispersion analysis. We use *in situ* onset times to derive the ion path length in the IPM but *in situ* peak-flux times to derive the electron path length, since for solar electrons the determination of peak-flux time is more precise; the onset determination is strongly affected by the pre-event background of interplanetary electrons.

Figure 5.2 shows examples of velocity dispersion analysis from event #10. In the left panel, the ion onset times, plotted versus the inverse velocity ($1/v$), fit well to a straight line, implying that a simultaneous solar injection followed by travel along the same path of length L=1.20±0.17 AU. In the right panel, the dispersion analysis of peak-flux times of electrons above 25 keV gives a path length of 1.27±0.09 AU. Both the estimated electron and ion path lengths are consistent with the 1.19 AU smooth spiral field length for the observed solar wind speed of 370 km/s, suggesting that both electrons and ^{3}He-rich ions propagated through the IPM nearly scatter-free. In fact, similar results are obtained for all the ten electron/^{3}He-rich SEP events. In this study, thus, we assign a scatter-free path length of 1.2 AU for all the electrons and ions, to a good approximation.

5.3.2 Forward-fitting of solar injections

As described in Chapter 4, for nearly scatter-free SEP events with good statistics, we can obtain the particle injection profiles at the Sun from triangular fitting to the intensity-time profiles observed at 1 AU, by taking into account the propagation through the IPM and the instrument response (energy band). This procedure was done for the 2000 June 4 event (see Fig. 5.3) for both electrons and ions and for the other nine events for electrons.

5.3.2.1 The 4 June 2000 event (#4)

As shown by the black curves in Figure 5.3, the 4 June 2000 event (#4) was detected by WIND/3DP from ~0.43 to 310 keV for electrons and by ACE/ULEIS from ~0.08 to 3.26 MeV/nucleon (from ~10.3 to 1.67 hour/AU, in terms of $1/V$) for carbon and heavier ions. For electrons, the triangular-fitting analysis is applied to energy channels from 0.63 to 310 keV, excluding the 13 and 18.9 keV channels because of poor statistics at those energies. The fits (red curves in left panels of Figure 5.3 and top panel of Figure 5.6) are very good through the rapid-rise, rapid-fall phase. Afterwards, the observed electron fluxes show a strong, much slower decay at energies above ~2 keV, mainly due to particle reflection. During this event, the WIND spacecraft was located ~78 Re upstream of the Earth and magnetically connected to the Earth's bow shock. At energies above 25 keV (see Figure 5.4), strong reflected electron populations (bottom; often seen in SST (above 25 keV) when the spacecraft is close and magnetically connected to the Earth's bow shock) were detected propagating inward towards the Sun with fluxes ~20-40% smaller than outward-traveling populations (top); these inward-traveling electrons were also preceded by a very weak upstream particle event above 25 keV that

originated from the acceleration at the Earth's bow shock and arrived at ~ 0710UT at the spacecraft. These reflected electrons were also detected at energies of ~3-20 keV by EESA-H but with poor statistics. As these electrons traveled inward along converging IMF lines, they would be mirrored back and propagate outward again to superimpose on initial outward-traveling populations, leading to a strong, slow decay in flux. Compared to low-energy electrons, high-energy electrons are able to repeat this reflection cycle several more times within a few hours, and thus they show a stronger slow-decay due to the accumulation effects. Note that in the left bottom panel of Figure 5.3, a second electron peak was detected at 310 keV (probably also at 180 keV) about 10 min after the first peak, possibly due to a second solar electron injection that had a much harder spectrum and thus was "buried" in the strong slow-decay of the first peak at lower energies. Here, the triangular fitting is constrained only by the first peak.

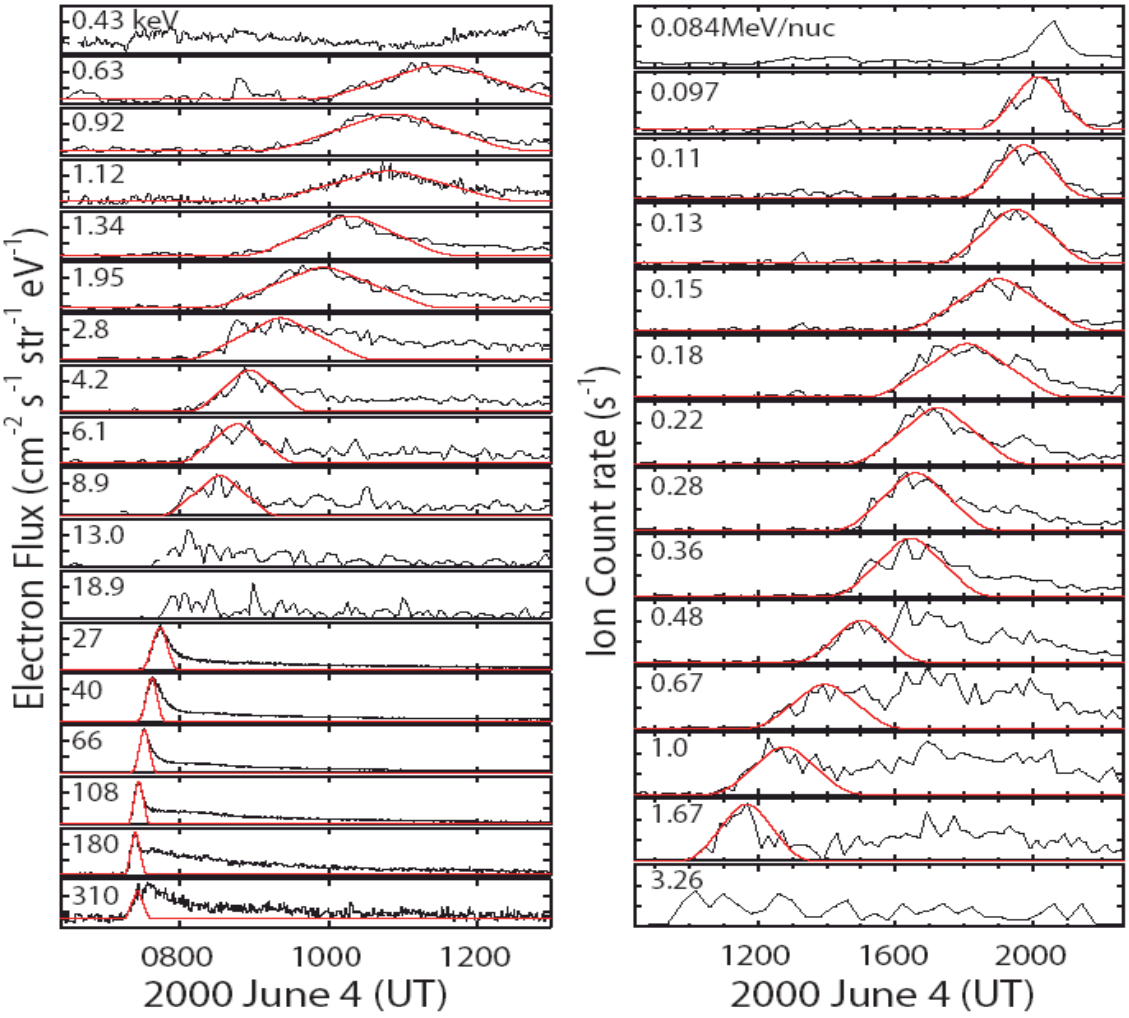

Figure 5.3. Triangular fitting to the temporal profiles of electron fluxes (left) and ion count rates (right) for event #4 on 4 June 2000. The black curves show the observations and the red curves are the best fits.

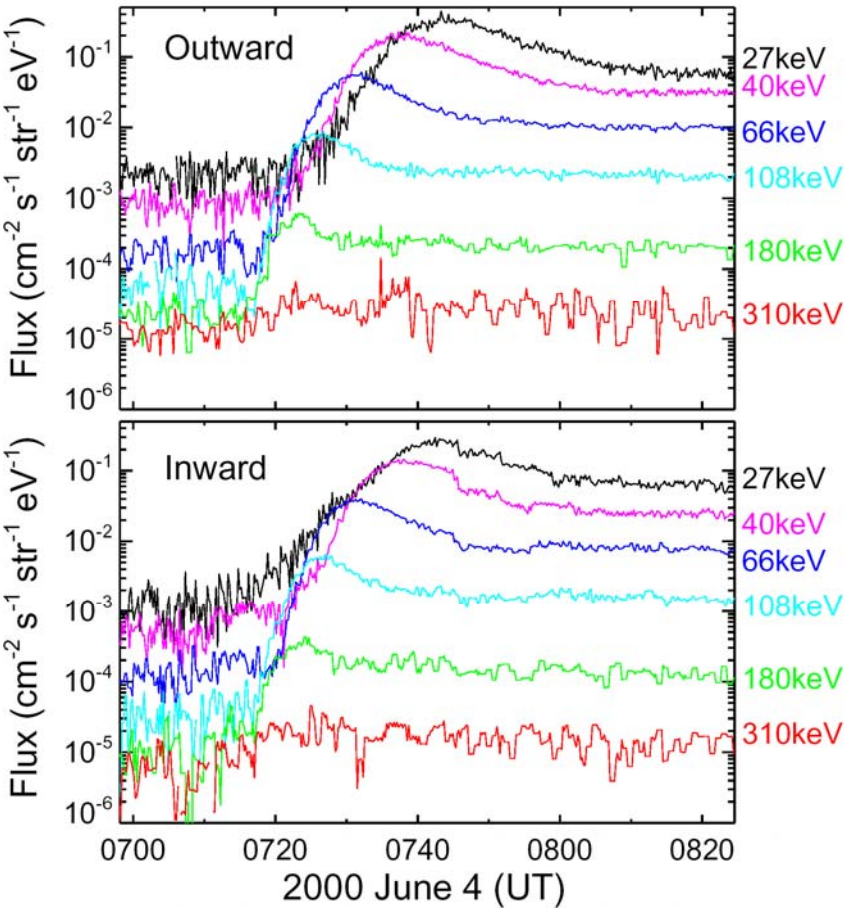

Figure 5.4. The temporal profile of background-subtracted fluxes of outward-traveling (top) and inward-traveling (bottom) electrons at 27-310 keV for event #4 on 4 June 2000.

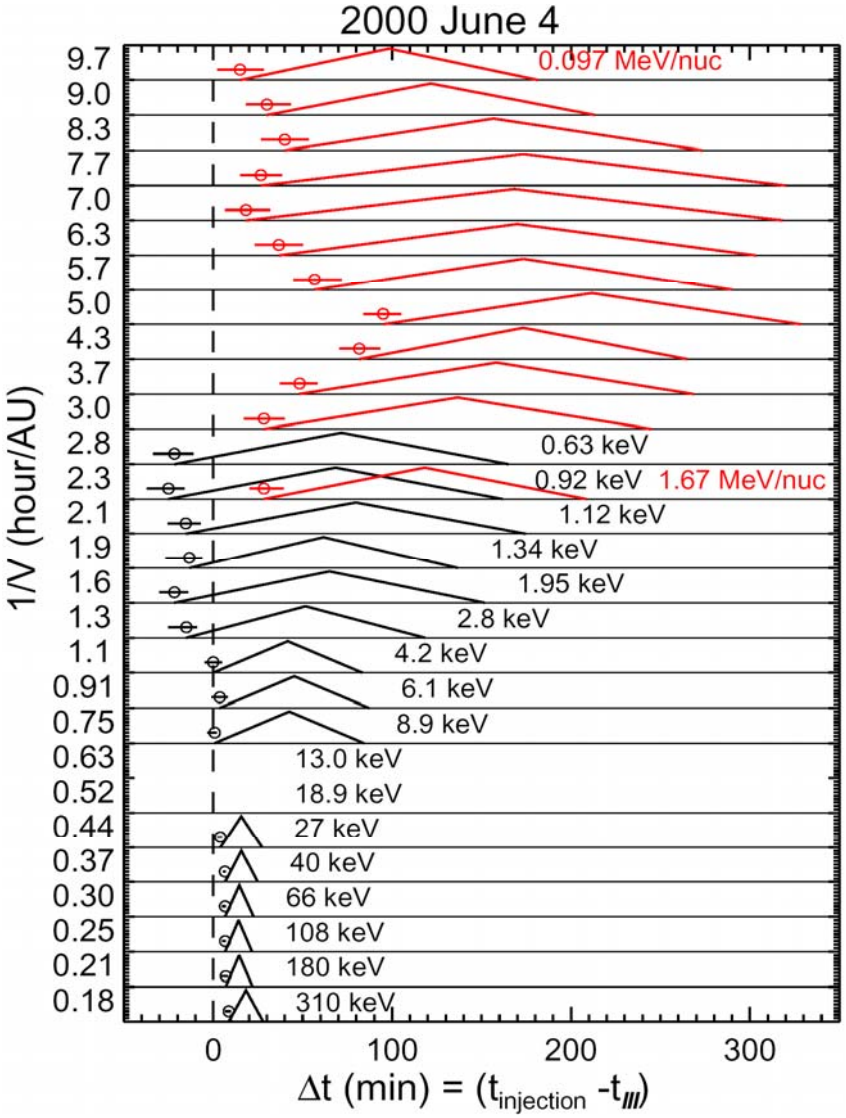

Figure 5.5. Inferred solar injection profiles of electrons (black) and ions (red) for event #4 on 4 June 2000. The X-axis shows the time in min, with respect to the release time of type III radio burst at the Sun (dash line). The Y-axis shows the energy in terms of 1/speed. The circles indicate the start-time of particle injections.

For ions, the triangular fitting is applied to energy channels from ~0.1 to 1.67 MeV/nucleon, corresponding to the $1/V$ channels from ~9.67 to 2.33 hour/AU (channel center values). The fits (shown as red curves in right panels of Figure 5.3 and bottom panel of Figure 5.6) are generally good through the rapid-rise, rapid-fall phase. Afterwards, the observed ion count rates show another peak occurring around 1700UT almost simultaneously at energies of 0.48-1.67 MeV/nucleon, possibly due to the passage of a flux rope with high fluxes at those energies.

Figure 5.5 shows the corresponding triangular injection profiles of electrons (black) and ions (red) at the Sun, with open circles representing the start time. The uncertainties in the start-time are estimated from the fit to *in situ* observations, as shown in Figure 5.6 for the 0.92 keV

electron and 1.67 MeV/nucleon ion channels. The green and blue curves are chosen as upper and lower limits of fitting to the rise of particle intensity-time profiles; the limits on the start-times of the corresponding injection are shown as error bars in Figure 5.5. Note that the 0.92 keV electrons and 1.67 MeV/nucleon ions have the same velocity of ~0.060*c*. The *in situ* observations (Figure 5.3 and 5.6) show the 1.67 MeV/nucleon ions have about the same event duration as the 0.9 keV electrons, but with a clear delay of ~ 50 minutes. Thus, the solar injections of ions and electrons with the same velocity have about the same duration, but with a ~50 minute ion delay, as shown in Figure 5.5.

In this SEP event, electron injections below 4 keV start 18.6±9.6 min before the coronal release of the type III burst and last for ~130-190 min, and electron injections at 4-9 keV start at about the type III burst time (1.5±4.4 min after) and last for ~ 80 min, while electron injections above 25 keV have much shorter durations (~15-20 min) and clearly delayed starts (6.7±1.5 min) relative to the type III burst. The ion injections at 0.1-1.67 MeV/nucleon start 42±13 min after the type III burst and have long durations (~170-300 min). The top and middle panels of Figure 5.7 compare the start-time of low-energy electron injections (black dash lines), high-energy electron injections (blue dash lines) and ion injections (red dash lines) with the type III radio burst. The coronal release time of the type III burst is estimated from the time of maximum emission observed *in situ* at ~ 14 MHz, after subtracting the photon travel time of 500 s from the Sun to Earth, and it is indicated by the arrow in Figure 5.7.

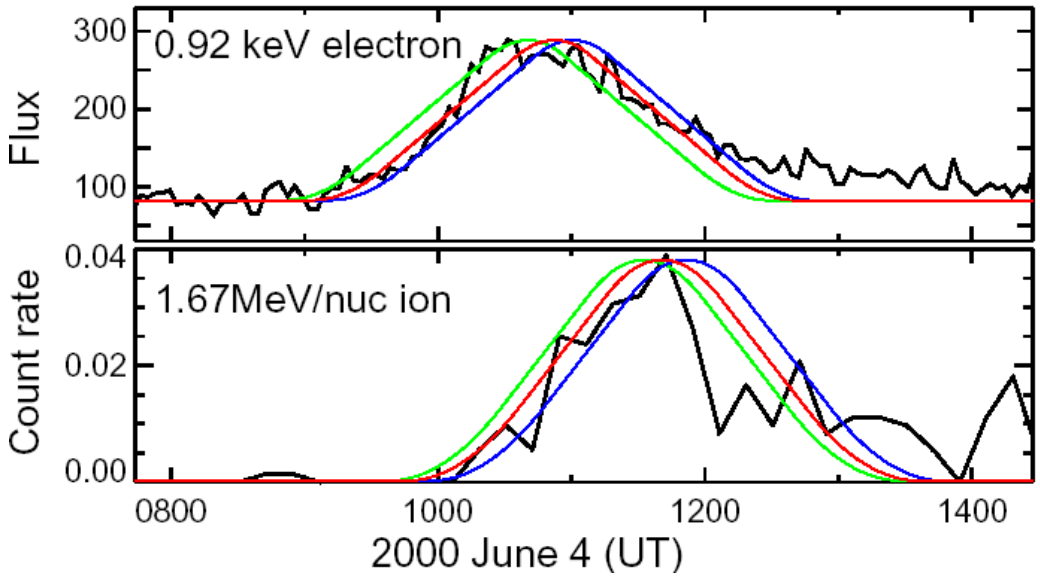

Figure 5.6. Examples of error analysis for the 0.92 keV electron channel (top) and 1.67 MeV/nucleoun ion channel (bottom). The red curves are the best fits to the fast-rise, fast-fall of *in situ* particle temporal profiles (black curves). The green and blue curves are the upper and lower limits of fitting, respectively.

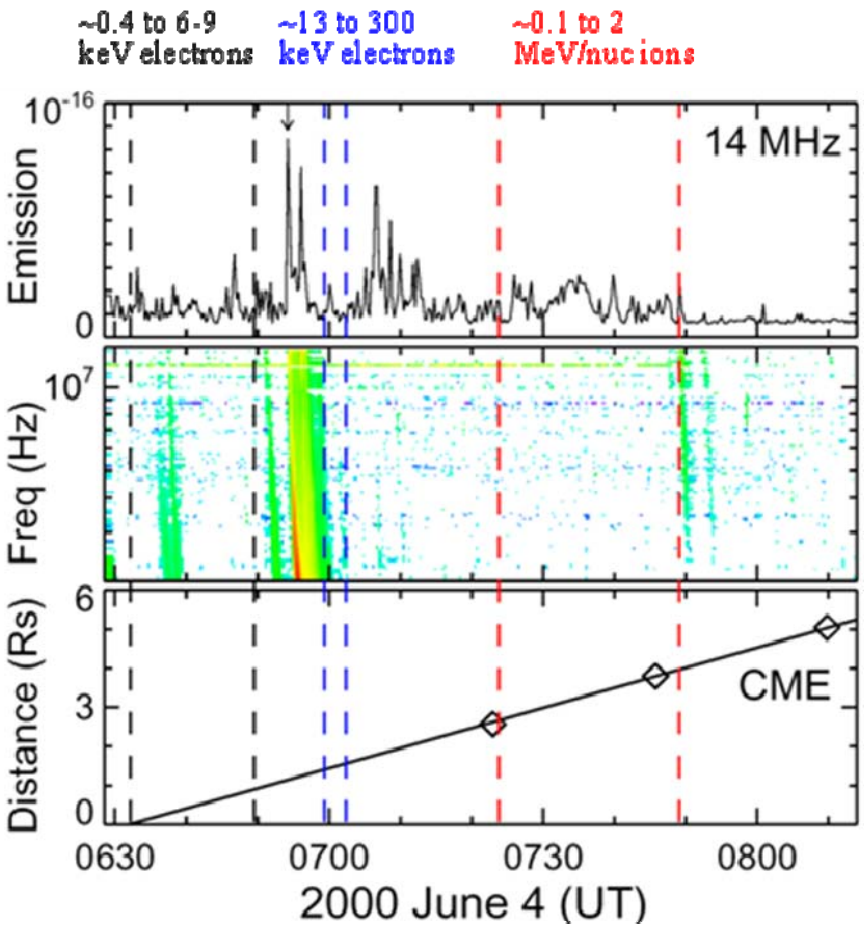

Figure 5.7. Temporal comparison for event # 4 on 4 June 2000. The top panel shows the radio emission intensity measured at ~14 MHz (WIND/WAVES), with the black arrow indicating the time of maximum emission. The middle panel is the dynamic radio spectrogram at decametric to hectometric wavelengths (WIND/WAVES). The bottom panel shows the CME distance from the Sun's center versus time (SOHO/LASCO). The shown radio and CME data have been shifted back by the photon travel time of ~500 s from the Sun to Earth. The vertical black, blue and red lines show the range of the start-times of inferred solar injections, respectively, for low-energy (~0.4 to 6-9 keV) electrons, high-energy (~9-13 to 300 keV) electrons and ions (~0.1 to 2 MeV/nucleon).

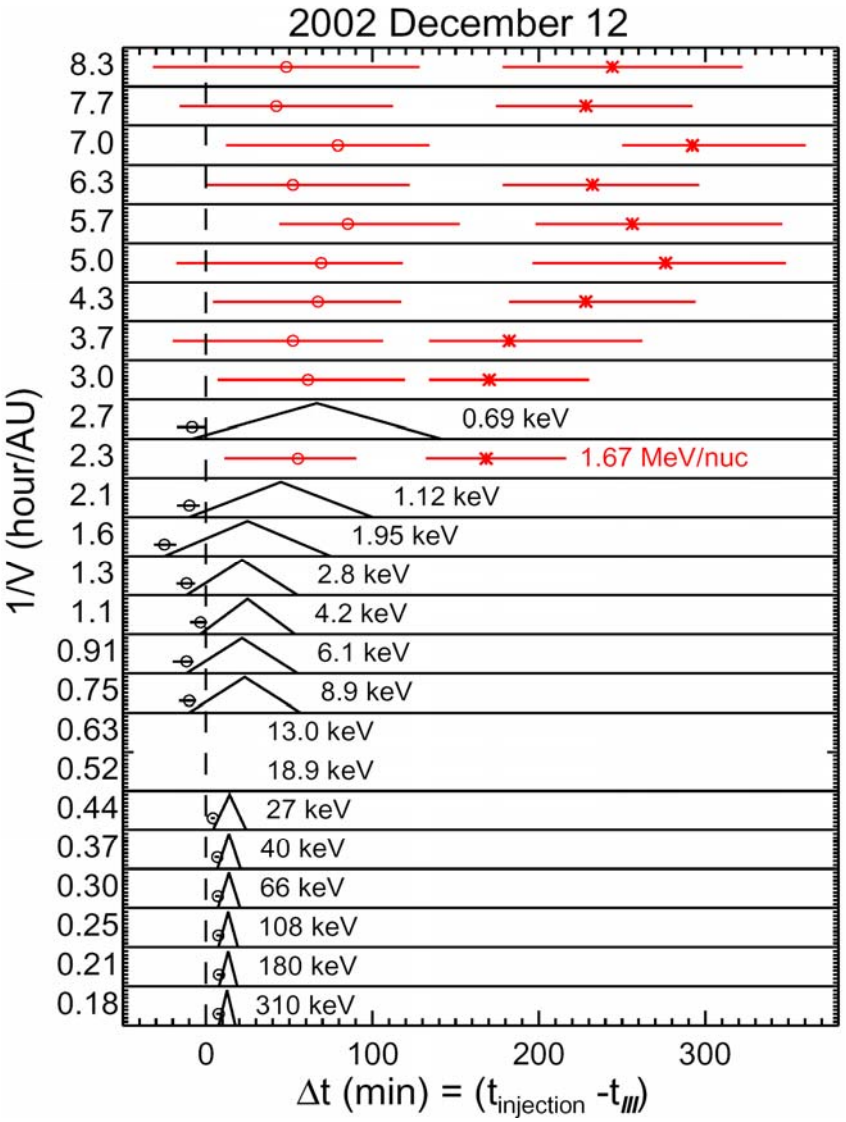

Figure 5.8. Inferred solar injection profiles of electrons (black) and ions (Red) for event #10 on 12 December 2002. The X-axis shows the time in min, with respect to the release time of type III radio burst at the Sun (dash line). The Y-axis shows the energy in terms of 1/speed. The black circles indicate the start-time of electron injections. The red circles (asterisks) represent the start-time (peak-time) of ion injections that is time-shitted from *in situ* observations by transit along a 1.2 AU path.

5.3.2.2 The other nine events

For the other nine electron/^{3}He-rich SEP events, the triangular-fitting analysis is applied to the *in situ* electron observations, but it is inappropriate for the *in situ* ion observations due to the lack of good statistics. Instead, the start-time (peak-time) of solar ion injection at energy E, t_{SUN}, is estimated from the *in situ* start-time (peak-time) of ion count rate observed at the spacecraft, t_{SC}, by subtracting the travel time along a 1.2 AU path length: $t_{SUN}(E) = t_{SC}(E) - 1.2\text{AU}/V(E)$. The uncertainties in the start-time and peak-time of solar ion injections are constrained entirely

by those *in situ* observations, typically on the order of ± 1 hour. The duration of solar ion injections is assumed to be twice the rise time from onset to maximum, i.e., an isosceles triangle-shaped injection pulse.

Similar results are obtained for the nine events. Figure 5.8 shows the triangular electron injection profiles (black) and the start-time (red circles) and peak-time (red asterisks) of ion injections at the Sun for the 12 December 2002 event (# 10). A delay is clearly evident between ion and electron channels with similar velocities. In this event, electron injections of ~0.7 to 9 keV start 11.7 ±6.6 min before the coronal release of the type III burst and last for ~60-150 min, electron injections of 27 to 310 keV begin 6.8±1.2 min after the type III burst and have shorter durations (~10-20 min), and ion injections of 0.13 to 1.67 MeV/nucleon begin 61±62 min after the type III burst and last for ~220-420 min. A gap occurs at 8.9-13 keV for electrons due to a poor statistics at those energies. For this event, the triangular fitting was not applied to the 0.92 keV electron channel (EESA-H) that has the same velocity as the 1.67 MeV/nucleion ion channel, due to fluctuations occurring in flux at the onset and rise of the 0.92 keV channel. However, the injections of the 0.69 and 1.12 keV electrons have a much shorter duration than the injection of the 1.67 MeV/nucleon ions, unlike the 4 June 2000 event where the electron and ion injections at the same velocity have about the same duration.

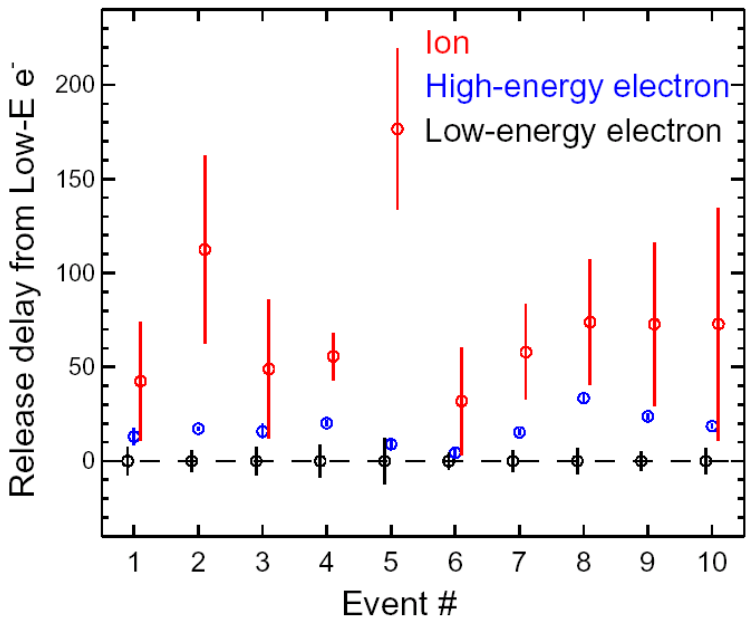

Figure 5.9. Particle release delay after low-energy electrons for the ten electron/^{3}He-rich SEP events. The black, blue and red circles represent the start-time of inferred low-energy electron injections, high-energy electron injections and ion injections, respectively.

5.3.2.3 Summary

In Table 5.1, Column 4, 6 and 8 (5, 7 and 9) list the derived start-time (duration) of solar particle injections, respectively, for ^{3}He-rich ions at ~ 0.1-2 MeV/nucleon, electrons of 0.4 to 6-9 keV and electrons of ~9-13 to 300 keV for the ten events. Figure 5.9 plots the start-time of ion injection (red circles) and high-energy electron injection (blue circles), with respect to the start-time of low-energy electron injection (black circles). In event #6, the injections of low-energy and high-energy electrons start at almost the same time (within 4 minutes), while the ion injection begins ~30±31 min later. Krucker et al. [1999] also found a small fraction of impulsive electron events where high-energy electrons were prompt relative to type III radio bursts. The average injection duration is ~110 min, ~25 min and ~200 min, respectively, for low-energy electrons, high-energy electrons and ^{3}He-rich ions. In the other nine events, ions are released at the Sun with a median delay of 79±16 min and 61±14 min, respectively, after low-energy and high-energy electrons. The event-average duration ranges from ~90 to 160 min for low-energy electrons, from~10 to 30 min for high-energy electrons, and from ~200 to 550 min for ^{3}He-rich ions.

5.4 Association with other solar phenomena

5.4.1 Type III radio bursts

It is known that type III radio bursts are generated by escaping electron beams traveling through the corona and IPM [see Lin, 1990 for summary]. All ten electron/^{3}He-rich SEP events studied here have an associated type III radio burst. For seven events (#2, 4 and 6-10), the associated type III radio burst was observed by the WIND/WAVES instrument from *in situ* local plasma frequency (~10-30 kHz) up to 14 MHz, and by ground-based radio observatories (Solar Geophysical Data (SGD)) from ~ 30 MHz up to 80-600 MHz. For event #3, the type III radio burst was observed up to ~14 MHz by WIND/WAVES, with ground observations unavailable. For these type III bursts, the coronal release time can be estimated by subtracting the photon travel time of 500 s along a 1 AU path from the *in situ* time of maximum emissions at ~ 14 MHz (see top panel of Figure 5.7, for example), and it is listed in Column 10 of Table 5.1. For the other two events (#1 and 5), however, the associated type III radio burst was observed by WIND/WAVES only up to 1-2 MHz; a type III storm was also reported at 20-90 MHz form 0100UT to 0720UT by SGD for event #1. For the two events, thus, the coronal release of associated type III bursts cannot be accurately obtained.

The eight events (#2-4 and 6-10) with a clear coronal release time of type III radio bursts can be divided into four groups, based on the timing between the type III burst and electrons. The first group is event #6 in which the injection start-time of both low-energy (~0.4 to 6-9 keV) and high-energy (~9-13 to 300 keV) electrons is consistent with the coronal release of the type III burst within the ~4 min uncertainties. The second group consists of event #3 and 7 in which the injection of low-energy electrons starts at the coronal release of the type III bursts, while the injection of high-energy electrons begins 15±3.9 min and 17±1.5 min after the type III bursts, respectively. The third group consists of event #8 and 9 in which the high-energy electron injection begins within 3 minutes of the coronal release of the type III bursts, while the low-energy electron injection starts 30±6.9 min and 21±5.2 min earlier than the type III bursts, respectively. The other three events (#2, 4, and 10) form the fourth group in which the high-

energy electron injection starts with a median delay of 7.0±0.8 min after the type III bursts, while the low-energy electron injection begins 11.6±4.1 min before the type III bursts.

5.4.2 SXR and Hα flares

For the ten electron/^{3}He-rich SEP events, Column 10 and 11 in Table 5.1 list the possible associated GOES SXR flares and Hα flares reported in SGD, respectively. Out of the ten events, none have GOES SXR flares associated with the start of low-energy (~0.4 to 6-9 keV) electron injections; only two (#5 and 8) have GOES C2.1 and C6.6 SXR flares, respectively, associated with the start of high-energy (~9-13 to 300 keV) electron injections; only one (#2) has a GOES M1.2 SXR flare associated with the start of ion injections; only three (#2, 3 and 8) have associated Hα flares, respectively, located at solar longitude W24º, W54º and W63º, so these flares are well connected to the vicinity of Earth through the IMF lines. Such poor associations are typical of electron/^{3}He-rich SEP events (see Chapter 1 and 3). However, some of these events might have unreported, small SXR flares (private conversation with H. Hudson and N. Nitta, 2006).

5.4.3 CMEs and Type II radio bursts

Nine of the ten electron/^{3}He-rich SEP events (except #1) occurred during the normal operation of the SOHO/LASCO chronograph, and all nine have an associated CME, as shown in Table 5.1. Column 15 lists the central position angle (P.A.), i.e., the angle of the midpoint of the CME apparent width measured counterclockwise from the solar North; Column 14 and 16 list the CME speed and angular width, respectively. All the associated CMEs originate at 247-299º P.A., on the west limb of the Sun where the WIND and ACE spacecraft are well connected to, and they move at a speed of ~580-1100 km/s. Six (#2-5 and 8-9) have an angular width of 7-33º, two (#7 and 10) have a width of 51-62º and one (#6) has a 140º width. Thus, all the associated CMEs are rather fast and most of them are pretty narrow, compared to the yearly average width of ~47°-61° and speed of ~300-500km/s for normal CMEs (20°< Width <120°) from a statistical study of nearly 7000 CMEs observed by SOHO/LASCO during 1996-2002 [Yashiro et al., 2004]. Note that the selection criteria of electron/^{3}He-rich SEP events used in this study are independent of CMEs, but the selected events have a one-to-one association with fast west-limb CMEs and a close association with narrow CMEs. These associations are remarkable since in general, only ~16% of ^{3}He-rich electron events are associated with fast, narrow west-limb CMEs (see Chapter 3).

For these associated CMEs, we can linearly extrapolate the CME heliocentric distance versus time profile back to the photosphere (1 R_S from the Sun's center) to estimate the CME launch time (listed in Column 13), after taking into account the photon transit time of 500 s to the Earth. We can also determine where the CME is at the start of solar particle injections. For example, bottom panel of Figure 5.7 shows the observed CME heliocentric distance versus time for the 4 June 2000 event (#4). This CME launches at about the start-time of low-energy (~0.4 to 6-9 keV) electron injections (black lines), and reaches an attitude of ~0.5 and ~1.7-3.0 R_S above the photosphere, respectively, at the start of high-energy (~9-13 to 300 keV) electron injections (blue lines) and ion injections (red lines). Figure 5.10 shows the projected CME heliocentric distances (if available) for the ten electron/^{3}He-rich SEP events. On average, the associated

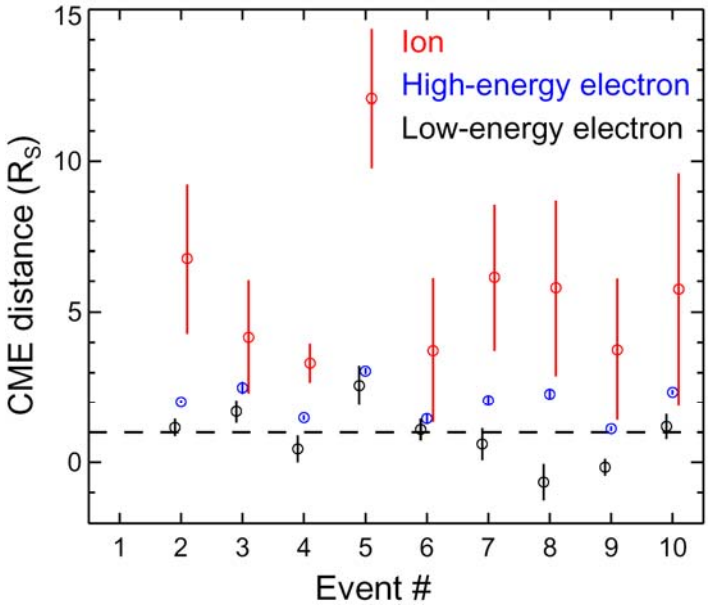

Figure 5.10. Projected CME distance from the Sun' center at the start of low-energy electron (black), high-energy electron (blue) and ion (red) solar injections. The horizontal dash line indicates the photosphere at 1 R_S where the CME launch is assumed to start from.

CMEs are at an altitude of 1.0±0.04 R_S and 4.7±0.8 R_S, respectively, at the start of high-energy electron and ion injections. The low-energy electron injections begin before the extrapolated CME launch in two events (#8, 9), close to the CME launch in six events (#2-4, 6, 7, 10) and after the CME launch in one event (#5).

For event #8, a coronal type II burst was reported at 25-180MHz (SGD), indicative of the occurrence of shocks low in the corona. The coronal onset of this type II burst occurs ~18 min after the start of high-energy electron injections at the Sun but close to the start of ion injections. At this type II onset time, the CME associated with event #8 has reached an altitude of ~2.8 R_S where the local plasma frequency should be much lower than 20 MHz [Leblanc et al., 1998]. However, this type II burst may be produced at the flanks of the CMEs at lower altitudes.

5.5 Summary and Discussion

By taking into account the interplanetary propagation and instrumental effects (energy band), we have investigated the particle injection in ten electron/^{3}He-rich SEP events with strongly scatter-free propagtion. The observed temporal profiles of electron fluxes at all energies in all the ten events fit well to triangular injections at the Sun with equal rise and fall times; this is also true of the observed temporal profiles of ion count rates in the 4 June 2000 event that has good ion statistics. For events without good ion statistics, the solar ion injections are estimated from the *in situ* onset and peak-time, after subtracting the ion travel time along a 1.2 AU path length. In the ten events, on average, the solar injection of ~0.1-2 MeV/nucleon, ^{3}He-rich ions begins 75±14 min and 57±13 min, respectively, after the injection of low-energy (~0.4 to 6-9 keV) electrons and high-energy (~9-13 to 300 keV) electrons. The event-average duration ranges from

~200 to ~550 min for ion injections, from ~90 to ~160 min for low-energy electron injections, and from~10 to ~30 min for high-energy electron injections.

Among the ten electron/^{3}He-rich SEP events, three have a Hα flare located at solar longitudes of W24-63º; three may have a GOES SXR flare of C-class and above; all have a type III radio burst; one may have a coronal type II radio burst. Nine events have the SOHO/LASCO coronagraph coverage, and all have a rather fast (>570km/s), west-limb CME that reaches a median altitude of ~1.0 and 4.7 Rs, respectively, at the start of high-energy electron injections and ion injections. Six out of the nine CMEs (#2-5, 8 and 9) have an angular width of 7-33º and the other three (#6, 7 and 10) have a wide width of 51-140º. Note that the electron/^{3}He-rich SEP events selected in this study have a one-to-one association with fast west-limb CMEs, with most of the associated CMEs being narrow, but in general, ~84% of ^{3}He-rich electron events lack the association with fast, narrow west-limb CMEs (see Chapter 3). This is probably due to the criteria used here that select strong (clear) ion events, and it suggests that strong acceleration of ^{3}He-rich ions is associated with the presence of fast, narrow CMEs.

In six out of the eight events with a clear coronal release time of type III radio bursts (#2-4, 6, 7, 10), the injection of low-energy (~0.4 to 6-9 keV) electrons begins 6.5±2.7 min earlier than the type III radio bursts but the injection of high-energy (>~13 to 300 keV) electrons starts 8.8±0.9 min after the type III bursts, confirming the results of Chapter 4 and Wang et al. [2006]. Thus, the source of the type III radio bursts can be identified with the low-energy electron injection; some delay is needed for velocity dispersion – the faster electrons running ahead of the slower ones – to produce the significant positive slopes in the electron reduced parallel velocity distribution function required for the growth of the Langmuir waves that, in turn, scatter to produce the type III radio emission at the fundamental and harmonic of the plasma frequency [see Lin 1990 for summary]. As mentioned previously, this is consistent with the arrival at 1 AU of ~1-10 keV electrons when the Langmuir waves that generate the type III radio emission are observed [Ergun et al., 2000; Wang et al, 2006]. In the other two events (#8, 9), the low-energy electron injection starts ~20-30 min earlier than the type III bursts, while the high-energy electron injection begins only 3 minutes after the type III bursts. Unlike other events in Table 5.1, however, these two electron events were both closely preceded by another event, with the rise of low-energy electrons superimposed on the decay tail of the corresponding previous event (see left panel of Figure 5.1, for example). Then in the two events, more delay may be needed for low-energy electrons to rise above the previous event to produce the significant positive slopes in the reduced parallel velocity distribution function.

Furthermore, in the ten events, the high-energy electron injections have ~2-20 times shorter durations and systematically delayed (~4-34 min; an average of 17.0±3.0 min) starts, compared to the low-energy electron injections with durations of ~50 min to several hours. In these highly scatter-free events, scattering in the IPM cannot account for both the delay of up to 34 min and the much shorter duration of inferred high-energy electron injections. This is consistent with our previous study (Chapter 4), suggesting that low-energy electrons may provide seed electrons for the delayed acceleration to high energies, e.g., by some propagating phenomena such as EIT waves and their coronal counterparts [Krucker et al., 1999], or upward moving CME-driven shocks [Haggerty and Roelof, 2002; Simnett et al., 2002]. In fact, all the nine events with available SOHO/LASCO coverage have associated west-limb CMEs that are at ~0.1-2.0 Rs altitude when the high-energy electrons are released. In six events (#2-4, 6, 7, 10), the start time of low-energy electron injection appears close to the extrapolated start of the CME eruption. As

suggested by Chapter 4, the low-energy electron injection and type III burst may be related to the initial CME eruption, with the injection continuing as the corona restructures while the CME continues outward [Maia & Pick, 2004; Klein et al., 2005].

Based on electron transport simulations, Kontar & Reid [2009] suggested another scenario that electrons at all energies are injected at the Sun as a single population, and the beam-plasma interactions in the IPM can strongly decelerate electrons below tens of keV, while electrons above are too dilute (due to fast V) to generate plasma waves and they propagate freely. Although several studies suggested that re-absorption of plasma waves enable electron beams to propagate large distances (in terms of AU) without catastrophic energy loss [e.g., Takakura & Shibahashi, 1976; Magelssen & Smith, 1977; Lin et al., 1981; Grognard, 1980], Kontar & Reid [2009] proposed that plasma waves at low phase velocities can be easily absorbed by the thermal plasma via Landau damping, so electrons are unable to gain energy from those waves; then the low-energy electrons detected *in situ* at 1 AU are originally injected at the Sun with higher energies and have traveled effectively faster than the detected energies suggest. This scenario could lead to the early electron injection (and also the flat energy spectrum) at low energies estimated here under propagation without energy loss. It also predicts that more than 99% of escaping energetic electrons would be lost en route to 1 AU. If half of the accelerated electrons at the Sun go down to generate hard X-rays (HXR) in high-density chromosphere (by non-thermal Bremsstrahlung process) and half go up and escape into the interplanetary space, then the number of electrons observed at 1AU would be only 1% of the number of HXR-producing electrons, consistent with previous studies [Lin ,1974; Krucker et al., 2007]. However, this scenario cannot explain the delayed injection of high-energy electrons after type III bursts.

In the ten electron/^{3}He-rich SEP events, the inferred injections of ~0.1-2 MeV/nucleon ^{3}He-rich ions show a systematical delay of ~ 1 hour after electrons at all energies. One possibility is that this ~ 1 hour delay may reflect a long acceleration time scale of ions. Models including the effects of stochastic acceleration, Coulomb energy loss and charge-changing process such as impact ionization and recombination [e.g., Kocharov et al., 2000; Kartavykh et al., 2006] suggest that a value of $N\tau_A \sim 10^{10} - 10^{11}$ s·cm^{-3} is required to reproduce the observed ionization states in electron/^{3}He-rich SEP events that increase with energy from Q_{Fe} ~13-15 at ~0.1 MeV/nucleon to Q_{Fe} ~18-20 at ~0.55 MeV/nucleon [Popecki, 2006], where N is the plasma density and τ_A is the acceleration time scale. If τ_A is ~ 1 hour, then N would be ~ $10^6 - 10^7$ cm^{-3}, corresponding to altitudes >~ 0.5 Rs, high in the corona. The acceleration mechanism is likely the resonance with wave modes that can preferentially heat/accelerate ^{3}He and heavy ions due to their unique charge-to-mass ratios. Fisk [1978] proposed the first viable mechanism for selective heating of ^{3}He by absorption of electrostatic ion cyclotron waves produced above the ^{4}He gyrofrequency. Temerin & Roth [1992] and Roth & Temerin [1997] noted an analogy of the presence of electron beams in impulsive SEP events with *in situ* terrestrial observations showing that precipitating electron beams generate oblique electromagnetic ion cyclotron (EMIC) waves that accelerate ions in the aurora. They suggested that a similar process might occur in solar flares: downward streaming electrons generate EMIC waves that resonate with the gyrofrequency of ^{3}He or the second harmonic of the gyrofrequencies of heavy ions. Several other people proposed resonant acceleration by shear Alfvén waves [Miller & Viñas, 1993], cascading MHD waves [e.g., Miller, 1998], plasma waves propagating parallel to the magnetic field [e.g., Liu et al., 2006], and firehose instability due to electron temperature anisotropy [Paesold et al., 2003]. However, those acceleration models give a typical acceleration time scale of seconds [e.g., Roth & Temerin,

1997; Liu et al., 2006], much shorter than the inferred ~ 1 hour delay of ion injections in the ten events.

A second possibility is that the delayed ion injection may be related to the acceleration occurring very high in the corona by shocks or other phenomena. In fact, for these ten SEP events, the associated west-limb CME reaches an altitude of ~2-11 Rs at the start of inferred ion injections. If the ion acceleration occurs at such altitudes, it would be difficult to obtain the typical ionization states in impulsive SEP events that are believed to be produced by stripping through a dense column density. But Mason et al. [1999] found that ^{3}He and Fe remnants from impulsive SEP events or solar flares can fill a substantial volume (>50%) of the in-ecliptic IPM during periods of high solar activities. They and Desai et al. [2001] suggested that such remnant impulsive material may provide a seed population for further acceleration by interplanetary shocks, leading to the ^{3}He and heavy ion enhancements observed in some gradual SEP events and interplanetary shocks. As an analogy, a similar process can occur high in the corona: propagating shocks or other waves further accelerate the remnant impulsive material at ~5-10 Rs. Then the delayed ion injections would be related to the transit of shocks or waves that start low in the corona at the time of the initial electron injection. However, this doesn't answer the question of where and how the remnant impulsive material is produced.

A third possibility is that in the selected electron/^{3}He-rich SEP events, ions may experience some scattering through the IPM and thus travel an "effective" path longer than the nominal 1.2 AU, leading to the delay of ion injections inferred under scatter-free propagation. However, this scenario contradicts the velocity dispersion analysis of *in situ* ion onsets at the spacecraft for the ten events, and so far, no ion pitch angle observations are available to verify the ion propagation in the IPM. In the future, the *in situ* particle observations close to the Sun by Solar Orbiter and Solar Probe Plus can help us investigate these possibilities and further understand the source of electron/^{3}He-rich SEP events.

6. Pitch angle distributions and temporal variations of solar impulsive electron events

6.1 Introduction

Solar impulsive electron events were first observed at energies above ~40 keV [Van Allen & Krimigis, 1965; Anderson & Lin, 1966], with fast rise –slow decay temporal profiles indicative of significant scattering in the IPM. Later, events were detected down to ~0.1 keV energies ([Gosling et al., 2003]), occasionally with fast rise-fast decay profiles that imply essentially scatter-free propagation in the IPM [Lin, 1974]. Near solar maximum, $>\sim 10^2$ events/month occur over the whole Sun [see Lin, 1985, and Chapter 3 for review], making these the most common impulsive solar particle acceleration phenomenon. They are often accompanied by low energy, ~MeV/nucleon ion emissions that are highly enriched in ^{3}He [Reames et al., 1985]. These electron/^{3}He-rich events form the class of "impulsive" SEP events.

For solar impulsive electron events, Krucker et al. [1999] found that the injection of the >25 keV electrons at the Sun were often delayed by ~10 up to ~30 minutes after the type III radio bursts at the Sun, and Haggerty & Roelof [2002] reported a median delay of ~10 min for 38-315 keV electrons. Wang et al. [2006; Chapter 4] showed that the flux-versus-time injection profiles at the Sun for three scatter-free electron events observed down to ~0.4 keV fit well to isosceles triangles (equal rise and fall times). They found that the ~13-300 keV electrons were injected starting 7.6±1.3 minutes after the type III bursts but the ~0.4-10 keV electrons were injected beginning 9.1±4.7 minutes before the type III bursts, indicating the ~0.4-10 keV electrons generate the radio emission (consistent with type III radio emissions and parent Langmuir waves observed *in situ* simultaneously with the arrival of ~2-10 keV electrons at 1 AU [Ergun et al, 1998]). Cane & Erickson [2003] and Cane [2003] argued from radio observations that the delays of high-energy electrons were due to propagation effects in the IPM. In this study, we will use *in situ* electron observations to examine the propagation of different energy electrons in the IPM for solar impulsive electron events.

As energetic electrons propagate outward from the Sun along diverging IMF lines, we expect that adiabatic motion (the invariance of $\sin^2\alpha/B$) would focus them to small pitch angle (PA), α, but nonadiabatic wave-particle interactions can scatter them to large PA. Thus, *in situ* observations of electron pitch angle distributions (PADs) provide important information on interplanetary propagation and local electron-wave interactions, while the intensity-time profiles integrate the effects of propagation from the Sun to Earth. Using ISEE-3 electron observations of ~ 2 keV to 1 MeV, Potter et al. [1980] and Lin et al. [1981] reported that the PAHM (PA width at half maximum) of PADs was < 13° for electrons below ~ 10 keV and >30-40° above 15 keV.

With WIND three-dimensional electron observations from solar wind plasma to >300 keV, we examine PADs for five solar impulsive electron events that have short time durations, low pre-event background and good count statistics. We find that at low energies, the PAHM of PADs is below 30° (limited by the instrument resolution) and it does not change with time through the peak. After the peak, PAHM increases up to 40-70° in the slow-decay tail (when present). At high energies, the PAHM increases with energy, e.g., from ~40° at 40 keV to ~ 80° at ~ 300 keV for the peak; it also increases with time, e.g., from ~40° at onset to ~ 80º-100° at the slow decay for 60 keV. The energy transition between the two populations occurs at ~10 to

30 keV, varying from event to event, and appears to depend on the local solar wind thermal proton gyroradius ρ_{Tp} (or proton temperature Tp). We also find evidence for local small-angle scattering or magnetic mirroring across 90° PA above 40 keV.

6.2 Observations and data analysis

The WIND 3DP instrument provides full three-dimensional measurements of electron distributions from solar wind thermal plasma to ~400 keV [Lin et al., 1995]. Silicon semiconductor telescopes (SST) measure ~20-400 keV electrons with energy resolution of ~7 keV FWHM and $\Delta E/E \approx 0.3$ and angular resolution of 22.5°×36º, while electron electrostatic analyzers (EESA-L and EESA-H) measure ~3 eV-30 keV electrons with $\Delta E/E \approx 0.2$ and angular resolution of 22.5°×22.5º. The flux in each three-dimensional angular bin is assigned the PA calculated for its central axis using the vector IMF direction measured by the WIND MFI instrument [Lepping et al., 1995]. Then the three-dimensional data are sorted into eight PA bins with a 22.5° angular resolution, with a small degree of overlap between adjacent bins. If the IMF points sunward (anti-sunward), then the four PA bins – 90-112.5°, 112.5-135°, 135-157.5°, 157.5-180° – cover electrons traveling outward from (toward) the Sun and the other four bins – 0-22.5°, 22.5-45°, 45-67.5°, 67.5-90° – cover inward-traveling (outward-traveling) electrons.

We select five solar impulsive electron events with short time durations, strongly scatter-free flux-time profiles, low pre-event background and good count statistics observed by WIND/3DP from ~0.3 to ~300 keV - the *in situ* onset times for these events are 2349UT on 11 July 1998, 1845UT on 29 August 1998, 0600UT on 18 July 2001, 1424UT on 20 October 2002, and 0432UT on 21 October 2002. During the five events, the WIND spacecraft was located in the solar wind, without magnetic connection to the Earth's bow shock. In this section, we illustrate the characteristics of these events with detailed observations of one representative event on 20 October 2002, followed by brief descriptions of the other four events.

6.2.1 The 20 October 2002 event

The 20 October 2002 impulsive electron event was clearly detected down to ~0.26 keV and up to >~310 keV, and was preceded by another event with poorer count statistics. The left panel of Figure 6.1 shows the outward-traveling electron fluxes (averaged over 90-180° PA since the IMF pointed sunward) versus time at energies from ~0.2 to 310 keV (center energy for each channel). The right panels of Figure 1 show the electron PADs at 0.3-310 keV normalized by the PA averaged flux for each time bin and energy channel. Isotropic distributions show normalized values around 1 (green) in all PA directions, but beamed distributions have larger values (red) in the beaming direction and lower values (indigo) at other PAs.

Figure 6.2 shows electron fluxes versus time in four outward (90-112.5°, 112.5-135°, 135-157.5°, 157.5-180°) and four inward (0-22.5°, 22.5-45°, 45-67.5°, 67.5-90°) PA bins at 66 keV (left) and 4.2 keV (right), after subtracting pre-event electron background and instrumental background. At 66 keV, the flux-time profiles at 1 AU exhibit three peaks, #1, 2 and 3, successively, at ~1437UT, 1610UT, and 1640UT. At 4.2 keV, only the peak #1 and 2, respectively, at ~1550UT and 2120UT, are clearly evident above background in the flux-time profiles. An abrupt flux increase occurred during 1525-1535UT simultaneously in all inward PA bins (also evident in outward PA bins with low fluxes) at all energies from 27 to 310 keV,

coincident with the sudden rotation of the IMF to a strongly northward direction (bottom panels of Figure 6.2), suggesting a change in magnetic connection to the Sun.

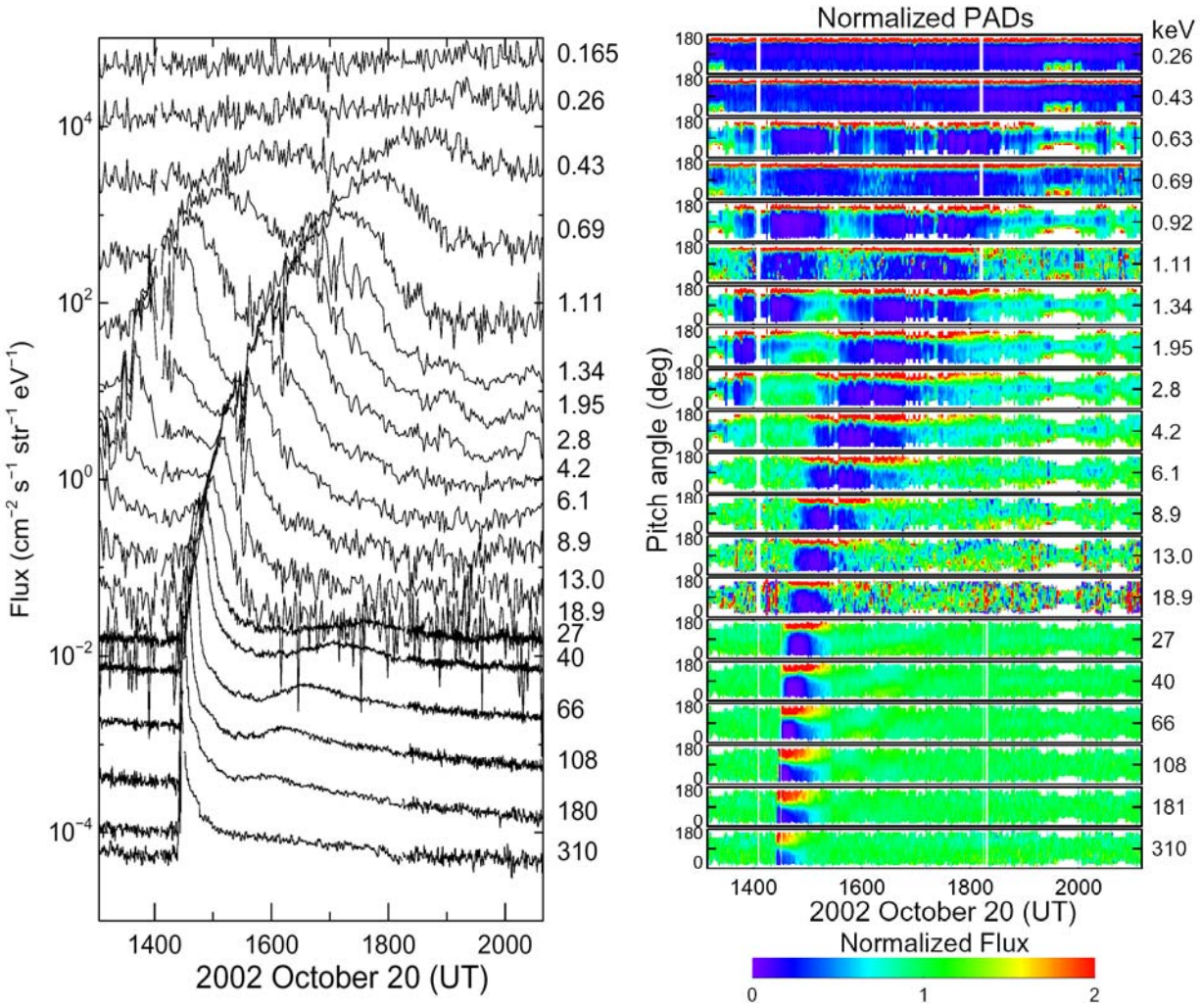

Figure 6.1. Overview plot for the 20 October 2002 event. The IMF was pointing towards the Sun. Left panel shows the flux of electrons travelling anti-parallel (outward) to the IMF observed by EESA-L (0.17-1.11 keV; 96-second average), EESA-H (1.34-18.9 keV; 96-second average) and SST (27-310 keV; 12-second average). Right panels show electron PADs normalized by the PA averaged flux for each time bin. Isotropic distributions show normalized values around 1 (green) in all PA directions, but beamed distributions have larger values (red) in the beaming direction and lower values (indigo) in other directions. Another impulsive electron event occurred a few hours earlier with less count statistics.

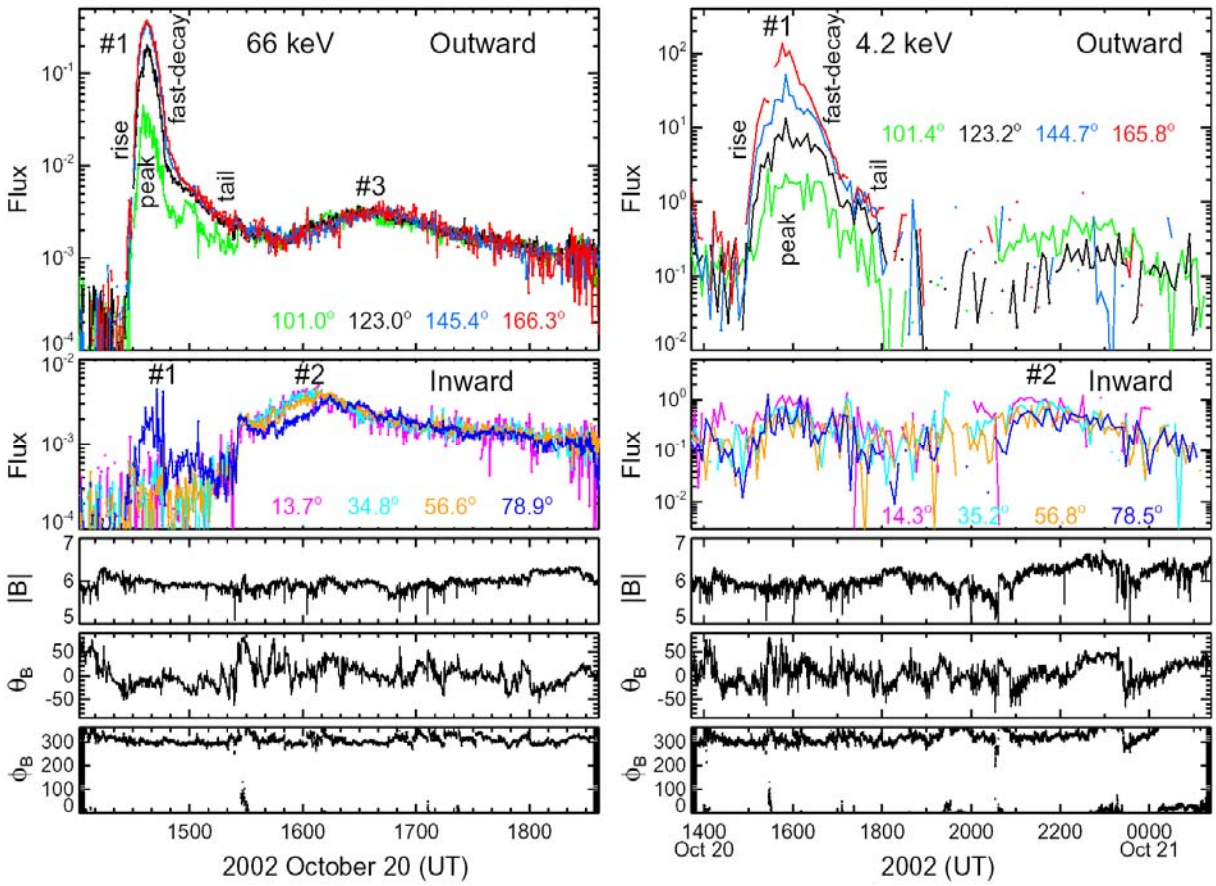

Figure 6.2. The temporal profiles of background-subtracted electron fluxes at 66 keV (left) and 4.2 keV (right) in four outward-traveling (90-112.5°, 112.5-135°, 135-157.5°, 157.5-180°) and four inward-traveling (0-22.5°, 22.5-45°, 45-67.5°, 67.5-90°) PA bins for the 20 October 2002 event. Colored curves indicate the 12-second (5-minute) average flux in different PA bins at 66 keV (4.2 keV). The bottom panels show the magnitude, polar angle and azimuthal angle of the IMF measured by WIND/MFI. In left panel, a sudden flux increase occurred at ~1525-1535UT in four inward PA bins (also in outward PA bins having low fluxes) at 27-310 keV, related to the sudden change in the IMF (especially in the direction).

6.2.1.1 Peak #1

6.2.1.1.1 Outward-traveling electrons

Peak #1, detected from ~0.26 to 310 keV, is due to the initial passage of outward-traveling electrons at the spacecraft. The flux-time profiles at all energies exhibit a nearly symmetric rapid-rise, rapid-decay peak, followed by a slow decay (negligible below ~1keV) at flux levels much lower than the peak (left panel of Figure 6.1). Velocity dispersion is clearly evident from ~0.3 to 310 keV. For electrons above ~25 keV, the times, t_i, of the peak fluxes at different velocities, $V_i = c\sqrt{1-\left(\frac{m_e c^2}{m_e c^2 + E_i}\right)^2}$, fit well to a straight line (see the bottom of left panel of Figure 6.3), $L = V_i[t_i - t_o]$, implying a simultaneous solar injection at these energies with the peak time t_{01}

= 1412±0002 UT followed by travel along the same path of length L_1=1.25±0.10 AU. For electrons below 15 keV, the linear fit to the peak-flux times gives a path length estimate of L_{1b}=1.16±0.08 AU (see the right panel of Figure 6.3) and a release peak-time of t_{01b} = 1422±0006 UT. The two lengths are consistent with each other within errors, and slightly larger than the smooth spiral field length of 1.06 AU calculated for the observed solar wind speed V_{sw} of 660 km/s. Such profiles and velocity dispersion imply that most of outward-traveling electrons (those in the peak #1) propagated through the IPM with little or no backscattering (mean free path > 1 AU), since significant backscattering (mean free path <~ 0.4 AU) through the IPM would produce a very asymmetric peak with a strong, very slow decay [Lin 1974] and a much larger path length.

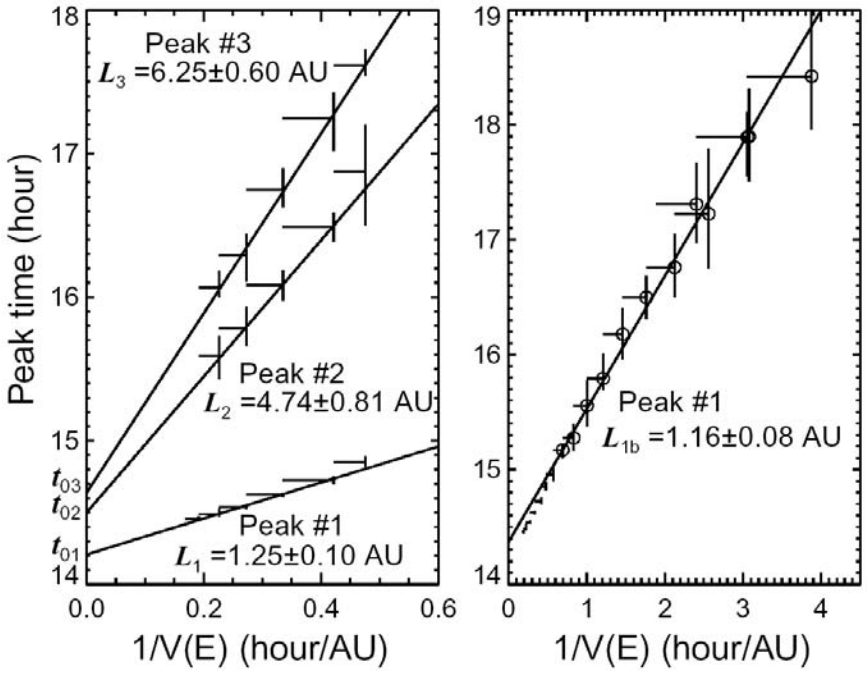

Figure 6.3. The velocity dispersion analysis of the peak-flux time versus the inverse speed above 25 keV (left) and below 15 keV (right) for the 20 October 2002 event. For each energy channel/band, the speed V_i is determined by the lower bound since the flux decreases rapidly with energy due to the hard energy spectrum. Left panel shows the times for peak #1 (bottom), #2 (middle) and #3 (top) above 25 keV. These times align well on a straight line as a function of the inverse speed, $t_i = t_o + L/V_i(E)$, giving estimates of the path length L (slope) and the release time t_0 (y-axis intercept). Right panel shows the times for peak #1 above 15 keV (crosses) and below (circles), with the linear fit to the peak times below 15 keV.

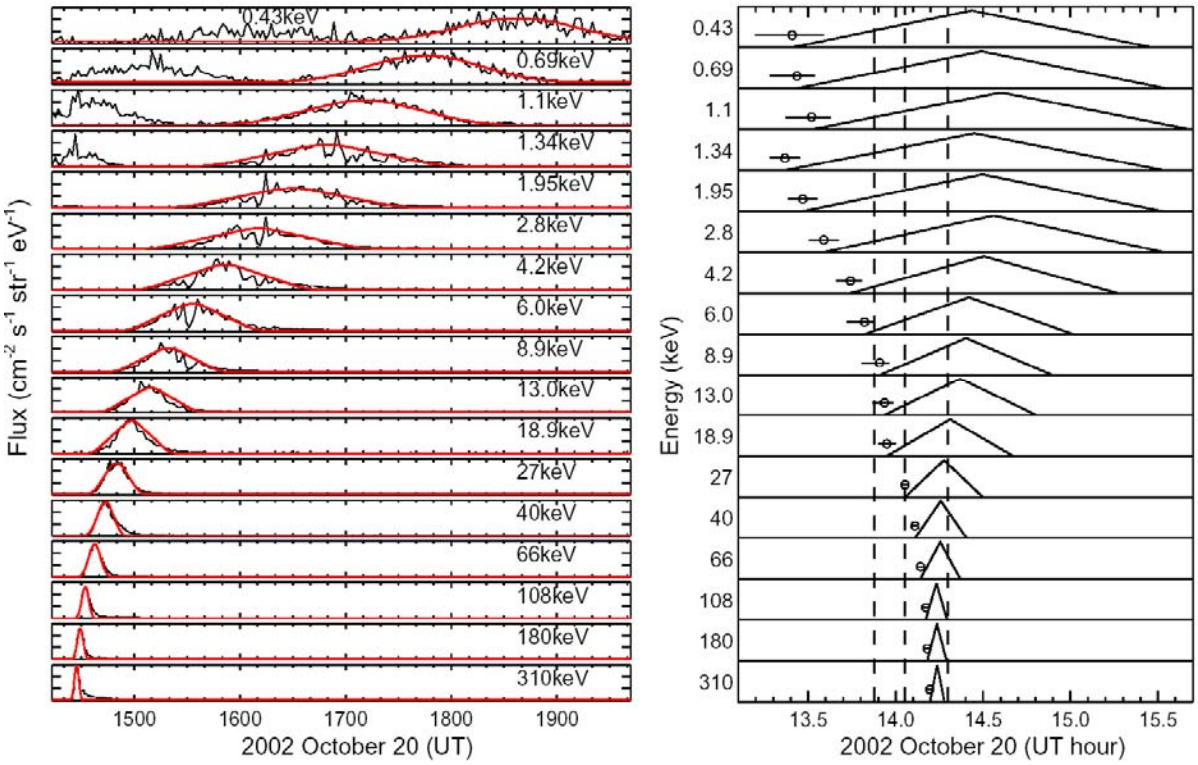

Figure 6.4. Triangular injection fitting for the 20 October 2002 event at 0.4-310 keV. Left: The red curves are the best fits to the fast-rise, fast-fall of in situ temporal profiles of electron fluxes at 1 AU (black curves). Right: Inferred electron injection profiles at the Sun. The circles indicate the start time of solar electron injections, while the vertical dash lines indicate the solar release of type III radio bursts.

For the outward-travelling electrons in peak #1, we obtain the injection profiles at the Sun from forward fitting to the flux-time profiles observed at 1 AU, by assuming triangular injections with equal rise and fall times, and taking into account the scatter-free propagation along a 1.2 AU path through the IPM and the instrument response (see Chapter 4, for details of triangular fitting). Left panels of Figure 6.4 show that the fits (red curves) are very good through the rapid-rise, rapid-fall phase. Afterwards, the observed electrons fluxes (black curves) show a very weak (<2% of the peak flux), slow decay tail at energies above ~ 1 keV. The inferred triangular injection profiles at 0.4-310 keV are shown in right panel of Figure 6.4. This event has three possible type III radio bursts measured at ~14 MHz by WIND/WAVES. On average, electron injections above ~13 keV start 14.3 ± 1.6 minutes after the coronal release of the first type III radio burst at 1353UT and last for ~ 20 minutes, while electron injections below ~6-9 keV begin 20.0 ± 6.9 minutes earlier than the first type III burst and last for ~ 110 minutes.

Figure 6.5 shows the normalized 3-D angular distributions of 1.3 and 13 keV (from EESA-H) and of 27-108 keV (from SST) electrons measured at time of the peak flux at each energy. The diamond (cross) indicates the 180° (0º) PA direction averaged over ~24 s for SST distributions or ~96 s for EESA-H. The black curves represent every 10º iso-PA contour, from 10º to 170º. Electrons are beamed outward along the magnetic field (180° PA). At 1.3, 13 and 27 keV, the 3-D angular distributions exhibit similar PAHMs of ~30º or less, limited at low energies by

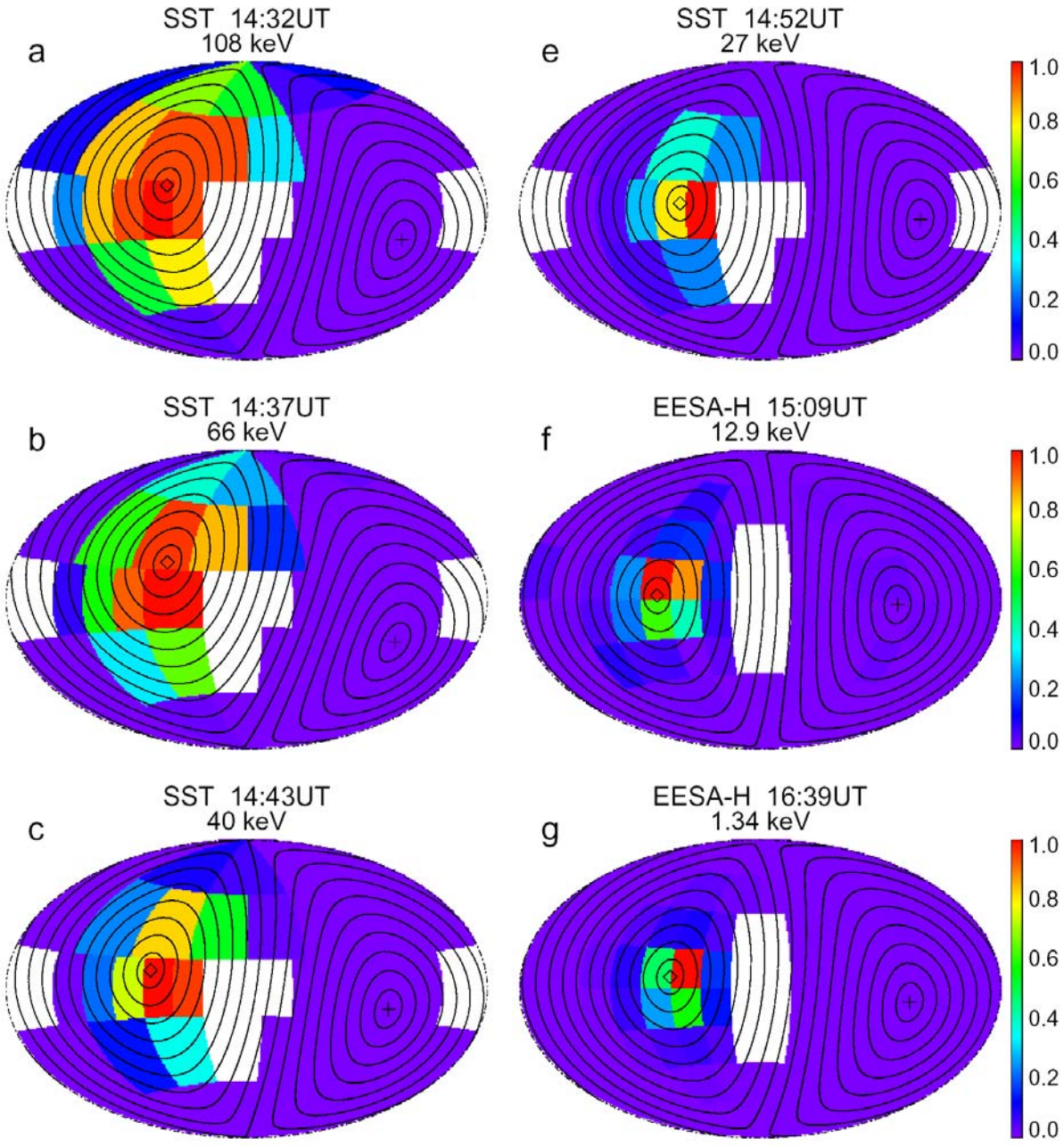

Figure 6.5. The normalized 3-D electron angular distributions measured at the peak of 1.3 and 13 keV (EESA-H) and of 27-108 keV (SST) for the 20 October 2002 event. The SST distributions are averaged over ~ 24 s and the EESA-H distributions are averaged over ~96 s, after removal of the pre-event background. The high-background bins due to solar X-rays have been excluded. The cross (diamond) indicates the direction parallel (anti-parallel) to the IMF. The black curves represent the iso-PA contours at every 10º.

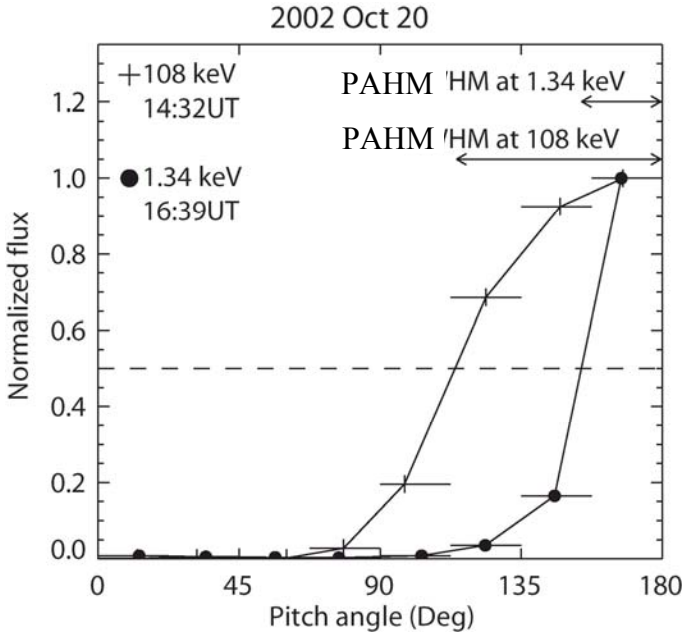

Figure 6.6. Background-subtracted electron PADs measured at 1.34 (dots) and 108 (crosses) keV for the 20 October 2002 event. The PADs are normalized to a maximum of 1.0. The PAHM is indicated by double-ended arrows at the top. Note that the inward-traveling flux is small but clearly evident at 67.5-90° PA at 108 keV.

instrumental resolution. At 40-108 keV, however, the distributions clearly broaden with increasing energy, consistent with the electron PADs measured during the peak #1 (right panels of Figure 6.1). Figure 6.6 compares the normalized PADs of 1.34 and 108 keV at the peak after background subtraction. The beam at 108 keV is ~2.5 times broader (PAHM of 66° vs. <~ 26°, as determined from linear interpolation between two nearest bins bracketing the half value of maximum flux) than at 1.34keV. The top right panel of Figure 6.7 shows the typical PAHM as a function of energy at the rise, peak, fast-decay and slow-tail for this event (indicated by labels in Figure 6.2).

At ~0.4-27 keV, the electron PADs are strongly beamed along the IMF (right panels of Figure 6.1) with PAHM <~30° on the rise and through the peak (the top right panel of Figure 6.7). The maximum flux in the field-aligned 157.5-180° PA bin is ~3-8 times larger than the adjacent 135-157.5° PA bin (see the top right panel of Figure 6.2, for example). Simulations of the instrumental angular response show that these ratios correspond to an actual PAHM of <~ 15°. These highly anisotropic PADs at low energies would be expected when electrons undergo adiabatic focusing along diverging IMF lines with very little PA scattering. After the peak, the beamed PADs gradually broaden with time for ~20-70 min until the PAHM reaches typically ~50-60° in the slow tail (when present). Above ~ 50°, the simulations show the PAHM determined by the procedure of Figure 6.6 would reflect the actual PAHM. This PA broadening is related to later arrivals of electrons at smaller parallel speeds $V_{||} = V|\cos(\alpha)|$ and/or the increasing scattering. In the decay phase, although field-aligned ($V_{||} \sim V$) electrons dominate the flux, non-field-aligned (smaller $V_{||}$) electrons show a slower flux decrease (see the top right panel

of Figure 6.2, for example), and then their flux ratio to field-aligned electrons increases with time, leading to the broadening of PADs with time.

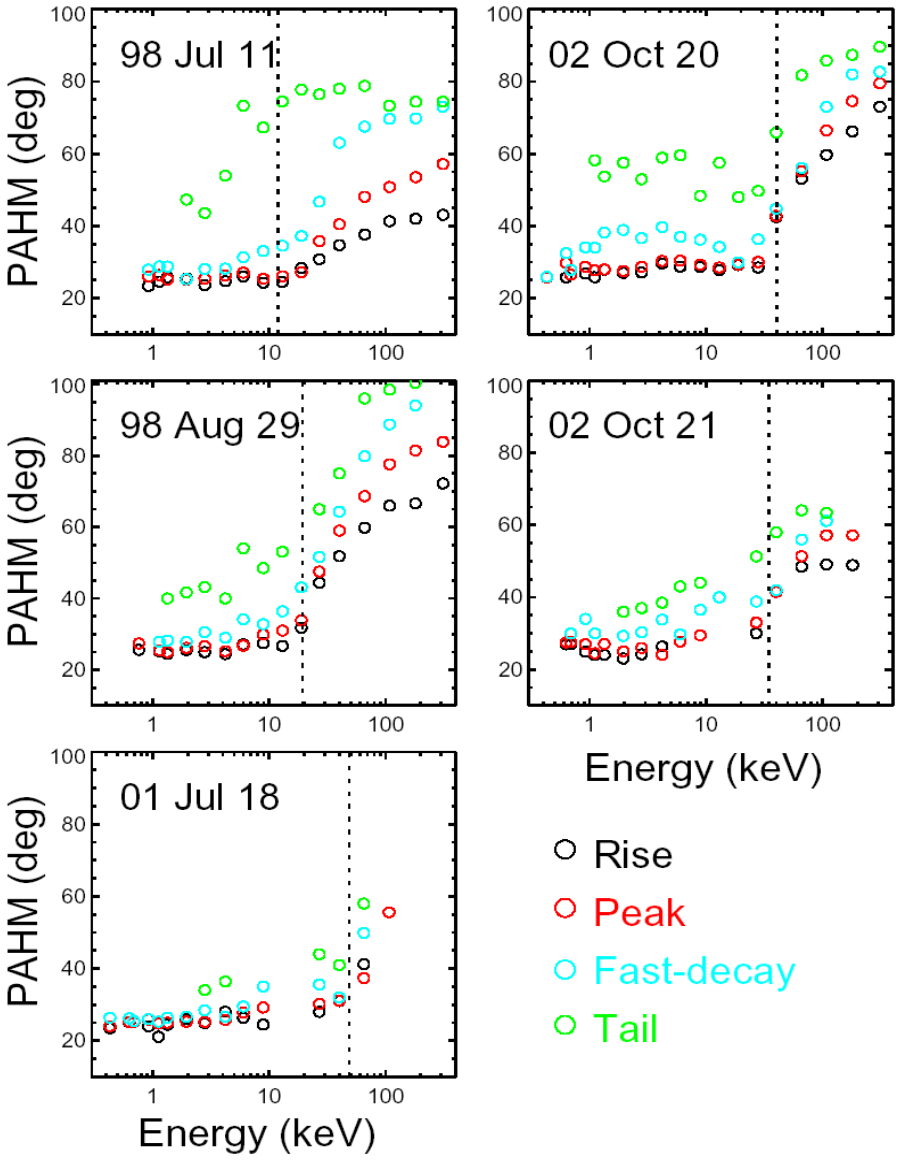

Figure 6.7. The energy dependence of the typical PAHM at the rise (black), peak (red), fast-decay (blue) and slow-tail (green) in the five solar impulsive electron events. In the 11 July 1998 and 20 October 2002 event, the tail PAHM is determined before the arrival of inward-traveling electrons in the peak #2. The dash lines indicate the transition energy E_0 between two populations with different PAHM behaviors.

At ~30-300 keV, the electron PADs broaden with energy and the maximum flux in the field-aligned 157.5-180° PA bin becomes similar to the adjacent 135-157.5° PA bin. During the peak, the PAHM increases from 42° at 40 keV to 80° at 310 keV, but the flux-time profiles keep a strongly "scatter-free" shape. Such PADs and temporal profiles imply that at high energies, outward-traveling electrons experienced strong local PA scattering that would broaden the PA distribution without significantly distorting the temporal profile, with scattering strength increasing with energy. These PADs also broaden with time after onset above 70 keV, as expected for later arrivals of scattered electrons and/or the increasing scattering, while below 70 keV the PADs broaden after the fast decay (this is not seen in the other four events). In the slow-decay tail, after the PAHM reaches around 65°, 80°, 85°, 87° and 90°, respectively, at 40, 66, 108, 180 and 310 keV, it stays roughly constant until the start of peak #2 (when present).

6.2.1.1.2 Local inward-traveling electrons

During the peak #1, an inward-flux increase was clearly detected at ~66-310 keV (see Figure 6.2 and 6.6, for example). It appears only in the 67.5-90° PA bin with the maximum slightly delayed from the adjacent outward 90-112.5° PA bin, while no significant fluxes show above the background in the other three inward PA bins. The flux ratio of the inward 67.5-90° PA bin to the adjacent outward 90-112.5° PA bin is 8-15% at the peak and increases to 20-50% during the decay. The overlapping between adjacent PA bins, introduced by the instrumental response, would only account for a flux ratio < 5%. Thus, the inward flux observed at 66-310 keV was mainly due to inward-traveling electrons, likely caused by local weak, small-angle scattering across 90° PA, or adiabatic mirroring near 90° PA at stronger downstream IMF that is close to the spacecraft. For example, the IMF was 6.3 nT around 1415UT at the spacecraft (bottom panels of Figure 6.2), and at the observed V_{sw} of 660 km/s, this field would travel only <~ 0.006AU beyond at 1437UT when the 66 keV outward-traveling electrons peaked at the spacecraft with an IMF of ~ 6.0 nT. So these electrons would very shortly (<7 s) encounter a 5% larger (6.3nT vs. 6nT) field strength downstream. Then electrons at 90-103° PA (a fraction within the 90-112.5° PA bin) could presumably be reflected to 77-90° PA, based on adiabatic invariance of $\sin^2\alpha/B$. Those local inward-traveling electrons would be mirrored back soon by converging IMF.

In EESA (below 30 keV), an inward-flux increase occurred in all inward PA bins during the peak #1 (see right panels of Figure 6.2, for example). At each energy channel, this increase temporally correlated well with the flux increase in the field-aligned, outward 157.5-180° PA bin but have a magnitude of only < 2% of the outward flux. Such increase is likely caused by scattering of a small fraction of outward-traveling electrons at the entrance of EESA. In SST, an abrupt flux "bump" occurred during 1427-1432 UT simultaneously in all inward PA bins at all energies above 66 keV (not shown), probably associated with the passage of a flux tube of different particle fluxes at those energies [Mazur et al., 2000].

6.2.1.2 Peak #2 (inward-traveling)

At 66 keV (left panels of Figure 6.2), the flux-time profiles of inward-traveling electrons show a broad, nearly symmetric peak (#2) around 1610UT in the 0-90° PA bins, with the maximum that is ~1-10% of the peak #1 at 1437UT in the outward 90-180° PA bins. This symmetric inward peak was clearly detected at 27-180 keV, with a velocity dispersion giving an injection peak-time t_{02} = 1430±0017 UT and a path length L_2=4.74±0.81 AU (middle of left panel of Figure 6.3). It suggests that these inward-traveling electrons originated far beyond the spacecraft, likely from magnetic mirroring/scattering of outward-traveling electrons by an abrupt boundary at the heliocentric distance of ~2 AU (since L_2-L_1 ≈ 3.5 AU, about two times the smooth spiral field length between the Earth and the 2.2 AU heliocentric distance for the observed V_{sw} of 660 km/s), whereas across-90°-PA scattering spread out over a long path would favor a slow-rise, very slow-delay profile. At 1 AU, these electrons also show rather isotropic PADs, implying that strong scattering occurred only near the spacecraft so that it isotropized the PAD in the inward hemisphere without distorting the temporal profile. Note that the peak #2 in 78.9º PA bin shows a delay after other PA bins; this is discussed in the § 6.2.1.4. The peak #2 was poorly detected below 25 keV by EESA-H, due to the low signal-to-noise ratio (see right panels of Figure 6.2, for example).

6.2.1.3 Peak #3 (outward-traveling)

At 1 AU, the *in situ* flux-time profiles of outward-traveling electrons exhibit a rough symmetric peak (#3) at 27-180 keV, superimposed on the slow-decay of the peak #1 (left panel of Figure 6.1 and left top panel of Figure 6.2). The velocity dispersion analysis of those peak-flux times gives an injection peak-time t_{02} = 1438±0013 UT and a path length L_3= 6.25±0.60 AU (top of left panel of Figure 6.3). These outward-traveling electrons mainly originated from reflection of inward-traveling electrons in the peak #2 by converging IMF between the Sun and Earth, e.g., at the heliocentric distance of ~ 0.3 AU estimated from the smooth spiral field model. These electrons also show isotropic PADs, implying the presence of local strong PA scattering.

6.2.1.4 PA dispersion

If the electrons at the same energy are produced simultaneously at all PAs and then all propagate the same distance l to reach the spacecraft without scattering, then electrons with larger $V_{\parallel}$ would arrive earlier, i.e., $t(\alpha)= t_o^{'} + l/V_{\parallel}(\alpha)$; this is called PA dispersion. Under scatter-free conditions, the estimate of distance l would be equal/close to the path length L estimated from the velocity dispersion. Under diffusive conditions, the l could be of the order of the average travel distance between scatterings near the spacecraft, giving a rough estimate of the local mean free path. In Figure 6.8, the peak-flux times of the 66 keV electrons at different α linearly fit to a distance l of 0.004±0.05 AU for the peak #1 (bottom) and an l of 0.21±0.19 AU for the peak #2 (top), indicative of small local mean free path and thus strong local scattering near the spacecraft.

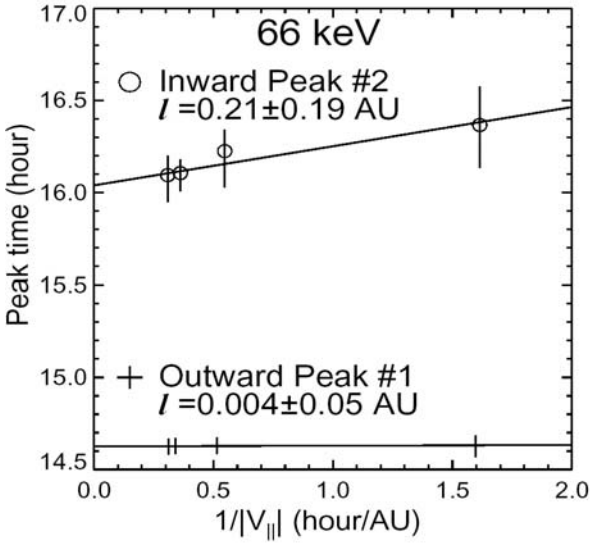

Figure 6.8. Examples of the PA dispersion analysis of the peak-flux time versus inverse parallel speed for the 20 October 2002 event. The crosses indicate the times of peak #1 in four outward PA bins at 66 keV, and the circles indicate the times of peak #2 in four inward PA bins. The slope of the linear fit, $t(\alpha) = t'_o + l/V_{||}(\alpha)$, gives estimate of the travel distance l, if electrons propagate scatter-free. The PA α is determined as the average PA for each PA bin.

6.2.1.5 Summary

In the 20 October 2002 event, the electron flux-time profiles at 1 AU exhibit three peaks, #1, 2 and 3, successively. The peak #1, detected at 0.3-310 keV, was the initial passage of outward-traveling electrons at the spacecraft. Some of these outward-traveling electrons were turned back at a radial distance of ~1 AU beyond the spacecraft by magnetic mirroring/scattering. Then they propagated inward and passed the spacecraft to produce the peak #2 at energies of 27-180 keV (and perhaps also below 25 keV). As those inward-traveling electrons continued propagating toward the Sun, they were eventually reflected back by converging IMF and then traveled outward again to yield the peak #3 detected at 27-180 keV at 1 AU.

During the peak#1, at ~0.4-27 keV, electrons exhibit strongly scatter-free temporal profiles and highly anisotropic PADs, indicating nearly scatter-free propagation through the IPM at those energies. At ~30-300 keV, electrons exhibit strongly scatter-free temporal profiles but less anisotropic PADs that broaden with energy, suggesting that high-energy electrons experienced some energy-dependent scattering and strong scattering could only occur near 1 AU. In addition, local inward-traveling populations were detected just across 90° PA at 66-310 keV during the peak #1, likely resulting from local small-angle scattering or magnetic mirroring of outward-traveling electrons across 90° PA.

The velocity dispersion analysis of *in situ* peak-times above 25 keV shows that the estimated injection peak-time, t_{02}(1430±0017UT) and t_{03}(1438±0013UT), for peak #2 and 3, appear systematically delayed after the estimate t_{01}(1412±0002UT) for peak #1 (see left panel of Figure 6.3). These estimates are obtained under assumption that in a given peak, all the electrons above 25 keV traveled the same distance from the Sun to the spacecraft. However, if all the electrons in

the three peaks were injected at the same t_{01} at the Sun, then the actual travel distance at energy E would be $L(E) = L_j + v(E) \times (t_{0j} - t_{01})$, where the peak index j =1, 2 or 3. Thus, the delay of t_{02} and t_{03} implies that in peak #2 and 3, electrons at higher energies traveled an actual longer distance than at lower energies. This is consistent with PAD observations above 25 keV, suggesting that higher-energy electrons experienced relatively stronger scattering.

6.2.2 The other four impulsive electron events

The 11 July 1998, 29 August 1998, 18 July 2001 and 21 October 2002 events have similar scatter-free time profiles and beamed PADs.

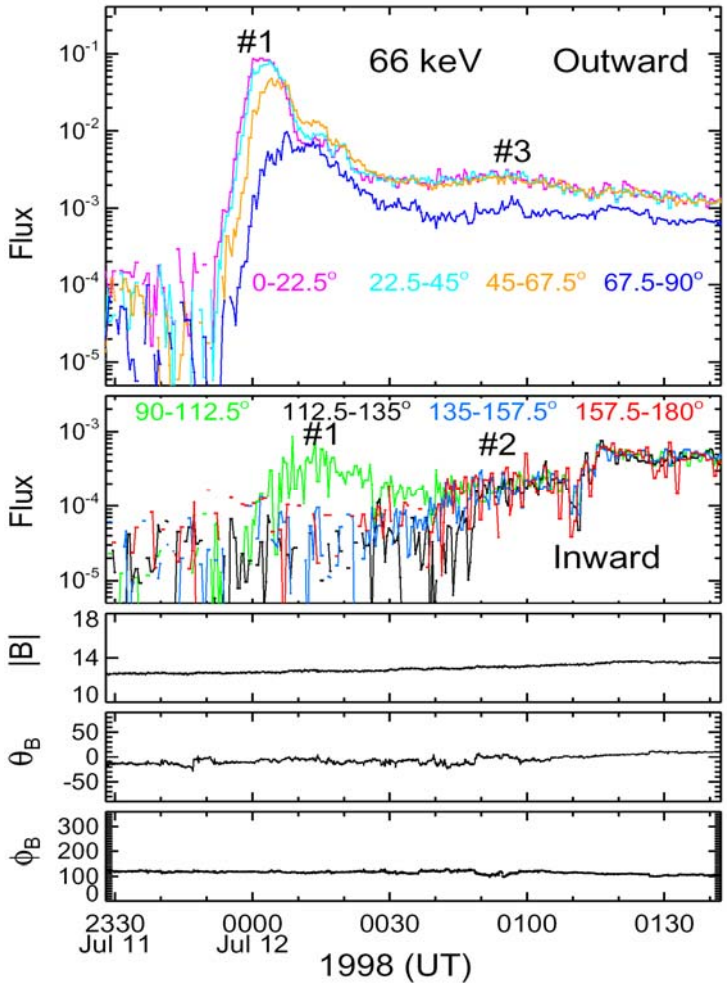

Figure 6.9. The temporal profiles of background-subtracted electron fluxes at 66 keV in four outward-traveling (0-22.5°, 22.5-45°, 45-67.5°, 67.5-90°) and four inward-traveling (90-112.5°, 112.5-135°, 135-157.5°, 157.5-180°) PA bins for the 11 July 1998 event. Colored curves indicate the flux in different PA bins. The bottom panels show the magnitude, polar angle and azimuthal angle of the IMF.

6.2.2.1 The 11 July 1998 event

The 11 July 1998 event was detected near the center of a magnetic cloud where the IMF line is presumably less coiled (the topology of magnetic flux rope favors more helical field lines at larger distance from its axis) [Larson et al., 1997]. In this event, the IMF pointed away from the Sun. Figure 6.9 shows background-subtracted electron fluxes versus time in four outward (0-90°) and four inward (90-180°) PA bins at 66 keV. The flux-time profiles exhibit three peaks, #1, 2 and 3, successively, at ~0002UT, 0055UT and 0057UT on July 12. An abrupt flux "bump" occurred during 0009UT−0021UT simultaneously in all outward PA bins at all energies from 27 to 310 keV, and another abrupt flux increase occurred at 0110 UT simultaneously in all inward PA bins (also evident in outward PA bins that have low fluxes) at all energies from 27 to 108 keV, both probably caused by the passage of a flux tube of high particle fluxes at those energies [Mazur et al., 2000].

The peak #1, detected at ~0.9-310 keV, was caused by the initial passage of outward-traveling electrons at the spacecraft. The velocity dispersion analysis of the peak times above 25 keV gives an injection peak-time of 2340±0002UT and a path length of 1.21±0.10 AU, comparable to the 1.16 AU smooth spiral field length calculated for the measured average V_{sw} of ~390 km/. The PADs of these outward-traveling electrons can be divided into two groups (top left panel of Figure 6.7). At 0.9-13 keV, the PAHM is below 27° (limited by the instrumental resolution) and doesn't change from onset through peak; afterwards, it increases with time until reaches ~50-70° in the decay. At ~19-300 keV, the PADs become broader and their PAHM increases with both energy and time, e.g., from 30° (43°) at onset to 47° (73°) at the fast-decay for 27 keV (310 keV). These suggest that low-energy electrons propagated nearly scatter-free, while high-energy electrons experienced more scattering with strength increasing with energy. In addition, for peak #1, the PA dispersion analysis of peak times in different PA bins gives an average travel distance *l* of 0.09±0.03 AU and 0.28±0.14 AU, respectively, at energies above 15 keV and below, indicative of stronger local scattering for high-energy electrons.

During the peak #1, the local inward-traveling electrons were clearly detected at 40-180 keV only in the 90-112.5° PA bin, with a flux maximum slightly delayed from the adjacent outward 67.5-90° PA bin (see Figure 6.9, for example). The flux ratio of the inward 90-112.5° PA bin to the outward 67.5-90° PA bin is 7-10% at the peak and increases to 20-30% afterwards. The observed inward flux was due to inward-traveling electrons likely resulting from local small-angle scattering or mirroring across 90° PA.

Because of closed connected IMF lines within the magnetic cloud (unlike open IMF lines in undisturbed solar wind), sooner or later, electrons in the peak #1 propagated toward the Sun and some of them were mirrored back by stronger field. At 1 AU, the mirrored electrons started to arrive and produce a peak (#2) at 27-180 keV in inward PA bins, about 20-40 minutes after the peak #1 (see Figure 6.9, for example). But their velocity dispersion was obscured by the abrupt flux increase at 0110 UT that was probably associated with the passage of a flux tube of high particle fluxes. As these electrons continued propagating along closed field lines, they were mirrored back again by strong IMF close to the Sun. Then they passed the spacecraft once more to yield a small peak (#3) at 27-180 keV in outward PA bins, superimposed on the slow-decay tail of the peak # 1. The velocity dispersion analysis of those peak times gives an injection peak-time of 2343±0020UT and a path length of 3.56±0.81 AU.

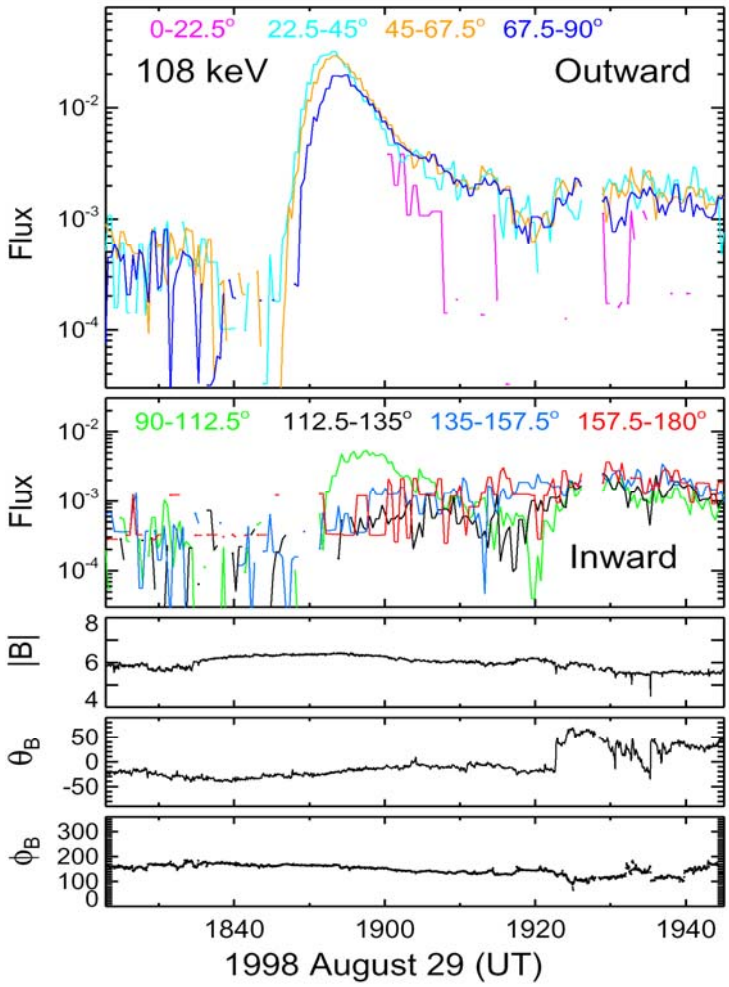

Figure 6.10. The temporal profiles of background-subtracted electron fluxes at 108 keV in four outward-traveling (0-22.5°, 22.5-45°, 45-67.5°, 67.5-90°) and four inward-traveling (90-112.5°, 112.5-135°, 135-157.5°, 157.5-180°) PA bins for the 29 August 1998 event. Colored curves indicate the flux in different PA bins. The bottom panels show the magnitude, polar angle and azimuthal angle of the IMF.

6.2.2.2 The 29 August 1998 event

The 29 August 1998 event was detected at ~0.8-300 keV with the IMF pointing away from the Sun and the average V_{sw} of ~550 km/s (corresponding to a 1.09 AU smooth spiral field length). A 1.14±0.10 path length is obtained from the velocity dispersion analysis of peak times above 25 keV. Figure 6.10 shows background-subtracted electron fluxes versus time in four outward (0-90°) and four inward (90-180°) PA bins at 108 keV. The flux-time profiles of outward-traveling electrons exhibit a rapid-rise, rapid-decay peak, followed by a slow decay at much lower flux levels. A data gap occurred from 1813UT to1900UT in the field-aligned (0-22.5°) PA bin at all energies above 25 keV. In this event, electron PADs exhibit different behaviors at energies below ~10 keV and above (middle left panel of Figure 6.7). At ~0.8-10 keV, the PAHM remains below 30° (limited by the instrumental resolution) through the peak. At

~13-300 keV, the PAHM increases with both energy and time from ~27° at onset for 13 keV up to ~100° in the slow tail for 200-300 keV.

During the peak, the local inward-traveling electrons were detected at 66-180 keV only in the 90-112.5° PA bin, with a flux maximum delayed from the adjacent outward 67.5-90° PA bin (see Figure 6.10, for example). The flux ratio of the inward 90-112.5° PA bin to the outward 67.5-90° PA bin is ~20-30% at the peak and afterwards increases to 40-60%, indicating that these inward-traveling electrons originated from local small-angle scattering or mirroring of a fraction of electrons in the 67.5-90° PA bin across 90° PA. An abrupt flux "bump" occurred during 1906-1917UT simultaneously in all inward PA bins at all energies of 27-66 keV (not shown), probably caused by the passage of a flux tube of high particle fluxes at those energies [Mazur et al., 2000].

6.2.2.3 The 18 July 2001 event

The 18 July 2001 event was detected at ~0.4-180 keV with the V_{sw} of 670 km/s (corresponding to a 1.06 AU smooth spiral field length) and the IMF pointing away from the Sun. The velocity dispersion analysis of peak times above 25 keV gives a path length of 1.13±0.35 AU. In this electron event, the PAHM of PADs remains roughly constant below 30° (limited by the instrumental resolution) from onset through peak at energies below ~10 keV, and it broadens with both energy and time at energies above 25 keV from ~30° up to ~60° (bottom left panel of Figure 6.7), while statistics were poor between 10-25 keV. Figure 6.11 shows background-subtracted electron fluxes versus time in four outward (0-90°) and four inward (90-180°) PA bins at 40 keV.

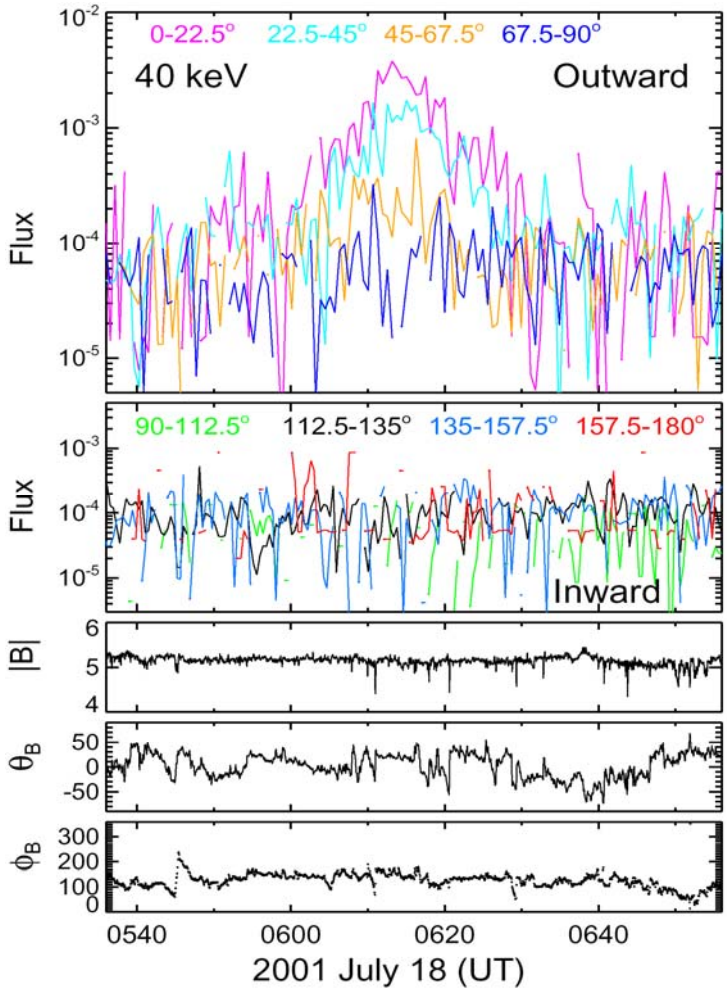

Figure 6.11. The temporal profiles of background-subtracted electron fluxes at 40 keV in four outward-traveling (0-22.5°, 22.5-45°, 45-67.5°, 67.5-90°) and four inward-traveling (90-112.5°, 112.5-135°, 135-157.5°, 157.5-180°) PA bins for the 2001 July 18 event. Colored curves indicate the flux in different PA bins. The bottom panels show the magnitude, polar angle and azimuthal angle of the IMF.

6.2.2.4 The 21 October 2002 event

The 21 October 2002 event was detected at ~0.3-180 keV with the IMF pointing toward the Sun. The velocity dispersion analysis of peak times above 25 keV gives a 1.14±0.10 AU path length, close to the 1.07 AU the smooth spiral field length calculated for the observed V_{sw} of 610 km/s. In this event, the PAHM remains below 30° (limited by the instrumental resolution) from onset through peak at energies below ~10 keV, and it broadens with both energy and time above 25 keV from ~30° up to ~65° (middle right panel of Figure 6.7), while poor statistics occurred between 10-25 keV. Figure 6.12 shows background-subtracted electron fluxes versus time in four outward (90-180°) and four inward (0-90°) PA bins at 40 keV.

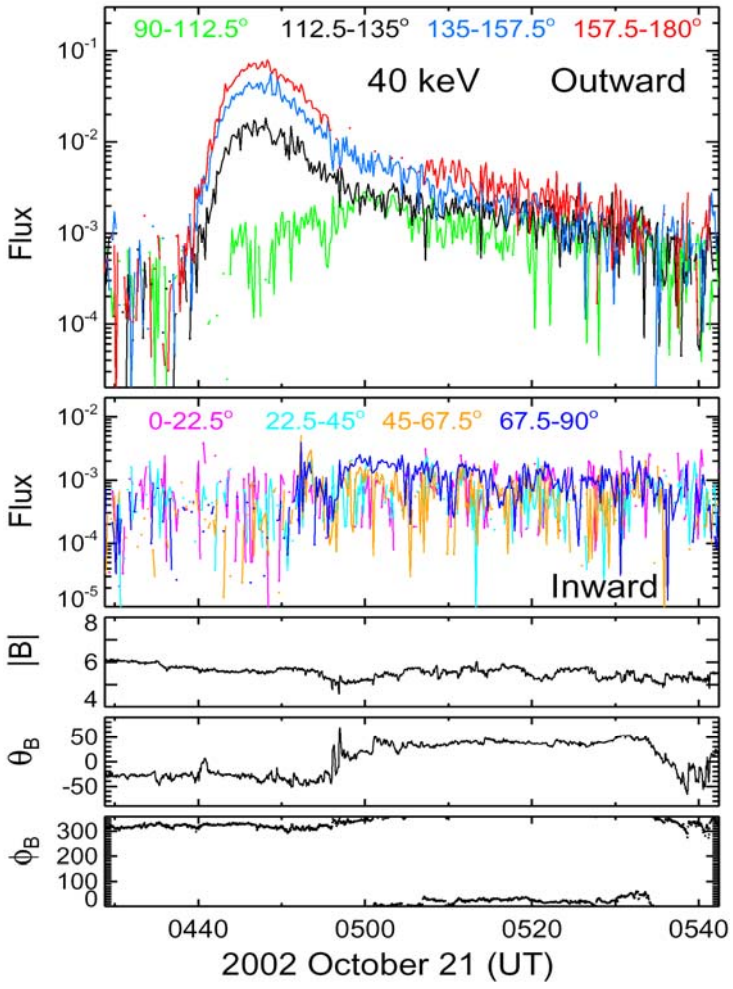

Figure 6.12. The temporal profiles of background-subtracted electron fluxes at 40 keV in four outward-traveling (90-112.5°, 112.5-135°, 135-157.5°, 157.5-180°) and four inward-traveling (0-22.5°, 22.5-45°, 45-67.5°, 67.5-90°) PA bins for the 21 October 2002 event. Colored curves indicate the flux in different PA bins. The bottom panels show the magnitude, polar angle and azimuthal angle of the IMF.

6.3 Summary and Discussion

After correction for pre-event background, we have investigated five solar impulsive electron events with strongly scatter-free temporal profiles at ~0.3-300 keV. Their electron PADs exhibit two different behaviors at low and high energies, with the energy transition E_0 varying from ~10 to 30 keV from event to event (see Figure 6.7). At low energies (~0.3keV to E_0), the PAHM remains roughly constant below 30° (corresponding to an actual PAHM of <~15°, limited by the instrumental response) from onset through peak. At high energies (E_0 to 300 keV), the PAHM increases with both energy and time, e.g., from ~30° (50°) at E_0 up to 85° (100°) at 300 keV at the peak (slow-tail). It suggests that in these events, low-energy electrons propagated essentially scatter-free through the IPM, while high-energy electrons experienced more PA scattering, with scattering strength increasing with energy. For high-energy electrons, the observed flux-time profiles retain a rapid-rise, rapid-decay peak and the estimated path length is only ~4-18% longer than the smooth spiral field length, indicating that strong scattering, if it existed within 1 AU, only occurred near 1 AU since strong scattering (mean free path <~ 0.4 AU) throughout the inner solar system would produce a fast-rise, very slow-decay (with the e-folding decay time of > 4hours for mean free path <~ 0.4 AU) peak [Lin, 1974] and a much larger path length.

Figure 6.13 shows the ratio, Λ, of the peak flux of outward-traveling scattered electrons to field-aligned scatter-free electrons for the five solar impulsive electron events. Here, we use the field-aligned outward PA bin to determine the flux for scatter-free electrons and the other three outward PA bins to average the flux for outward-traveling scattered electrons. The peak-flux ratio Λ is plotted versus the electron gyroradius $\rho_e = \gamma m_e v_e/qB$ in terms of the local thermal proton gyroradius $\rho_{Tp} = \sqrt{2m_p kT_p}\,/\,qB$. The average kTp (where k is the Boltzmann constant), determined from the solar wind proton distribution measured by WIND/3DP ion electrostatic analyzers (PESA-L), was 6.8, 11.5, 33.4, 26.6 and 22.1 eV, respectively, for the 11 July 1998, 29 August 1998, 18 July 2001, 20 October 2002 and 21 October 2002 event. Open symbols indicate the peak-flux ratio Λ at high energies (E_0 to 300 keV) for the five events, while crosses show the Λ at low energies (~0.3 keV to E_0) for the 20 October 2002 event, which is representative of the low-energy Λ in the five events.

For the five electron events, although the energy transition E_0 varies from ~10 to 30 keV and the Tp varies from ~7 to 33 eV, the E_0 always corresponds to a ρ_{e0} ~ 0.7-1.2 ρ_{Tp}, close to the spatial scale breakpoint near ρ_{Tp} in the solar wind turbulence power spectrum ($P \propto \lambda^{\beta}$) between the inertial range (β =5/3) above and dissipation range (β ~3) below [Leamon et al., 1999]. At energies for electrons with gyroradius < ρ_{e0}, the ratio of the peak flux of scattered electrons to field-aligned scatter-free electrons, Λ, remains < 10%. At energies for electrons with gyroradius > ρ_{e0}, the peak-flux ratio Λ increases with ρ_e from ~10-15% to ~50-80%, fitting to a power-law with exponents of ~1.6-2.3. These results can be explained in terms of electron resonant interactions with the solar wind turbulence at $\lambda \sim \rho_e$. Low-energy electrons would be weakly scattered because of weak power densities for resonant fluctuations/waves at scale $\lambda < \rho_{Tp}$ (the dissipation range). High-energy electrons would scatter more due to stronger power densities for fluctuations/waves at scale $\lambda > \rho_{Tp}$ (the inertial range), and the power-law increase of Λ with ρ_e may be associated with the power-law increase of turbulence power density with λ. Note that the 11 July 1998 event, detected during a magnetic cloud in the slow solar wind, gives similar results to the other four electron events detected in the normal fast solar wind.

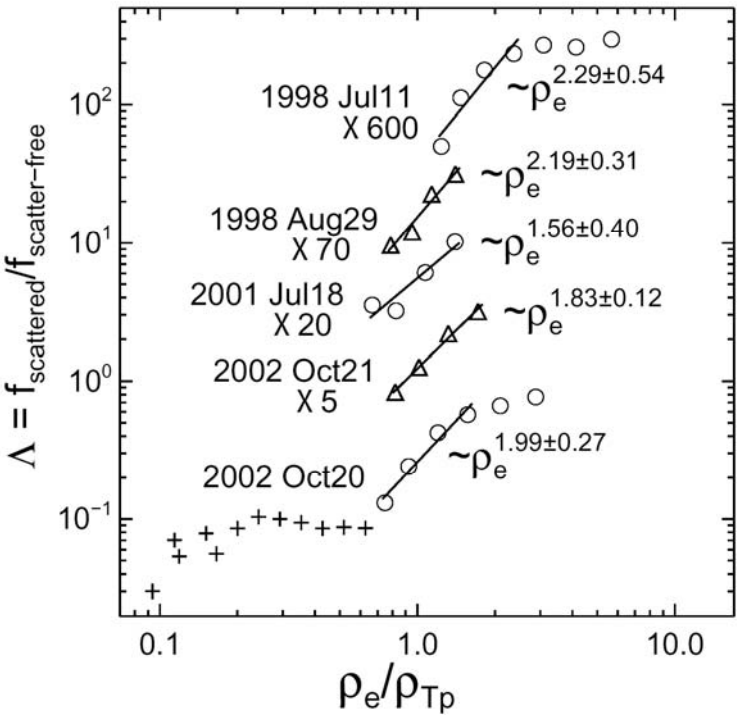

Figure 6.13. The ratio Λ of the peak flux of outward-traveling scattered electrons and field-aligned scatter-free electrons for the five solar impulsive electron events. The X-axis shows the electron gyroradius (ρ_e) in terms of the observed local thermal proton gyroradius (ρ_{Tp}) in the solar wind. After background subtraction, we use the field-aligned outward PA bin to determine the flux for scatter-free electrons and the other three outward PA bins to calculate the average flux for outward-traveling scattered electrons. For the 20 October 2002 event, the crosses show the peak-flux ratio Λ for low-energy electrons that had essentially scatter-free PADs, and the bottom open circles show high-energy electrons that had scattered PADs. For the other four events, the open symbols show the ratio Λ at high energies, which has been multiplied by different factors. The power-law fit to high-energy ratios is presented.

The resonance scattering would depend on the proton temperature Tp as well as the electron energy. The Tp decreases as $r^{-0.8}$ to $r^{-1.0}$ from 0.3 to 1.0 AU [Totten et al., 1995] and as $r^{-0.5}$ to $r^{-0.7}$ beyond 1 AU [Gazis & Lazarus, 1982; Richardson et al., 1995] for both fast and slow solar wind, where r is the heliocentric distance. As solar energetic electrons propagate away from the Sun, then, the resonant wave scale in term of ρ_{Tp}, $\lambda/\rho_{Tp} \sim \rho_e/\rho_{Tp} \sim \gamma v_e/\sqrt{Tp}$, gradually increases with r. Electrons would start to encounter "efficient" resonate scattering by waves of $>\sim\rho_{Tp}$ at heliocentric distance r_0. The r_0 decreases with increasing electron energy, e.g., r_0 is ~0.2, 0.9 and 9 AU, respectively, for 100, 20 and 2 keV, if Tp varies as $r^{-1.0}$ with a value of 10 eV at 1 AU. En route to 1 AU, therefore, as well as adiabatic focusing, low-energy electrons presumably undergo very little scattering, while high-energy electrons experience "efficient" scattering along a distance ($L(1AU) - L(r_0)$) increasing with energy. This is consistent with the PAD observations in the five events.

Assuming scatter-free propagation for the first-arriving electrons at 1 AU, Krucker et al. [1999] found the injection of the >25 keV electrons were often delayed by ~10 to ~30 min after the type III radio bursts at the Sun, and Haggerty & Roelof [2002] found a median delay of ~10 min for 38-315 keV electrons. Using forward triangular-fitting, Wang et al. [2006; Chapter 4] obtained the electron injection profiles at the Sun for three impulsive electron events, and found that the solar injection of the ~13-300 keV electrons started ~8 min after the type III bursts and ~17 min after the ~0.4-10 keV electrons. Here, we show that although high-energy electrons were scattered, strong scattering likely occurred only near 1 AU and the estimated electron path length is <~1.3 AU. Even for a 1.3 AU travel distance, the electron travel time is only ~2 min longer at 300 keV and ~5 min longer at 30 keV, compared to propagation along a 1.1 AU length. Thus, the previously reported delay of ~10-30 min for high-energy electrons cannot be explained by propagation effects in the IPM (as proposed by Cane & Erickson [2003] and Cane [2003]), and this delay must reflect the actual delay in the solar injection of high-energy electrons.

We also find evidence for local small-angle scattering or magnetic mirroring across 90° PA. During the peak of outward-traveling electrons, inward-traveling electrons were detected just across 90° PA at 40-180keV, 66-180keV and 66-300 keV, respectively, in the 11 July 1998, 29August 1998 and 20 October 2002 event. Compared to electrons in the adjacent outward PA bin, these inward-traveling electrons show a slightly delayed maximum flux with a ~7-30% magnitude, suggesting that they were produced locally by small-angle scattering or magnetic mirroring of a fraction of the outward-traveling electrons in the adjacent PA bin across 90° PA. If the source is resonance scattering, then it cannot be explained by the theories that resonance scattering is suppressed around 90° PA (so-called the resonance gap) [Jokipii, 1966; Schlickeiser, 1989]. If the source is magnetic mirroring, then the downstream IMF strength would be larger by only < 17%, since the >~ 17% stronger magnetic field can reflect all the electrons, not just a fraction of them, in the 22.5° wide, outward PA bin next to 90° PA. On the other hand, at energies below 40-66 keV in the three events, outward-traveling electrons had relatively small fluxes in the PA bin next to 90° PA, so the local inward-traveling populations produced by scattering or mirroring would be insignificant with regard to the background.

In the 20 October 2002 event, a fraction of initial outward-traveling electrons (in the peak #1) were turned back likely by structures with enhanced IMF/waves at the heliocentric distance of ~ 2AU. These structures might be the corotating interaction region (CIR) shocks generated by the compression between fast and slow solar wind, that form typically at a heliocentric distance of > 1.5 AU [Smith & Wolfe, 1976]. As these electrons traveled toward the Sun, they were mirrored back by converging IMF and propagated outward again. These inward-traveling and newly outward-traveling populations were successively detected above 25 keV at 1 AU, each showing a rough symmetric peak (#2 and 3, respectively) in the flux-time profile but rather isotropic PADs. Such observations may suggest that strong scattering could occur near 1 AU. Moreover, the velocity dispersion analysis shows that the estimated injection peak-time for peak #2 and 3 is systematically delayed after the estimate for peak #1. This implies that at higher energies, the scattering was relatively stronger and then led to an actual longer electron path. In the 11 July 1998 event, similar electron populations, peak #2 and 3, were also detected, and they were caused by reflection during propagation along the closed IMF lines in the magnetic cloud.

Based on the results of this chapter, we can conclude the following:

1) In solar impulsive electron events, low-energy (<~ 10-30 keV) and high-energy (>~ 10-30 keV) electrons propagate differently, with substantially more scattering at high energies. Such scattering is consistent with waves/turbulence at scale >~ the thermal ion gyroradius, that could be generated by solar wind ions.

2) At high energies, even though there is more scattering, the scattering is not enough to produce the detected electron injection delays as suggested by Cane & Erickson [2003] and Cane [2003].

3) There is evidence for local small-angle scattering and/or magnetic reflection across 90° PA.

4) There is also evidence for reflection/scattering by distant structures (e.g., CIRs) that produces a peak of inward-traveling electrons and then by strong IMF close to the Sun that produces another peak of outward-traveling electrons. At high energies, scattering is not enough to destroy such peaks, even after a long propagation.

7. Conclusions and Future work

This final chapter summarizes the conclusions of research presented in this thesis, and discusses future observations using new instrumentation and orbit/mission.

7.1 Conclusions

The primary conclusions of this thesis are listed as follows:

1) Similar to sunspots and SXR flares, the observed occurrence rate of solar electron events near the Earth shows a strong solar-cycle variation: ~10/year at solar minimum but ~190/year at solar maximum. After correction for the effect of high background from previous events, etc., the estimated occurrence frequency of solar electron events exhibits a good power-law distribution: $dN/dJ=A\times J^{-\gamma}$; at 40 keV, the estimated occurrence rate near the Earth is ~1000/year at solar maximum and ~30/year at solar minimum above ~2.9×10^{-4} (cm^2 s str eV)$^{-1}$ (the detected minimum peak flux at 40 keV), up to one order of magnitude larger than the observed occurrence rate. This implies that many small electron events are likely missed due to high background or limited instrument sensitivity. If the power-law distribution extends down to much lower fluxes, then the electron event occurrence rate could be even orders of magnitude larger. In addition, for type III storms that consist of groups of extremely frequent type III bursts, the associated electron events would occur so frequently that they would completely merge together en route to 1 AU. These weak and/or bursty solar electron events may contribute to the formation of the quiet-time or slowly varying "superhalo" interplanetary electron population [Lin, 1998]. The *in situ* observation close to the Sun will help us to verify the above speculations (see §7.2.2).

2) Solar energetic electron events have a one-to-one association with type III radio bursts and a close association with ^{3}He-rich ion emissions; these ^{3}He-rich electron events or electron/^{3}He-rich SEP events have a close association with narrow (<~ 60°) CMEs. Previous studies have shown that type III radio bursts are closely associated with coronal jets (when present) observed in SXR and EUV [Aurass et al., 1994; Kundu et al., 1995; Raulin et al., 1996; Christe et al., 2008]. Such jets are interpreted as signatures of magnetic reconnection between closed active-region loops and open filed lines, and they might appear as faint and narrow CMEs high in the corona [Shimojo & Shibata, 2000; Kahler et. al., 2001; Y. M. Wang et al., 2006].

For the electron/^{3}He-rich SEP events selected in our case study, the low-energy (~0.4 to 6-9 keV) electron injection starts ~9 min before the coronal release of the type III radio burst (see Figure 7.1); the high-energy (~13 to ~300 keV) electron injection starts ~8 min after the type III burst and occurs when the associated CME passes altitudes of ~1-6 R_S; the injection of ~MeV/nucleon, ^{3}He-rich ions begins ~1 hour later when the associated CME is at altitudes of ~ 2-10 R_S.

Thus, we think that in electron/^{3}He-rich SEP events, low-energy electrons are accelerated in jets that are ejected upward from magnetic reconnection sites between closed and open

field lines, and these electrons generate type III radio bursts; high-energy electrons are accelerated at >~ 1 R_S by CMEs acting on the seed electrons provided by the low-energy injection; ~MeV/nucleon, ^{3}He-rich ions are accelerated by selective resonance with electron-beam generated waves [Temerin & Roth, 1992] and/or by fast, narrow CMEs. To further verify where and when particles are accelerated in these SEP events, we need *in situ* particle observations close to the Sun (see § 7.2.2)

3) In the IPM within 1 AU, low-energy (<~ 10-30 kev) electrons propagate essentially scatter-free, while high-energy (>~ 10-30 keV) electrons experience more scattering with increasing energy. Such scattering is caused by resonance with waves/turbulence at scale >~ the thermal proton gyroradius in the solar wind, that could be generated by solar wind protons. Although a transition to more scattering occurs at energies where the electron injection delays are detected, the scattering is not enough to produce these delays as suggested by Cane [2003]. The *in situ* observation close to the Sun will improve our understanding of the particle propagation through the IPM.

4) We find evidence for local small-angle scattering or magnetic reflection across 90° PA, and evidence for reflection/scattering by distant structures (e.g., CIRs) and by strong IMF close to the Sun.

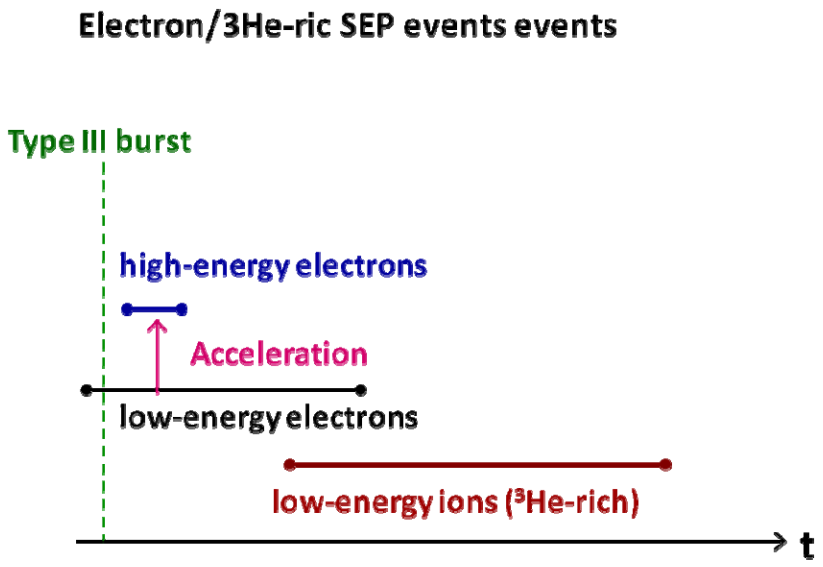

Figure 7.1. Schematic of the timing and duration of particle injections in electron/^{3}He-rich SEP events. The horizontal black line represents the low-energy (~0.3 to 6-9 keV) electron injection with duration of ~1-3 hours, the horizontal blue line the high-energy (9-13 to ~300 keV) electron injection with duration of ~10-30 minutes, and the horizontal dark red line the ~MeV/nucleon, ^{3}He-rich ion injection with duration of ~3-9 hours. The vertical green dash line indicates the coronal release of type III radio bursts.

7.2 Future work

7.2.1 New instrumentation

In the past, silicon semiconductor detectors (SSDs) have typical thresholds of ~20-30 keV (e.g., SST in WIND/3DP), so electrostatic analyzers (e.g., EESA in WIND/3DP) are widely used to measure particles at energies below ~20-30 keV. However, electrostatic analyzers have significant intrinsic background (mainly caused by radioactivity of the microchannel plate glass) and relatively small geometric factor, so that they are unable to detect very weak SEP events. Therefore, a new instrument was developed with next-generation SSDs and electronics that brought their energy threshold down to well below ~ 20 keV (see §7.2.1.1).

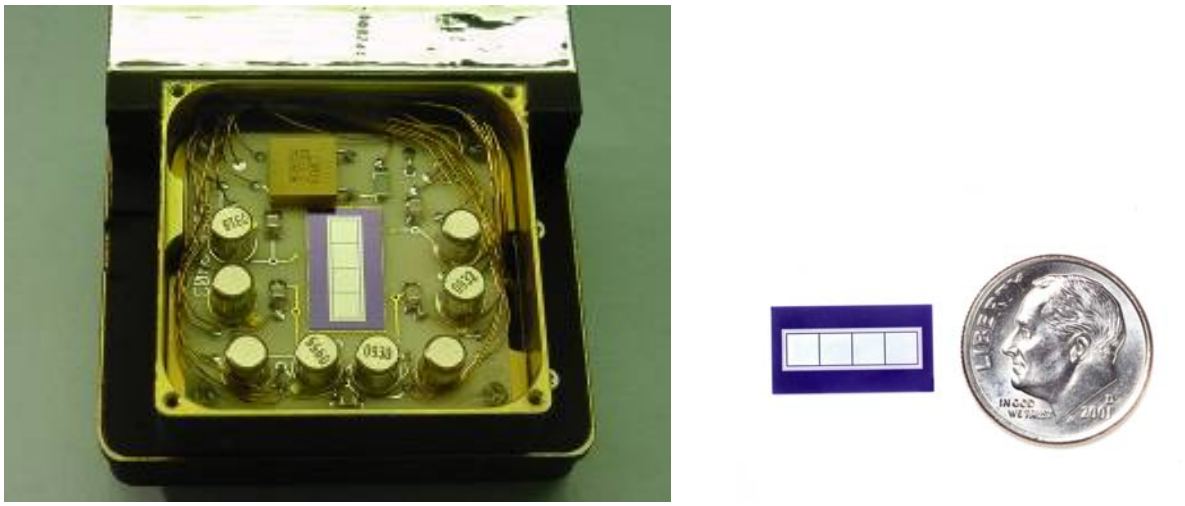

Figure 7.2. Left: Detector board back side shown in housing. Right: Size comparison between the four pixel (each 0.09 cm^2) SSDs with guard rings and the dime.

7.2.1.1 STE

The prototype of the new-generation electron sensors is the STE (SupraThermal Electron) instrument [Lin et al., 2008] – part of the IMPACT (In situ Measurements of Particles and CME Transients) investigation [Luhmann et al., 2008], one of the four instrument packages on the two STEREO (Solar TErrestrial RElations Observatory) spacecraft (launched October 2006). The STE instrument, developed by Space Sciences Laboratory at University of California, Berkeley, utilizes arrays of small (3mm × 3mm, low capacitance) SSDs (Figure 7.2), fabricated with an unusually thin (200Å) window dead layer, so <~2 keV electrons can penetrate and be detected. The SSDs are surrounded by a guard ring and cooled to ~30 to –90° C to minimize leakage current, and coupled to state-of-the-art pulse-reset front-end electronics to obtain an electronic threshold of ~1.5 keV for electrons, well below the typical SSD thresholds of >~20-30 keV, e.g., SSTs of WIND/3DP. STE also detects ions, neutrals, and X-rays [see Hsieh et al., 2009] that penetrate the window (neutrals will be immediately stripped in traversing the SSD window and then detected as an ion in the active volume of the SSD) and deposit >~2 keV in the SSD active

volume (>~4 keV for incident protons/hydrogen). EUV/UV/visible light is absorbed in the SSD window leading to increased leakage current, but at the level of geocoronal emissions the STE performance is unaffected. Compared to previous sensors (electrostatic analyzers) below ~20-30 keV, e.g., EESA-H in WIND/3DP, STE provides much lower intrinsic background and about 2 orders of magnitude increase in sensitivity, while requiring about an order of magnitude less resources - few cm size, ~100 grams mass, ~100s milliwatts power. It also provides intrinsic energy resolution of <~1 keV FWHM, with the particles counts binned into energy channels of $\Delta E/E$ ~10-25%.

STE has two oppositely directed arrays of four detectors - STE-U(0, 1 ,2, 3) and STE-D(0, 1, 2, 3), respectively, observing particles coming from and toward the Sun. Each STE-D (U) detector has a FOV of 65°×16.8° (57°×14.5°) full width half maximum (FWHM), forming a total FWHM FOV of 65°×67° (57°×58°) nominally centered on the nominal Parker spiral field direction and a total geometric factor of 0.1 (0.08) $cm^2 \cdot sr$. However, STE-U is unexpectedly saturated by sunlight scattered into detectors, likely due to its relocation from the original design in the spacecraft's shadow to the spacecraft's front side; STE-U performed well when the spacecraft was behind the Earth (part of the early orbit) and the sunlight was blocked by the Earth's body.

Figure 7.3 summaries the typical STE-D observations of solar impulsive electron events (black cross), interplanetary super-halo (>~ 2 keV) electrons (green circle), upstream ion events (red circle), terrestrial energetic neutral atoms (ENAs) from the ring current (green cross; submitted to Geophysical Research Letters), anomalous ENAs (red dot) and galactic X-rays from SCO X-1 [Hsieh et al., 2009] (blue cross). The upstream ion events originate from the acceleration at the Earth's bow shock or the leakage of magnetospheric particles accelerated within the magnetosphere. ENAs are produced by charge exchange of energetic ions with cold neutrals and they freely escape along a straight line from their place of birth, allowing remote sensing of space plasma.

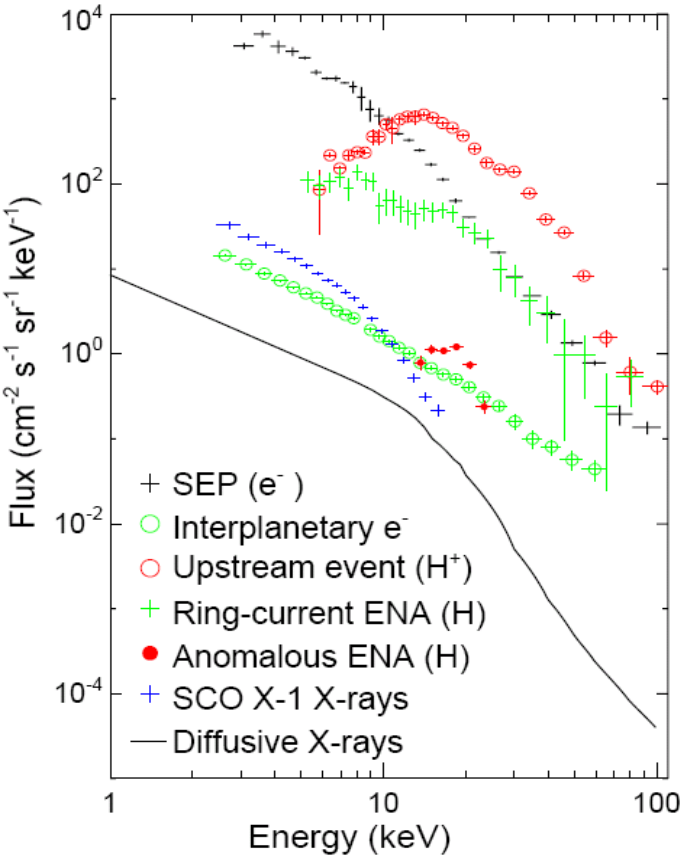

Figure 7.3. STEREO/STE-D observations. The black crosses show the electron peak fluxes for the impulsive SEP event on November 19, 2006. The red circles show the proton fluxes for the 13 November 2006 upstream ion event. The green circles show the typical fluxes of interplanetary super-halo electrons. The green crosses show the hydrogen ENA fluxes originating from the Earth's ring current on November 6, 2006. The red dots show anomalous ENA fluxes observed in 2007 January. The blue crosses show the observed X-ray fluxes from SCO X-1. The black curve represents the predicted background in STE induced by diffusive X-rays.

7.2.1.2 STEIN

A modified version of STE, called STEIN (SupraThermal Electrons, Ions, & Neutrals**),** adds a simple parallel plate electrostatic deflection system in front to the STE sensor to separate electrons from ions from neutrals (Figure 7.4). Low-energy electrons and ions are swept to opposite sides to be detected by the two edge detectors, while neutrals (un-deflected) and high-energy ions and electrons (less deflected) are detected by the two center detectors. The deflection voltage can be swept to cover a wide range of ion and electron energies (up to ~ 40 keV) and angles. By measuring the energy spectra from the edge detectors for each deflection voltage step and exploiting the convolved energy-angle response, we can obtain both energy and angular information for electrons and ions. On the other hand, the deflection voltage can completely sweep ions and electrons up to ~20 keV away from the two center detectors, allowing the clean detection of neutrals up to ~ 20 keV. The STEIN edge detectors and center detectors have total sweep-averaged geometric factors of 0.002 and 0.02 cm^2 sr, respectively.

STEIN will be flown as part of the payload of the upcoming NSF-funded CubeSat mission "CINEMA" (Cubesat for Ion, Neutral, Electron, MAgnetic fields) planned for launch in late 2011, to measure terrestrial electrons, ions and neutrals. And two more CINEMAs are planned to be developed and flown by Kyung Hee University, as part of the Korean World Class University program. STEIN is also part of the Energetic Particle Detector suite on Solar Orbiter (§7.2.2.1).

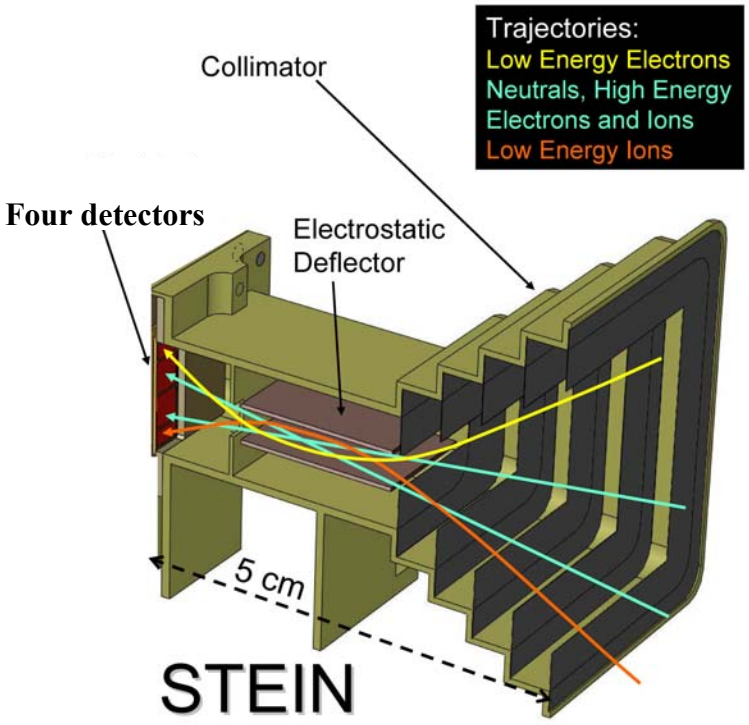

Figure 7.4. Cutaway view of STEIN, showing schematic particle trajectories: low-energy electrons (red) and ions (yellow), neutrals and high-energy electrons and ions (blue). Taken from the CINEMA proposal.

7.2.2 New missions

Since the discovery of SEP events in 1942 [Forbush, 1946], almost all *in situ* SEP observations have been made near 1 AU and beyond. Such observations integrate the information of particle injection at the Sun and the effects of propagation from the Sun to Earth or beyond. Thus, direct measurements closer to the sun could significantly improve our understanding of SEP acceleration and transport. These near-Sun measurements will be provided by the following upcoming missions to visit the inner heliosphere within ~0.2 AU (Solar Orbiter) or ~10 R_S (Solar Probe Plus).

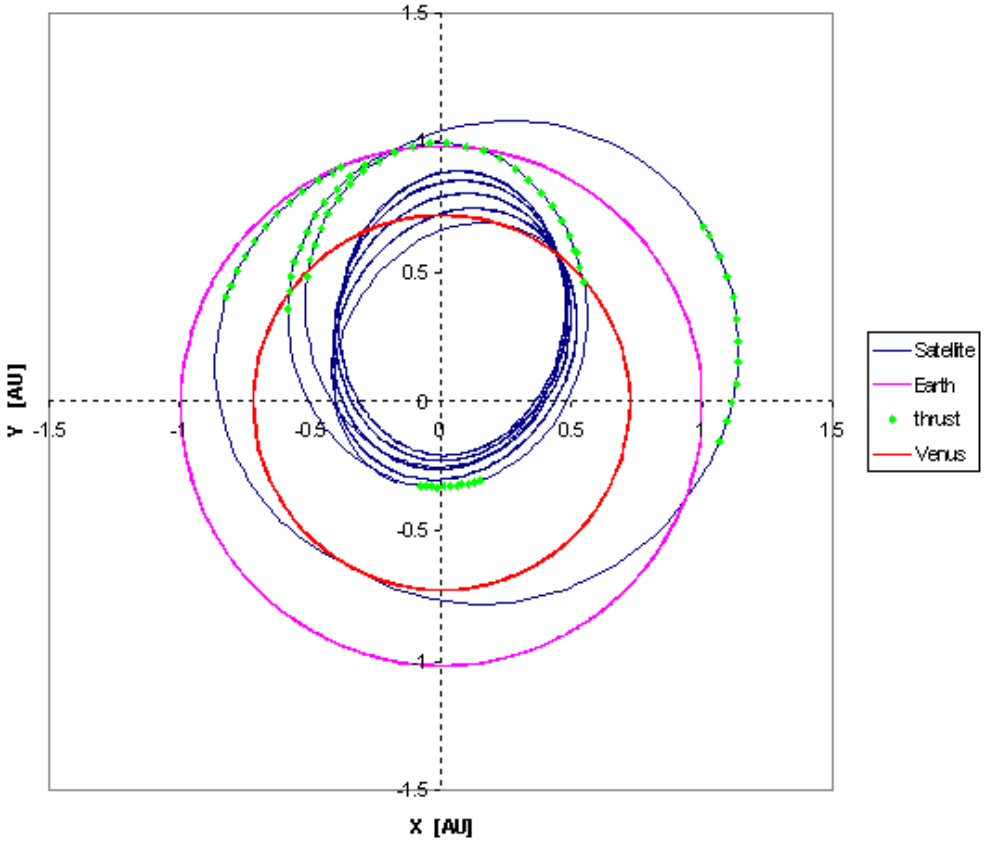

Figure 7.5. The predicted Solar Orbiter's trajectory projected on the ecliptic plane. The dark blue curve represents the 150-day-long elliptical solar orbits of Solar Orbiter. The red curve represents the Earth's orbit and the purple curve shows the Venus's orbit.

7.2.2.1 Solar Orbiter

Solar Orbiter (SolO) is a European Space Agency (ESA) mission, as part of a joint ESA-NASA Heliophysical Explorers programme that also includes NASA's Solar Sentinels mission, and will provide unprecedented close-up and high-latitude observations of the Sun. Its main scientific goals are:

- to determine in-situ the properties and dynamics of plasma, fields and particles in the near-Sun heliosphere;
- to survey the fine detail of the Sun's magnetized atmosphere;
- to identify the links between activity on the Sun's surface and the resulting evolution of the corona and inner heliosphere, using solar co-rotation passes;
- to observe and characterize the Sun's polar regions and equatorial corona from high latitudes.

SolO is a three-axis stabilized spacecraft equipped with instruments for both in-situ measurements and remote-sensing observations: Energetic Particle Detector (including STEIN and the Suprathermal Ion Spectrograph), Extreme Ultraviolet Imager, Magnetometer, Coronagraph, Visible Imager & Magnetograph, Radio and Plasma Waves, Heliospheric Imager, EUV Spectrometer, X-ray Imager, Solar Wind Plasma Analyser. About 3.4 years after the launch (planned in ~ 2015-2018), SolO will be placed into an elliptical orbit about the Sun with perihelia ranging from 0.23 to 0.38 AU and aphelia from 0.73 to 0.88 AU (see Figure 7.5). After an in-ecliptic phase of perihelion passes where it is nearly corotating with the Sun, SolO will utilize multiple Venus gravity assist maneuvers to increase the inclination of its orbit to progressively higher heliolatitudes, reaching ~34° by the end of its extended mission.

For SEP observations at heliocentric distances of ~0.2 AU, the propagation effects would be much less than at 1 AU; the *in situ* particle flux would be ~ 25 times larger than the *in situ* flux at 1 AU. Thus, such close-up measurement would allow detection of weaker SEP events and more accurate estimates of particle acceleration and release at the Sun. These measurements will also improve our understanding of the particle propagation within ~0.2 AU, and between ~0.2 and 1 AU by comparison with the measurements at 1 AU.

7.2.2.2 Solar Probe Plus

Solar Probe Plus (SP+) is a proposed NASA's mission that will perform the humanity's first visit to the solar corona. Approaching as close as 9.5 R_S from the Sun's center, SP+ will employ a combination of *in situ* and remote measurements to achieve the mission's primary scientific goals:

- to determine the structure and dynamics of the magnetic fields at the sources of the fast and slow solar wind;
- to trace the flow of energy that heats the corona and accelerates the solar wind;
- to determine what mechanisms accelerate and transport energetic particles;
- to explore dusty plasma near the Sun and its influence on solar wind and energetic particle formation.

After the planned launch in May 2015, SP+ will orbit the Sun 24 times with a 3.4°-inclination from the ecliptic, utilizing seven Venus flybys to reduce the perihelion distance from 35 R_S to a minimum of 9.5 R_S (see Figure 7.6). On the final three orbits, SP+ will fly within 9.5 R_S of the Sun's center. During the designed mission life of ~ 7years, SP+ will spend a total of 961 hours inside 20 R_S, 434 hours inside 15 R_S and 30 hours inside 10 R_S. At such close-up

vantage points, the *in situ* particle measurements combined with remote-sensing observations can provide crucial evidence to understand where, when and how SEPs are accelerated.

For SEP observations at heliocentric distances of <~ 10 R_S, the *in situ* particle flux would be ~ 400 times larger than the *in situ* flux at 1 AU, allowing detection of much weaker SEP events, and accurate estimates of particle acceleration and release at the Sun. Such locations would also allow clear detection of short-duration or bursty SEP events occurring close together; at 1AU, those events will be mixed together by propagation. In addition, the PADs measured at distances of ~10 R_S can directly tell us the altitudes of particle release, based on adiabatic magnetic focusing (due to the invariance of $\sin^2\alpha/B$). For example, if particles are released with isotropic PADs and the IMF decreases as r^{-2}, then a 60º PA width measured at 10 R_S indicates the solar release occurring at 8.7 R_S, and a measured 10º width indicates the release at 1.7 R_S. For gradual SEP events [Kahler, 1994] and perhaps also some impulsive SEP events (see Chapter 5) that are accelerated at ~10 R_S, direct measurements in the acceleration region would provide crucial evidence for the nature of the acceleration, e.g., the shock geometry, the existence of waves, the acceleration temporal and spatial scale, and the seed populations. Finally, the comparison between observations from SP+, SolO and the spacecrafts at 1 AU (e.g, on WIND, ACE and STEREO) will allow a comprehensive study of the particle propagation from the Sun to 1 AU.

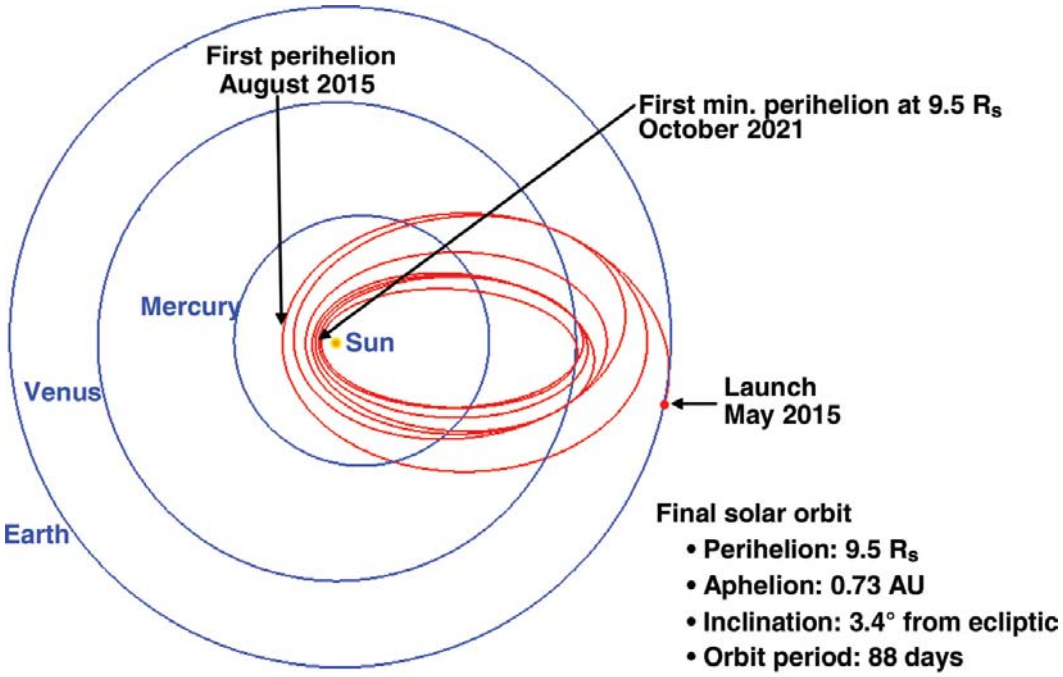

Figure 7.6. The Solar Probe Plus trajectory.

References

Anderson, K. A., and R. P. Lin (1966), Observations on the Propagation of Solar-Flare Electrons in Interplanetary, *Space, Phys. Rev. lett.*, **16**, 1121-1124.

Andrews, M. D. (2003), A search for CMEs associated with big flares, *Solar Phys.*, **218**, 261–279.

Armstrong, T. P., M. E. Pesses, and R. B. Decker (1985), Shock Drift Acceleration, in *Collisionless Shocks in the Heliosphere: Review of Current Research, Geophys. Monogr. Ser.,* vol. **35,** edited by B. T. Tsurutani and R. G. Stone, p. 271, AGU, Washington, D. C..

Aurass, H., K.-L. Klein, and P. C. H. Martens (1994), First detection of correlated electron beams and plasma jets in radio and soft x-ray data, *Sol. Phys.*, **155**, 203.

Ball, L. and D. B. Melrose (2001), Shock Drift Acceleration of Electrons, Publications of the Astronomical Society of Australia, Volume **18**, Issue 4, pp. 361-373.

Benz, A.O. (2002), *Plasma Astrophysics: Kinetic Processes in Solar and Stellar Coronae*, vol. 279 of Astrophysics and Space Science Library, Kluwer, Dordrecht, Netherlands; Boston, U.S.A., 2nd edn.

Berger, M. J., S. M. Seltzer, S. E. Chappell, J. C. Humphreys, and J. W. Motz (1969), Response of silicon detectors to monoenergetic electrons with energies between 0.15 and 5.0MeV, *Nucl. Instrum. Methods*, **69**, 181.

Carrington, R. C. (1859), Description of a Singular Appearance seen in the Sun on September 1, 1859. *Monthly Notices of the Royal Astronomical Society*, **20**, 13 – 15.

Cane, H. V., R. E. McGuire, and T. T. von Rosenvinge (1986), Two classes of solar energetic particle events associated with impulsive and long-duration soft X-ray flares, *Astrophys. J.*, **301**, 448.

Cane, H.V. (2003), Near-Relativistic Solar Electrons and Type III Radio bursts, *Astrophys. J.,* **598**, 1403.

Cane, H.V., and W.C. Erickson (2003), Energetic particle propagation in the inner heliosphere as deduced from low-frequency (<100 kHz) observations of type III radio bursts, *J. Geophys. Res.,* **108**, 1203.

Christe, S. S. Krucker, and R. P. Lin (2008), Hard X-Rays Associated with Type III Radio Bursts, *Astrophys. J.,* **680**, L149-152.

Cliver, E. W. (2009), History of research on solar energetic particle (SEP) events: the evolving paradigm, *Universal Heliophysical Processes, Proceedings of the International Astronomical Union, IAU Symposium,* **257**, 401-412.

Cliver, E. W., S. W. Kahler., and D. V. Reames (2003), Coronal Shocks and Solar Energetic Proton Events, Proceedings of the 28th International Cosmic Ray Conference, July 31-August 7, Trukuba, Japan, p.3331.

Coleman, P. J. (1968), Turbulence, Viscosity, and Dissipation in the Solar-Wind Plasma , *Astrophys. J.*, **153**, 371.

Crosby, N. B., M. J. Aschwanden, and B. R. Dennis (1993), Frequency distributions and correlations of solar X-ray flare parameters, *Solar Physics*, **146**, 177-190.

Denskat, K.U., and E. M. Neubauer (1983), Observations of hydromagnetic turbulence in the solar wind, in M. Neugebauer (ed.), *Solar Wind Five,* NASA Conf. Publ., CP-2280, p.81.

Desai, M. I., G. M. Mason, J. R. Dwyer, J. E. Mazur, C. W. Smith, and R. M. Skoug (2001), Acceleration of ^{3}HE Nuclei at Interplanetary Shocks, *Astrophys. J.,* **553**, L89-92.

Drake, J. F., M. Swisdak, , H. Che, and M. A. Shay (2006), Electron acceleration from contracting magnetic islands during reconnection, *Nature*, **443**, 553

Drake, J. F., P. A. Cassak,M. A. Shay, M. Swisdak, and E. Quataert (2009), A Magnetic Reconnection Mechanism for Ion Acceleration and Abundance Enhancements in Impulsive Flares, *Astrophys. J.*, **700**, 16-20.

Dulk, G. A. (1985), Radio emission from the sun and stars, *ARA&A*, **23**, 169.

Earl, J. A. (1976), The effect of adiabatic focusing upon charged-particle propagation in random magnetic fields, *Astrophys. J.*, **205**, 900-919.

Ergun, R.E., et. al. (1998), Wind spacecraft observations of solar impulsive electron events associated with solar type III radio bursts, *Astrophys. J.,* **503**, 435.

Fisk, L. A. (1978), ^{3}He-rich flares - A possible explanation, *Astrophys. J.*, **224**, 1048-1055.

Forbush, S. E. (1946), Three Unusual Cosmic-Ray Increases Possibly Due to Charged Particles from the Sun, *Phys. Rev*., **70**,771.

Franz, H.B., P. Sharer, K. Ogilvie, and M. Desch (2001), Wind Nominal Mission Performance and Extended Mission Design. *J. Astronaut. Sci.* **49 (1)**, 145-167.

Gazis, P. R. and A. J. Lazarus (1982), Voyager observations of solar wind proton temperature:1-10 AU, *Geophys. Res. Lett.*, **9**, 431-434.

Gopalswamy, N., S. Nunes, S. Yashiro, and R. A. Howard (2004), Variability of solar eruptions during cycle 23, *Adv. Space Res.*, **34(2)**, 391-396.

Gopalswamy, N., E. Aguilar-Rodriguez, S. Yashiro, S. Nunes, M. L. Kaiser, R. A. Howard (2005), Type II radio bursts and energetic solar eruptions, *J. Geophys. Res.* **110**, A12S07.

Gosling, J. T., et al. (2003), Solar electron bursts at very low energies: Evidence for acceleration in the high corona?, Geophys. Res. Lett., **30(13)**, 1697, doi:10.1029/2003GL017079.

Grognard, R. J.-M. (1982), Numerical simulation of the weak turbulence excited by a beam of electrons in the interplanetary plasma, *Solar Phys.,* **81**, 173-180.

Harrison, R. A. (1995), The nature of solar flares associated with coronal mass ejection, *A&A*, **304**, 585.

Haggerty, D.K. and E.C. Roelof (2002), Near-Relativistic Beam-Like Electron Events Observed at 1 AU, *Astrophys. J.,* **579**, 841.

Hey, J. S. (1946), Solar Radiations in the 4-6 Metre Radio Wave-Length Band, *Nature*, **157**, 47-48.

Heyvaerts, J., Priest, E. R., and Rust, D. M. (9177), An emerging flux model for the solar flare phenomenon, *Astrophys. J.*, **216**, 123.

Hirayama, T. (1974), Theoretical Model of Flares and Prominences. I: Evaporating Flare Model, *Sol. Phys.*, **34**, 323-338.

Hsieh, K. C., et al. (2009), A Re-Interpretation of STEREO/STE Observations and Its Consequences, *Astrophys. J.*, **694**, L79-82.

Hsieh, K. C., and J. A. Simpson (1970), The Relative Abundances and Energy Spectra of ^{3}He and ^{4}He from Solar Flares, *Astrophys. J.*, **162**, L191

Ho, G. C., E. C. Roelof, G. M. Mason, D. Lario, and J. E. Mazur, Onset study of impulsive solar energetic particle events, *Adv. Space Res.*, **32(12)**, 2679-2684.

Jokipii, J. R. (1966), Pitch-Angle Dependence of First-Order Fermi Acceleration at Shock Fronts, *Astrophys. J.*, **145**, 616.

Kahler, S. W. (1994), Injection profiles of solar energetic particles as functions of coronal mass ejection heights, *Astrophys. J.*, **428**, 837.

Kahler, S. W., D. V. Reames, and N. R. Jr. Sheeley (2001), Coronal Mass Ejections Associated with Impulsive Solar Energetic Particle Events, *Astrophys. J.*, **562**, 558-565.

Kahler, S. W., E. Hildner, and M. A. I. van Hollebeke (1978), Prompt solar proton events and coronal mass ejections, *Solar Phys.* **57**, 429.

Kahler, S. W., E. W. Cliver, H. V. Cane, R. E. McGuire, D. V. Reames, N. R. Jr. Sheeley, and R. A. Howard (1987), Solar Energetic Proton Events and Coronal Mass Ejections Near Solar Minimum, *Proc. 20th Int. Cosmic Ray Conf.*, *Moscow* **3**, 121.

Kahler, S.W., N. R. Jr. Sheeley, R. A. Howard, M. J. Koomen, D. J. Michels, R. E. McGuire, T. T. von Rosenvinge, and D. V. Reames (1984), Associations between coronal mass ejections and solar energetic proton events, *J. Geophys. Res.* **89**, 9683.

Kartavykh, Y.Y., W. Dröge, G.A. Kovaltsov, andV.M. Ostryakov (2006), *Adv. Space Res.*, **38**, 516.

Klecker, B., D. Hovestadt, M. Scholer, G. Gloeckler, F. M. Ipavich, C. Y. Fan, and L. A. Fisk (1984), Direct determination of the ionic charge distribution of helium and iron in ^{3}He-rich solar energetic particle events, *Astrophys. J.*, **281**, 458-462.

Klecker, B., E. Möbius, and M. A. Popecki (2007), Ionic Charge States of Solar Energetic Particles: A Clue to the Source, *Space Sci. Revs.*, **130**, 273-282.

Klecker, B., E. Möbius, M. A. Popecki, L. M. Kistler, H. Kucharek, and M. Hilchenbach (2006), Observation of energy-dependent ionic charge states in impulsive solar energetic particle events, *Adv. Space Res.*, **38**, 493-497.

Klein, K.-L., S. Krucker, G. Trottet, and S. Hoang (2005), Coronal phenomena at the release of solar energetic electron events, *Astron. Astrophys.*, **431**, 1047.

Kliem, B. (1994), Particle orbits, trapping and acceleration in a filamentary current sheet model. *Astrophys. J.*, **90**, 719–-727.

Kocharov, L., G.A. Kovaltsov, J. Torsti, and V.M. Ostryakov (2000), *Astron. Astrophys.*, **357**, 716.

Kontar, E. P., and H. A. S. Reid (2009), Onsets and Spectra of Impulsive Solar Energetic Electron Events Observed Near the Earth, *Astrophys. J.*, **695**, L140-144.

Krucker, S., D. E. Larson, R. P. Lin, and B. J. Thompson (1999), On the Origin of Impulsive Electron Events Observed at 1 AU, *Astrophys. J.,* **519**, 864.

Krucker, S., E. P. Kontar, S. Christe, and R. P. Lin (2007), Solar Flare Electron Spectra at the Sun and near the Earth, *Astrophys. J.*, **663**, L109-112.

Kundu, M. R., J. P. Raulin, N. Nitta, H. S. Hudson, M. Shimojo, K. Shibata, and A. Raoult (1995), Microwave and Hard X-Ray Observations of Footpoint Emission from Solar Flares,*Astrophys. J.*, **454**, 522.

Larson, D. E., et al. (1997), Tracing the topology of the October 18-20, 1995, magnetic cloud with ~0.1-10^2 keV electrons, *Geophys. Res. Lett.*, **24**, 1911-1914.

Leamon, R. J., C. W. Smith, N. F. Ness and H. K. Wong (1999), Dissipation range dynamics: Kinetic Alfvén waves and the importance of β_e, *J. Geophys. Res.*, **104**, 22331-22344.

Leblanc, Y., G. A. Dulk, and J.-L. Bougeret, Tracing the Electron Density from the Corona to 1AU, *Solar Phys.,* **183**, 165–180.

Lee, M. A. (1983), Coupled hydromagnetic wave excitation and ion acceleration at interplanetary traveling shocks, *J. Geophys. Res*., **88**, 6109.

Lemaire, J., and M. Scherer (1973), Kinetic models of solar and polar winds, *Rev. Geophys.*, **11**, 427.

Lepping, R. P., et. al. (1995), The Wind Magnetic Field Investigation, *Space Sci. Rev.*, **71**, 207-229.

Lin, R. P. (1974), Non-relativistic solar electrons, *Space Sci. Rev.*, **16**, 189.

—. (1985), Energetic solar electrons in the interplanetary medium, *Solar Phys.,* **100**, 537–561.

—. (1990), in *Basic Plasma Processes on the Sun*, ed. E.R. Priest and V. Krishnan, p. 467, International Astronomical Union, The Netherlands.

—. (1998), WIND observations of suprathermal electrons in the interplanetary medium, *Space Sci. Rev.*, **86**, 61-78.

—. (2005), Relationship of solar flare accelerated particles to solar energetic particles (SEPs) observed in the interplanetary medium, *Adv. Space Res.*, **35(10)**, 1857-1863.

Lin, R. P., D. W. Potter, D. W., D. A. Gurnett, and F. L.Scarf (1981), Energetic electrons and plasma waves associated with a solar type III radio burst, *Astrophys. J.*, **251**, 364-373.

Lin, R. P., and K. A. Anderson (1967), Electrons > 40 keV and protons > 500 keV of solar origin, *Solar Phys.,* **1**, 446-464.

Lin, R. P., et al. (1995), A three-dimensional plasma and energetic particle investigation for the Wind spacecraft, *Space Sci. Rev.*, **71**, 125.

—. (1996), Observation of an impulsive solar electron event extending down to ~0.5 keV energy,

Geophys. Res. Lett., **23**, 1211, 1996.

—. (2008), The STEREO IMPACT Suprathermal Electron (STE) Instrument, *Space Sci. Rev.*, **136**, 241–255.

Liu, S., V. Petrosian, and G. M. Mason (2006), Stochastic Acceleration of ^{3}He and ^{4}He in Solar Flares by Parallel-propagating Plasma Waves: General Results, *Astrophys. J.*, **636**, 462.

Luhmann, J. G.;, et al. (2008), STEREO IMPACT Investigation Goals, Measurements, and Data Products Overview, *Space Sci. Rev.*, **136**, 117–184.

Luhn, A., B. Klecker, D. Hovestadt, and E. Möbius (1987), The mean ionic charge of silicon in ^{3}He-rich solar flares, *Astrophys. J.*, **317**, 951-955.

Magelssen, G. R., and D. F. Smith (1977), Nonrelativistic electron stream propagation in the solar atmosphere and type III radio bursts, *Sol. Phys.*, **55**, 211-240.

Maia D., and M. Pick (2004), Revisiting the origin of impulsive electron events: Coronal magnetic restructuring,, *Astrophys. J.,* **609**, 1082.

Mancuso, S., J. C. Raymond, J. Kohl, Y.-K. Ko, M. Uzzo, and R. Wu (2003), Plasma properties above coronal active regions inferred from SOHO/UVCS and radio spectrograph observations, *Astron. Astrophys.*, **400**, 347-353.

Markovskii, S. A., B. J. Vasquez, and C. W. Smith (2008), Statistical Analysis of the High-Frequency Spectral Break of the Solar Wind Turbulence at 1 AU, *Astrophys. J.*, **675**, 1576-1583.

Mason, G. M. (2007), ^{3}He-Rich Solar Energetic Particle Events, *Space Sci. Rev.*, **130**, 231-142.

Mason, G. M., et. al. (1998), The Ultra-Low-Energy Isotope Spectrometer (ULEIS) for the ACE spacecraft, *Space Sci. Rev.*, **86**, 409-448.

Mason, G. M. et al. (2004), Abundances of Heavy and Ultraheavy Ions in ^{3}He-rich Solar Flares, *Astrophys. J.*, **606**, 555-564.

Mason, G. M., J. E. Mazur, and J. R. Dwyer (1999), ^{3}He Enhancements in Large Solar Energetic Particle Events, *Astrophys. J.*, **525**, L133-136.

Mazur, J. E., G. M. Mason, J. R. Dwyer, J. Giacalone, J. R. Jokipii, and E. C. Stone (2000), Interplanetary Magnetic Field Line Mixing Deduced from Impulsive Solar Flare Particles, *Astrophys. J.*, **532**, L79-82.

Melrose, D. B. (1974), Resonant scattering of particles and second phase acceleration in the solar corona, *Solar Phys.*, **37**, 353-365.

Miller, J. A. (1998), Particle Acceleration in Impulsive Solar Flares, *Space Science Revs.*, **86**, 79-105.

Miller, J. A., and A. F. Vinas (1993), Ion acceleration and abundance enhancements by electron beam instabilities in impulsive solar flares, *Astrophys. J.*, **412**, 386-400.

Miller, J. A., T. N. Larosa, and R. L.Moore (1996), Stochastic Electron Acceleration by Cascading Fast Mode Waves in Impulsive Solar Flares, *Astrophys. J.*, **461**, 445.

Moebius, E., M. Scholer, D. Hovestadt, B. Klecker, and G. Gloeckler (1982), Comparison of helium and heavy ion spectra in ^{3}He-rich solar flares with model calculations based on stochastic Fermi acceleration in Alfvén turbulence, *Astrophys. J.*, **259**, 397-410.

Nelson, G. S. and Melrose, D. B. (1985), Type II Bursts, in N. Labrum and D. J. McLean (eds.), *Solar Radiophysics*, Cambridge, Cambridge University Press, pp. 333–359.

Newton, H. C. (1943), Solar flares and magnetic storms. *Monthly Notices of the Royal Astronomical Society*, **103**, 244.

Nitta, N. V., et. al. (2008), Coronal Jet Observed by Hinode as the Source of a ^{3}He-rich Solar Energetic Particle Event, *Astrophys. J.*, **675**, L125-128.

Paesold, G., R. Kallenbach, and A. O. Benz (2003), Acceleration and Enrichment of ^{3}He in Impulsive Solar Flares by Electron Firehose Waves, *Astrophys. J.*, **582**, 495-505.

Pallavicini, R., S. Serio, and G. S. Vaiana (177), A survey of soft X-ray limb flare images - The relation between their structure in the corona and other physical parameters, *Astrophys. J.*, **216**, 108-122.

Parker, E. N. (1958), Dynamics of the interplanetary gas and magnetic fields, *Astrophys. J.*, **128**, 664-676.

Raulin, J. P., M. R. Kundu, H. S. Hudson, N. Nitta, and A. Raoult (1996), Metric Type III bursts associated with soft X-ray jets, *Astron. Astrophys.*, **306**, 299

Pick, M., G. M. Mason, Y.-M. Wang, C. Tan, and L. Wang (2006), Solar Source Regions for ^{3}He-rich Solar Energetic Particle Events Identified Using Imaging Radio, Optical, and Energetic Particle Observations, *Astrophys. J.*, **648**, 1247-1255.

Popecki, M. A. (2006), in *Solar Eruptions and Energetic Particles*, ed. by N. Gopalswamy, R.A. Mewaldt, J. Torsti., AGU Geophysical Monograph, vol. **165**, pp. 127–135

Potter, D. W., R. P. Lin, and K. A. Anderson (1980), Impulsive 2–10 keV solar electron events not associated with flares, *Astrophys. J.*, **236**, L97–L100.

Richardson, J. E., et al. (1995), Radial evolution of the solar wind from IMP 8 to Voyager 2, *Geophys. Res. Lett.*, **22**, 325-328.

Saito, K., A. I. Poland, and R. H. Munro (1977), A study of the background corona near solar minimum, *Sol. Phys.*, **55**, 121.

Schlickeiser, R. (1989), Cosmic-ray transport and acceleration. I - Derivation of the kinetic equation and application to cosmic rays in static cold media, *Astrophys. J.*, **336**, 243-263.

Sheeley, N. R., Jr., Howard, R. A., Koomen, M. J., & Michels, D. J. (1983), Associations between coronal mass ejections and soft X-ray events, *Astrophys. J.*, **272**, 349.

Shimojo, M., and Shibata, K. (2000), Physical parameters of solar X-ray jets, *Astrophys. J.*, **542**, 1100.

Simnett, G.M., E. C. Roelof, and D. K. Haggerty (2002), The Acceleration and Release of Near-relativistic Electrons by Coronal Mass Ejections, *Astrophys. J.,* **579**, 854.

Smith, E. J., and J. H. Wolfe (1976), Observations of interaction regions and corotating shocks between one and five AU: Pioneers 10 and 11, *Geophys. Res. Lett.,* **3**, 137.

Snyder, C. W., M. Neugebauer and U. R. Rao (1963), The solar wind velocity and its correlation with cosmic ray variations and with solar and geomagnetic activity, *J. Geophys. Res*., **68**, 6361-6370.

Speiser, T. W. (1965), Particle trajectories in model current sheets, 1. Analytical solutions, *J. Geophys. Res.*, **70**, 4219-4226.

St. Cyr, O. C., and D. F. Webb (1991), Activity associated with coronal mass ejections at solar minimum - SMM observations from 1984-1986, *Sol. Phys.*, **136**, 379.

Reames, D. V. (1995), Solar energetic particles: A paradigm shift, *Revs. Geophys.*, **33**, 585-589.

—. (1999), Particle Acceleration at the Sun and in the Heliosphere, *Space Science Rev.*, **90**, 413.

Reames, D.V., T. T.von Rosenvinge, and R. P. Lin (1985), Solar ^{3}He-rich events and nonrelativistic electron events - A new association, *Astrophys. J.,* **292**, 716.

Roth, I. and M. Temerin (1997), Enrichment of ^{3}He and Heavy Ions in Impulsive Solar Flares, *Astrophys. J.*, **477**, 940

Takakura, T., and H. Shibahashi (1976), Dynamics of a cloud of fast electrons travelling through the plasma, *Sol. Phys.*, **46**, 323-346.

Temerin, M. and I. Roth, The production of ^{3}He and heavy ion enrichment in ^{3}He-rich flares by electromagnetic hydrogen cyclotron waves, 1992, *Astrophys. J.*, **391**, L105

Totten, T. L., J. W. Freeman, J. W. and S. Arya (1995), An empirical determination of the polytropic index for the free-streaming solar wind using HELIOS 1 data, J. Geophys. Res., **100**, 13-17.

Tousey, R. (1973), The solar corona, *Space Res.,* **13**, 713.

Treumann, R. A. and T. Terasawa (2001), Electron Acceleration in the Heliosphere, *Space Sci. Rev.*, **99**, 135-150.

Trubnikov, B. A. (1965), Particle interactions in a fully ionized plasma, *Rev. Plasma Phys.*, **1**, 105.

Tsuneta, S. (1997), Moving Plasmoid and Formation of the Neutral Sheet in a Solar Flare, *Astrophys. J.*, **483**, 507-514.

Tu, C.-Y. and E. Marsch (1995), MHD structures, waves and turbulence in the solar wind: Observations and theories, *Space Sci. Rev.*, **73**, 1.

Tylka, Allan J., and M. A. Lee (2006), A Model for Spectral and Compositional Variability at High Energies in Large, Gradual Solar Particle Events, *Astrophys. J.*, **646**, 1319-1334.

Van Allen, J.A., and S.M. Krimings (1965), Impulsive Emission of 40-kev Electrons from the Sun, *J. Geophys. Res.,* **70**, 5737.

Vourlidas, A., D. Buzasi, R. A. Howard, and E. Esfandiari (2002), Mass and energy properties of LASCO CMEs, Solar variability: from core to outer frontiers, Ed. A. Wilson. ESA SP-506, Vol. **1**. Noordwijk: ESA Publications Division, p. 91.

Wang, L., R. P. Lin, S. Krucker, and G. M. Mason (2005), A Study of the Solar Injection for Eleven Impulsive Electron/3He-Rich Sep Events, *Proceedings of the Solar Wind 11 / SOHO*

16, edited by B. Fleck, T.H. Zurbuchen, H. Lacoste, p. 457, 12 - 17 June 2005, Whistler, Canada.

Wang, L., R. P. Lin, S. Krucker, and J.T. Gosling (2006), Evidence for double injections in scatter-free solar impulsive electron events, *Geophys. Res. Lett.*, **33**, L03106, doi:10.1029/2005GL024434.

Wang, Y.-M., M. Pick, and G. M. Mason (2006), Coronal Holes, Jets, and the Origin of ^{3}He-rich Particle Events, *Astrophys. J.*, **639**, 495-509.

Wild, J. P., J. D. Murray, and W. C. Rowe (1954), Harmonics in Spectra of Solar Radio Disturbances, *Austr. J. Sci. Res*,. **A7**, 439–459.

Wild, J. P., S. F. Smerd, and A. A. Weiss (1963), Solar Bursts, *ARAA*, **1**, 291.

Yashiro, S., N. Gopalswamy, G. Michal=ek, O. C. St. Cyr, S. P. Plunkett, N. B. Rich, and R. A. Howard (2004), A catalog of white light coronal mass ejections observed by the SOHO spacecraft, *J. Geophys. Res.* **110**, A07105,

Zank, G.P., W. K. M. Rice, and C. C. Wu (2000), Particle acceleration and coronal mass ejection driven shocks: A theoretical model, *J. Geophys. Res.*, **105**, 25079-25095.

Zhang, T. X. (1999), Solar ^{3}He-rich Events and Electron Acceleration in Two Stages, *Astrophys. J.*, **518**, 954.

Appendices

List of Acronyms and Abbreviations

3DP	the Three-Dimensional Plasma & Energetic Particles instrument
ACE	Advanced Composition Explorer
amu	Atomic Mass Unit
AU	Astronomical Unit
CINEMA	Cubesat for Ion, Neutral, Electron, MAgnetic fields
CME	Coronal Mass Ejection
EESA	Electron Electrostatic Analyzer
EIT	Extreme ultraviolet Imaging Telescope
EMIC	Electromagnetic Ion Cyclotron
EPACT	Energetic Particle Acceleration, Composition and Transport experiment
EUV	Extreme Ultraviolet
FOV	Field of View
FWHM	Full Width at Half Maximum
GSE	Geocentric Solar Ecliptic
GOES	Geostationary Orbiting Environmental Satellites
HXR	Hard X-ray
IMF	Interplanetary Magnetic Field
IMPACT	In situ Measurements of Particles and CME Transients investigation
IPM	Interplanetary Medium
ISEE	International Sun-Earth Explorer
LASCO	Large Angle Spectrometric Coronagraph
MCP	Microchannel Plate
MFI	the Magnetic Fields Instrument
MHD	Magnetohydrodynamics
PA	Pitch Angle
PAD	Pitch Angle Distribution
PAHM	Pitch Angle width at Half Maximum
PESA	Ion Electrostatic Analyzer
SEP	Solar Energetic Particle
SEPICA	Solar Energetic Particle Charge Analyser

SGD	Solar Geophysical Data
SOHO	Solar and Heliospheric Observatory
SolO	Solar Orbiter
SP+	Solar Probe Plus
SST	Silicon Semiconductor Telescope
STE	SupraThermal Electron instrument
STEIN	SupraThermal Electrons, Ions, & Neutral instrument
STOF	Suprathermal TimeOf-Flight energetic particle sensor
STEREO	Solar TErrestrial RElations Observatory
SXR	Soft X-ray
ULEIS	Ultra Low Energy Isotope Spectrometer
WAVES	the Plasma and Radio Waves experiment

Appendices

List of Notations

B	Magnetic field strength
c	Light of speed
C	Count rate
L	Particle path length; Magnetic field line length
m_e	Electron mass
m_p	Proton mass
Q_{Fe}	Iron ionization state
r	Heliocentric distance
Re	Earth radius
R_S	Solar radius
Tp	Solar wind proton temperature
V_{SW}	Solar wind speed
α	Pitch angle
λ	Wave length/scale
ρ_e	Electron gyroradius
ρ_{Tp}	Solar wind thermal proton gyroradius
Λ	Ratio of the peak of outward-traveling scattered electrons to field-aligned scatter-free electrons